N°d'ordre : 4000

THÈSE

en co-tutelle entre

L'UNIVERSITÉ BORDEAUX I

ÉCOLE DOCTORALE DE MATHÉMATIQUES ET INFORMATIQUE

et

L'UNIVERSITÀ DI PISA

SCUOLA DI DOTTORATO IN INGEGNERIA AEROSPAZIALE

présentée à

L'UNIVERSITÉ BORDEAUX I

par Edoardo LOMBARDI

pour obtenir le grade de

DOCTEUR

SPÉCIALITÉ : Mathématiques Appliquées et Calcul Scientifique
CURRICULUM : Fluidodinamica

LOW ORDER MODELLING FOR FLOW SIMULATION, ESTIMATION AND CONTROL

Thèse dirigée par M. Angelo IOLLO, Professeur
Mme Maria Vittoria SALVETTI, Professeur

commission d'examen :

M. Michel BERGMANN	Chargé de Recherche - INRIA Bordeaux Sud-Ouest	
M. Eric BLAYO	Professeur - Université Joseph Fourier	Rapporteur
M. Simone CAMARRI	Chercheur - Università di Pisa	
M. Thierry COLIN	Professeur - Université Bordeaux I	
M. Flavio GIANNETTI	Chercheur - Università degli studi di Salerno	
M. Angelo IOLLO	Professeur - Université Bordeaux I	Directeur
M. Laurent JACQUIN	Directeur de Recherche - DAFE/ONERA	Rapporteur
Mme Maria Vittoria SALVETTI	Professeur - Università di Pisa	Directeur

Verily, this vichyssoise of verbiage veers most verbose...

Acknowledgements

Without the support, guidance and patience of a lot of people this thesis would not have been accomplished.

I would like to express my deepest gratitude to my advisor Angelo Iollo, for his guidance, patience, and most importantly, his friendship during these years. I am deeply grateful to him for the long discussions on my work and for his continuous presence during the entire period of my research.
I thank my cotutelle advisor, Maria Vittoria Salvetti, for her guidance and for the fact to be always there to listen and give advice. I am grateful to her for giving me the possibility to work in the Departement of Aerospace Engineering in Pise.

I wish to thank for the review and the advices the referees Eric Blayo and Laurent Jacquin as well as the other members of committee Thierry Colin, Michel Bergmann, Simone Camarri, Flavio Giannetti.

A very special thank to my colleegues and mainly great friends Manlio and Lido with whom I am really pleased to work and to spend great days and evenings in Bordeaux and in Italy.

I am deeply indebted to Mario and I would like to thank for his friendship and his help especially during the “last dinner”.

A big thank to Jessie for her help and patience in our collaboration and for the infinite discussions during the coffee breaks.

Despite his opinion about football, I am grateful to Michel for his professional and useful support, in addition to the fun time spent in company.

I would also like to thank Valerio for his ideas and with whom is a great pleasure to work.

A great thanks the people with I spend a lot of time during these years in Bordeaux, Luca and his cooking, Poncherello for his good mood, Gatto and Haysam for precious help and wonderful welcome in Turin; a thank to the MC2 team in particular Heloise and her friends of intelligence service, Lisl for nice breaks and conversations, Yannick, Thomas and Victor for learning quickly my teaching in pool and for hosting me; I would like to thank Cecile for infecting me with the board game mania.

I would like to thanks l'allemand and il Cosimi for the fine sharing of a chaotic apartement in town.

Thanks to Marco who has in the hands the destiny of this final draft.

I would like to thank my friends Toro, Gessi, Barza and Lunino to make me feel Pratese everytime I came back in Italy.

A very special thanks goes to my family for all their support, encouragement and their constant presence.

I most want to thank Lisa for keeping herself close, even when far away.

This work was funded by the MENRT and INRIA. High performance computational resources were provided by IDRIS (Orsay, France) and DRIMM/M3PEC (Bordeaux, France). Local computer facilities were provided mostly by the Laboratory of Applied Mathematics (MAB) at Université Bordeaux I, France.

Réduction de modèles pour la simulation, l'estimation et le côntrole d'écoulements

L'objectif est de développer et de tester des instruments peu coûteux pour la simulation, l'estimation et le contrôle d'écoulements. La décomposition orthogonale aux valeurs propres (POD) et une projection de Galerkin des équations sur les modes POD sont utilisées pour construire des modèles d'ordre reduit des équations de Navier-Stokes incompressibles. Dans ce travail, un écoulement autour d'un cylindre carré est considéré en configuration bidimensionnelle et tridimensionnelle. Des actionneurs de soufflage/aspiration sont placés sur la surface du cylindre. Quelques techniques de calibration sont appliquées, fournissant des modèles précis, même pour les écoulements tridimensionnels avec des structures tourbillonaires compliquées. Une méthode d'estimation d'état, impliquant des mesures, est ensuite mise au point pour des écoulements instationnaires. Une calibration multi-dynamique et des techniques d'échantillonnage efficaces sont appliquées, visant à construire des modèles robustes à des variations des paramètres de contrôle. Nous amorçons une analyse de stabilité linéaire en utilisant des modèles d'ordre réduit linéarisés autour d'un état d'équilibre contrôlé. Les techniques présentées sont appliquées à écoulement autour du cylindre carré à des nombres de Reynolds compriscentre $Re = 40$ et $Re = 300$.

Mots clés: POD, modélisation d'ordre réduit, estimation, modèles robustes, contrôle

Low order modelling for flow simulation, estimation and control

The aim is to develop and to test tools having a low computational cost for flow simulation, estimation and control applications. The proper orthogonal decomposition (POD) and a Galerkin projection of the equations onto the POD modes are used to build low order models of the incompressible Navier-Stokes equations. In this work a flow past a square cylinder is considered in two-dimensional and three-dimensional configurations. Two blowing/suction actuators are placed on the surface of the cylinder. Calibration techniques are applied, providing stable and rather accurate models, even for three-dimensional wake flows with complicated patterns. A state estimation method, involving flow measurements, is then developed for unsteady flows. Multi-dynamic calibrations and efficient sampling techniques are applied to build models that are robust to variations of the control parameters. A linear stability analysis by using linearized low order models around a controlled steady state is briefly addressed. The presented techniques are applied to the square cylinder configuration at Reynolds numbers that range between $Re = 40$ and $Re = 300$.

Key words: POD, low-order modelling, estimation, robust models, control

Contents

List of Figures

Chapter 1

Introduction

In fluid dynamics one of the main topics is the study of the flow past *bluff bodies*. This kind of flow is interesting for the engineering and scientific community. Many examples of flows around bluff bodies can be found in engineering applications, for instance the flow around a wing at high incidence in the aeronautical and automotive industry, or the wind past a high rise building in civil engineering. When the Reynolds number overcomes a critical value, these flows are characterized by a vortex shedding wake. This phenomenon causes noise, structural vibrations and increase of drag and lift oscillation. The control of the von Kármán wake can bring several benefits, as for instance in terms of costs, noise and fuel consumption reduction.
The progress in computational fluid dynamics and the development of control theory over the last fifteen years, together with the availability of increasing computing resources, enable the consideration of the issue of the control of vortex shedding from a numerical point of view.
We refer to the review by Choi *et al.* (2008) for an exhaustive description of the state of the art. We distinguish passive and active control. Passive control, largely used for reducing the drag of a bluff body, consists in the modification of geometrical or physical features of the body, for instance by means of roughness and dimples, or splitter plates. No sensors or actuators are involved in this kind of control.
The active control involves one or more actuations, like rotation or oscillation of the bluff body, electromagnetic actions, blowing/suction or synthetic jets. Active control can be divided into two categories: active open-loop and active closed-loop control. In the case of open-loop control, the control law is pre-computed and applied without any information on the present state of the flow. The control input can be for instance a time-periodic or steady blowing and suction, or a periodic rotation applied to the body. In the case of active closed-loop control, the input is modified according to the state deduced from information on the the flow given by one or more sensors. Thus, the feedback control is adapted in real-time according to the evolution of the flow.
Hence, two main issues are involved in a closed-loop control: the accurate estimation of the state and the determination of the optimal reaction to the control actuator.
In real applications only a limited number of noisy observations (velocity, pressure, shear

stress) is available to perform a state estimation of the actual flow field. Stochastic and least squares based methods are widely used in order to approximate the entire flow field starting from a small set of measurements. However, this kind of observer becomes inaccurate when a very limited number of observations is available or when complex flows are considered.
Furthermore, the control input has to be optimized in order to minimize a defined cost function. In other words, given an objective function $\mathcal{J}$ (enstrophy, difference between the flow field and a reference steady solution, drag coefficient...), find the set of control parameters c_i (time evolution of the intensity of blowing/suction, feedback parameters...) that minimizes $\mathcal{J}$ such that certain constraints hold (Navier-Stokes equations...).
Such an *optimal control* problem (Gunzburger, 1997a) can be solved by a *gradient descent method*, implying a wide number of computations both of the functional and of its gradient to reach a minimum. In fluid mechanics, the discretization schemes of the Navier-Stokes equations normally used in industrial applications lead to a system with an extremely large number of degrees of freedom ($10^7 - 10^8$). The computational cost required (Bewley *et al.*, 2001; Min & Choi, 1999) makes use of such an optimal (or sub-optimal) control for large-scale problems impractical for real-time aplications.
Thus, the idea is to find a small dimensional surrogate of the original dynamical system (discretized Navier-Stokes equations) to be used in an iterative optimization procedure. The starting point is a representation of the state variables in a reduced basis. A projection of the system equations onto the basis leads to a reduced order model for the original problem. Many methods to obatin reduced order models exist and are used for control purposes, as those founded on Lagrange/Hermite bases or Krylov spaces, balanced truncation, Proper Orthogonal Decomposition (POD), balanced POD (Rowley, 2005), or vortex models (Protas, 2004). See Ito & Ravindran (1998) for a review.
In this research work we use the Proper Orthogonal Decomposition. In particular the *snapshots method* to compute POD modes introduced by Sirovich (Sirovich, 1987) is adopted. The Galerkin-projection of the Navier-Stokes equations onto the POD basis leads to a reduced order model that can be employed in a flow estimation procedure and in an optimal control strategy.
Starting from a set of flow solutions (*database*), the POD is the truncated series that gives the best approximation of the flow fields from an energetic point of view. The main drawback for flow control is that the POD basis is not optimal to represent a flow generated using different system parameters with respect to those used to build the basis.
In order to employ a low order model for flow control and estimation, its accuracy and robustness have to be guaranteed. Indeed, a useful model has to reproduce precisely the dynamics contained in the database and at the same time it has to be robust to parameter variations or flow pattern evolutions.

The aim of this research work is to investigate and develop some tools, involving POD low order models, that circumvent the drawbacks described above (mainly the state estimation needed in a closed-loop control and the robustness required in a model) and that can be used in control tools. Although the described techniques are applied to a particular configuration, they are derived under a completely general point of view, and may be easily extended to other configurations. We considered a flow over a confined square cylinder with a Reynolds number varying between $Re = 40$ and $Re = 300$. Both two-dimensional and three-dimensional regimes are obtained depending on the Reynolds number. The control actuation is given by two blowing/suction jets placed on the surface of the cylinder.

The work, in addition to this introductive chapter, is organized as follows.
In the second chapter we describe the main techniques employed in this work. A brief description of the Proper Orthogonal Decomposition is furnished as well as details about *calibration* techniques used to adjust the low order model. Classical stochastic techniques and domain tessellation used in the following are also summarized.
In Chapter 3 the flow configuration mentioned above is described. A short overview of the Navier-Stokes code employed to obtain the flow simulations and references for details on the numerical set-up are provided. In this chapter the behaviour of the flow when the Reynolds number varies is also analyzed.
In the fourth chapter the problem of flow state estimation in an active closed-loop control is addressed. To this aim an accurate non-linear flow state observer based on POD reduced order modeling is developed. A method for estimating the dynamics is described and the obtained results are compared with those given by other existing techniques. Flow configurations with different complex patterns as well as several sensor placements are considered. In this application no control device is included, but the method can easily be extended for actuated flows.
In Chapter 5 models that depend explicitly on the control are examined. A methodology to derive robust low order models is provided. By robustness we mean the validity of the model when the control parameters are varied. The basic idea is to perform a *calibration* on multiple controlled dynamics in order to span a larger space of input parameters. The resulting models are tested in an open-loop context as well as in a feedback control configuration. Such a robust model is useful within a control optimization procedure performed in the reduced space.
Chapter 6 is dedicated to the study of an optimal sampling method, *i.e.* given the dimension of the database used to compute the POD basis, find an efficient way to sample the solution space in order to build the most robust basis and low order model possible. The aim of this procedure (coupled with the technique developed in chapter 5) is to provide a robust and cheap model that has to be updated as less as possible during an optimization procedure.
In Chapter 7 we analyze a linearized low order model for a feedback actuated flow, obtained from a set of solutions given by a non-linear Navier-Stokes code. The model is obtained starting from one or more transient dynamics of controlled flows and then linearized around a steady solution. The aim is to test the accuracy of such a low order model in estimating the global instability of the actual flow when feedback control is active. Moreover, a linear stability analysis is not always possible when working with complex tools like those typically used in engineering applications. Thus, the linearized

model, built starting from a non-linear code, can be used to perform a linear stability analysis of the reproduced flow.

Finally, in Chapter 8 Proper Orthogonal Decomposition is applied to the analysis of one dimensional fluid dynamics signals. No dynamical model is involved in this chapter. In order to detect the principal components of experimental signals, the POD modes are used to extract their main components from the original signals. The decomposition procedure was carried out in collaboration with Valerio Iungo (DIA, Università di Pisa), which provided the hot-wire experimental results. It is shown that POD analysis gives interesting results in terms of automatic detection of the main features of the flow.

Introduction

En méchanique des fluides un des thèmes principaux est l'étude des écoulements autour de corps épais. Ce type d'écoulement est intéressant pour la communauté d'ingénierie et scientifique. De nombreux exemples d'écoulements autour de corps épais peuvent être trouvés dans des applications industrielles, par exemple l'écoulement autour d'une aile à incidence élevée dans l'industrie aéronautique et autour d'un corps d'Ahmed dans l'industrie l'automobile, ou le vent autour un bâtiment de grande hauteur en génie civil. Lorsque le nombre de Reynolds est plus grand qu'une valeur critique, ces écoulements sont décollés et caractérisés par un sillage qui présente une allées tourbillonaire, (*vortex shedding*). Ce phénomène est reponsable de perturbations acoustiques, de vibrations structurelles, et de l'augmentation de traînée et oscillations de portance dans les applications aéronautiques. Le côntrole du sillage de von Kármán peut permettre de réduire le bruit acoustique et également de réduire la consommation carburant.
Au cours des quinze dernières années les progrés réalisés en calcul numérique pour la mécanique des fluides et le développement de la théorie du contrôle, ainsi que la disponibilité des ressources informatiques, ont permis de s'intéresser à la question du contrôle du détachement tourbillonnaire d'un point de vue numérique. Un état de l'art exhaustif peut être trouvé dans Choi *et al.* (2008). On distingue contrôle passif et contrôle actif. Le contrôle passif consiste généralement à modifier la géométrie ou les caractéristiques physiques du corps, par exemple la modification de la rugosité. Avec ce type de contrôle aucun capteur ou actionneur n'est impliqué.
Le contrôle actif implique une ou plusieurs actions temporelles, comme la rotation ou l'oscillation du corps, actions électromagnétiques, soufflage/aspiration ou jets synthétiques. Le côntrole actif peut être divisé en deux catégories : en boucle ouverte et en boucle fermée. Dans le cas du contrôle en boucle ouverte, la loi de côntrole est pré-calculée et appliquée sans aucune information sur l'état réel de l'écoulement. Le cóntrole peut être par exemple une action de soufflage et aspiration périodique ou continue, ou une rotation périodique appliqué au corps.
Dans le cas d'un contrôle actif en boucle fermée, le contrôle est modifié en fonction de l'état déduit par des informations sur l'écoulement données par un ou plusieurs capteurs. Ainsi, l'action de contrôle est adapté en temps réel en fonction de l'évolution de l'écoulement. Donc, deux questions principales sont impliquées dans un contrôle en boucle fermée : l'estimation précise de l'état et la détermination de l'action optimale du contrôle.

En effet, dans des applications réelles, seulement un nombre limité d'observations bruyantes (vitesse, pression, contraintes, ...) est disponible pour effectuer une estimation de l'état du champ d'écoulement réel. Les méthodes stochastiques et les méthodes des moindres carrés sont largement utilisées afin de reconstruire le champ d'écoulement entier à partir d'un petit ensemble de mesures. Toutefois, ce type d'observateurs devient inexacte losqu'un nombre très limité d'observations est disponible, ou lorsque des écoulements complexes sont pris en compte.

En outre, le contrôle doit être optimisé afin de minimiser une fonction coût définie. En d'autres termes, étant donnée une fonction objectif $\mathcal{J}$ (enstrophie, différence entre le champ d'écoulement et une solution de référence stable, coefficient de traînée...), trouver l'ensemble des paramètres de contrôle c_i (évolution en temps de l'intensité du soufflage/aspiration, paramètres de feedback...) qui minimise $\mathcal{J}$ telle que certaines contraintes sont satisfaites (équations de Navier-Stokes...).

Un tel *problème de contrôle optimal* (Gunzburger, 1997a) peut étre résolu par une méthode basée sur le gradient de la fonction objectif, qui implique un grand nombre de calculs de la solution des équations d'état (ici, les équations de Navier-Stokes). En méchanique des fluides, les schemas de discrétisation des équations de Navier-Stokes normalement utilisés en applications industrielles conduisent à des systèmes avec un très grand nombre de degrés de liberté ($10^7 - 10^8$). Le coût de calcul nécessaire (Bewley *et al.*, 2001; Min & Choi, 1999) rend impraticable le contrôle optimale (ou sous-optimale) pour problèmes a grand échelle.

Ainsi, l'idée est de trouver un substitut de dimension réduite du système dynamique original (équations de Navier-Stokes discrétisées) à utiliser dans une procédure d'optimisation itérative. Le point de départ est une représentation des variables d'état sur une base réduite. Une projection des équations du système détaillé sur la base conduit á un modèle d'ordre réduit pour le problème original. De nombreuses méthodes de modélisation réduit existent et sont utilisés pour le contrôle, comme les méthodes fondées sur les bases de Lagrange/Hermite ou les espaces de Krylov, la balanced truncation, la Décomposition aux valeurs propres (POD), balanced POD (Rowley, 2005), les méthodes particulaires (vortex) (Protas, 2004). Une revue de ces méthodes peut être trouvée dans Ito & Ravindran (1998).

Dans ce travail de recherche nous utilisons la POD. En particulier, la *méthode de snapshot*, introduite par Sirovich (Sirovich, 1987) est adoptée pour calculer les modes POD. La projection de Galerkin des équations de Navier-Stokes sur la base POD conduit á un modèle d'ordre réduit qui peut être aussi bien employé dans une procédure d'estimation d'écoulement que dans une stratégie de contrôle optimal.

A partir d'un ensemble de solutions d'un écoulement (*base de données*), la POD est la série tronquée qui donne la meilleure approximation de la base de données des champs de l'écoulement d'un point de vue énergétique. L'inconvénient principal est que la base POD n'est pas optimale pour représenter un écoulement généré en utilisant différents paramètres d'entrée que ceux qui sont utilisés pour construire la base.

Afin d'utiliser un modèle d'ordre réduit pour le contrôle et l'estimation d'écoulement, sa précision et robustesse doivent être garantis. En effet, un modèle qui peut être utilisé dans une procedure de contrôle doit reproduire avec précision la dynamique contenue dans la base de données et en même temps il doit être robuste aux variations des paramètres d'entrée ou á évolutions de la configuration de l'écoulement.

L'objectif de ce travail de recherche est d'étudier et développer certains outils, impliquant des modèles d'ordre réduit basés sur la POD, qui éludent les inconvénients décrits ci-dessus (essentiellement l'estimation d'état nécessaire pour une application de contrôle en boucle fermée et la robustesse exigée pour un modèle) et qui peuvent être utilisés dans des procédures de contrôle. Bien que les techniques décrites sont appliquées à une configuration particulière, ils sont dérivés d'un point de vue tout à fait général, et peuvent être facilement étendues à d'autres configurations plus complexes. Nous avons considéré un écoulement sur un cylindre carré confiné avec un nombre de Reynolds variant entre $Re = 40$ et $Re = 300$. En fonction du nombre de Reynolds les écoulements sont calculés en deux ou trois dimensions. L'actionnement du contrôle est donné par deux jets de soufflage/aspiration placée sur la surface du cylindre.

La mémoire, en plus de ce chapitre introductif, est organisée comme suit.
Dans le deuxième chapitre, nous décrivons les principales techniques employées dans ce travail. Une brève description de la Décomposition aux valeurs propres (Proper Orthogonal Decomposition) est fournie ainsi que des détails sur des *techniques de calibration* utilisées pour ajuster le modèle d'ordre réduit. Les techniques stochastiques classiques et de decomposition de domaine utilisées dans les chapitres suivants sont également résumées.
Dans le chapitre 3, la configuration d'écoulement mentionnée ci-dessus est décrite. Un bref aperçu du code de resolution des équations de Navier-Stokes employé pour obtenir les simulations d'écoulement est fourni. Dans ce chapitre, le comportement de l'écoulement quand le nombre de Reynolds varie est également analysé.
Dans le quatrième chapitre, il est adressé le problème de l'estimation d'état de l'écoulement dans une procedure de contrôle actif en boucle fermée. Dans cet optique, nous avons développé un observateur d'état d'écoulement non linéaire basé sur la modélisation réduite POD. Une méthode d'estimation de la dynamique est décrite et les résultats obtenus sont comparés à ceux donnés par d'autres techniques existantes. Différentes configurations d'écoulement sont prises en compte avec diverses distributions de placement des senseurs. Dans cette application, aucun dispositif de contrôle n'est inclus, mais la méthode peut être facilement étendu pour les écoulements actionnés.
Dans le chapitre 5, nous étudions des modèles qui dépendent explicitement du contrôle. Une méthodologie pour calculer des modèles d'ordre réduit robustes est fournie. Par robustesse, nous entendons la precision du modèle à la prediction de la dynamique lorsque les paramètres de contrôle varient. L'idée de base est d'effectuer une *calibration* sur plusieurs dynamiques contrôlées afin de couvrir un plus grand espace des paramètres d'entrée. Les modèles résultants sont testés dans un contexte en boucle ouverte aussi bien que dans une configuration de contrôle en rétroaction. Un tel modèle robuste est utile dans une procédure d'optimisation de contrôle effectuée dans l'espace réduit.

La chapitre 6 est dédié à l'étude d'une méthode d'échantillonnage optimale, *ie* trouver un moyen efficace pour échantillonner le sous-espace des paramétres d'entrée du systéme afin de construire la base POD et le modèle réduit les plus robustes possible. Le but de cette procédure (couplée avec la technique développée dans le chapitre 5) est de fournir un modèle robuste, et peu cher d'un point de vue numérique, qui doit être mis à jour le moins possible au cours d'une procédure d'optimisation.
Dans le chapitre 7, nous analysons un modèle réduit linéarisé pour un écoulement actionné en feedback, obtenu en utilisant comme base de données un ensemble de solutions produites par un code de Navier-Stokes non-linéaire. Le modèle est obtenu à partir d'une ou plusieurs dynamiques de transitoires d'écoulements contrôlés, puis linéarisé autour d'une solution d'équilibre. L'objectif est de tester la précision d'un tel modèle d'ordre réduit à l'estimation de l'instabilité globale de l'écoulement réel lorsque le contrôle en rétroaction est actif. En outre, une analyse de stabilité linéaire n'est pas toujours possible lorsque l'on travaille avec des outils complexes, comme ceux qui sont habituellement utilisés dans des applications d'ingénierie. Donc, le modèle linéarisé, construit avec un code non linéaire, peut être utilisé pour effectuer une analyse linéaire de stabilité de l'écoulement reproduit.

Enfin, dans la chapitre 8, la POD est appliqué à l'analyse d'un signal d'écoulement expérimental. Aucun modèle dynamique est engagé dans ce chapitre. Afin de détecter les composantes principales des signaux expérimentaux, les modes POD sont utilisées pour extraire les modes propres des signaux originaux. La procédure de décomposition a été developpée en collaboration avec Valerio Iungo (DIA, Università di Pisa), qui a fourni les résultats expérimentaux obtenus par fil chaud. Il est montré que l'analyse POD donne des résultats intéressants en terme de détection automatique des caractéristiques principales de l'écoulement.

Chapter 2

Background on employed techniques

In this chapter we describe the main techniques employed in this work. A brief description of the Proper Orthogonal Decomposition is furnished as well as details about *calibration* techniques used to adjust the low order model. Classical stochastic techniques and domain tessellation used in the following are also summarized.

2.1 Low-order modeling

Due to the complexity of the non-linear equations of the system, that involve a huge number of degrees of freedom, many tools of control theory are impracticable for fluids for real-time applications. To avoid the large computational costs, model reduction is nedeed, *i.e.* a low-dimensional model which approximates the full high-dimensional dynamics must be obtained.

The model reduction technique discussed here is a *projection method*, *i.e.* it involves the projection of the equations of motion onto a subspace of the original space. There are many methods available for reducing both linear and non-linear systems (see Ito & Ravindran (1998); Antoulas *et al.* (2001); Weller (2009) for reviews), as for instance methods based on Lagrange/Hermite bases (Ito & Ravindran, 1998; Grepl *et al.*, 2005), on Krylov spaces (Willcox, 2000), balanced truncation (Moore, 1981), Proper Orthogonal Decomposition (POD), balanced POD (Rowley, 2005), vortex models (Protas, 2004). We concentrate our work on the *POD-Galerkin* method.

2.1.1 Proper orthogonal decomposition (POD)

The proper orthogonal decomposition (POD) provides a basis for a modal decomposition of an ensemble of functions. Its properties suggest that it is one of the best suited bases for various applications. The most important property is its *optimality*: it provides the most efficient way of capturing the dominant components of an infinite-dimensional process with only a limited number "modes".

POD was introduced in the context of fluid mechanics by Lumley (see Lumley (1967)), in order to identify and extract dominant features and trends of a turbulent flow: the coherent structures. In other disciplines the same procedure is named: Karhunen-Loève (K-L) decomposition (Karhunen, 1946; Loève, 1955), principal components analysis (Joliffe, 1986), Singular Value Decomposition (Golub & Van Loan, 1990) and EOFs. The functions obatined through this technique are variously called: empirical eigenfunctions, empirical basis functions, and proper orthogonal modes.

Further, the POD provides an optimal basis that can be used to project the equations of the dynamical system and then construct a reduced model. Finally, being the POD basis optimal in terms of energy, only a limited number of POD modes are needed to capture almost entirely the flow energy.

A comprehensive review of POD can be found in (Aubry *et al.* (1988); Sirovich (1987); Cordier & Bergmann (2002); Bergmann (2004)).

The fundamental idea behind the POD is straightforward. Let us assume to have a data set obtained through a numerical simulation over the time interval $[0, T]$ and arranged in N tensors $\{\boldsymbol{U}^{(1)}, \boldsymbol{U}^{(2)}, \ldots, \boldsymbol{U}^{(N)}\}$, where each tensor can represent for instance a snapshot of the velocity field at a given time

$$\boldsymbol{U}^{(k)} = \begin{pmatrix} (u(\boldsymbol{x}_1, t_k) & v(\boldsymbol{x}_1, t_k) & w(\boldsymbol{x}_1, t_k)) \\ (u(\boldsymbol{x}_2, t_k) & v(\boldsymbol{x}_2, t_k) & w(\boldsymbol{x}_2, t_k)) \\ & \vdots & \\ (u(\boldsymbol{x}_M, t_k) & v(\boldsymbol{x}_M, t_k) & w(\boldsymbol{x}_M, t_k)) \end{pmatrix}, \ \mathrm{t_1 = 0 \text{ and } t_N = T}$$

The aim is to find a low-dimensional subspace of $\mathcal{L} = span\{\boldsymbol{U}^{(1)}, \boldsymbol{U}^{(2)}, \ldots, \boldsymbol{U}^{(N)}\}$ that gives the best approximation of $\mathcal{L}$. To this end we define a unit norm vector $\boldsymbol{\phi}$ that has the same structure of the snapshots, i.e.

$$\boldsymbol{\phi} = \begin{pmatrix} (\phi_1(\boldsymbol{x}_1) & \phi_2(\boldsymbol{x}_1) & \phi_3(\boldsymbol{x}_1)) \\ (\phi_1(\boldsymbol{x}_2) & \phi_2(\boldsymbol{x}_2) & \phi_3(\boldsymbol{x}_2)) \\ & \vdots & \\ (\phi_1(\boldsymbol{x}_M) & \phi_2(\boldsymbol{x}_M) & \phi_3(\boldsymbol{x}_M)) \end{pmatrix} \qquad \text{with} \quad \|\phi\|^2 = (\phi\,, \phi) = 1$$

and whose mean square projection on the elements of $\mathcal{L}$ is the largest. Thus we determine such a function ϕ by maximizing the functional

$$\mathcal{J}_1 = \sum_{k=1}^{N} \left(\boldsymbol{U}^{(k)}, \boldsymbol{\phi}\right)^2$$

Let us set $u(\boldsymbol{x}_j, t_k) = u^1_{jk}$, $v(\boldsymbol{x}_j, t_k) = u^2_{jk}$, $w(\boldsymbol{x}_j, t_k) = u^3_{jk}$ and $\phi_h(\boldsymbol{x}_j) = \phi^h_j$ with $j = 1, \ldots, M, k = 1, \ldots, N$ and $h = 1, 2, 3$. In view of these assumptions and the Einstein notation for summations, the problem can be formulated as follows:
"find those $\boldsymbol{\phi}$, which maximize the functional

$$\mathcal{J}_1 = \phi^h_j u^h_{jk} u^l_{ik} \phi^l_i$$

under the constraint $\phi_j^h \phi_j^h = 1$."
This is equivalent to finding the extrema of the unconstrained functional

$$\mathcal{J}_2 = \phi_j^h u_{jk}^h u_{ik}^l \phi_i^l - \lambda_j \left(\phi_j^h \phi_j^h - 1 \right) \tag{2.1}$$

The vectors $\boldsymbol{\phi}$ that maximize $\mathcal{J}_2$ are given by the eigenvectors of a spatial correlation matrix which is M×M, thus solving the eigenproblem requires a very large number of calculations. Sirovich suggested a clever way to get around this difficulty, which consists of expressing $\boldsymbol{\phi}$ as a linear combination of the snapshots ("snapshot method", see Sirovich (1987) and Cordier & Bergmann (2002) for justification)

$$\boldsymbol{\phi} = \sum_{n=1}^{N} b_n \boldsymbol{U}^{(n)} \tag{2.2}$$

Hence by substituting $\phi_j^h = u_{jk}^h b_k$ in (2.1) one obtains

$$\mathcal{J}_2(\lambda_1, \ldots, \lambda_N, b_1, \ldots, b_N) = b_k \left(u_{jk}^h u_{jr}^h \right) \left(u_{ir}^l u_{is}^l \right) b_s - \lambda_j \left(b_k u_{jk}^h u_{jr}^h b_r - 1 \right)$$

The vanishing of the first derivatives of $\mathcal{J}_2$ with respect to the unknown $b_1, \ldots, b_N$ leads to the eigenproblem

$$\boldsymbol{R}\,\boldsymbol{b} = \lambda\,\boldsymbol{b}$$

where $R_{ks} = u_{jk}^h u_{js}^h$ and $\boldsymbol{b} = [b_1, b_2, ..., b_N]^T$. At this point, the time correlation matrix $\boldsymbol{R}$ is N×N and can be easily dealt with, as $N \ll M$. Since $\boldsymbol{R}$ is symmetric and positive definite, it has a complete set of orthonormal eigenvectors $\boldsymbol{f}_1, \ldots, \boldsymbol{f}_N$ and a set of real and positive eigenvalues $\lambda_1, \ldots, \lambda_N$. The eigenvalues form a decreasing and convergent series. Each eigenvalue represents the contribution of the corresponding mode $\boldsymbol{b}_n$ to the information content of the original data. Note that if $\boldsymbol{U}^{(n)}$ are, as here, the velocity fields, the information content reduces to the kinetic energy. By letting $\boldsymbol{b}_s = \boldsymbol{f}_s/\sqrt{\lambda_s}$ with $s = 1, \ldots, N$ we find a set $\boldsymbol{b}_1, \ldots, \boldsymbol{b}_N$ of orthogonal (non orthonormal) eigenvectors of $\boldsymbol{R}$ which satisfy the constraint $b_{ks} u_{jk}^h u_{jr}^h b_{rs} = 1$. Once we have calculated the set $\boldsymbol{b}_1, \ldots, \boldsymbol{b}_N$ that maximizes $\mathcal{J}_2$, we can finally retrieve the set of eigenfunctions $\boldsymbol{\phi}_1, \ldots, \boldsymbol{\phi}_N$ by means of the expansion (2.2), that is in terms of components

$$\phi_{jk}^h = u_{jn}^h b_{nk}$$

with $j = 1, \ldots, M, k = 1, \ldots, N, n = 1, \ldots, N$ and $h = 1, 2, 3$. These eigenfunctions are referred to as *POD modes*. Since the POD eigenfunctions can be represented as linear combinations of the realizations, they inherit all the linear properties of the original data. For instance, the eigenfunctions are divergence free for incompressible flows. Moreover, the eigenfunctions verify the boundary conditions of the numerical simulation used to determine the flow realizations. Let us write the inner product between two generic POD modes:

$$(\boldsymbol{\phi}_k\,, \boldsymbol{\phi}_s) = \phi_{jk}^h \phi_{js}^h = b_{rk} u_{jr}^h u_{jq}^h b_{qs} = b_{rk} \lambda_s b_{rs} = \lambda_s \frac{f_{rk}}{\sqrt{\lambda_k}} \frac{f_{rs}}{\sqrt{\lambda_s}} = \delta_{ks} \sqrt{\frac{\lambda_s}{\lambda_k}} = \delta_{ks}$$

where δ is the Kronecker delta tensor. The above relationship proves that the POD modes form a complete orthonormal set.

The snapshots (instantaneous velocity fields) can be expanded with arbitrary accuracy in terms of a limited number $N_r \geq 1$ of POD eigenfunctions:

$$\boldsymbol{U}(\boldsymbol{x}, t) = \sum_{n=1}^{N_r} a_n(t)\boldsymbol{\phi}_n(\boldsymbol{x}) \tag{2.3}$$

The original goal of obtaining a low-dimensional subspace which approximates the set $\mathcal{L}$ can be achieved by neglecting the less energetic modes in that expansion, i.e., the modes that correspond to the smallest eigenvalues. In practice, since $\sum_{i=1}^{N_r} \lambda_i$ represents the energy amount contained in the first N_r modes, we could choose N_r so that the ratio $\sum_{i=1}^{N_r} \lambda_i \Big/ \sum_{i=1}^{N} \lambda_i$ is larger than a given threshold, for instance 99%.

2.1.2 Low order model of Navier-Stokes equations

We now describe the reduction of the Navier-Stokes equations to a low-dimensional set of ordinary differential equations (ODEs). This reduction in fluid mechanics, means passing from about $10^7 - 10^8$ degrees of freedom given by a discretization of the Navier-Stokes equations via numerical schemes, to a dynamical system of $10 - 100$ ODEs. To this end, we apply the concepts introduced above through the POD description.

POD-Galerkin model

Let us refer to the case where the considered snapshots are only velocity fields (an exemple with snapshots formed by velocity and pressure fields is treated in (chapter 5). The starting point is a representation of the velocity field $\boldsymbol{u}(\boldsymbol{x}, t)$ in terms of N_r empirical eigenfunctions, $\boldsymbol{\phi}^i(\boldsymbol{x})$, obtained by Proper Orthogonal Decomposition (see Lumley (1967) and section §2.1.1)

$$\widetilde{\boldsymbol{u}}(\boldsymbol{x}, t) = \overline{\boldsymbol{u}}(\boldsymbol{x}) + \sum_{i=1}^{N_r} a_i(t)\boldsymbol{\phi}^i(\boldsymbol{x}) \tag{2.4}$$

where $\boldsymbol{u}(\boldsymbol{x}, t) : \mathbb{R}^n \times [0, T] \to \mathbb{R}^n$, $\Phi^i(\boldsymbol{x}) : \mathbb{R}^n \to \mathbb{R}^n$, $n \in \{2, 3\}$ according to the physical space dimension, $\overline{\boldsymbol{u}}(\boldsymbol{x})$ is some reference velocity field that satisfies the same boundary conditions as the snapshots and $a_i(t) : I = [0, T] \subset \mathbb{R} \to \mathbb{R}$. $\overline{\boldsymbol{u}}(\boldsymbol{x})$ is subtracted from the snapshots to ensure that the new snapshots are equal to zero on the boundaries. In the following if not indicated, the reference field is assumed be the average of the original snapshots.

Let us consider the non-dimensional incompressible Navier-Stokes equations:

$$\begin{aligned} \frac{\partial \boldsymbol{u}}{\partial t} + (\boldsymbol{u} \cdot \nabla)\boldsymbol{u} &= -\nabla p + \frac{1}{Re}\Delta \boldsymbol{u} \\ \nabla \cdot \boldsymbol{u} &= 0 \end{aligned} \qquad \text{in } \Omega \times (0, T) \tag{2.5}$$

Since the POD modes are divergence-free by construction, if we substitute expansion (2.4) in (2.5) and perform a *Galerkin projection* onto the POD modes, we obtain the following nonlinear ordinary differential system:

$$\begin{cases} \dot{a}_r(t) &= A_r + C_{kr}a_k(t) - B_{ksr}a_k(t)a_s(t) - \mathcal{P}_r \\ a_r(0) &= (\boldsymbol{u}(\boldsymbol{x},0), \boldsymbol{\phi}^r) \\ 1 \leq r \leq N_r \end{cases} \tag{2.6}$$

where:

$$\begin{aligned} &A_r = -((\overline{u}\cdot\nabla)\overline{u}, \boldsymbol{\phi}^r) + \frac{1}{Re}(\Delta\overline{u}, \boldsymbol{\phi}^r) \\ &B_{ksr} = ((\boldsymbol{\phi}^k\cdot\nabla)\boldsymbol{\phi}^s, \boldsymbol{\phi}^r) \\ &C_{kr} = -((\overline{u}\cdot\nabla)\boldsymbol{\phi}^k, \boldsymbol{\phi}^r) - ((\boldsymbol{\phi}^k\cdot\nabla)\overline{u}, \boldsymbol{\phi}^r) + \frac{1}{Re}(\Delta\boldsymbol{\phi}^k, \boldsymbol{\phi}^r) \\ &\mathcal{P}_r = (\nabla p, \boldsymbol{\phi}^r) \end{aligned}$$

We note that since the snapshots satisfy the continuity equation, the modes do also. This implies that the pressure term $\mathcal{P}_r$, by integration by parts, is equal to $\int_{\partial\Omega} p\boldsymbol{\phi}^r \cdot \bar{\boldsymbol{n}}\, ds$. If velocity field is (almost) constant at the boundaries, the POD modes are (almost) zero there. The pressure term therefore disappears (can be neglected).

The initial value problem (2.6) is a reduced order model of the Navier-Stokes equations called *POD-Galerkin* model.

Calibration procedure

A vast literature concerning the *POD-Galerkin* modeling for fluid flows exists (Galletti *et al.*, 2006; Buffoni *et al.*, 2006; Galletti *et al.*, 2004; Ma & Karniadakis, 2002), and some results show the possible interest of using POD in applications such as flow control (Bergmann *et al.*, 2005; Gillies, 1998; Graham *et al.*, 1998; Ravindran, 2006; Afanasiev & Hinze, 2001).
However, several problems related to the idea of modeling a flow by a small number of variables are open. One of the issues is the asymptotic stability of the models obtained. Often such models are capable of correctly reproducing the dynamics over small time intervals, whereas the asymptotic behavior converges to incorrect limit cycles (Ma & Karniadakis, 2002). This issue is related to both numerical artifacts and to an improper representation of the solution (Iollo *et al.*, 2000; Rempfer, 2000; Noack *et al.*, 2003). Moreover, by neglecting the less energetic modes, also their interaction with the more energetic modes is neglected and this leads to a lack of dissipation in the reduced order model. To avoid this loss in dissipation, in (Bergmann *et al.*, 2005) and (Rempfer & Fasel, 1994) numerical viscosity is added aimed to stabilize the model.

On the other hand, in order to model the interaction between the unresolved modes with the resolved ones, the terms of the low-order model can be "calibrated", fitting the prediction of the dynamical reduced model on the actual Navier-Stokes solution. Only the terms A_r and C_{kr} are modified. Indeed, as shown in (Galletti *et al.*, 2006), we could in principle write the solution of the equation for the unresolved modes as a function of the resolved ones and then inject this solution into the equation for the resolved modes. Thus, performing calibration over A_r and C_{kr}, can be interpreted as finding the MacLaurin expansion of this function up to the linear term. Note that when the pressure term $\mathcal{P}_r$ is not identically equal to zero, its effect is also considered in the terms A_r and C_{kr}.

This approach (Galletti *et al.*, 2006) was used with good results in (Buffoni *et al.*, 2006) and in (Couplet *et al.*, 2005) for complicated three-dimensional and turbulent flows respctively.

In view of the orthogonality of the POD modes, the inner product of the i-th snapshot and the r-th mode represent the reference value of coefficient $a_r(t)$ computed at the time t_i, that is $a_r^{ex}(t_i) = (\boldsymbol{u}(\boldsymbol{x}, t_i), \boldsymbol{\phi}^r)$. Since the snapshots of the flow are N, there will be a discrete set of N reference values for each amplitude $a_r(t)$. We can pass from the discrete to the continuous in the time variable by defining $\hat{a}_r(t)$ as the spline that interpolates the set of points $\{(t_1, a_r^{ex}(t_1)), \ldots, (t_N, a_r^{ex}(t_N))\}$.

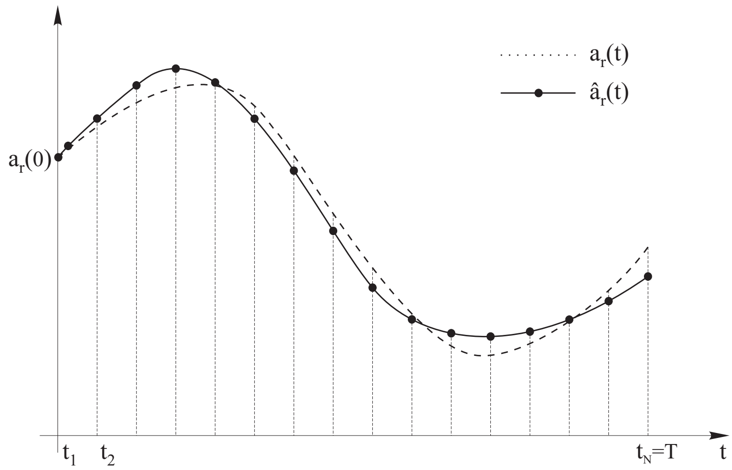

Figure 2.1: Projection vs. prediction.

Now, the coefficients A_r and C_{kr} can be found so that the amplitudes $a_r(t)$ computed by solving (2.6) (dashed line in the sketch of figure 2.1), are as close as possible to the corresponding reference amplitudes $\hat{a}_r(t)$ (solid line in the sketch of figure 2.1. Recalling that $T = t_N$, this objective is reached by minimizing the functional

$$\mathcal{J}_3 = \int_0^T \sum_{r=1}^{N_r} (a_r(t) - \hat{a}_r(t))^2 \, \mathrm{d}t$$

under the constraints (2.6). By applying the technique of the Lagrange multipliers the previous problem is equivalent to finding the extremum of the free functional

$$\mathcal{J}_4 = \int_0^T \sum_{r=1}^{N_r} (a_r(t) - \hat{a}_r(t))^2 \, \mathrm{d}t + \int_0^T b_k \left[\dot{a}_k(t) - A_k - C_{lk} a_l(t) + B_{lsk} a_l(t) a_s(t)\right] \mathrm{d}t$$

To this end, the vanishing of the Fréchet derivatives of $\mathcal{J}_4(a_r(t), b_r(t), A_r, C_{kr})$ with respect to all its arguments is to be imposed. This leads to the following direct-adjoint problem

$$\begin{cases} \dot{a}_r(t) \; = \; A_r + C_{kr} a_k(t) - B_{ksr} a_k(t) a_s(t) \\ a_r(0) \; = \; = (\boldsymbol{u}(\boldsymbol{x}, 0), \boldsymbol{\phi}^r) \end{cases} \qquad \text{direct problem} \qquad (2.7)$$

$$\begin{cases} -\dot{b}_r(t) \; = \; \left[C_{rk} - (B_{lrk} + B_{rlk}) a_l(t)\right] b_k(t) - 2\left[a_r(t) - \hat{a}_r(t)\right] \\ \;b_r(T) \; = \; 0 \end{cases} \qquad \text{adjoint problem} \qquad (2.8)$$

$$\begin{cases} \int_0^T b_r(t) dt = 0 \\ \int_0^T a_k(t) b_r(t) dt = 0 \end{cases} \qquad \text{optimality conditions} \qquad (2.9)$$

where all the subscripts go from 1 to N_r. Those equations are discretized with a pseudo–spectral collocation method along the t axis. The functions $a_r(t), b_r(t)$ and $\hat{a}_r(t)$ are sampled at the N_t Gauss-Lobatto points $t_i = T/2\,(1 - \xi_i)$ with $\xi_i = \cos \pi (i-1)/(N_t - 1)$ and $i = 1, \ldots, N_t$, that is $a_{ir} = a_r(t_i), b_{ir} = b_r(t_i)$ and $\hat{a}_{ir} = \hat{a}_r(t_i)$. An interpolation is performed to retrieve the values of these functions out of the nodes t_i, more precisely

$$\begin{aligned} a_r(t) &\approx \sum_{j=1}^{N_t} \psi_j \left(1 - \frac{2}{T} t\right) a_{jr} \\ b_r(t) &\approx \sum_{j=1}^{N_t} \psi_j \left(1 - \frac{2}{T} t\right) b_{jr} \\ \hat{a}_r(t) &\approx \sum_{j=1}^{N_t} \psi_j \left(1 - \frac{2}{T} t\right) \hat{a}_{jr} \end{aligned}$$

where $\xi = 1 - 2\,t/T$ and $\psi_j(\xi)$ are the Lagrangian interpolating polynomials based on the nodes ξ_i. The time derivatives of the first two interpolated functions at the nodal values are then

$$\begin{aligned} \dot{a}_r(t_i) &\approx -\frac{2}{T} \sum_{j=1}^{N_t} \left.\frac{\mathrm{d}\psi_j}{\mathrm{d}\xi}\right|_{\xi_i} a_{jr} = \sum_{j=1}^{N_t} D_{ij}\, a_{jr} \\ \dot{b}_r(t_i) &\approx -\frac{2}{T} \sum_{j=1}^{N_t} \left.\frac{\mathrm{d}\psi_j}{\mathrm{d}\xi}\right|_{\xi_i} b_{jr} = \sum_{j=1}^{N_t} D_{ij}\, b_{jr} \end{aligned} \qquad (2.10)$$

The differentiation matrix can be found in (Canuto *et al.*, 1988) and is equal to

$$D_{ij} = -\frac{2}{T}\left.\frac{\mathrm{d}\psi_j}{\mathrm{d}\xi}\right|_{\xi_i} = -\frac{2}{T}\begin{cases} \dfrac{c_i}{c_j}\dfrac{(-1)^{j+i}}{\xi_i-\xi_j} & j\neq i \\ -\dfrac{1}{2}\dfrac{\xi_i}{1-\xi_i^2} & j=i\neq 1, N_t \\ \dfrac{2(N_t-1)^2+1}{6} & j=i=1 \\ -\dfrac{2(N_t-1)^2+1}{6} & j=i=N_t \end{cases}$$

with $c_1 = c_{N_t} = 2$ and $c_2 = \cdots = c_{N_t-1} = 1$.

The optimality condition can be rewritten in terms of the interpolated functions in the follow way

$$\int_0^T a_k(t)b_r(t)\,\mathrm{d}t \approx \sum_{i=1}^{N_t}\sum_{j=1}^{N_t} a_{ik}\, I_{ij}\, b_{jr} \tag{2.11}$$

where the integrals

$$I_{ij} = \int_0^T \psi_i(\xi)\psi_j(\xi)\,\mathrm{d}\xi \qquad \text{with} \quad i,j=1,\ldots,N_t$$

are calculated by means of the Legendre quadratures. Finally by virtue of (2.10) and (2.11) the equations (2.7),(2.8) and (2.9) are discretized as follows

$$\begin{array}{lll}
a_{1r} = a_r(0) & & r=1,\ldots,N_r \\
D_{ij}a_{jr} - A_r - C_{lr}a_{il} + B_{lsr}a_{il}a_{is} = 0 & i=2,\ldots,N_t, & r=1,\ldots,N_r \\
D_{ij}b_{jr} + C_{rs}b_{is} - (B_{lrs}+B_{rls})a_{il}b_{is} - 2\left[a_{ir}-\hat{a}_{ir}\right] = 0 & i=1,\ldots,N_t-1, & r=1,\ldots,N_r \\
b_{N_t r} = 0 & & r=1,\ldots,N_r \\
1_i\, I_{ij}\, b_{jr} = 0 & & r=1,\ldots,N_r \\
a_{ik}\, I_{ij}\, b_{jr} = 0 & k=1,\ldots,N_r & r=1,\ldots,N_r
\end{array}$$

where $\mathbf{1}$ is a N_t-dimensional array of ones. These are $2N_tN_r + N_r^2$ algebraic equations in the $2N_tN_r + N_r^2$ unknowns which are solved with a Newton method that converges quickly. The former procedures can be viewed as a sort of **"calibration"** of the model on the given database. We denote this procedure by *state calibration* method.

The number N_t must be large enough in order to give a good description of the high frequency amplitudes, consequently it is to be increased as N_r goes up.

Although very accurate, the computational cost of this calibration procedure is not negligible when the number of modes is large or when the flow shows a large span of time frequencies.

For this reason, we used an alternative method, as already suggested in (Galletti *et al.*, 2004), that delivers a reasonable model at the cost of a matrix inversion.

The idea is simple. We ask that the terms A_r and C_{kr} in (2.6) are such that the error on the time derivative

$$\mathcal{J}_5 = \int_0^T \sum_{r=1}^{N_r} \left(\dot{a}_r(t, \hat{\boldsymbol{a}}) - \dot{\hat{a}}_r(t) \right)^2 \mathrm{d}t$$

is minimised. Where $\dot{a}_r(t, \hat{\boldsymbol{a}})$ are the time-derivative of the amplitudes given by model when the reference amplitudes are used

$$\dot{a}_r(t, \hat{\boldsymbol{a}}) \;=\; A_r + C_{kr}\hat{a}_k(t) - B_{ksr}\hat{a}_k(t)\hat{a}_s(t)$$

Thus, while the *state calibration* method is a calibration on the state of the system, this technique, denoted by *dynamics calibration* method, is a calibration on the dynamics. It can be seen that this technique amounts to a minimization of the model residual when the reference coefficients are used. Moreover, this method is equivalent to the intrinsic stabilization scheme developed in (Kalb & Deane, 2007).

The vanishing of the derivatives of $\mathcal{J}_5(A_r, C_{kr})$ with respect to A_r, C_{kr} leads to the linear system

$$\begin{cases} C_{kr} \int_0^T \hat{a}_k(t)\, dt + A_r T & = \int_0^T \dot{\hat{a}}_r(t)\, dt + B_{ksr} \int_0^T \hat{a}_k(t)\hat{a}_s(t)\, dt \\ C_{kr} \int_0^T \hat{a}_k(t)\hat{a}_m(t)\, dt + A_r \int_0^T \hat{a}_m(t)\, dt & = \int_0^T \dot{\hat{a}}_r(t)\, \hat{a}_m(t)\, dt + B_{ksr} \int_0^T \hat{a}_k(t)\hat{a}_s(t)\hat{a}_m(t)\, dt \end{cases} \tag{2.12}$$

$\forall r, m \in \{1, \ldots, N_r\}$. All the integrals in the above equations are known and, for each r, a set of $N_r + 1$ linear equations is obtained for the coefficients A_r and C_{kr}. Note that in the N_r systems to be solved only the right-hand side changes.

Poisson pressure model

If the original snapshots are only the velocity fields, as in the procedure described in the previous sections, the low order model is a simple velocity model. It is however useful to have an approximation of the pressure field, for instance to estimate the aerodynamics forces around bodies or to compute the residual of the Navier-Stokes equations. Thus, when the dynamical model is derived only for the velocity, we have to provide an estimation of the pressure. An independent POD procedure is performed also for the pressure fields. This leads to a set of POD pressure modes ψ^n. The pressure at each time instant can be developed in terms of the first N_r^p modes :

$$p(\boldsymbol{x}, t) = \bar{p}(\boldsymbol{x}) + \sum_{i=1}^{N_r^p} b_i(t)\psi^i(\boldsymbol{x}) \tag{2.13}$$

where $\bar{p}(\boldsymbol{x})$ is the pressure field of the same reference solutions used for the velocity.

We recall the Poisson equation for incompressible flows:

$$\Delta p(x, t) = -\nabla \cdot (\boldsymbol{u}(\boldsymbol{x}, t) \cdot \nabla \boldsymbol{u}(\boldsymbol{x}, t)) \tag{2.14}$$

Using the expansion for $p(\boldsymbol{x},t)$ and $\boldsymbol{u}(\boldsymbol{x},t)$ in terms of the first N_r^p and N_r modes respectively, the projection of the Poisson equation onto the retained pressure modes leads to the following system:

$$\begin{cases} L^p_{il} b_l(t) \quad = \quad A^p_i + C^p_{ij} a_j(t) + B^p_{ijk} a_j(t) a_k(t) \\ a_j(t) c(t) \\ 1 \leq i, l \leq N^p_r \\ 1 \leq j, k \leq N_r \end{cases} \tag{2.15}$$

where:

$$\begin{aligned} L^p_{ij} &= (\Delta \psi^k, \psi^r) \\ A^p_i &= -(\Delta \bar{p}, \psi^r) - (\nabla \cdot (\bar{\boldsymbol{u}} \cdot \nabla \bar{\boldsymbol{u}}, \psi^r)) \\ C^p_{ij} &= -((\nabla \cdot (\bar{\boldsymbol{u}} \cdot \nabla \boldsymbol{\phi}^k), \psi^r) - (\nabla \cdot (\boldsymbol{\phi}^k \cdot \nabla \bar{\boldsymbol{u}}), \psi^r)) \\ B^p_{ijk} &= -(\nabla \cdot (\boldsymbol{\phi}^k \cdot \nabla \boldsymbol{\phi}^s), \psi^r) \end{aligned}$$

This *Poisson model* enables computation of the pressure coefficients $b_i(t)$ at each time instant at which the velocity coefficients $a_i(t)$ are known.
In order to fit the pressure model to the database solutions, we can perform a calibration procedure as described above also for the Poisson model. We let $\hat{b}_i(t)$ be the temporal coefficients obtained by projecting the pressure fields onto the POD subspace. The coefficents L^p_{ij}, A^p_i and C^p_{ijk} are chosen by minimizing the norm of the residual obtained by substituting $\hat{a}_r(t)$ into (2.15)

$$\mathcal{J}_6 = \int_0^T \sum_{r=1}^{N_r} \left(L^p_{rl} b_l(t)(t, \hat{\boldsymbol{a}}) - L^p_{rl} \hat{b}_l(t) \right)^2 \mathrm{d}t$$

The vanishing of the derivatives of $\mathcal{J}_6(L^p_{ij}, A^p_i, C^p_{ij})$ with respect to L^p_{ij},A^p_i and C^p_{ij} leads to a simple linear system for L^p_{rl},A^p_i and C^p_{ij} analogous to (2.12). As previously the non linear term B^p_{ijk} results from the Galerkin projection and is not calibrated.

2.2 Linear and Quadratic stochastic estimation

In this section, following the review of Gordeyev (Gordeyev, 2000), we provide a description of the Linear and the Quadratic Stochastic Estimation.

The *Stochastic Estimation* is a method used to extract structures by approximating an average field in terms of the event data at some given locations. In other words, SE reconstructs a flow field, by using a knowledge of the flow at some selected points in space and time. Given a vector of data $\boldsymbol{E}$, which represent the measured events at points and time $(\boldsymbol{x\prime}, t\prime)$, the approximation of $\boldsymbol{u}$ by stochastic estimation, denoted by $\hat{\boldsymbol{u}}$, is taken as the conditional average $\langle \boldsymbol{u} \mid \boldsymbol{E} \rangle$. Adrian, in 1977, introduces a technique to estimate conditional averages for any arbitrary conditions. The idea is to expand $\langle \boldsymbol{u} \mid \boldsymbol{E} \rangle$ in a Taylor series about $\boldsymbol{E} = 0$ as

$$\hat{u}_i = \langle \boldsymbol{u} \mid \boldsymbol{E} \rangle = L_{ij} E_j + N_{ijk} E_j E_k + \ldots \tag{2.16}$$

(repeated subscripts are summed) and truncate this series at some degree (Adrian (1977),Adrian (1979),Naguib *et al.* (2001)). The unknown coefficient tensors $\boldsymbol{L}, \boldsymbol{N}, \ldots$ can be determined by requiring the mean-square error between the approximation and the conditional average to be minimal,

$$\langle [\langle \boldsymbol{u} \mid \boldsymbol{E} \rangle - L_{ij} E_j - N_{ijr} E_j E_r - \ldots]^2 \rangle \rightarrow min$$

The minimization leads to the orthogonality principle, which states that the error must be statistically uncorrelated with each of the event data

$$\langle [\langle \boldsymbol{u} \mid \boldsymbol{E} \rangle - L_{ij} E_j - N_{ijr} E_j E_r - \ldots] E_k \rangle = 0$$

The case where the series contains only the first order term, simple algebra leads to a set of linear algebraic equations for the estimates of the coefficients L_{ij}

$$\langle E_j E_k \rangle L_{ij} = \langle u_i E_k \rangle \tag{2.17}$$

This Stochastic Estimation then is called the *Linear Stochastic Estimation (LSE)*,

$$\hat{u}_i = \text{ linear estimator of } \langle \boldsymbol{u} \mid \boldsymbol{E} \rangle = L_{ij} E_j \tag{2.18}$$

where $L_{ij} = L_{ij}(\boldsymbol{x}, \boldsymbol{x\prime})$ and $\boldsymbol{x\prime}$ is the location of the event data. Cross correlation tensor $\langle E_j E_k \rangle$ between each of the event data and between the data and the quantity to be estimated $\langle u_i E_k \rangle$ must be obtained by independent means (Adrian (1977)). If $\boldsymbol{u} = \boldsymbol{u}(\boldsymbol{x}, t)$ is the velocity field and the event data consists of velocity vectors $\boldsymbol{E} = (\boldsymbol{u\prime}, t\prime)$ at the location $\boldsymbol{x\prime}$, then $\langle E_j E_k \rangle = \langle u_j u_k \rangle$ is the Reynolds stress tensor and $\langle u_i E_k \rangle = \langle u_i u\prime_k \rangle = R_{ik}(\boldsymbol{x}, \boldsymbol{x\prime}, t, t\prime)$ is the two-point, second-order, space-time velocity correlation. Thus, the knowledge of R_{ik} gives the ability to approximate any conditional averaged quantities.

LSE, as well as POD, uses the cross-correlation tensor $\boldsymbol{R}$ to extract structures from the flow. The connection between LSE and POD is straightforward to be found (Breteton (1992)). Recall, that general POD decomposes the flow into an infinite number of orthogonal modes $\boldsymbol{\phi}_n(\boldsymbol{x}; t)$, for them to be found from the eigenproblem

$$\boldsymbol{R}\,\boldsymbol{b} = \lambda\,\boldsymbol{b}$$

The eigenmodes are used to decompose the flow field as

$$\boldsymbol{u}(\boldsymbol{x}, t) = \sum_{n=1}^{\infty} a_n(t) \boldsymbol{\phi}_n(\boldsymbol{x}) \tag{2.19}$$

The cross-correlation tensor itself can be represented in terms of the orthogonal functions as

$$\boldsymbol{R}(\boldsymbol{x}\prime,\boldsymbol{x};t\prime,t)=\sum_{n=1}^{\infty}\lambda_n\boldsymbol{\phi}_n(\boldsymbol{x}\prime,t\prime)\boldsymbol{\phi}_n(\boldsymbol{x},t) \tag{2.20}$$

Using (2.17), (2.19) and (2.20), the equation (2.18) can be rewritten as

$$\boldsymbol{u}(\boldsymbol{x}\prime;t\prime)=\boldsymbol{u}(\boldsymbol{x},t)\sum_{n=1}^{\infty}\boldsymbol{\phi}_n(\boldsymbol{x},t)\boldsymbol{f}_n(\boldsymbol{x}\prime,t) \tag{2.21}$$

where $\boldsymbol{f}_n(\boldsymbol{x}\prime,t)=\lambda_n\boldsymbol{\phi}_n(\boldsymbol{x}\prime,t)/\sum_{n=1}^{\infty}\lambda_n\boldsymbol{\phi}_n^2(\boldsymbol{x}\prime,t\prime)$ can be viewed as relative contribution or weight of each mode,$\boldsymbol{\phi}_n(\boldsymbol{x},t)$, to the conditional average. Therefore, LSE can be treated as a weighted sum of an infinite number of POD modes. Hence, when two or more distinctive structures exist in the flow, LSE could give a wrong representation of coherent structures, while POD decompose the flow in terms of all the orthogonal modes.

If LSE does not capture the conditional average accurately, the estimation could be improved to draw out more of the details. Thus LSE is extended to the *Quadratic Stochastic Estimation (QSE)* (Adrian (1979),Naguib *et al.* (2001)) by including the next term in the Taylor series (2.16). The minimization of the mean-square error leads to a set of linear equation for L_{ij}^{quad} and N_{ijk}

$$\begin{array}{lcl}\langle E_jE_k\rangle L_{ij}^{quad}+\langle E_jE_rE_k\rangle N_{ijr} & = & \langle u_iE_k\rangle\\ \langle E_jE_kE_s\rangle L_{ij}^{quad}+\langle E_jE_rE_kE_s\rangle N_{ijr} & = & \langle u_iE_kE_s\rangle\end{array} \tag{2.22}$$

where L_{ij}^{quad} is in general different from L_{ij}.

Note that as long as the temporal separation is zero for all the correlations, then some of the above equations become linearly dependent because

$$\langle E_1E_2\rangle=\langle E_2E_1\rangle$$

Thus, the number of coefficients in (2.22) can be greatly reduced because no single combination of subscripts needs to be repeated.

Finally, the LSE/QSE can be used to estimate directly the whole velocity field by using some measured events at given points. However, for our applications, the procedure to set up the full correlation matrices is very demanding in terms of computational costs. For this reason the LSE/QSE (and the estimation techniques described hereafter) are used to estimate the time dependent modal coefficients $a_r(t)$ instead of the whole space-time velocity fields $\boldsymbol{u}(\boldsymbol{x},t)$. Then, in the following we set $\boldsymbol{u}=a_r$ as conditional event in *Stochastic Estimation.*

2.3 Spectral stochastic estimation

One of the difficulties of accurately applying Adrian's classical approach described above is the preservation of the time scales associated with the conditional event estimate. For this (Ewing & Citriniti, 1999) introduce the *Spectral Stochastic Estimation* substituting the spatial conditional average with a spectral term. In this way not only the amplitude of *conditional eddy* is preserved, but also the characteristic frequencies between the unconditional and conditional events (Tinney *et al.* (2006)).

Moreover, the linear estimate of a random variable is accurate only for separations between the unconditional and conditional terms that are smaller than the Taylor microscale. Thus, the spectral features of conditional estimates should be considered more carefully where spatial separations greater than the Taylor microscale (according to Adrian 1996) exist between the estimated structure and the unconditional source field.

Following (Ewing & Citriniti, 1999) the Fourier coefficients of the unconditional field are used to estimate the Fourier coefficients of the conditional event. Being

$$\begin{aligned} \hat{u}_i^f &= \textstyle\int_{-\infty}^{\infty} u_i(t) e^{-ift}\, dt \\ E_i^f &= \textstyle\int_{-\infty}^{\infty} E_i(t) e^{-ift}\, dt \end{aligned}$$

the $f-th$ coefficients of the Fourier transforms of the conditional and the unconditional event respectively, the SLSE gives the estimate $\hat{u}_i^f$:

$$\hat{u}_i^f = \langle \boldsymbol{u}^f \ \mid \ \boldsymbol{E}^f \rangle = \Gamma_{ij}^f E_j^f \tag{2.23}$$

Similarly for the LSE the error between the approximation and the conditional average can be written for each frequency

$$\langle [\langle \boldsymbol{u}^f \ \mid \ \boldsymbol{E}^f \rangle - \Gamma_{ij}^f E_j^f]^2 \rangle$$

The minimization of the error leads to the same orthogonality principe of the LSE but in the frequency domain. The spectral estimation coefficients are then obtained by the solution of the linear system

$$\langle E_j^f E_k^{f*} \rangle \Gamma_{ij}^f = \langle u_i^f E_k^{f*} \rangle \tag{2.24}$$

where $*$ is the complex conjugate.

The *Spectral Stochastic Estimation*, differently from LSE and QSE, preserves the spectral characteristics of the conditional events and, in case of time lag between the unconditional source and the conditional event, due to the fact that the correlation in frequency is equivalent to a convolution in time, it contains the separation in time of the estimated condition.

2.4 General least-square technique

From a general point of view we describe briefly a least-squares technique. Smooth curves can be fit to data in a variety of ways using the least-square technique *LSQ*. The functions that are used for the fit do not need to be integer powers of the independent variable. It is possible to use any function as long as it is linearly related to the dependent variable through a constant. For example any function y can be expressed as follows:

$$y = a_1 f_1(x) + a_2 f_2(x) + \cdots + a_n f_n(x) = \sum_{j=1}^{n} a_j f_j(x)$$

The error at any particular data point is given by:

$$e_i = y_i - [a_1 f_1(x) + a_2 f_2(x) + \cdots + a_n f_n(x)]$$

and the total error for a set of N points is:

$$S = \sum_{i=1}^{N} e_i^2 = \sum_{i=1}^{N} \{y_i - [a_1 f_1(x) + a_2 f_2(x) + \cdots + a_n f_n(x)]\}^2$$

In order to minimize the error we differentiate the former with respect to each of the constants a_j and set each resulting equation equal to zero. For example:

$$\frac{\partial S}{\partial a_1} = 2 \sum_{i=1}^{N} f_1(x_i)\{y_i - [a_1 f_1(x) + a_2 f_2(x) + \cdots + a_n f_n(x)]\} = 0$$

Therefore, n equations of the following form result:

$$\begin{aligned}
a_1 \sum_{i=1}^{N} f_1^2(x_i) + a_2 \sum_{i=1}^{N} f_1(x_i) f_2(x_i) + \cdots + a_n \sum_{i=1}^{N} f_1(x_i) f_n(x_i) &= \sum_{i=1}^{N} y_i f_1(x_i) \\
a_1 \sum_{i=1}^{N} f_2(x_i) f_1(x_i) + a_2 \sum_{i=1}^{N} f_2^2(x_i) + \cdots + a_n \sum_{i=1}^{N} f_2(x_i) f_n(x_i) &= \sum_{i=1}^{N} y_i f_2(x_i) \\
&\vdots \\
a_1 \sum_{i=1}^{N} f_n(x_i) f_1(x_i) + a_2 \sum_{i=1}^{N} f_n(x_i) f_2(x_i) + \cdots + a_n \sum_{i=1}^{N} f_n^2(x_i) &= \sum_{i=1}^{N} y_i f_n(x_i)
\end{aligned}$$

Consequently this represents a system of linear equations of the form:

$$[A]\,\vec{a} = \vec{b}$$

where

$$A_{j_k} = \sum_{i=1}^{N} f_j(x_i) f_k(x_i)$$

and

$$b_j = \sum_{i=1}^{N} y_i f_j(x_i)$$

or

$$\begin{bmatrix} \sum f_1^2 & \sum f_1 f_2 & \sum f_1 f_3 & \cdots & \sum f_1 f_n \\ \sum f_2 f_1 & \sum f_2^2 & \sum f_2 f_3 & \cdots & \sum f_2 f_n \\ \vdots & \vdots & \vdots & \vdots & \vdots \\ \sum f_n f_1 & \sum f_n f_2 & \sum f_n f_3 & \cdots & \sum f_n^2 \end{bmatrix} \begin{bmatrix} a_1 \\ a_2 \\ \vdots \\ a_n \end{bmatrix} = \begin{bmatrix} \sum y_i f_1(x_i) \\ \sum y_i f_2(x_i) \\ \vdots \\ \sum y_i f_n(x_i) \end{bmatrix} \tag{2.25}$$

Thus, solution of the system of linear equations (2.25) gives the desired unknown coefficients a_i.

2.5 Centroidal Voronoi Tessellation

Referring to (Du *et al.*, 1999) we furnish a simple description of the Centroidal Voronoi Tessellation. Let us start from the definition of a *Voronoi Tessellation*.
Definition. Given a region Ω and a set of points $\{z_i\}_{i=1}^N$, the generators, a Voronoi Tessellation is a partition of Ω into regions $\{V_i\}_{i=1}^N$ enclosing the points closer, according to the Euclidean distance, to z_i than to any other generator. Each V_i is the Voronoi region associated to z_i., and is defined by

$$V_i = \{z \in \Omega | |z - z_i| < |z - z_j|, j = 1, \dots, N \,\text{and}\, j \neq i\}$$

The set $\{V_i\}_{i=1}^N$ is a *Voronoi tessellation* of Ω.

In figure 2.2 an example of Voronoi tessellation corresponding to a random distribution on a square domain is plotted. The Voronoi regions are known also as Dirichlet

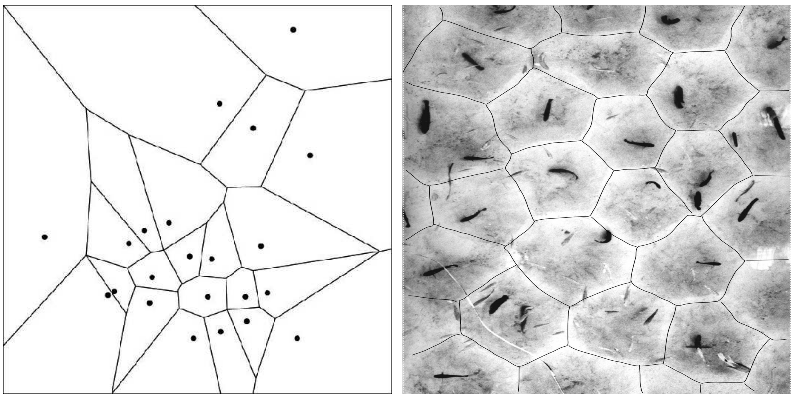

(a) Voronoi tessellation. (b) Voronoi tessellation in nature.

Figure 2.2: Voronoi tessellation

regions, area of influence polygons, Meijering cells, Thiessen polygons, and S-mosaics, depending on the application.

For each region V of the Voronoi tessellation, given a density function ρ defined in Ω, the mass centroid z^* of the region is defined as

$$z^* = \frac{\int_V z\rho(z)dz}{\int_V \rho(z)dz}$$

A *Centroidal Voronoi Tessellation* (CVT) is a particular Voronoi tessellation where the generators of the region are themselves the mass centroids, *i.e.* $z_i = z_i^*$. Then, a CVT is a collection of Voronoi regions in which each generator is located at the same point as its mass centroid. This situation is special since, in general, arbitrarily chosen points are not the centroids of their associated Voronoi regions. In general this CVT tessellation is not unique. Centroidal Voronoi tessellations, because their natural optimization properties, are used in many scientific and engineering applications as image compression, quadrature, finite difference methods, distribution optimal of resources, biology, statistics, and the territorial behavior of animals. (see (Du *et al.*, 1999)). In figure 2.2(b) an example of distribution of territory in nature. The territories are quasi-polygonal and they are very close to a Voronoi tessellation.

In order to compute a CVT we refer in this work to a simple and one of the most adopted methods, the **Lloyd** algorithm (see Du *et al.* (2007) for a review on the convergence of the algorithm). The method is essentially an iterative procedure consisting in sequential Voronoi tessellations and deplacement of the generator in the centre of mass of the associated region. The procedure is stopped when a criterion of convergence is reached. The algorithm is summarized below.

0. Start with an initial distribution of generators $\{z_i\}_{i=1}^N$
1. Construct the *Voronoi Tessellation* associated to the generators $\{z_i\}_{i=1}^N$
2. Take as new generators the centre of mass of the regions $\{V_i\}_{i=1}^N$, *i.e.* $\{z_i\}_{i=1}^N = \{z_i^*\}_{i=1}^N$ calculated by using a given density function $\rho(z)$.
3. Repeat steps 1 and 2 until convergence is met.

When the convergence is reached, the generators correspond to the centre of mass of each region. The resulting tessellation is a *Centroidal Voronoi Tessellation*.

Chapter 3

Flow setup and numerical simulation

The flow over an infinitely long square cylinder symmetrically confined by two parallel planes is considered. A sketch showing the geometry, the frame of reference and the adopted notation is plotted in figure 3.1. At the inlet, the incoming flow is assumed to have a Poiseuille profile with maximum center-line velocity U_c. The considered Reynolds numbers, based on the maximum center-line velocity U_c $Re = U_c L/\nu$, are taken in the interval $Re = (40, 180)$ and $Re = 300$.

The numerical code used in this study is AERO, a compressible Navier-Stokes code. AERO was developed by Bruno Koobus (Université Montpelllier II) and Charbel Farhat (Stanford University). We thank Bruno Koobus and Alain Dervieux (INRIA Sophia-Antipolis) to authorize the use of the code for this work. Details concerning the grids and the numerical set up are reported in Buffoni *et al.* (2006) and they are briefly summarized hereafter.

In AERO the Navier-Stokes equations for compressible flows are discretized in space using a mixed finite-volume/finite-element method applied to unstructured tetrahedrizations. The adopted scheme is vertex centered and P1 Galerkin finite elements are used to discretize the diffusive terms.

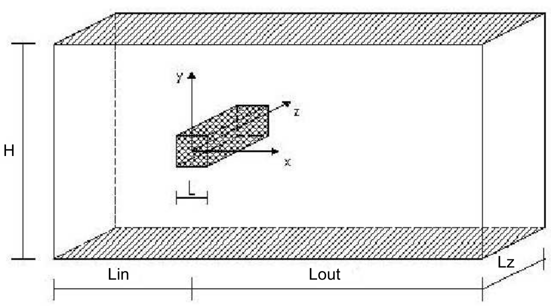

Figure 3.1: Computational domain Ω.

A dual finite-volume grid is obtained by building a cell C_i around each vertex i through the rule of medians. The convective fluxes are discretized on this tessellation, i.e. in terms of fluxes through the common boundaries shared by neighboring cells.

The Roe scheme (Roe (1981)) represents the basic upwind component for the numerical evaluation of the convective fluxes $\mathcal{F}$:

$$\Phi^R\left(W_i,\ W_j,\ \vec{n}\right) = \frac{\mathcal{F}\left(W_i,\ \vec{n}\right) + \mathcal{F}\left(W_j,\ \vec{n}\right)}{2} - \gamma_s P^{-1}|P\mathcal{R}|\ \frac{(W_j - W_i)}{2}$$

in which, $\Phi^R\left(W_i,\ W_j,\ \vec{n}\right)$ is the numerical approximation of the flux between the i-th and the j-th cells, W_i is the solution vector at the i-th node, $\vec{n}$ is the outward normal to the cell boundary and $\mathcal{R}\left(W_i,\ W_j,\ \vec{n}\right)$ is the Roe matrix. The matrix $P(W_i,\ W_j)$ is the Turkel-type preconditioning term, introduced to avoid accuracy problems at low Mach numbers (Guillard & Viozat (1999)). Finally, the parameter γ_s, which multiplies the upwind part of the scheme, permits a direct control of the numerical viscosity, leading to a full upwind scheme for $\gamma_s = 1$ and to a centered scheme when $\gamma_s = 0$. The spatial accuracy of this scheme is only first order. The MUSCL linear reconstruction method ("Monotone Upwind Schemes for Conservation Laws"), introduced by van Leer (1977), is employed to increase the order of accuracy of the Roe scheme. This is obtained by expressing the Roe flux as a function of the reconstructed values of W at the cell interface: $\Phi^R\left(W_{ij},\ W_{ji},\ \vec{n}_{ij}\right)$, where W_{ij} is extrapolated from the values of W at nodes i and j. A reconstruction using a combination of different families of approximate gradients (P1-elementwise gradients and nodal gradients evaluated on different tetrahedra) is adopted, which allows a numerical dissipation made of sixth-order space derivatives to be obtained. The MUSCL reconstruction is described in detail in Camarri *et al.* (2004), in which the capabilities of this scheme in concentrating the numerical viscosity effect on a narrow-band of high-frequency fluctuations is also discussed.

The time marching algorithm is implicit and based on a backward difference scheme. A first-order semi-discretization of the jacobians is adopted together with a defect-correction procedure (Martin & Guillard (1996)); the resulting scheme is second-order accurate in time.

Characteristics based inflow and outflow boundary conditions are used. At the inflow the Poiseuille flow is assumed to be undisturbed. Periodic boundary conditions are imposed in the spanwise direction and no-slip conditions are forced on the cylinder and on the lateral walls.

As in Buffoni *et al.* (2006) two different computational domains are used, for carrying out two-dimensional and three-dimensional simulations, which differ only for the spanwise extent of the domain. In both cases, with reference to figure 3.1, the blockage ratio $\beta = L/H$ is equal to 1/8 and $L_{in}/L = 12$ and $L_{out}/L = 20$. For two-dimensional simulations, the spanwise length adopted is $L_z/L = 0.6$, and it was systematically checked that the simulated spanwise velocity was negligible. For the three-dimensional simulations, the spanwise length of the domain is $L_z/L = 6$. This value in Buffoni *et al.* (2006) was selected following the experimental results for the unconfined square-cylinder flow (Luo *et al.* (2003)), which show a maximum spanwise length of the three-dimensional structures equal to $5.2L$ and the indications given in Sohankar *et al.* (1999) and Saha *et al.*

(2003) for the numerical study of the three-dimensional wake instabilities of a square cylinder in an open uniform flow. The used grids are composed by $7.5 \cdot 10^5$ and by $6.6 \cdot 10^6$ elements for the two-dimensional and the three-dimensional simulations respectively.

Since we intend to simulate an incompressible flow, the simulations were performed by assuming that the maximum Mach number of the inflow profile is $M = 0.1$. This value allows compressibility effects to be reasonably neglected in the results.

The flow shows non trivial dynamical features. A von Kármán vortex street develops past the cylinder when the Reynolds number increases above a critical value as a result of a global instability. This value is a function of the blockage ratio, i.e. the ratio between the cylinder side and the channel height (L/H).
The critical Reynolds number, based on the mass inflow, varies in the literature between 50 and 90 (Okajima, 1982; Sohankar *et al.*, 1999; Breuer *et al.*, 2000). In Davis *et al.* (1984) it was found that the non-dimensional shedding frequency (the Strouhal number) reaches a maximum and then decreases as the Reynolds number increases. This phenomenon is generally ascribed to the shift of the separation point from the trailing to the leading square corners. The resulting flow is also characterized by the interaction of the vortical wake and the walls leading to some peculiar features, like the fact that the vertical position of the spanwise vortices is opposite to the one in the classical von Kármán street (Camarri & Giannetti, 2007). In figure 3.2, where istantaneous vorticity isocontours obtained for $Re = 180$ are plotted, this phenomenon is clearly visible.

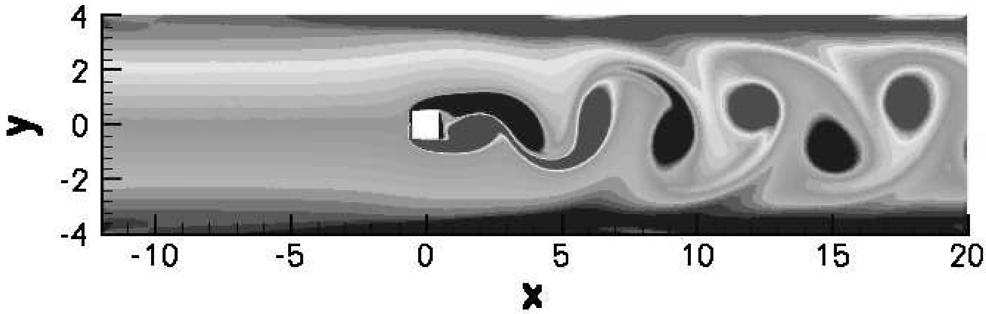

Figure 3.2: Instantaneous isocontours of vorticity of a snapshot at $Re = 180$.

Although this peculiar structure of the vortex street, even at $Re = 180$ the behavior of the aerodynamic forces is the one typically found in 2D simulations of bluff body flows. Indeed, the time variation of the lift coefficient is perfectly periodic at the shedding frequency. Thus, for Reynolds numbers $Re = (40, 180)$ the flow can be considered two-dimensional.
Two different three-dimensional instability modes, initially identified in circular cylinder flows, have been found for unconfined square cylinders in experiments (Luo *et al.*, 2003) and in the Floquet instability analysis (Robichaux *et al.*, 1999). The first one, mode A, occurs at lower Reynolds and is characterized by the formation of large-scale wavy vortex loops. The other one, mode B, is characterized by shorter, fine-scale vortex loops.

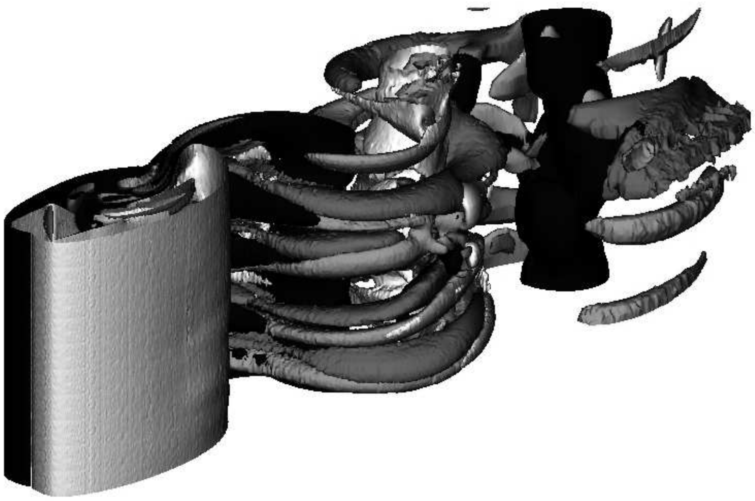

Figure 3.3: Streamwise and spanwise vorticity components in the wake at $Re = 300$. Isosurfaces correspond to $\omega_z = -0.4$ (black) and $\omega_z = 0.4$ (gray) are plotted. The streamwise tubes identify $\omega_x = 0.4$ and $\omega_x = -0.4$ respectively.

For unconfined square cylinders, mode A was found to occur at $Re \simeq 160$ and mode B at $Re = 190 - 200$. Indeed, the flow at $Re = 300$ is completely three-dimensional (for the confined square cylinder the mode B occurs at $Re \simeq 220$), and the situation is even more complex, due to instabilities developing in the span-wise direction. The flow is no longer periodic and exhibits complicated flow patterns. As shown in (Buffoni *et al.* (2006)) the developed three-dimensional flow presents small vortical loops in the wake and they connect the vortex tubes of the von Kármán street. These spanwise vortex tubes are

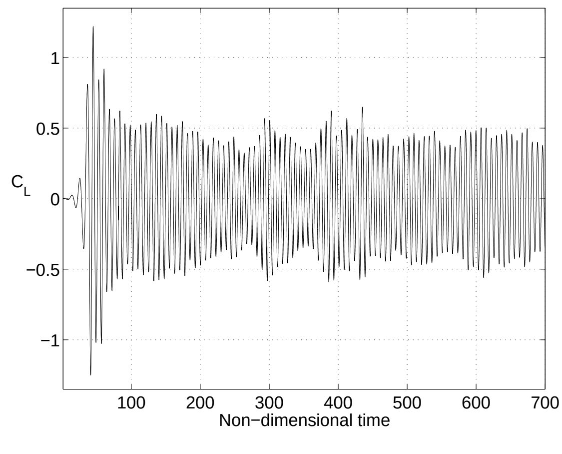

Figure 3.4: Time variation of lift coefficient Cl at $Re = 300$.

in turn corrugated and distorted by the motion induced by the streamwise vortices. In figure 3.3 isosurfaces of streamwise and spanwise vorticity are shown. It is clear the complexity of the flow structures, with the evidence of strongly three-dimensional flow patterns.

In figure 3.4 the time history of the lift coefficient calculated on the cylinder is plotted. The three-dimensional effects of the spanwise dynamics leading to significant modulations of the amplitude of lift oscillations, even in the transient of the vortex shedding.

Chapter 4

A non-linear observer for an unsteady three-dimensional flow

The problem of deriving an accurate estimation of the velocity field in an unsteady flow, starting from a limited number of measurements, is of great importance in the design of a feedback control. Indeed, the knowledge of the velocity field is a fundamental element in deciding the appropriate actuator reaction to different flow conditions.
Also in other applications it may be necessary, or advisable, to monitor the flow conditions in regions which are difficult to access, or where probes cannot be fitted without causing interference problems. Similar problems arise in physics when trying to filter data resulting from a chaotic system, see for example (Abarbanel *et al.*, 1993).

The starting point is the Galerkin representation of the velocity field $\boldsymbol{u}(\boldsymbol{x}, t)$ in terms of N_r empirical eigenfunctions, $\boldsymbol{\phi}^i(\boldsymbol{x})$, obtained by Proper Orthogonal Decomposition (POD) (see section §2.1.2).

For a given flow, the POD modes can be computed once and for all, using Direct Numerical Simulation (DNS), or on highly resolved experimental velocity fields, such as those obtained by particle image velocimetry. An instantaneous velocity field can thus be reconstructed by estimating the coefficients $a_i(t)$ of its Galerkin representation.

One simple approach to estimating the POD coefficients is to approximate the flow measurements in a least square sense, as done, for instance, in (Galletti *et al.*, 2004). A similar procedure is also used in the estimation based on gappy POD, see (Everson & Sirovich, 1995), (Venturi & Karniadakis, 2004) and (Willcox, 2006). Another possible approach, the linear stochastic estimation (LSE), is based on the assumption that a linear correlation exists between the flow measurements and the value of the POD modal coefficients (see, for instance, Bonnet *et al.* (1994)).

However, these approaches encounter difficulties in giving accurate estimations when three-dimensional flows with complicated unsteady patterns are considered, or when a very limited number of sensors is available. Under these conditions, for instance, the least squares approach mentioned above (LSQ) rapidly becomes ill conditioned. This simply reflects the fact that more and more different flow configurations correspond to the same set of measurements. To circumvent these problems, many contributions in the literature have sought to determine the best sensor placement (see e.g. Schmit & Glauser (2005), Cohen *et al.* (2004), Cohen *et al.* (2006), Willcox (2006)). For example in Willcox (2006), a systematic approach to sensor placement is formulated within the gappy POD framework using a condition number criterion.

In order to improve estimation performance, extensions of the above methods have been proposed: quadratic stochastic estimation (QSE) Adrian (1977), Naguib *et al.* (2001) and spectral linear stochastic estimation (SLSE) Ewing & Citriniti (1999). They allow more accurate estimations than LSQ or LSE methods, but, in fact, neither takes into account the underlying dynamic model that the POD coefficients must satisfy, *i.e.*, a finite dimensional equivalent of the Navier-Stokes equations that is obtained by Galerkin projection of the flow equations on the POD modes retained for the representation of the velocity field.

In the literature one finds estimation techniques that take into account the underlying partial differential equations, using control theory tools Falb (1970). Classical estimations based on such methods are those applied in meteorology data assimilation where the mismatch between predictions and observations is minimized as function of the initial conditions (Gunzburger, 2003; Le Dimet & Talagrand, 1986) (4D-VAR) (see Park (2009) for a review). More recent applications of these ideas are those used in seismology, where the source of an earthquake is sought once the ground displacement is measured Akcelik *et al.* (2003). Computing the exact solution of such inverse problems requires large computational facilities for realistic cases since the state equation, the adjoint equation and the optimality conditions must be simultaneously solved. In this sense, the novelty of the present study is to discuss an approach that combines a linear estimation of the coefficients $a_i(t)$ with an appropriate non-linear low-dimensional flow model. Compared to the classical inverse problems mentioned above, the solution is obtained with a negligible computational effort, at the cost of obtaining an approximate solution. The degree of approximation will be related to the possibility of an actual low-order representation.

The approach that we propose combines a linear estimation of the coefficients $a_i(t)$ with an appropriate non-linear low-dimensional flow model. This approach is similar to the one of reduced 4D-VAR, where a low dimensional space is used to approximate only the control variables (Robert *et al.*, 2005; Robert & Verron, 2006) or also to build the low order model and its adjoint to be used in the optimization procedure (Cao *et al.*, 2007; Daescu & Navon, 2008).

Thus, our objective is to understand whether a non-linear observer outperforms existing linear flow observers.

Moreover, instead of what was done, for example, in Hoepffner *et al.* (2005), this study is confined to a deterministic framework, since the model, as well as the measurements, are supposedly not affected by noise. The measurements are not affected by noise in the sense that we do not take into account the errors introduced by the actual instruments. The model is not affected by noise in the sense that although it will only be approximate, we will not try to mimic the model deviations by adding noise with appropriate statistical characteristics. Our results will show that, within this framework, dynamic estimations based on low-order models turn out to be more satisfactory than static approaches, *i.e.*, those which use no model.

In addition, we address the issue of the sensitivity of the proposed approach to sensor type and location. Finally, we present applications to a two-dimensional periodic flow and to a flow, which is characterized by a significant three-dimensionality and non-periodic dynamics.

4.1 Flow set up and low order model

We consider the flow configuration reported in chapter §3. Two Reynolds numbers $Re = U_c L/\nu$ were considered, one at which the flow is two-dimensional ($Re = 150$) and the other one leading to a three-dimensional flow in the wake ($Re = 300$). We used the computational domain shown in figure 3.1, $L/H = 1/8$, $Lin/L = 12$, $Lout/L = 20$ and $Lz/L = 0.6$ for the two-dimensional case, whereas $L/Lz = 6$ for the three-dimensional one. All the quantities mentioned in the following have been made non-dimensional by L (side of the cylinder) and U_c (center-line velocity at inflow). The behaviour of the two flows given by DNS are described in section §3. Let us underline that in the two dimensional flow obtained at $Re = 150$ is a classic periodic vortex street. While the three-dimensional case is much more complex; the flow is not periodic and presents complicated flow structures.

The POD modes $\boldsymbol{\phi}^k(\boldsymbol{x})$ are found using the snapshot method (Sirovich (1987), section §2.1.1)

$$\boldsymbol{\phi}^k = \textstyle\sum_{i=1}^N b_i^k \boldsymbol{U}^{(i)}$$

where $\boldsymbol{U}^{(i)} = \boldsymbol{u}(\boldsymbol{x}, t_i)$ are simple velocity flow snapshots taken at times $t_i \in [0, T]$, N is the number of snapshots, $k \in \{1, \dots, N\}$. Only a limited number of modes, N_r, is used to represent the velocity field. In particular we chose $N_r = 6$ for the two-dimensional case. For the three-dimensional case, because of the compexity of the flow, we derived two models with larger numbers of modes $N_r = 20$ and $N_r = 60$, respectively.

A Galerkin projection of the incompressible Navier-Stokes equations over the retained POD modes leads to the N_r-dimensional dynamical system

$$\begin{aligned} &R_r(\boldsymbol{a}(t)) = \dot{a}_r(t) - A_r - C_{kr} a_k(t) + B_{ksr} a_k(t) a_s(t) = 0 \\ &a_r(0) = (\boldsymbol{u}(\boldsymbol{x}, 0) - \overline{\boldsymbol{u}}(\boldsymbol{x}), \boldsymbol{\phi}^r) \end{aligned} \tag{4.1}$$

where $\boldsymbol{a}(t) : I \to \mathbb{R}^{N_r}$ and $\boldsymbol{a}(t) = \{a_1(t), \dots, a_{N_r}(t)\}$; r, k and s run from 1 to N_r and the Einstein summation convention is used. As explained in section §2.1.2 the scalar coefficients B_{ksr} come directly from the Galerkin projection of the non-linear terms in the Navier-Stokes equations, and they can easily be expressed in terms of the POD modes. The scalar terms A_r and C_{kr} are *calibrated*. Note that the term A_r appears because in this case we extracted the time average field on $[0, T]$ from the snapshots.

In this chapter we consider the two calibration methods described in section §2.1.2. The first consists in solving an inverse problem, where the coefficients A_r and C_{kr} are found in order to minimize the difference, measured in the L^2 norm, between the model prediction and the actual reference solution (called *state calibration*). The resulting model for the two-dimensional flow configuration considered here is very accurate in describing the asymptotic attractor (Galletti *et al.* (2004) and Galletti *et al.* (2006)). For the three-dimensional case, it was shown in Buffoni *et al.* (2006) that the calibrated model is capable of accurately reproducing the complicated flow dynamics resulting from the interaction of the three-dimensional vortex wake with the confining walls inside the calibration interval. Although very accurate, the computational cost of obtaining this model is not negligible, since in the three-dimensional case the number of modes is larger.

For this reason, we use also the alternative method, the *dynamics calibration*, that gives a reasonable model at the cost of a matrix inversion. The time interval where the calibrations are performed $[0, T]$ is the same as that considered for building the POD modes.

4.2 Non-linear observer

Our aim is to provide an estimation of the modal coefficients starting from N_s flow measurements $f_k,\ k \in \{1, \ldots, N_s\}$. Let $\hat{a}_r(t)$ be the projection of the velocity field $\boldsymbol{u}(\boldsymbol{x}, t)$ over the r-th POD mode and $\alpha_r(t)$ be its estimated value at time t.

We assume that each measurement f_k is a scalar quantity which depends linearly on the instantaneous velocity field $\boldsymbol{u}(\boldsymbol{x}, t)$. For instance, f_k can be a point-wise measurement of a velocity component, or of a shear stress, or it can be a spatial average of a linear combination of velocity components.

The available spatial information may be exploited by using a LSQ approach (see section §2.4 for details), as done in Galletti *et al.* (2004). At any given time τ of measurement, thanks to the linearity of f_k with respect to $\boldsymbol{u}(\boldsymbol{x}, t)$ and to the modal decomposition of the velocity field (see Eq. (2.4)), f_k can be written in terms of POD modes

$$f_k\left(\boldsymbol{u}\left(\boldsymbol{x}, \tau\right)\right) \simeq \sum_{r=1}^{N_r} a_r(\tau) f_k\left(\boldsymbol{\phi}^r\right) \tag{4.2}$$

where $f_k\left(\boldsymbol{\phi}^r\right)$ is obtained by applying f_k to the vector field associated to mode $\boldsymbol{\phi}^r$. For instance, if f_k is the measurement of the v-component of the velocity $f_k\left(\boldsymbol{\phi}^r\right)$ is the v-component of the r-th POD mode. The following least-squares problem then has to be solved for every τ where f_k are available

$$\min_{\{\omega_1(\tau), \ldots, \omega_{N_r}(\tau)\}} \sum_{k=1}^{N_s} \left(f_k\left(\boldsymbol{u}\left(\tau\right)\right) - \sum_{j=1}^{N_r} \omega_j(\tau) f_k\left(\boldsymbol{\phi}^j\right) \right)^2 \tag{4.3}$$

where $\omega_j(t)$ is an optimization variable representing the mode coefficient at time τ.

This minimization leads to a N_r-dimensional linear system of equations. Once this system is solved, the estimated modal coefficients can be written

$$\alpha_j(\tau) = \sum_{k=1}^{N_s} \Upsilon_{kj} f_k\left(\boldsymbol{u}\left(\tau\right)\right) \tag{4.4}$$

where Υ is a known rectangular matrix of size $N_s \times N_r$. The error minimization (4.3) leads to a linear representation of the estimated modes as functions of the measurements. When the number of the modes retained is larger than the number of sensors, matrix Υ is rank deficient. In such cases we opted for a Tikhonov regularization technique: among the infinite number of solutions we chose the one that minimizes the sum of the squared residuals and the norm of the solution multiplied by a small positive factor.

The LSE approach (section §2.2 for a review), conversely, exploits temporal rather than spatial information and is based on the assumption that a linear relation exists between the modal coefficients and the measurements

$$\alpha_j(\tau) = \sum_{k=1}^{N_s} \Lambda_{kj} f_k\left(\boldsymbol{u}\left(\tau\right)\right) \tag{4.5}$$

where Λ is now an unknown rectangular matrix of size $N_s \times N_r$. This matrix is determined by imposing that $\forall r \in \{1, \ldots, N_r\}$ and $\forall k \in \{1, \ldots, N_s\}$

$$\int_0^T \hat{a}_j(t)\, f_k\left(\boldsymbol{u}\left(t\right)\right)\, dt = \int_0^T \sum_{m=1}^{N_s} \Lambda_{mj} f_m\left(\boldsymbol{u}\left(t\right)\right) f_k\left(\boldsymbol{u}\left(t\right)\right)\, dt \tag{4.6}$$

The time interval $[0, T]$ is the same as that considered for building the POD modes. Hence, since the left-hand side is known, a set of linear equations is obtained; these uniquely define the matrix Λ.

The LSQ and and LSE both provide linear estimation of the modal coefficients. Matrices Υ and Λ have the same size, although the coefficients are different. In the following we overcome the assumption of a linear relation.

Let us assume that a certain number of measurements at consecutive times τ_m, $m \in \{1, \ldots, N_m\}$ are available. The main idea of the dynamic-estimation approach proposed here is to impose that the coefficients of the modal expansion of the velocity field give the best approximation of the available measurements, using either LSQ (4.4) or LSE (4.5), and that at the same time they satisfy as closely as possible the non-linear low-order model (4.1).

In the LSQ case this is done by minimizing the sum of the residuals of (4.4) and the residuals of (4.1) for all times τ_m. More precisely, let $\boldsymbol{\alpha}(t) : \mathbb{R} \to \mathbb{R}^{N_r}$ and $\boldsymbol{\alpha}(t) = \{\alpha_1(t), \ldots, \alpha_{N_r}(t)\}$, we have

$$\boldsymbol{\alpha}(t) = \underset{\boldsymbol{\omega}(t)}{\operatorname{argmin}} \sum_{m=1}^{N_m} \left[\sum_{r=1}^{N_r} R_r^2(\boldsymbol{\omega}(\tau_m)) + C_R \sum_{r=1}^{N_r} \left(\omega_r(\tau_m) - \sum_{k=1}^{N_s} \Upsilon_{kr} f_k\left(\boldsymbol{u}\left(\tau_m\right)\right) \right)^2 \right] \tag{4.7}$$

where $\boldsymbol{\omega}(t) = \{\omega_1(t), \ldots, \omega_{N_r}(t)\}$ is an optimization variable standing for the mode coefficients vector at time t. The parameter C_R is a weight, giving more or less importance to the measurements (LSQ) or to the dynamic model in the definition of the residual norm. This parameter could be replaced by a matrix that takes into account a priori information like the reliability of some of the measurements versus others, or the model error statistics. In the numerical experiments reported here, this parameter was set in a heuristic way, leaving further developments to future investigations.

The minimization of this functional is reduced to a non-linear algebraic problem. As in Galletti *et al.* (2006) and in section §2.1.2, a pseudo-spectral approach is used and each $a_r(t)$ is expanded in time using Lagrange polynomials defined on Chebyshev-Gauss-Lobatto collocation points. The necessary conditions for the minimum are obtained by the adjoint method and they result in a non-linear set of algebraic equations for the coefficients of the Lagrange polynomials. The solution is obtained by a Newton method, which, in the present applications, usually converges in a few iterations. The complexity of the method is equivalent to the complexity of any technique employed to solve a system of non-linear algebraic equations. The systems we are dealing with are usually small ($N_r \cdot N_m$ unknowns) and hence the computational time to find the solution is small.

The solution to problem (4.7) provides an estimation for the POD modal coefficients for all retained modes and for all instants at which measurements are available. This enables the reconstruction of the entire flow field at the same instants through equation (2.4). The above method, therefore, represents a non-linear observer of the flow state. In the following, it will be referenced as K-LSQ.

A similar approach can be obtained for the LSE technique, by substituting, in Eq. (4.7), the residuals of Eq. (4.4) by those of Eq. (4.5). This approach is referenced as K-LSE.

In the literature, there exist other flow estimation techniques that are non-linear in the flow measurements. In the following we will compare the results of the proposed non-linear dynamic estimation to one of them, the quadratic extension of LSE (Adrian (1977), Naguib *et al.* (2001)). LSE is based on the assumption that equation (4.5) is just the first term of a Taylor expansion with respect to the sensor measurements, whereas QSE takes into account the second order term, too (see section §2.2). Hence, we have

$$\alpha_j(\tau) = \sum_{k=1}^{N_s} \Lambda_{kj} f_k\left(\boldsymbol{u}\left(\tau\right)\right) + \sum_{k=1}^{N_s} \sum_{m=1}^{N_s} \Omega_{kmj} f_k\left(\boldsymbol{u}\left(\tau\right)\right) f_m\left(\boldsymbol{u}\left(\tau\right)\right) \tag{4.8}$$

where the scalar coefficients Λ_{kj} and Ω_{kmj} are obtained using double, triple and quadruple correlations between measurements in an equation equivalent to (4.6). This approach is referred to as QSE.

Once the matrices appearing in equations (4.4) (4.5) and (4.8) are computed, the estimation of the modal coefficients at a certain time is based on the measurements made at the same time.

In contrast, Ewing & Citriniti (1999), Tinney *et al.* (2006) proposed to take into account integrated temporal data by assuming a linear dependence between the modal coefficients and the flow measurements in a non-local way, and working in the frequency domain. Let $\hat{\alpha}$ be the Fourier transform of α and $\hat{f}_j$ that of f_j, then for each frequency we set

$$\hat{\alpha}_j = \sum_{k=1}^{N_s} \hat{\Gamma}_{kj} \hat{f}_k \tag{4.9}$$

where $\hat{\Gamma}_{kj}$ is a matrix obtained by appropriate ensemble averages and depends on the frequency. In the time domain this amounts to a convolution integral between the measurements and the time dependent matrix Γ. We call this approach, with reference to section §2.3, SLSE. As compared to QSE and SLSE, the dynamic estimation procedure that we propose is non-linear and, at the same time, it takes into account the evolution of the modal coefficients in time by constraining such evolution to a model, in the weak sense determined by equation (4.7).

Concerning the applicability of the methods described above, it is important to recall that the LSE and LSQ approaches are readily applicable to real-time estimation, QSE also, although the cost of this last approach scales as N_s^2 instead of linearly as in the previous two cases. Conversely, the SLSE approach is more difficult to use for real-time estimations, since it uses the whole temporal history of the measurements, collected in a time interval, coupled together (linearly) via the Discrete Fourier Transform (DFT). This implies that the estimation problem must be tackled after having collected enough temporal information and it consists of a number of LSE problems equal to the number of retained frequencies, plus additional DFT's of the measurements and of the estimated POD coefficients. Similarly to what was done in the SLSE approach, in the present dynamic estimations the temporal histories of the measurements are coupled together (non-linearly) by the dynamic POD model. This aspect can pose difficulties in a real-time application. Nevertheless, a proposal for their prospective implementation for real-time estimation is the following. The flow state at a given time t^* could be estimated by considering the measurements taken at that time and at the previous $N_m - 1$ ones. At the following sampling time, the corresponding new measurements are added and the oldest ones are dropped, keeping the number of measurements considered constant. In other words, reconstruction is carried out using a fixed number of measurements distributed in a time interval which is located before t^*, and which translates as time increases. The sampling rate (*i.e.* $\tau_m - \tau_{m-1}$) and N_m can be tuned in order to decrease the computational costs while granting the level of accuracy required by the particular application. Moreover, when a new set of measurements is added, the Newton method for solving the non-linear system would be restarted from the previous solution, which is already close to the final solution, thus definitely reducing the number of iterations for convergence (only one iteration could be necessary). In contrast with the other methods, the proposed approaches need a working Galerkin model as a fundamental ingredient. The construction of such a model can be carried out from the information needed to build the POD database, a necessary step for all the methods considered here. Therefore no additional information is needed as compared to other approaches. Moreover, when using the *dynamics calibration* method, the cost of building such a model is negligible.

4.3 Results and discussion

The K-LSQ and K-LSE are used to reconstruct the flow in the configuration described in section §3, both in the two- ($Re = 150$) and three-dimensional ($Re = 300$) cases. Results are compared to those obtained by the most common techniques available in the literature and reviewed in the Introduction of this chapter.

Accuracy in the prediction of the single modal coefficients and in the reconstruction of the velocity fields were evaluated. In both cases, differences with respect to the reference case (DNS) were quantified in terms of relative error in the L^2 norm, *i.e.*, the L^2 norm of the difference between the estimated and the reference quantity divided by the norm of the reference quantity.

Several parameters are involved in the set-up of the K-LSQ and K-LSE models. They are related to (i) the dynamic POD model: number of retained modes, calibration interval, number and temporal distribution of available snapshots; (ii) the selected flow measurements: number, type and collocation.

As for the flow measurements, both velocity and shear-stress sensors were used. While velocity measurements are often considered in the literature, due to their widespread use in practice, shear-stress sensors are less common. Nevertheless, they were used here mainly because they are challenging from a numerical point of view, as they involve spatial derivatives of the POD modes. Also, they can be implemented in practice although limitations of accuracy and time resolution may exist (see, for instance, Spazzini *et al.* (1999)). Different sensor locations were tested, to account for the sensitivity of the proposed approaches to sensor placement. Since the performance of the standard techniques such as LSE or LSQ is influenced by sensor placement, some sensor configurations were selected following the suggestions given for LSE in Cohen *et al.* (2004). On the other hand, none of the considered sensor configurations is optimized for K-LSE or K-LSQ, in order to verify the sensitivity of such methods with respect to sensor placement. In fact, optimal sensor placement may turn out to be a time-consuming operation for complex three-dimensional flows.

4.3.1 Two-dimensional case: $Re = 150$

The low-order model of the two-dimensional flow is obtained using 95 snapshots, uniformly distributed throughout two vortex shedding cycles ($T \simeq 13$ is the non-dimensional duration of the time interval), and by retaining $N_r = 6$ modes, for a percentage of reconstructed energy $E \approx 99.7\%$. In figure 4.1 the first component of the first and the third POD mode is plotted. The calibration of the model is performed in the same interval using 81 collocation points with *state calibration* method. As shown in Galletti *et al.* (2004), the calibrated model accurately reproduces the flow inside and outside the calibration interval.

For this rather simple flow, we consider the situation in which a limited number of measurements are available, *i.e.* only 2 sensors. Three different configurations were analyzed, two involving streamwise velocity sensors and one involving shear-stress sensors.

The velocity sensors were placed in relation to the spatial structure of the streamwise component of the first two POD modes. In particular, in the first configuration one streamwise velocity sensor is placed on the maximum of the first POD mode which is closest to the cylinder ($P1 \simeq (2.39, 0.52)$) and one in the middle, between P1 and the minimum of the second POD mode closest to the cylinder ($\simeq (1.96, 0.50)$). The second configuration has the first streamwise velocity sensor in P1 and the second one at

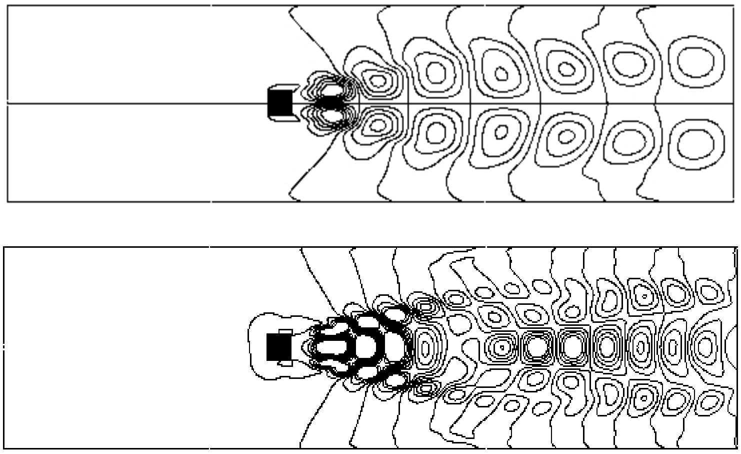

Figure 4.1: First component of the first (top) and the third (bottom) POD modes. $Re = 150$

point $(1.98, -0.76)$. A third configuration was considered with two shear-stress sensors located on the confining walls ($y = \pm 4.0$) at $x = 4$, in a region which satisfies the following criteria on a shedding cycle: the rms value of the shear-stresses is maximum and the reconstruction error of the shear-stresses is minimum for a given number of POD modes.

The parameter C_R in the formulation of the K-LSQ and K-LSE approaches (see equation (4.7)) is set equal to 1. It has been checked that the results do not significantly change if it varies in a neighborhood of this value.

The errors in the prediction of the modal coefficients given by LSQ, LSE, QSE, K-LSQ and K-LSE in the first (velocity sensors) and third (shear-stress sensors) configurations are reported in tables 4.1(a) and 4.1(b)), respectively. The values obtained for the second considered sensor configuration are not shown since they are very similar to those of the first one.

The time interval over which reconstruction is performed is approximately 13 time-units long (non-dimensional time); it contains two shedding cycles, and it starts just after the end of the time interval on which the POD model was built and calibrated.

Tables 4.2(a) and 4.2(b) show the relative reconstruction errors on the velocity components and on their fluctuating part. It appears that two (velocity or shear-stress) sensors are not sufficient to obtain reliable predictions of the modal coefficients by LSQ or LSE. Accuracy problems persist also with the QSE approach, even if in this case the predictions are more accurate than those obtained with LSQ or LSE.

This leads to severe errors in the estimation of the fluctuating part of the velocity field since the first two POD modes represent about 94.8% of the fluctuating energy. Even if the mean flow energy is important with respect to the fluctuating energy, errors in the modal coefficients lead to detectable errors in the reconstruction of the velocity components. Note that the reconstruction errors on the vertical component are larger

Tab. 4.1(a)	$e(a_1)$%	$e(a_2)$%	$e(a_3)$%	$e(a_4)$%	$e(a_5)$%	$e(a_6)$%
LSQ	36.33	64.75	280.55	265.66	145.31	117.94
LSE	71.06	27.12	99.71	97.97	99.91	99.93
QSE	20.67	13.03	20.66	40.99	91.05	88.01
K-LSQ	0.47	0.55	2.58	2.66	4.65	4.67
K-LSE	0.82	0.76	9.82	9.82	14.98	15.59

Tab. 4.1(b)	$e(a_1)$%	$e(a_2)$%	$e(a_3)$%	$e(a_4)$%	$e(a_5)$%	$e(a_6)$%
LSQ	63.61	84.81	109.32	107.17	100.53	101.39
LSE	46.87	91.97	102.83	100.99	101.40	100.21
QSE	33.32	56.00	78.28	41.62	95.31	75.64
K-LSQ	0.06	0.09	6.06	6.09	9.72	9.56
K-LSE	2.99	3.08	7.07	8.31	17.99	18.47

Table 4.1: Relative percentage errors (in L^2 norm) on the estimation of the POD modal coefficients ($e(a_i)$) in the first (a) and third (b) sensor configuration. In this case time-averaging is carried out over the estimation time period.

than those on the streamwise one. This is simply because the contribution of the mean flow on the vertical component is much lower than on the streamwise component. Tables 4.1 and 4.2 show that both K-LSQ and K-LSE give an accurate estimation not only of the first two modal coefficients, but of all the retained modes. This leads to a precise estimation of the velocity field as well as of its fluctuating part. Moreover, the accuracy of the results is very similar, whether using shear-stress or velocity sensors, indicating a weak sensitivity of the approach to the type and location of the sensors. This is not the case for the LSQ, LSE and QSE methods, which show a higher sensitivity to these aspects, confirming what has already been reported in the literature. When the number of sensor increases, the difference between static and dynamic estimations tend to reduce, as they both tend to the correct values of the Galerkin coefficients.

We compare our results to those of Cohen *et al.* (2004), Tab. 2(a) 13-th case. With LSE and 2 sensors they found $e(a_1) \simeq 76.6\%$ and $e(a_2) \simeq 15.1\%$, errors that are similar to those reported in table 4.1(a) for LSE. Using the dynamic estimation, the errors on the same coefficients are two orders of magnitude lower. Furthermore, using the K-LSQ method and two shear-stress sensors (table 4.1(b)) the first two modal coefficients are estimated with an error lower than 0.1%, *i.e.*, three orders of magnitude lower than LSE. The estimation results relative to K-LSQ and K-LSE are practically identical if the low-order models are built either by *state* or *dynamics calibration* method.

The computational times are basically negligible for all cases: the static estimations are accomplished within a fraction of a second (0.0003s for LSE on a normal personal computer), whereas the dynamic estimations take a longer but still very small time (K-LSQ: 0.6s, K-LSE: 0.3s on the same computer).

Tab. 4.2(a)	$\overline{e(U)}\%$	$\overline{e(V)}\%$	$\overline{e(U')}\%$	$\overline{e(V')}\%$
LSQ	10.31	57.49	72.15	65.88
LSE	6.32	37.14	53.96	54.26
QSE	2.41	16.06	20.65	23.45
K-LSQ	0.63	3.97	5.39	5.80
K-LSE	0.69	4.42	5.93	6.46

Tab. 4.2(b)	$\overline{e(U)}\%$	$\overline{e(V)}\%$	$\overline{e(U')}\%$	$\overline{e(V')}\%$
LSQ	10.60	64.57	74.31	73.82
LSE	8.05	46.14	68.32	67.44
QSE	4.70	28.28	39.81	41.37
K-LSQ	0.65	4.10	5.54	6.00
K-LSE	0.77	4.91	6.54	7.17

Table 4.2: Relative percentage errors (in L^2 norm) on the estimation of the velocity components ($\overline{e(U)}$,$\overline{e(V)}$) and of their fluctuating part ($\overline{e(U')}$,$\overline{e(V')}$), in the first (a) and third (b) sensor configuration. In this case time-averaging is carried out over the estimation time period.

4.3.2 Three-dimensional case: $Re = 300$

In the case of $Re = 300$, as already seen in chapter 3, the flow patterns are definitely more complex than those in the previous one.

Two low-order models of the developed three-dimensional flow were derived retaining the first 20 or 60 POD modes obtained from a database of 151 snapshots, uniformly distributed over eight vortex shedding cycles ($\simeq$ 52 non-dimensional time units from 360 to 412). Calibration was carried out in the same time interval using *dynamics calibration* method (see section §2.1.2). The results obtained by integrating the dynamic model within the calibration interval are reported in figures 4.2 and 4.3, in which the calibrated POD coefficients are compared to those obtained from the projection of the fully resolved Navier-Stokes simulations. A comparison between the results obtained using the two different calibration techniques (*state* and *dynamics calibration*) is also provided. Model given by the *state calibration* is of course more accurate, although the differences become almost negligible as the number of modes retained increases. In both cases, the POD model shows a good accuracy inside the calibration interval. However, in the three-dimensional case, these results tend to deteriorate outside the time interval in which the calibration is performed, as shown in the following. Furthermore, we analyze the ability of the retained POD modes to represent the flow field in the interval in which the flow estimation is carried out. This time interval being about 82 time units after the end of the calibration interval (at time 494), and is approximately 30 time units long, including approximately 4 shedding cycles. In table 4.3 we give the minimum error that we can hope to achieve when reconstructing the fluctuating part of the velocity components. The minimum error corresponds to the case where the

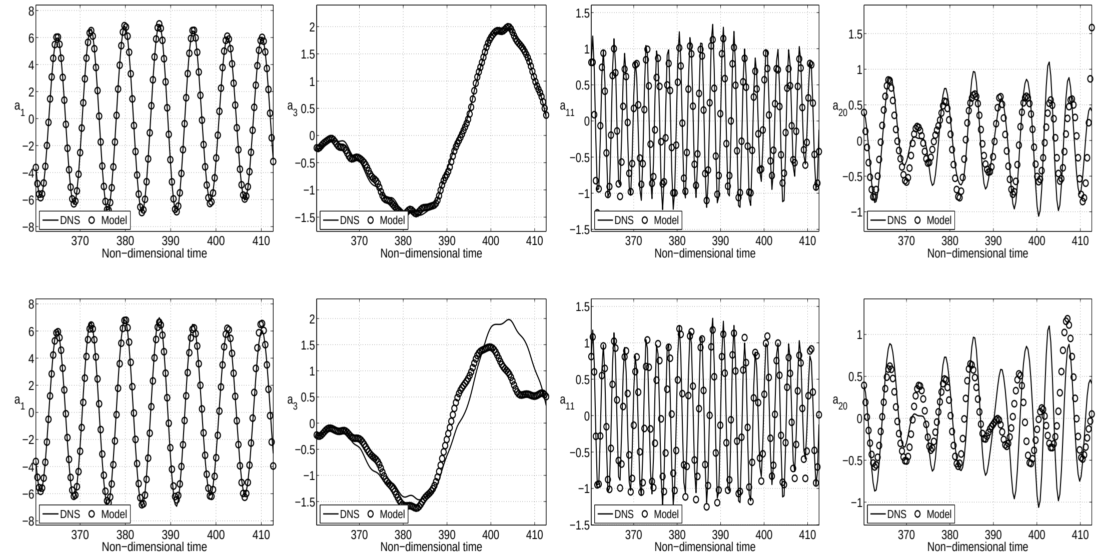

Figure 4.2: Three-dimensional flow: projection of the fully resolved Navier-Stokes simulations over the POD modes (continuous line) vs. the integration of the dynamical system inside the calibration interval, obtained retaining the first 20 POD modes (circles). The first row is relative to *state calibration*, the other to *dynamics calibration*. Only some representative coefficients are shown.

estimated POD coefficients coincide with those obtained by projecting the reference Navier-Stokes solution over the POD modes, *i.e.*, $\hat{a}_r(t) = \alpha_r(t)$. This error is computed over the entire domain, and over a subset defined by $0 \leq x/L \leq 6$, which corresponds to the near wake of the cylinder. These errors are not small, even if we increase the number of modes from 20 to 60, as shown in table 4.3. In fact, using a larger number of POD modes does not help in general. Using 60 modes instead of 20 does not reduce significantly the representation error because the modes from 20 to 60 are not statistically relevant outside the reference interval where the snapshots were taken. In other words, in order to increase the representativeness of those modes (20 to 60) outside the reference interval one should take larger databases encompassing longer time lags. However, the problem is that the convergence rate of the POD modes with respect to the number of snapshots included in the database is very low. In this case, for example, using 60 modes, the relative approximation error goes down from 40% to 30% when the database goes from 151 snapshots to 912 snapshots, that is the limit of our computational resources.

The largest errors are on the spanwise component, since the retained POD modes poorly represent this component of the velocity as it is not energetically significant, in average, with respect to the remaining ones. This aspect might be improved working on the construction of the POD basis choosing, for instance, a different norm which gives more weight to the spanwise component of the velocity or which corresponds to a quantity different from kinetic energy.

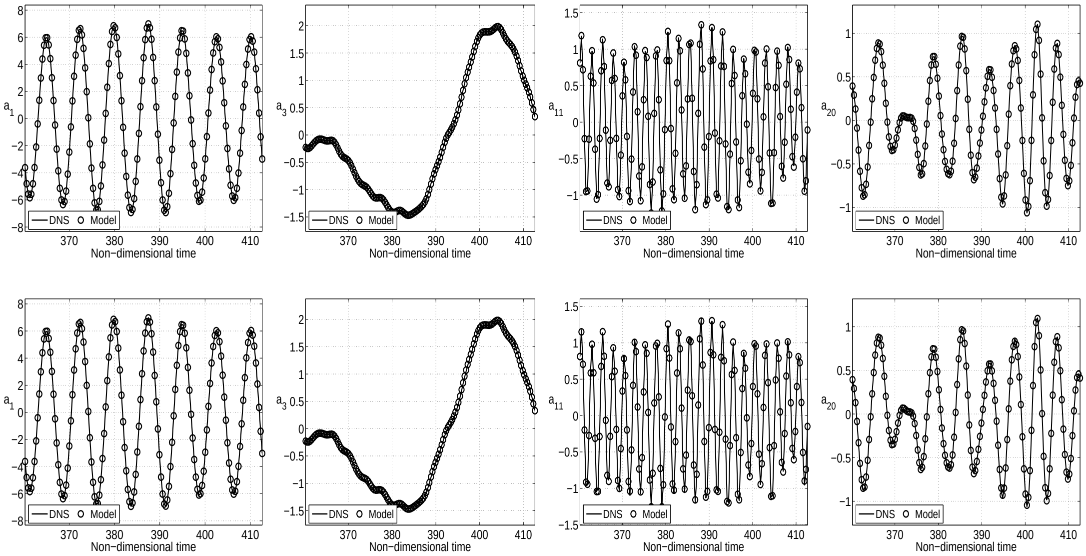

Figure 4.3: Three-dimensional flow: projection of the fully resolved Navier-Stokes simulations over the POD modes (continuous line) vs. the integration of the dynamical system inside the calibration interval, obtained retaining the first 60 POD modes (circles). The first row is relative to *state calibration*, the other to *dynamics calibration*. Only some representative coefficients are shown

In other words, the accuracy of the best possible reconstruction is limited from above by the capability of the POD modes to actually represent the flow outside the time interval where the snapshots were taken, which however, increases using a larger snapshots database, as shown in Buffoni *et al.* (2006). Note, however, that this problem is common to all the considered reconstruction techniques, since they all use the POD representation of the velocity field. Because of the complexity of the flow, more measurements

	$\overline{e(U'_{ent})}\%$	$\overline{e(V'_{ent})}\%$	$\overline{e(W'_{ent})}\%$	$\overline{e(U'_{06})}\%$	$\overline{e(V'_{06})}\%$	$\overline{e(W'_{06})}\%$
20 modes	57.48	43.41	95.57	47.27	43.21	99.37
60 modes	56.78	41.76	94.72	46.34	41.21	98.77

Table 4.3: Minimum errors on the fluctuating part of the velocity components. 20 and 60 POD modes, over the entire flow field (*ent*) and over the near wake (06). The time interval considered is 82 non-dimensional time units (about 10 shedding cycles) away from the time interval where the POD modes were derived.

were used for the reconstruction procedure, organized in five different configurations, two involving only velocity measurements and three involving both velocity and shear-stress measurements (see figure 4.4 for a hypothetical sensor configuration involving both velocity and shear-stress sensors). In the last three configurations, the shear-stress sensors

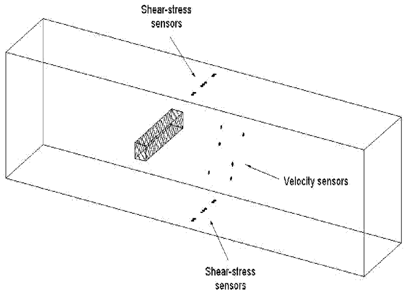

Figure 4.4: Hypothetical placement of velocity and shear-stress sensors.

were selected following the same criterion adopted in the 2D case, they are 14 in number and in all considered cases are symmetrically placed on both the confining walls ($y = \pm 4$) at $x = 4$ and $z = \{1.2, 1.5, 2.7, 3, 3.3, 4.5, 4.8\}$. The placement of the velocity sensors has again been chosen on the basis of the spatial structure of the streamwise velocity of the first 12 POD modes. The different configurations are listed below, together with a brief description of the rationale for the placement of the velocity sensors:

a) 24 velocity sensors distributed on 6 equispaced slices in the axial (z) direction; on each slice, the sensors are on the lines connecting the maximum and minimum, closest to the cylinder, of the first two POD modes. On each segment, the sensors are approximately in the middle, but slightly closer to the extrema of the first POD mode.

b) 24 velocity sensors distributed on 4 equispaced slices in the axial (z) direction; on each slice, 3 points are selected in the region of overlapping between the maxima and minima of the low-frequency POD modes (modes 3, 4, 7, 8, 9 and 10) and 3 on the overlapping region of the extrema of the vortex shedding modes (modes 1, 2, 5, 6, 7, 11 and 12) (see Buffoni *et al.* (2006) for details on the separation between low-frequency and vortex-shedding POD modes).

c) 14 shear-stress sensors and 10 velocity sensors distributed on 5 equispaced slices in the axial (z) direction; on each slice, the velocity sensors are placed on the maximum and minimum closest to the cylinder of the first POD mode.

d) 14 shear-stress sensors and 10 velocity sensors. 6 equispaced slices in the axial (z) direction are considered. On 4 slices, 2 velocity sensors are placed as in the previous case. Two sensors are placed on the remaining slices, corresponding respectively to the maximum and minimum of the third POD mode (low frequency mode).

e) 14 shear-stress sensors and 6 velocity sensors located in the wake, at the points reported in table 4.4.

The parameter C_R of equation (4.7) was selected by experimenting with different values. For example, in figure 4.5(a), we show the L^2 relative error for the reconstruction by

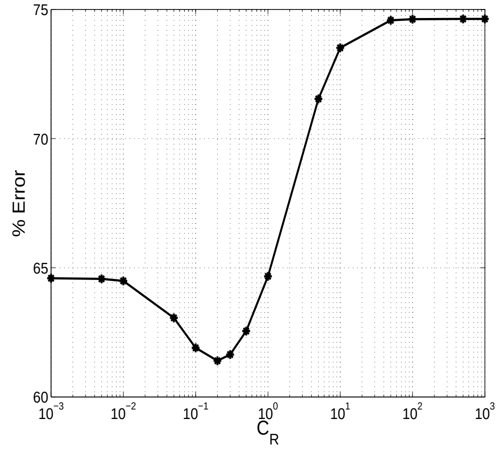

(a)

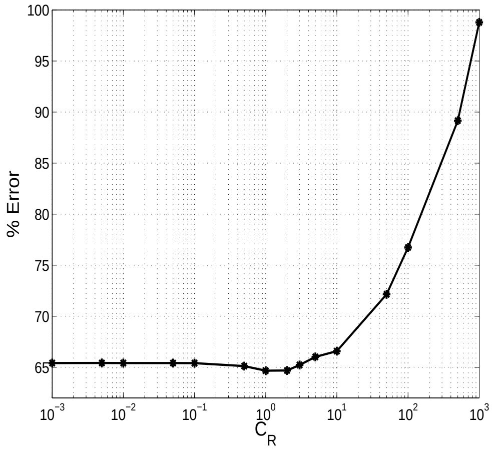

(b)

Figure 4.5: Relative percent error in the reconstruction of the fluctuating U component, when varying C_R: (a) KLSE, (b) KLSQ

Velocity sensor	x	y	z	Velocity sensor	x	y	z
1	5.02	0.96	2.00	4	6.01	0.96	4.00
2	7.00	0.96	2.00	5	5.02	-0.96	4.00
3	6.01	-0.96	2.00	6	7.00	-0.96	4.00

Table 4.4: Positions of the velocity sensors in the three-dimensional case, configuration (e).

K-LSE of the fluctuating U component, as a function of C_R. The results are relative to configuration (b). The plotted curve shows a minimum for $C_R = 0.2$ and therefore in the following we chose $C_R = 0.2$ for K-LSE. Note that for $C_R \geq 10^2$ the results are basically those of a simple LSE. A similar analysis was performed using K-LSQ (see figure 4.5(b)) and the best value that was selected is $C_R = 1$.

Results relative to configuration (b) are reported in figure 4.6, where some representative modal coefficients predicted by the POD model calibrated by *dynamics calibration* with 20 modes, LSQ, LSE, K-LSQ, K-LSE and SLSE are plotted, together with the projection of the DNS velocity fields on the corresponding POD mode. Results for configuration (b) are shown because the sensor placement is appropriate for the LSE method, as already discussed, and this makes the comparison with the proposed approaches more comprehensive.

In figure 4.6, left column, one can observe that, in contrast with the two-dimensional case and as previously stated, the POD model is less accurate outside the calibration interval. However, long after the end of the calibration interval, the model remains stable, and the error bounded. The results obtained with the other sensor configurations or with model given by *state calibration* are similar to those reported in figure 4.6, except for LSE

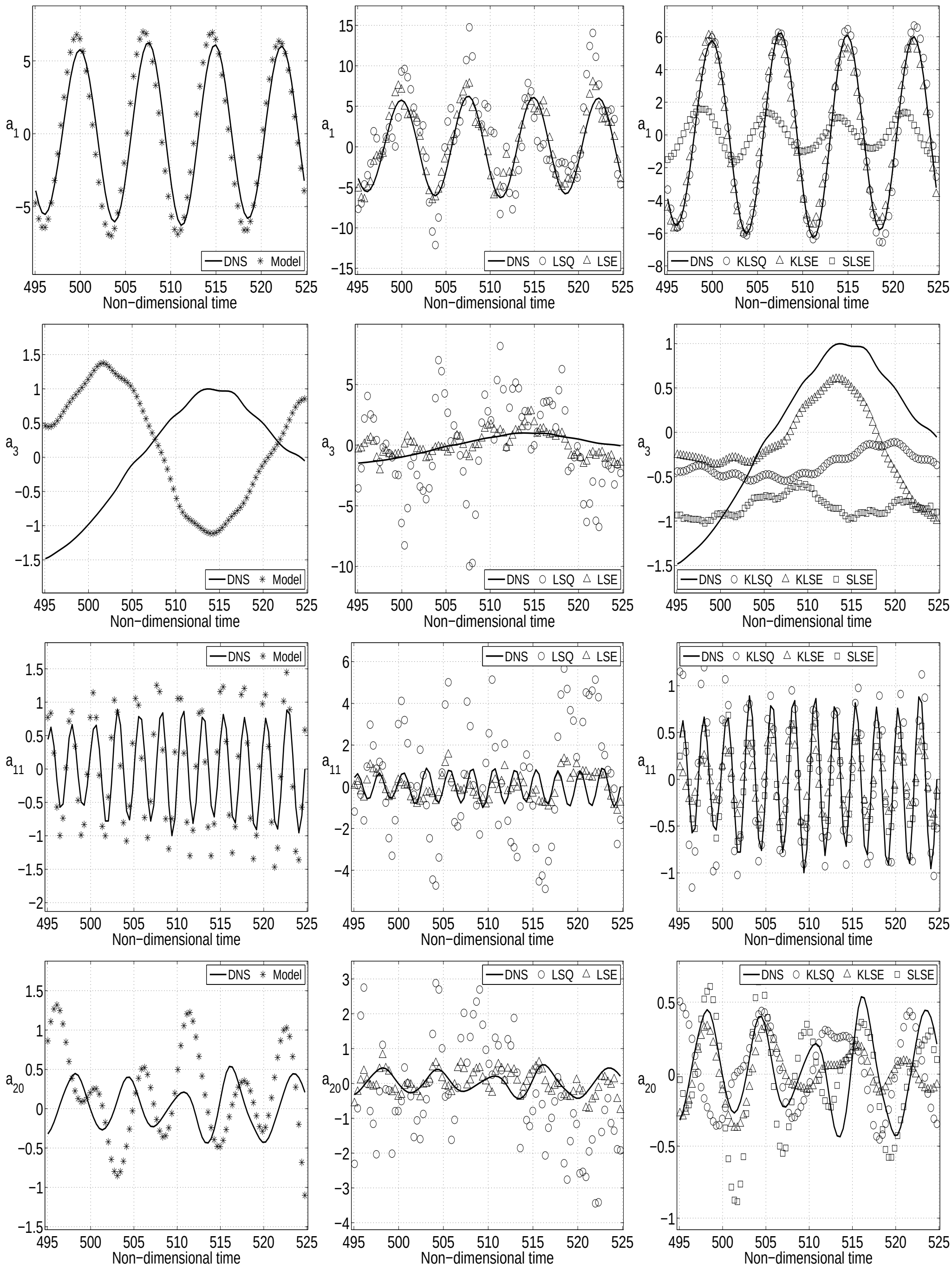

Figure 4.6: Estimation of some representative modal coefficients in the three-dimensional case, for sensor configuration (b) and far from the calibration interval, together with the reference values evaluated from the DNS simulation. Note that the same graph is reported in the three columns but the axis scales are different. Model by *dynamics calibration* with 20 modes.

SC (a)	$\overline{e(U'_{ent})}\%$	$\overline{e(V'_{ent})}\%$	$\overline{e(W'_{ent})}\%$	$\overline{e(U'_{06})}\%$	$\overline{e(V'_{06})}\%$	$\overline{e(W'_{06})}\%$
KLSQ	63.54	49.77	101.11	48.78	44.92	106.65
KLSE	62.63	48.37	100.95	47.22	44.26	101.71
SLSE	66.39	49.12	104.92	49.77	46.59	110.60

SC (b)	$\overline{e(U'_{ent})}\%$	$\overline{e(V'_{ent})}\%$	$\overline{e(W'_{ent})}\%$	$\overline{e(U'_{06})}\%$	$\overline{e(V'_{06})}\%$	$\overline{e(W'_{06})}\%$
KLSQ	64.67	49.77	102.26	49.94	48.35	108.64
KLSE	61.40	47.03	98.45	47.17	43.73	101.09
SLSE	95.77	91.14	110.56	91.15	89.14	112.42

Table 4.5: Reconstruction errors obtained with the *dynamics calibration* model and 20 modes for sensor configurations (a) and (b). Errors computed on the entire domain (*ent*) and in the near wake (06).

and LSQ methods which are less accurate as they are more sensitive to sensor placement. In figure 4.6 it is seen that LSE and LSQ, provide reasonable predictions only for the first two modal coefficients, that are associated with the vortex-shedding dynamics. The second modal coefficient, not shown in the figure, is identical to the first one except for a phase shift of $\pi/2$ in time. However, the results in terms of approximation are the same. The predictions of the remaining modes are completely unreliable. When dynamic estimation is applied, or when the SLSE approach is used, predictions are definitely improved. In particular, this is true for modes like a_1 or a_{11} that are related to the vortex-shedding, *i.e.*, almost periodic with a period that is the same or a multiple of the vortex-shedding period. The prediction of the remaining modes is less accurate (see a_3 and a_{20}), especially when very low frequencies are dominant, as in the case of a_3. However, the overall accuracy is significantly improved in comparison with the LSQ and LSE approaches alone. The static estimations are accomplished within a fraction of a second (0.0012s for LSE), whereas the dynamic estimations still take less than a minute (K-LSQ: 21s, K-LSE: 25s).

In tables 4.5 and 4.6, the actual errors obtained using 20 modes are given. The errors of LSE and LSQ are not included since they are larger than the others. We observe that the dynamic approaches are systematically more accurate than SLSE and that the reconstruction errors can be considered satisfactory as they are close to the minimum error possible (see table 4.3). Furthermore the reconstruction errors progressively increase moving away from the cylinder in the downstream direction. Concerning the spanwise component of the velocity, as previously discussed, errors are large since the retained POD modes themselves poorly represent this component of velocity (see tables 4.5 and 4.6).

As an example of an actual estimation in the physical space, we considered two points located on the symmetry plane orthogonal to the spanwise direction. They were selected in order to represent the typical results obtained. In figure 4.7 we show the actual U' and V' components of the velocity obtained by DNS, the projection on the POD basis

SC (c)	$\overline{e(U'_{ent})}\%$	$\overline{e(V'_{ent})}\%$	$\overline{e(W'_{ent})}\%$	$\overline{e(U'_{06})}\%$	$\overline{e(V'_{06})}\%$	$\overline{e(W'_{06})}\%$
KLSQ	62.68	48.72	100.00	48.53	45.54	103.87
KLSE	66.76	51.78	99.42	53.94	51.87	103.85
SLSE	76.01	56.46	112.81	53.60	52.72	118.65

SC (d)	$\overline{e(U'_{ent})}\%$	$\overline{e(V'_{ent})}\%$	$\overline{e(W'_{ent})}\%$	$\overline{e(U'_{06})}\%$	$\overline{e(V'_{06})}\%$	$\overline{e(W'_{06})}\%$
KLSQ	67.54	53.44	104.86	52.16	48.86	111.07
KLSE	64.35	51.14	101.01	52.06	50.58	105.30
SLSE	70.95	55.75	108.64	55.24	55.30	116.96

SC (e)	$\overline{e(U'_{ent})}\%$	$\overline{e(V'_{ent})}\%$	$\overline{e(W'_{ent})}\%$	$\overline{e(U'_{06})}\%$	$\overline{e(V'_{06})}\%$	$\overline{e(W'_{06})}\%$
KLSQ	132.40	97.56	162.68	96.73	100.01	183.59
KLSE	64.37	49.63	99.49	52.10	50.20	103.12
SLSE	79.12	58.98	115.97	57.16	55.15	124.96

Table 4.6: Reconstruction errors obtained with the *dynamics calibration* model and 20 modes for sensor configurations (c), (d) and (e). Errors computed on the entire domain (*ent*) and in the near wake (06).

SC (b)	$\overline{e(U'_{ent})}\%$	$\overline{e(V'_{ent})}\%$	$\overline{e(W'_{ent})}\%$	$\overline{e(U'_{06})}\%$	$\overline{e(V'_{06})}\%$	$\overline{e(W'_{06})}\%$
KLSE 20M	61.40	47.03	98.45	47.17	43.73	101.09
KLSE 60M	61.37	46.70	98.65	46.93	42.85	100.77

Table 4.7: Comparison between reconstruction errors obtained with model given by *dynamics calibration* and 20 or 60 modes for sensor configuration (b). Errors computed on the entire domain and in the near wake.

as well as the estimation obtained by K-LSE, using the *dynamics calibration* model, 20 POD modes and sensor configuration (b). We observe that the estimation is accurate for the point in the wake where the time evolution is smooth. At the other point, located on the horizontal axis in a region where highly three-dimensional phenomena take place, we observe sudden bursts of activity that are filtered away by the estimation, at least for the U component.

The K-LSQ, K-LSE and SLSE methods are similar in the sensitivity of the predictions to sensors type and placement, which is generally low. Nevertheless, the predictions given by the K-LSE method are systematically the most insensitive to sensor placement. Table 4.7 compares the results obtained with 20 modes and those obtained with 60 modes, using the *dynamics calibration* model and sensor configuration (b). A slight improvement of the estimation can be observed. The same conclusion applies for the other sensor configurations not reported here. Using model obtained via *state calibration* the results are basically the same as those shown here.

In figure 4.8 the velocity components obtained by DNS at $t = 426.6$ (a snapshot

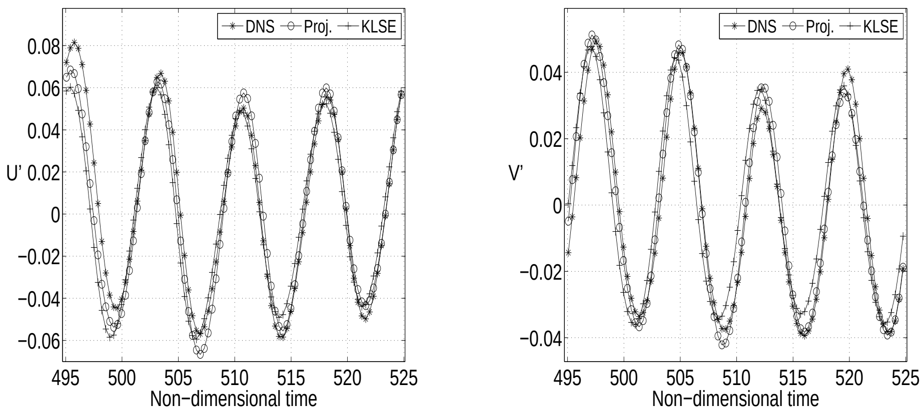

(a)

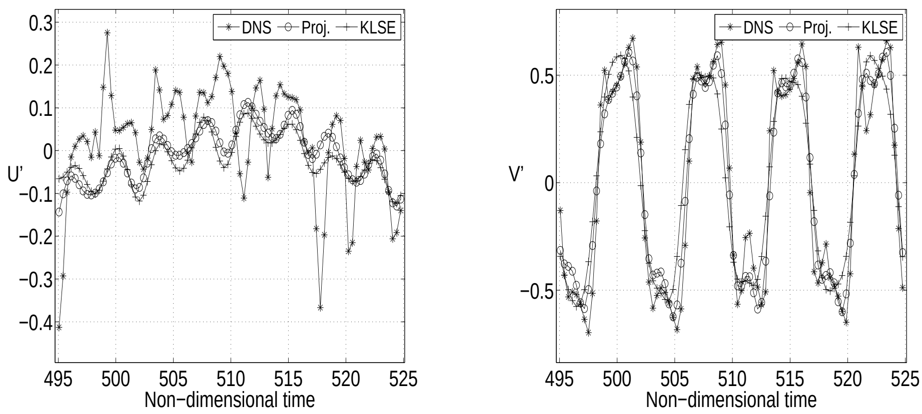

(b)

Figure 4.7: Reconstruction of U' and V' components of the velocity at points (a) x/L = 2.55, y/L = 2.51, z/L = 3.00 , (b) x/L = 5.45, y/L = 0.00, z/L = 3.00.

outside the database used for the construction and calibration of the POD model) are plotted together with their projections on the space of the retained POD modes. These projections represent the best approximation of the flow which can be estimated with the retained POD modes, and with the prediction given by the K-LSE method. It can be seen that the main structures characterizing the streamwise and lateral velocity fields are well reconstructed. As for the spanwise velocity component, the reconstruction accuracy is not satisfactory, but this is due to the fact that it is one order of magnitude lower than the other components, as already discussed.

The estimation of the POD modal coefficients and of the reconstruction of the flow velocity field enable the reconstruction of the aerodynamical forces on the cylinder. Indeed, we can define the lift and the drag coefficients on the square cylinder in the classical way

$$C_l(t) = \frac{\int_S \left((p(x,t) - p_0) \cdot \bar{n} + \mathbf{T}(x,t) \cdot \bar{t}\right) \, dS}{\frac{1}{2} U_c^2 S} \cdot \bar{j}$$
$$C_d(t) = \frac{\int_S \left((p(x,t) - p_0) \cdot \bar{n} + \mathbf{T}(x,t) \cdot \bar{t}\right) \, dS}{\frac{1}{2} U_c^2 S} \cdot \bar{i}$$

where p_0, U_c are the reference pressure and velocity at the inflow respectively and $\mathbf{T}$ is the viscous stress tensor.
The entire pressure field, and in particular the pressure field around the square cylinder, is reconstructed by using the POD pressure coefficients obtained by the *Poisson model* (2.15) described in section §2.1.2. The POD for pressure fields and the calibration procedure of the resulted *Poisson model* are performed in the time interval $[0, T]$ as that considered to compute the POD modes and the dynamical model for the velocity. The number of POD pressure modes retained is $N_r^p = 20$. In figure 4.9 the actual lift and drag coefficients, outside the POD database and the calibration interval, are plotted together with the coefficients obtained by using the projection of the entire flow fields onto the retained POD modes N_r and N_r^p and with C_l and C_d reconstructed by using the K-LSE estimation with sensors configuration (b). The model provides a good reconstruction of the aerodynamical forces. Indeed, the lift coefficient is well reconstructed with good accuracy both in amplitude and in phase. The reconstruction of drag coefficient is almost exact in phase but it is not accurate in amplitude. As for the spanwise velocity component, this is due to the fact that the amplitude oscillation is small if compared with the oscillation of the lift coefficient (one order of magnitude smaller). However, even for the drag coefficient, the average value is well estimated, as suggested by the figure 4.9.

4.4 Conclusions

We devised a method to build a non-linear observer for unsteady flows. This method is based on the coupling of a non-linear low-dimensional model of the flow with a linear technique that estimates the coefficients of the flow representation in terms of POD

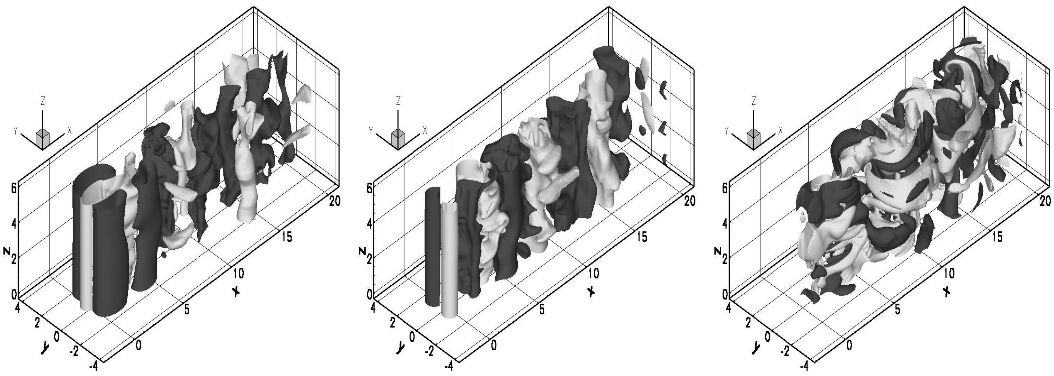

(a)

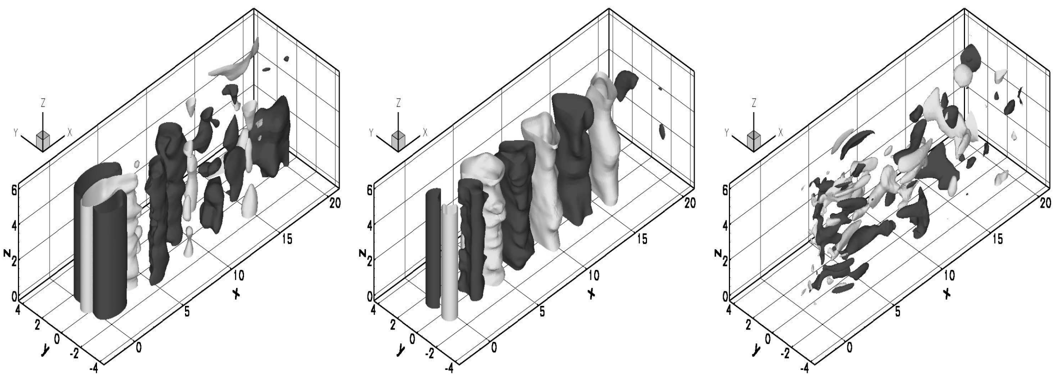

(b)

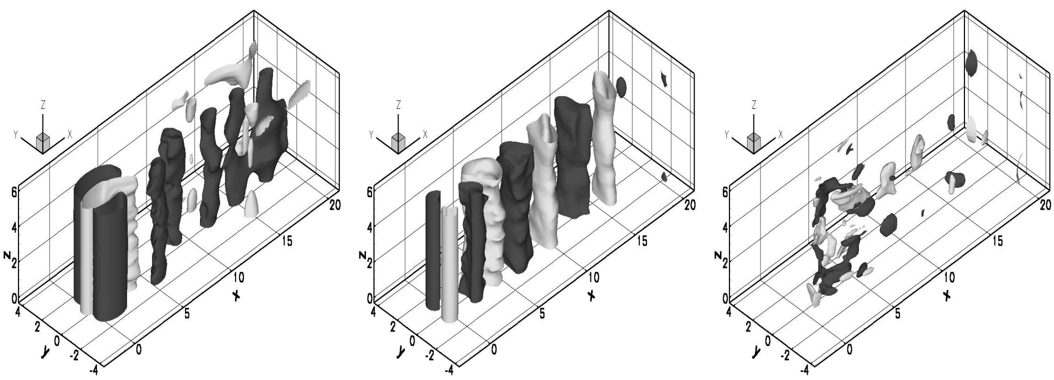

(c)

Figure 4.8: Isosurfaces of the velocity components u (left, grey = 0.5, dark grey = 1.0), v (center, grey = -0.25, dark grey = 0.25) and w (right, grey = -0.075, dark grey = 0.075) of a snapshot outside the database: (a) actual snapshot, (b) snapshot projected on the retained POD modes,(c) reconstructed snapshot using the K-LSE technique with the sensor configuration (b).

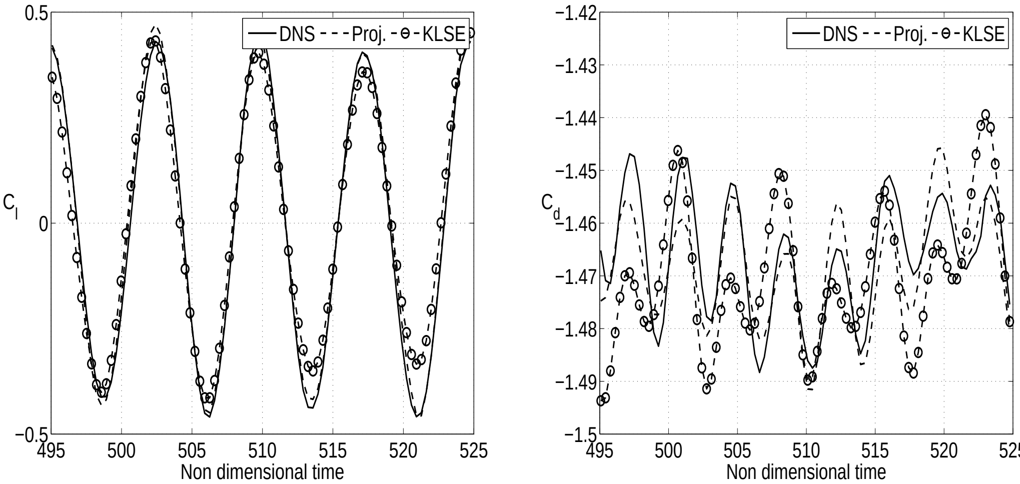

Figure 4.9: Reconstruction of Cl and Cd using KLSE results .vs. actual Cl and Cd and their prjoections on the POD modes.

modes. The underlying idea is that the estimated flow should approximately satisfy the POD model. The coupling leads to a nonlinear minimization problem solved by a pseudo-spectral approach and a Newton method.

The non-linear observer was applied to the laminar flow around a confined square cylinder at two different Reynolds numbers; for the first the flow is two-dimensional, while in the second case complicated three-dimensional phenomena occur in the wake.

In the two-dimensional case, with a limited number of sensors, the proposed procedure is able to give a significantly more accurate estimation of the POD coefficients and of the whole velocity field than the LSQ, LSE and QSE approaches.

In the three-dimensional case, the flow dynamics are more complex, and not only LSE and LSQ, but also the calibrated POD dynamical system provide poor coefficient estimations when used outside the calibration interval. Conversely, the proposed procedure, combined with either LSQ or LSE, gives satisfactory predictions of the coefficients of those POD modes that are related to vortex shedding. For the remaining modes, the accuracy is lower. Nevertheless, the instantaneous velocity fields are reconstructed with an accuracy close to the best possible, which is the one that would be obtained by projecting the DNS fields on the retained POD modes. The actual lift and drag coefficients, even if the amplitude of the oscillations of the drag coefficient are not perfectly captured, are well reconstructed for the three-dimensional case.

Moreover, K-LSE and K-LSQ methods are weakly sensitive to sensor type and placement. The results obtained with the proposed approaches are comparable to those obtained by the SLSE approach, which also uses the temporal history of the flow measurements, but in the Fourier space. This latter technique has a computational complexity which is significantly larger than that of LSE or LSQ, and comparable to that of the proposed approaches.

From the present study, it appears that, probably, for flows characterized by complex dynamics, the major limitation of all estimation techniques based on POD is indeed the ability of the retained POD modes to adequately representing the flow field.

Thus, one way to improve the present results for the three-dimensional case is to include statistical information concerning the errors both in the model and in the measured quantities, since the POD modes do not give an accurate representation of the flow field. Including the parameter C_R in the formulation is indeed a rudimental approach that shows the influence of the relative weight given to the model or the measurements.

Another way is obviously to build a more accurate POD model. A possibility is to take larger data bases to compute POD modes having better approximation properties. However, this may not be pushed too far because of the huge amount of computational resources required for managing large DNS datasets. Indeed, as shown in (Buffoni *et al.*, 2006), even with using a huge POD database, the increasing of the representativity of the POD modes outside the database is not significant.

Another promising approach in this direction could be to modify the scalar product used in the definition of the POD modes in such a way as to take into account the most observable events in the flow.

The K-LSQ and K-LSE described here for non-controlled flows can be easily extended to controlled flows. Thus, for control purposes, the estimation techniques could be applied in a closed-loop controller, when the knowledge of the whole flow field is required. Indeed, the K-LSQ and K-LSE, being weakly sensitive to sensors position, are good candidates to be used with realistic sensors normally used in active control of flow past bluff bodies as pressure sensors placed on the surface.

One of the main limitations of the method can be the robustness of the adopted low-order model to the parameters variation. Indeed, the reduced model, if used within an estimation procedure, has to be accurate for any parameters configuration. The issue of building a robust low-order model will be examined in the next chapters.

Chapter 5

Robust POD modeling of actuated vortex wake

The study of this chapter is concentrated on the problem of deriving accurate and robust low order models of actuated fluid flows. In the previous chapter the issue of the asymptotic stability of the models was overcame by the two techniques of calibration, the *state* and the *dynamics* calibration. We showed that it is possible to obtain accurate low-order models even of complicated three-dimensional flows. The models obtained are both accurate inside the interval of calibration and, even if not accurate, stable longer in time. Here we extend the identification problem to cases where the flow is actuated by devices that can affect locally or globally the velocity and pressure fields. The objective is to derive a low-order model that provides accurate predictions and, most importantly, that is robust to variations of the control law employed. Indeed, the aim is, by using low-order models, to make possible to optimize controls for large-scale problems that would not be otherwise solvable in terms of computational size. Indeed, the main drawback is that the POD model is not able to represent the dynamics of a flow generated with different control parameters.

The main idea is to identify the manifold over which the non-linear dynamics of the POD modes lies, when the input to the system is varied. In this spirit, several dynamics are included in the POD and calibration procedures are coupled with a Tikhonov type regularization. The case of a precomputed control (open-loop) as well as the case of a feed-back control (closed-loop) are studied.
Applications of this method is straight forward for models other than the Navier-Stokes equations.

5.1 Flow setup and low order model

With reference to the geometry described in chapter §3, and skecthed again in figure 5.1(a) we consider a two-dimensional configuration, *i.e.* $L_z/L = 0.6$. Thus the Reynolds numbers considered in this chapter are such that the flow can be considered two-dimensional. As already asserted, the two three-dimensional instability, mode A

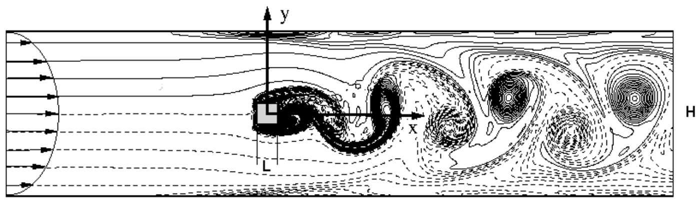

(a) Flow configuration and isocontour of vorticity of a snapshot at $Re = 150$ (dashed lines represent negative values).

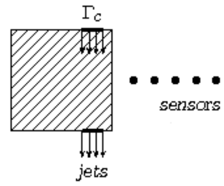

(b) Placement of synthetic jet and sensors for control

Figure 5.1: Sketch of the flow configuration with control actuation.

and mode B, occur, for unconfined square cylinders, at $Re \simeq 160$ and $Re = 190 - 200$ respectively (chapter §3).

However large control inputs can promote three-dimensional behavior at lower Reynolds numbers. This occurrence is neglected in the present framework.

In order to introduce a control device, aimed to stabilize the flow around the cylinder, two jets are placed on the cylinder driven in opposite phase, as shown in figure 5.1(b). Details concerning the geometry of the jets are in (Weller *et al.*, 2009).

The presence of an actuator is modeled by imposing a new boundary condition on a small surface Γ_c of $\partial\Omega$, with width $L_{\Gamma_c} = 0.2L$:

$$\boldsymbol{u}(\boldsymbol{x}, t) \cdot \boldsymbol{n}(\boldsymbol{x}) = c(t), \quad \boldsymbol{x} \in \Gamma_c$$

Since the two actuators are driven in opposite phase:

$$v(\boldsymbol{x}, t) = c(t), \quad \boldsymbol{x} \in \Gamma_c$$

Our interest in reduced-order models is that they can be useful for control purposes. For example, using measurements of the vertical velocity at points $\boldsymbol{x}_j$ in the cylinder wake, and not an estimation of all the state flow, we can define a proportional control law:

$$c(t) = \sum_{j=1}^{N_s} \mathsf{K}_j (v(\boldsymbol{x}_j, t) - v^0(\boldsymbol{x}_j))$$

where N_s denotes the number of sensors used and $v^0(\boldsymbol{x}_j)$ the vertical velocity of the target flow field at points $\boldsymbol{x}_j$. We could then use the model to compute the set of feedback gains K_j that minimize the vortex shedding in the cylinder wake. In particular if the target field is the steady unstable solution, as in (Li & Aubry, 2003; Weller *et al.*, 2009), and the sensors are placed in the center-line, being $v^0(\boldsymbol{x}_j) = 0$, the proportional control law becomes:

$$c(t) = \sum_{j=1}^{N_s} \mathsf{K}_j (v(\boldsymbol{x}_j, t))$$

However the use of feedback control laws, rather than precomputed ones, can induce extra errors in the models (see section §5.3.1). As a first step, we will therefore look at examples in which the controls are trigonometrical series.

Given a numerical simulation of the Navier-Stokes equations performed over a time interval $[0, T]$, and the velocity field saved at N_t time instants $t_i \in [0, T]$, this yields a data set $\{\boldsymbol{u}^i(\boldsymbol{x}) = \boldsymbol{u}(\boldsymbol{x}, t^i)\}_{i=1..N_t}$. On this database we perform a POD procedure, as described in section §2.1.1, using the snapshot method to compute the POD modes $\{\boldsymbol{\phi}^r\}_{r=1...N_r}$.
In the case of forced flow, the snapshots depend on the control law $c(t)$ used. In this chapter we consider POD bases derived from numerical simulations obtained using several different control laws. There are many other parameters that could be varied, but since here the aim is to study the effect of a control law, we set ourselves in the following framework:

- Time instants, Reynolds number, domain geometry, placement of the actuators will be the same for all the snapshots in the database.

- The control law $c(t)$ will be varied

The data set used for the POD is therefore written:

$$\{\boldsymbol{u}^{i,\ell}(\boldsymbol{x}) =\}_{i=1..N_t,\ell=1..N_c}$$

where N_c denotes the number of control laws considered. If $\mathcal{C} = \{c_1, c_2, \cdots, c_{N_c}\}$ is the set of control laws used to obtain the database, the ensuing POD basis is denoted $\boldsymbol{\phi}(\mathcal{C})$. In the first part of this chapter, $\mathcal{C}$ is reduced to a single element which we denote $c(t)$.

The choice of the control law used to obtain the database greatly influences the resulting model, which is only locally accurate. Here, the idea is that if the model is used within an optimization loop for control purposes, then an initial choice of control law should be made by to start the optimization (in the next chapter a method to perform an optimal initial sampling is described). A series of suboptimal controls are then generated during the procedure, and the corresponding solutions can be added to the database. With this in mind, the choice of proportional feedback control laws introduced in (5.3.2) can be seen as corresponding to initial guesses of the optimal gain coefficients.

In the non-controlled case (see section §2.1.1), we lift the boundary conditions on the velocity fields by defining a new set of snapshots:

$$\boldsymbol{w}(\boldsymbol{x}, t) = \boldsymbol{u}(\boldsymbol{x}, t) - \bar{\boldsymbol{u}}(\boldsymbol{x})$$

where $\bar{\boldsymbol{u}}$ is some reference velocity field that satisfies the same boundary conditions as the snapshots. In the present configuration, it can be the steady unstable solution, or a time average of the snapshots.

When an extra boundary condition is imposed on the cylinder for control purposes, the snapshots are chosen to be:

$$\boldsymbol{w}(\boldsymbol{x},t) = \boldsymbol{u}(\boldsymbol{x},t) - \bar{\boldsymbol{u}}(\boldsymbol{x}) - c(t)\boldsymbol{u}_c(\boldsymbol{x})$$

where $\boldsymbol{u}_c(\boldsymbol{x})$ satisfies the following criteria:

$$\boldsymbol{u}_c(\boldsymbol{x}) = 0 \text{ on } \Gamma\backslash\Gamma_c \text{ and } \boldsymbol{u}_c(\boldsymbol{x}) = 1 \text{ on } \Gamma_c$$

This is obtained as proposed in (Galletti *et al.*, 2006), i.e. considering the time-averaged flow field ($\boldsymbol{u'}(\boldsymbol{x})$) obtained by activating a jet with an intensity $c(t) = c^* = -0.05$ and defining $\boldsymbol{u_c}(\boldsymbol{x})$ as:

$$\boldsymbol{u_c}(\boldsymbol{x}) = \frac{1}{c^*}\left(\boldsymbol{u'}(\boldsymbol{x}) - \bar{\boldsymbol{u}}(\boldsymbol{x})\right), \tag{5.1}$$

The low-dimensional solution is now written:

$$\widetilde{\boldsymbol{u}}(\boldsymbol{x},t) = \bar{\boldsymbol{u}}(\boldsymbol{x}) + c(t)\boldsymbol{u}_c(\boldsymbol{x}) + \sum_{k=1}^{N_r} a_k(t)\boldsymbol{\phi}^k(\boldsymbol{x}) \tag{5.2}$$

The substitution of the low-dimensional solution with control actuation in the Navier-Stokes equations and the Galerkin projection onto the first N_r POD modes, yields a system of ordinary differential equations analogous to (2.6) with extra terms:

$$\left\{\begin{array}{lcl} \dot{a}_r(t) & = & A_r^G + C_{kr}^G a_k(t) + B_{ksr}^G a_k(t)a_s(t) + \mathcal{P}_r \\ & + & E_r^G \dot{c}(t) + F_r^G c^2(t) + G_r^G c(t) + H_{kr}^G a_k(t)c(t) \\ a_r(0) & = & a_r^0 \\ 1 \leq r \leq N_r & & \end{array}\right. \tag{5.3}$$

where:

$$\begin{aligned}
&A_r^G = -((\bar{\boldsymbol{u}}\cdot\nabla)\bar{\boldsymbol{u}},\boldsymbol{\phi}^r) + \frac{1}{Re}(\Delta\bar{\boldsymbol{u}},\boldsymbol{\phi}^r)\\
&B_{ksr}^G = -((\boldsymbol{\phi}^k\cdot\nabla)\boldsymbol{\phi}^s,\boldsymbol{\phi}^r)\\
&C_{kr}^G = -((\bar{\boldsymbol{u}}\cdot\nabla)\boldsymbol{\phi}^k,\boldsymbol{\phi}^r) - ((\boldsymbol{\phi}^k\cdot\nabla)\bar{\boldsymbol{u}},\boldsymbol{\phi}^r) + \frac{1}{Re}(\Delta\boldsymbol{\phi}^k,\boldsymbol{\phi}^r)\\
&E_r^G = (\boldsymbol{u}_c,\boldsymbol{\phi}^r)\\
&G_r^G = -((\bar{\boldsymbol{u}}\cdot\nabla)\boldsymbol{u}_c,\boldsymbol{\phi}^r) - ((\boldsymbol{u}_c\cdot\nabla)\bar{\boldsymbol{u}},\boldsymbol{\phi}^r) + \frac{1}{Re}(\Delta\boldsymbol{u}_c,\boldsymbol{\phi}^r)\\
&F_r^G = ((\boldsymbol{u}_c\cdot\nabla)\boldsymbol{u}_c,\boldsymbol{\phi}^r)\\
&H_{rk}^G = ((\boldsymbol{u}_c\cdot\nabla)\boldsymbol{\phi}^k,\boldsymbol{\phi}^r) + ((\boldsymbol{\phi}^k\cdot\nabla)\boldsymbol{u}_c,\boldsymbol{\phi}^r)\\
&\mathcal{P}_r = (\nabla p,\boldsymbol{\phi}^r)
\end{aligned}$$

We note that since the snapshots satisfy the continuity equation, the modes do also, even with control actuation. This implies, for the reasons explained in section §2.1.2, that $\mathcal{P}_r$ can be neglected.

Setting:

$$\boldsymbol{X}_r^G = \left[A_r^G,\, \{B_{ksr}^G\}_{k,s=1\cdots N_r},\, \{C_{kr}^G\}_{k=1\cdots N_r},\, E_r^G,\, F_r^G,\, G_r^G,\, \{H_{kr}^G\}_{k=1\cdots N_r}\right]^t$$

and

$$\begin{aligned}\boldsymbol{f}(\boldsymbol{a}(t), c(t), \dot{c}(t)) = \Big[&1,\, \{a_k(t)a_s(t)\}_{k,s=1\cdots N_r},\, \{a_k(t)\}_{k=1\cdots N_r},\\ &\dot{c}(t),\, c^2(t),\, c(t),\, \{a_k(t)c(t)\}_{k=1\cdots N_r}\Big]\end{aligned}$$

the N_r first equations in (5.3) can be written in the compact form:

$$\dot{a}_r(t) = \boldsymbol{f}(\boldsymbol{a}(t), c(t), \dot{c}(t)) \cdot X_r^G$$

The initial value problem (5.3) is a reduced order model of the Navier-Stokes equations for an actuated flow.

5.2 Robust low order models

Calibration method and partial calibration

The idea of calibration (section §2.1.2) is to keep the structure of the above model while adjusting the coefficients of the system so its solution is closer to the desired one. In order to build a model that fits a dynamics given by a particular control law $c(t)$ we use the *dynamics calibration* method. Indeed, with control actuation the number of modes needed to represent the flow dynamics could be large. Thus, for the *state calibration* method, although the resulting low-order models are accurate for actuated flows, as shown in (Galletti *et al.*, 2006), the computational costs are excessive.
The *dynamics calibration* method (§2.1.2) can be interpreted as approximating the error

$$e_r(t) = \dot{\hat{a}}_r(t) - \boldsymbol{f}(\hat{\boldsymbol{a}}(t), c(t), \dot{c}(t)) \cdot \boldsymbol{X}_r^G$$

by a quadratic function of all the non-discarded temporal coefficients, $c(t)$ and $\dot{c}(t)$. Other choices for the approximation of e_r lead to partial calibration problems.
For example, if we suppose $e_r \approx A_r^E + C_{kr}^E a_k + G^E c$, *i.e.* if we chose to calibrate only the constant terms and the terms linear in a_r and c, then we will solve:

$$\min_{\boldsymbol{X}_1^C} \sum_{r=1}^{N_r} \int_0^T \left(\dot{\hat{a}}_r(t) - \boldsymbol{f}_1(t) \cdot \boldsymbol{X}_{r,1}^C - \boldsymbol{f}_2(t) \cdot \boldsymbol{X}_{r,2}^G\right)^2 dt \tag{5.4}$$

where

$$\begin{aligned}\boldsymbol{X}_{r,1}^C &= \left[A_r^C,\, \{C_{kr}^C\}_{k=1\cdots N_r},\, G_r^C\right]^t\\ \boldsymbol{X}_{r,2}^G &= \left[\{B_{ksr}^G\}_{k,s=1\cdots N_r},\, E_r^G,\, F_r^G,\, \{H_{kr}^G\}_{k=1\cdots N_r}\right]^t\end{aligned}$$

and

$$\begin{aligned}\boldsymbol{f}_1(t) &= \left[1,\, \{a_k(t)\}_{k=1\cdots N_r},\, c(t)\right]\\ \boldsymbol{f}_2(t) &= \left[\{a_k(t)a_s(t)\}_{k,s=1\cdots N_r},\, \dot{c}(t),\, c^2(t),\, \{a_k(t)c(t)\}_{k=1\cdots N_r}\right]\end{aligned}$$

Of course, other choices of the terms to be calibrated can be made. For a general formulation we denote N_{cal} the number of terms of vector $\boldsymbol{X}_r$ that are calibrated, and we have $N_{cal} \leqslant N_r^2 + 2 \times N_r + 4$. Chosen the terms to be calibrated, this approach involves solving N_r linear symmetric systems of size N_{cal}^2:

$$\int_0^T \boldsymbol{f}_1^t(t)\boldsymbol{f}_1(t)\,dt \quad \boldsymbol{X}_{r,1}^{\boldsymbol{C}} = \int_0^T \boldsymbol{f}_1^t(t)\left(\dot{\hat{a}}_r(t) - \boldsymbol{f}_2(t)\cdot \boldsymbol{X}_{r,2}^{\boldsymbol{G}}\right)\,dt \tag{5.5}$$

At this point two choices need to be made: the number of modes we want to keep in the model, and which system coefficients to calibrate.
The control law affects or may affect all the coefficients of the POD representation of the solution. However there are a number of modes that we need not consider in the expansion since they are energetically not very significant and therefore have little effect on solution accuracy. This of course does not mean that they are dynamically irrelevant because they can trigger or sustain an instability. Indeed that is one of the reasons why a model obtained by Galerkin projection without calibration has a very poor dynamical performance. In our experience, the larger N_r, the better the conditioning of the calibration problem and the dynamical evolution of the model. Therefore N_r is limited only by the size of the resulting calibration problem. For controlled flows, for Reynolds numbers in a range of $60 - 150$, choosing N_r to be in the $40 - 60$ range represents a good compromise between accuracy and computational time.
Concerning calibration, again we choose not to calibrate the N_r^3 terms $\boldsymbol{B}_{ksr}$.

Once the model has been calibrated to fit a particular control law $c(t)$, it can of course be integrated using another control law. Denoting the input control law $c^{\mathrm{I}}(t)$, the calibrated model is written:

$$\mathcal{R}(\{c\})\begin{cases}\dot{a}_r(t) &= \boldsymbol{f}(\boldsymbol{a}(t), c^{\mathrm{I}}(t), \dot{c}^{\mathrm{I}}(t))\cdot \boldsymbol{X}_r\\ a_r(0) &= a_r^0\\ 1\le r\le N_r\end{cases} \tag{5.6}$$

where by denoting $\mathcal{R}(\{c\})$ the model we put in evidence that it was calibrated using the control $c(t)$.

Well-posedness and robustness

We suppose that the control is obtained using a proportional feedback law (section §4.1):

$$c(t) = \sum_{j=1}^{N_s} \mathsf{K}_j v(\boldsymbol{x}_j, t)$$

We consider the new calibration problem:

$$\min_{\boldsymbol{X}} \sum_{r=1}^{N_r} \int_0^T \left(\dot{\hat{a}}_r(t) - \boldsymbol{f}(\hat{\boldsymbol{a}}(t), \hat{c}(t), \dot{\hat{c}}(t)) \cdot \boldsymbol{X}_r \right)^2 dt \tag{5.7}$$

where $\hat{c}$ is the control law reconstructed by using the low-dimensional velocity and it is defined by:

$$\hat{c}(t) = \sum_{j=1}^{N_s} \mathsf{K}_j \widetilde{v}(\boldsymbol{x}_j, t) = \sum_{j=1}^{N_s} \mathsf{K}_j \left(\bar{v}(\boldsymbol{x}_j) + \hat{c}(t) v_c(\boldsymbol{x}_j) + \sum_{r=1}^{N_r} \hat{a}_r(t) \phi_v^r(\boldsymbol{x}_j) \right) \tag{5.8}$$

This last approach makes the reduced order model a feedback model, which is useful if we want to use the model to determine an optimal feedback law. The problem is however under-determined.
We reformulate (5.8) to clearly show the dependency of $\hat{c}$ on $\hat{\boldsymbol{a}}$:

$$\hat{c}(t) = \kappa_0 + \sum_{r=1}^{N_r} \kappa_r \hat{a}_r(t) \tag{5.9}$$

where

$$\kappa_0 = \sum_{j=1}^{N_s} \frac{\mathsf{K}_j}{1 - \sum_{i=1}^{N_s} \mathsf{K}_i v_c(\boldsymbol{x}_i)} \quad \bar{v}(\boldsymbol{x}_j) \quad \text{and} \quad \kappa_r = \sum_{j=1}^{N_s} \frac{\mathsf{K}_j}{1 - \sum_{i=1}^{N_s} \mathsf{K}_i v_c(\boldsymbol{x}_i)} \quad \phi_v^r(\boldsymbol{x}_j)$$

We now look at the partial-calibration problem described above. The function $\boldsymbol{f}_1$ that appears in system (5.5) can be reformulated:

$$\boldsymbol{f}_1(t) = \left[1,\ \{\hat{a}_k(t)\}_{k=1\cdots N_r},\ \kappa_0 + \sum_{\ell=1}^{N_r} \kappa_\ell \hat{\boldsymbol{a}}_\ell(t) \right]$$

System (5.5) is therefore rank deficient. Indeed, the equations obtained vanishing the derivatives with respect to the terms C_{kr} are a linear combination of those obtained by vanishing the derivatives with respect to the terms G_r. The problem remains if more of the system coefficients are calibrated, and according to the choice made the rank of the problem matrix can even diminish with respect to N_{cal}.
This difficulty can however be solved by using one of the two methods proposed in the following (Tikhonov regularization, multiple calibration). Finally, the proportional feedback reduced order model is written:

$$\mathcal{R}^{\mathrm{F}}(\{\hat{c}\}) \begin{cases} \dot{a}_r(t) = \boldsymbol{f}(\boldsymbol{a}(t), c^{\mathrm{F}}(t), \dot{c}^{\mathrm{F}}(t)) \cdot \boldsymbol{X}_r \\ c^{\mathrm{F}}(t) = \sum_{j=1}^{N_s} \mathsf{K}_j \left(\bar{v}(\boldsymbol{x}_j) + c^{\mathrm{F}}(t) v_c(\boldsymbol{x}_j) + \sum_{r=1}^{N_r} a_r(t) \phi_v^r(\boldsymbol{x}_j) \right) \\ a_r(0) = a_r^0, \quad c^{\mathrm{F}}(0) = \hat{c}(0) \\ 1 \le r \le N_r \end{cases} \tag{5.10}$$

The system solved for calibration can be ill-posed even in cases different to the one just described. To understand why this is, it is sufficient to go back to the *state calibration method*. Solving the minimization problem

$$\begin{aligned} &\min_{a,\boldsymbol{X}} \sum_{r=1}^{N_r} \int_0^T \left(a_r(t) - \hat{a}_r(t)\right)^2 dt \\ \text{subject to} \qquad &\dot{a}_r(t) = \boldsymbol{f}(\boldsymbol{a}(t), c(t), \dot{c}(t)) \cdot \boldsymbol{X}_r \end{aligned} \tag{5.11}$$

involves solving a non-linear system for which the uniqueness of solution is not guaranteed. The state calibration functional can therefore have several local optima, and thus there are several possible choices for $\boldsymbol{X}$ that will lead to a low value of the error $\|\hat{\boldsymbol{a}} - \boldsymbol{a}\|$. Since these choices should also be good choices for the minimization problem (5.4), the matrix $\int_0^T \boldsymbol{f}_1^t \boldsymbol{f}_1 \, dt$ in (5.5) is in general almost singular. A model obtained by inverting this matrix is most often very unstable. To overcome this problem we propose a Tikhonov type regularization method which we describe hereafter.

Tikhonov regularization

In order to overcome the ill-posedness of the calibration problem (5.5), it seems reasonable to solve the following regularized problem, instead of (5.4):

$$\begin{aligned} \min_{\boldsymbol{X}_1^{\boldsymbol{C}}} \sum_{r=1}^{N_r} \int_0^T \Big(\dot{\hat{a}}_r(t) - \boldsymbol{f}_1(\hat{\boldsymbol{a}}(t)) \cdot \boldsymbol{X}_{r,1}^{\boldsymbol{C}} \quad &- \quad \boldsymbol{f}_2(\hat{\boldsymbol{a}}(t)) \cdot \boldsymbol{X}_{r,2}^{\boldsymbol{G}}\Big)^2 dt \\ &+\alpha \textstyle\sum_{r=1}^{N_r} \|\boldsymbol{X}_{r,1}^{\boldsymbol{C}} - \boldsymbol{X}_{r,1}^{\boldsymbol{G}}\|^2 \end{aligned} \tag{5.12}$$

where α is the Tikhonov regularization parameter.

The parameter α can be chosen by a classical technique. We start by plotting, for a set of values of α in $[10^{-6}, 10^{-2}]$, the error $\sum_r \|\dot{a}_r - \dot{\hat{a}}_r\|^2$ versus the coefficient variation $\|\boldsymbol{X}_1^{\boldsymbol{C}} - \boldsymbol{X}_1^{\boldsymbol{G}}\|^2$. This leads to a classical Tikhonov L-shaped curve, the corner point of which is optimal in the sense that it is a good compromise between the error on the dynamics and the distance from the original coefficients (Hansen, 1997). The value of α corresponding to this point can be chosen to perform the calibration procedure.

However, while a calibrated reduced order model $\mathcal{R}(\{c\})$ works well when integrated with $c^{\mathrm{I}}(t) = c(t)$, its behavior when integrated with a different control law is unpredictable. As such, the reduced order model can with difficultly be used for estimation and optimization purposes.

In the literature several methods are proposed for adapting reduced order modeling for control purposes, some successful examples can be found in (Hinze & Volkwein, 2005; Ravindran, 2007; Bergmann & Cordier, 2008). However for those cases, no calibration seems necessary for the models to work, but this is not the case for general control problems as shown in the following.

The originality of the model we propose hereafter, is the combination of multi control data sets with the calibration procedure. Such a model is fast to build and yet remains accurate for different control inputs.

Calibrating over more than one control law

We consider a data set that includes simulations obtained using different control laws. Letting:

$$\hat{a}_r^\ell(t) = \Big(\boldsymbol{u}^\ell(t), \boldsymbol{\phi}^r\Big)$$

the calibration problem becomes:

$$\min_{\boldsymbol{X}} \sum_{r=1}^{N_r} \sum_{\ell=1}^{N_c} \int_0^T \Big(\dot{\hat{a}}_r^\ell(t) - \boldsymbol{f}(\hat{\boldsymbol{a}}^\ell(t), c^\ell(t), \dot{c}^\ell(t)) \cdot \boldsymbol{X}_r\Big)^2 dt \tag{5.13}$$

We remark that although the size of the snapshot database is proportional to the number of controls considered, the size of the calibration problem remains constant. Furthermore, if $N_c > 1$, the rank deficiency previously discussed for proportional feedback no longer occurs.
The main idea is that as the number of controls N_c is increased, although the model can become a little less precise for the reference control, it is much more accurate for other control laws. In the next section we show some successful examples of this method at different Reynolds number, and for different kinds of control laws.
We refer to a model built using N_c control laws as an N_c-control model. Such a model is denoted $\mathcal{R}_\mathcal{C}$ where $\mathcal{C} = \{c_1, \cdots, c_{N_c}\}$.

5.3 Results and discussion

The described technique was applied in order to build a low order model of the actuated flow around the confined square cylinder in various configurations. We tested the prediction capabilities of the model for two different Reynolds number, $Re = 60$ and $Re = 150$, with precomputed and feedback control laws. In particular we built different models with one and more control laws and we analyzed their predictions with different controls.
In all the examples presented in the following, actuation is started only once the flow is fully developed. With the control turned on the simulation is performed for about seven vortex shedding cycles, and $N_t \approx 200$ snapshots are saved. $T \simeq 50$ is the non-dimensional duration of the time interval. The number of POD modes retained for the reduced order model is $N_r = 40$ for the case $Re = 60$ and $N_r = 60$ for the case $Re = 150$. We measure the accuracy of the model $\mathcal{R}(\mathcal{C})$ in the following way:

– Time coefficients dynamics:
For a given value of r, plot $a_r(t)$, solution of $\mathcal{R}(\mathcal{C})$ with input $c^{\mathrm{I}}(t)$, against $\hat{a}_r(t)$, projection of the full order solution onto the POD basis $\boldsymbol{\phi}(\mathcal{C})$. In the examples $r = 3$ is usually chosen because it was the mode for which the differences between models were the most remarkable.

– Computation of the integration error:

$$\mathcal{E}(\mathcal{C}, c^{\mathrm{I}}) = \|\boldsymbol{a} - \hat{\boldsymbol{a}}\| / \|\hat{\boldsymbol{a}}\|$$

where $\|\boldsymbol{a}\|^2 = \int_0^T \sum_r a_r^2(t)\, dt$

In the examples with feedback laws we use only one sensor placed in the cylinder wake. Choosing the center of the cylinder as the origin of a coordinate system, we denote $\boldsymbol{x}_s = (x_s, y_s)$ the position of the sensor. The integration error $\mathcal{E}^{\mathrm{F}}(\mathcal{C}, \mathsf{K}^{\mathrm{I}})$ is measured in the same way as for the non-feedback case.
Our first goal is that the model should be able to reproduce the DNS data to which was fitted, we therefore expect $\mathcal{E}(\mathcal{C}, c^{\mathrm{I}})$ to be small if $c^{\mathrm{I}} \in \mathcal{C}$. Our second goal is that the model must be robust to parameter variation. As the difference between $c^{\mathrm{I}}(t)$ and the controls in $\mathcal{C}$ increases, the error $\mathcal{E}(\mathcal{C}, c^{\mathrm{I}})$ grows. We seek a model for which this growth rate is as low as possible.

5.3.1 Divergence of a classical Reduced Order Model

A simulation at $Re = 60$ was performed using feedback control with a sensor placed at $(x_s, y_s) = (0.7, 0.0)$ and $\mathsf{K} = 1$. We denote $c(t)$ the time history of the control law obtained by the simulation.
We compare the results obtained with the POD Galerkin model (5.3) and with the calibrated model $\mathcal{R}(\{c\})$ (see system (5.6) for model formulation). The model integration error $\mathcal{E}(\{c\}, c)$ is equal to 23% for the non-calibrated model, and to 0.136% for the calibrated model.
For a feedback model, the difference is even more important. We integrated the feedback system (5.10) with $\mathsf{K} = 1$, once with $\boldsymbol{X}$ obtained by Galerkin projection, and once with $\boldsymbol{X}$ calibrated as described in 5.2. We obtained an integration error $\mathcal{E}^{\mathrm{F}}(\{\hat{c}\}, 1)$ of 117% in the first case, against an error of 4% in the other. An example of the errors, in terms of time dynamics, that the non-calibrated model can produce are shown in figure 5.2. In

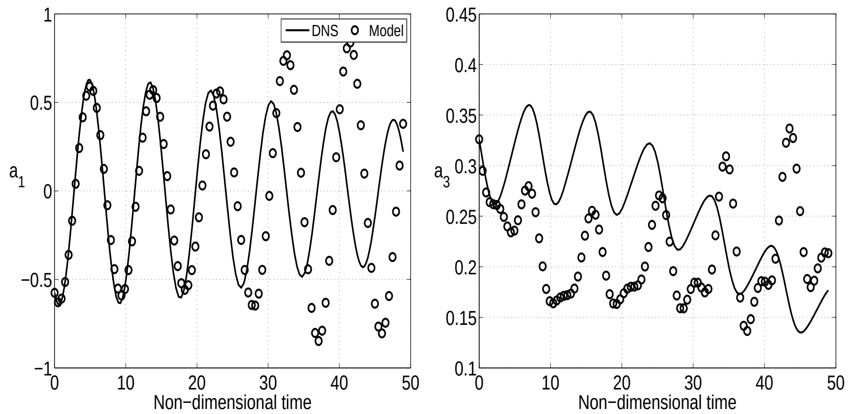

Figure 5.2: Projection of the DNS simulations onto POD modes vs. integration of the dynamical system (5.10) with $\boldsymbol{X} = \boldsymbol{X}^{\boldsymbol{G}}$

figure 5.3 we plot the control law $c^{\mathrm{F}}(t)$ computed when integrating the feedback model, and on the same figure, the original control law $c(t)$. Results for the non-calibrated case are plotted on the right: the distance between $c^{\mathrm{F}}(t)$ and $c(t)$ increases with time, meaning that at each time step, new errors are added to the model. Calibration is therefore all the more essential when considering feedback control.

In order to calibrate, regularization is needed to get well-conditioned inverse problems as

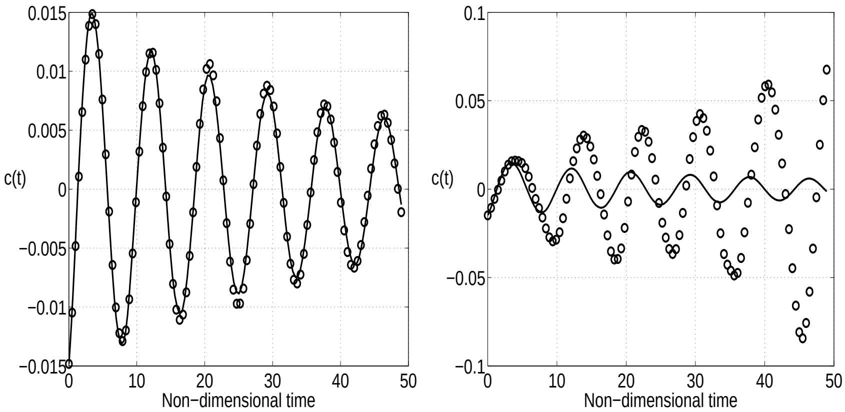

Figure 5.3: c_1 (continuous line) versus c^{F}, when the model is calibrated (left) and when it is not (right)

mentioned before and shown in the following. However, the choice of the regularization parameter α is not an easy one.

For example, we performed a simulation at $Re = 150$ using a feedback control with a sensor placed at $(x_s, y_s) = (0.7, 0.0)$ and $\mathsf{K} = 0.8$. The calibration described in 5.2 was performed with $\alpha \approx 0$. This led to an ill-conditioned system to be solved and to a model which was not very accurate, and not robust at all to parameter variations. The effect of α on model results is shown in figure 5.4. The two top figures show the third modal coefficient obtained by projection and by integrating the model with $\mathsf{K} = 0.8$. On the left, we plot the results obtained when the model was built with $\alpha = 1.6 * 10^{-6}$: at the end of the time period the model diverges from the DNS results. With a higher value, $\alpha = 10^{-3}$, this problem no longer occurs, as shown on the right. The same test was then performed with a different value of K in order to see the model capability of predicting a dynamics to which it was not fitted. The results are shown in the same figure: divergence was immediate for a low value of α, whereas for a higher value, the model, although not accurate, was at least stable. It appears that, when using an higher regularization parameter, the calibration system is well conditioned, the model more accurate and more stable when integrated with a different control law to those used for calibration. In the following the parameter α is determined using the L-method with the restriction that any values of α below a certain threshold are excluded.

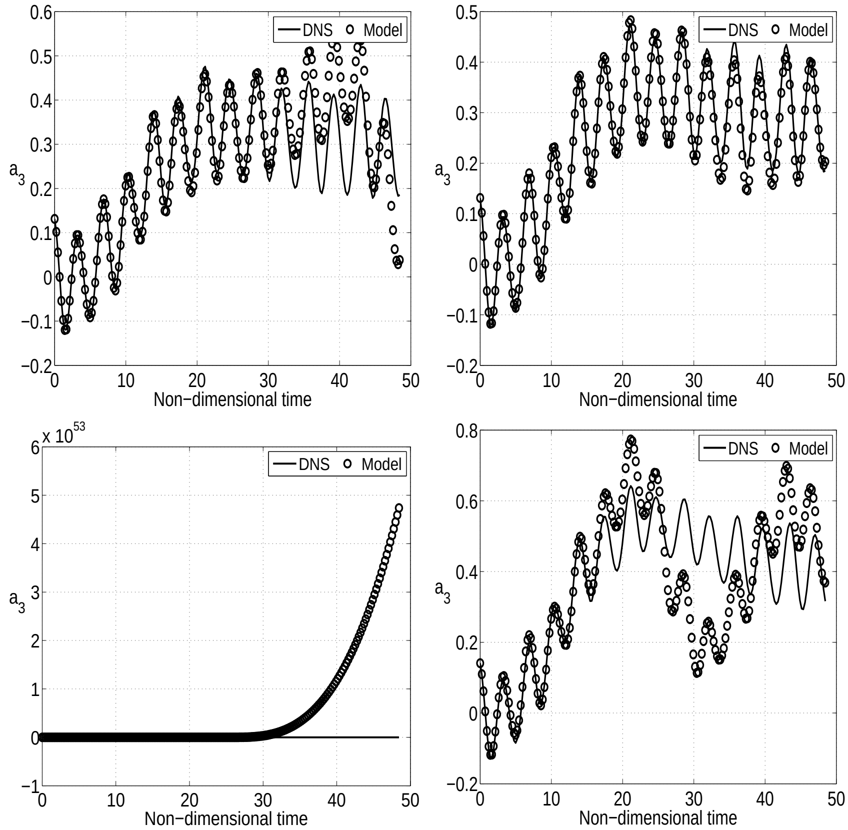

Figure 5.4: a_3 DNS (continuous line) with $\mathsf{K} = 0.8$ (top) and $\mathsf{K} = 1.3$ (bottom) versus a_3 obtained when the model is calibrated with $\alpha = 1.6 * 10^{-6}$ (left) and when $\alpha = 10^{-3}$ (right)

5.3.2 Testing model robustness: $Re = 60$ and $Re = 150$

In this section we present the improvements brought to model robustness by introducing calibration over several control laws. For both Reynolds numbers, $Re = 60$ and $Re = 150$, the same experiment was performed:

Step 1 : Build 1- , 2- and 3-control models

We started by choosing three control laws which we denote $c_1(t)$, $c_2(t)$ and $c_3(t)$. For each control we performed a simulation of the Navier-Stokes equations, saving 200 snapshots for each simulation. We then defined seven control sets:

$$\text{Three 1-control sets: } \mathcal{C}^1 = \{c_1\}, \mathcal{C}^2 = \{c_2\}, \mathcal{C}^3 = \{c_3\}$$

$$\text{Three 2-control sets: } \mathcal{C}^4 = \{c_1, c_2\}, \mathcal{C}^5 = \{c_1, c_3\}, \mathcal{C}^6 = \{c_2, c_3\}$$

$$\text{One 3-control set: } \mathcal{C}^7 = \{c_1, c_2, c_3\}$$

For each control set $\mathcal{C}^i$, we computed a POD basis $\boldsymbol{\phi}(\mathcal{C}^i)$ and a calibrated reduced order model $\mathcal{R}(\mathcal{C}^i)$ by solving problem (5.13).
In the following we refer to $c_1(t)$, $c_2(t)$ and $c_3(t)$ as the *model control laws*.

Step 2 : Run the model with different control laws

We next chose several other control laws which we denote $c_j^{test}(t)$. Each of these *test control laws* was used as input for the Navier-Stokes equations, and for the seven reduced order models $\mathcal{R}(\mathcal{C}^i)$ described above. The snapshots from the Navier-Stokes simulations were projected onto the seven POD bases $\boldsymbol{\phi}(\mathcal{C}^i)$. This procedure made it possible to compute the model integration errors $\mathcal{E}_i^j = \mathcal{E}(\mathcal{C}^i, c_j^{test})$, and compare the efficiency of each model.
For measuring model robustness, it is useful to have some idea of how much the dynamics we are trying to predict, differ from those included in the model. We therefore need to find a way, for each model, to measure the distance between the $N_t \times N_c$ snapshots that were used to build it, and the N_t snapshots obtained using a *test* control law. To do this we proceed in the following way : if the control set $\mathcal{C}^i$ is composed of N_c control laws, then the *distance* between the simulations associated to $\mathcal{C}^i$, and the one obtained using $c_j^{test}(t)$, is defined as:

$$\Delta_i^j = \frac{1}{N_c} \sum_{l=1}^{N_c} \left(\|\hat{\boldsymbol{a}}^l - \hat{\boldsymbol{a}}^j\| / \|\hat{\boldsymbol{a}}^l\| \right)$$

where the terms $\hat{\boldsymbol{a}}^n$ ($n = j$ or $n = 1 \cdots l$) result from projecting the snapshots onto the POD basis $\boldsymbol{\phi}(\mathcal{C}^i)$.
The results are plotted in figure 5.7 and figure 5.11 at $Re = 60$ and $Re = 150$ respectively. For each value of model i, the model integration error $\mathcal{E}_i^j$ is plotted versus the *distance* Δ_i^j. We note that the three controls used to build the models were in fact included in the test set, which explains why there are 3 points at $\Delta_i^j = 0$.

Results for $Re = 60$

In figure 5.5 we plot the control laws used to build the models. The three control laws are linear combination of trigonometrical functions. For each control law we plot the third modal coefficient $\hat{a}_3(t)$ to give an idea of the dynamics induced. The figure also shows the prediction for this coefficient given by the 3-control model $\mathcal{R}(\mathcal{C}^7)$. The model results are accurate: the reduced order model was successfully calibrated to fit several dynamics.

Eleven extra control laws were used for testing. A few examples are plotted in figure 5.6. For these examples we also plot the third modal coefficient obtained by projection and by model integration. Some discrepancies in coefficient amplitude are observed, but overall the model predicts the right time dynamics.
In figure 5.7 we look at the results obtained with the different models, using the distances and errors described above. The first point to be made is that the model error is almost

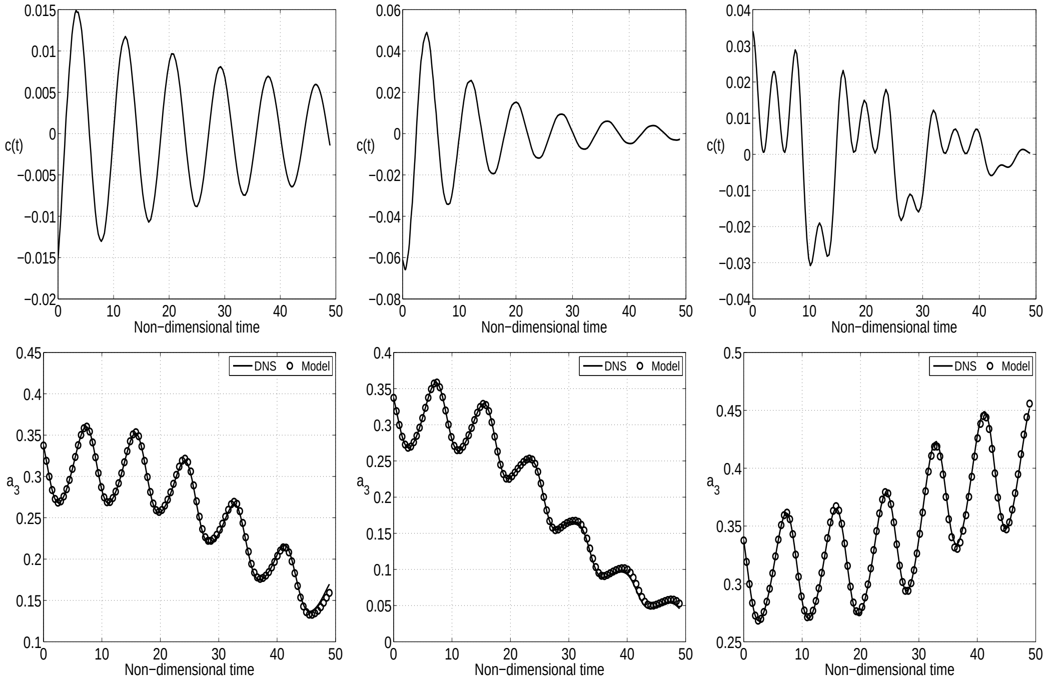

Figure 5.5: Control laws used to build the models (top); a_3 DNS (continuous line) vs prediction by 3-control model (symbols) - $Re = 60$

zero when the distance from the model is zero. This confirms that 1-control models work well when integrated with the control law to which they were fitted. The errors then increase with the distance from the model, as was expected.

The graph highlights the disadvantage of 1-control models. In the best case the difference between projection and prediction coefficients becomes higher than 20% as soon as the distance from the model exceeds 40%. In contrast, for the 2-control and 3-control models, the error stays under 20%, even when the distance increases. In figure 5.8 we plot isolines of the vorticity at time $t = T$ for one of the test control laws (the third control law in figure 5.6). Time coefficients were obtained by solving $\mathcal{R}(\mathcal{C})$ with $\mathcal{C} = \{c_1, c_2\}$. The velocity field was then reconstructed using the first ten of these coefficients and the first ten POD modes in $\boldsymbol{\phi}(\mathcal{C})$. The reconstructed vorticity is presented along with the vorticity obtained by running the Navier-Stokes equations with the test control law. The controls used to build the model caused a slight decrease in vortex size (see figure 5.5, bottom left) whereas actuation used in the test caused a slight increase in vortex size (see figure 5.6, bottom right) . We note that the model was able to predict such features, and that at the end of the simulation time, the structure of reconstructed flow is almost identical to that of the real flow. In contrast, the 1-controls were not able to identify this. If the same reconstruction is performed using $\mathcal{C} = \{c_1\}$ for example, the flow appears almost stable at $t = T$, meaning the model predicted the opposite behavior to what actually happened.

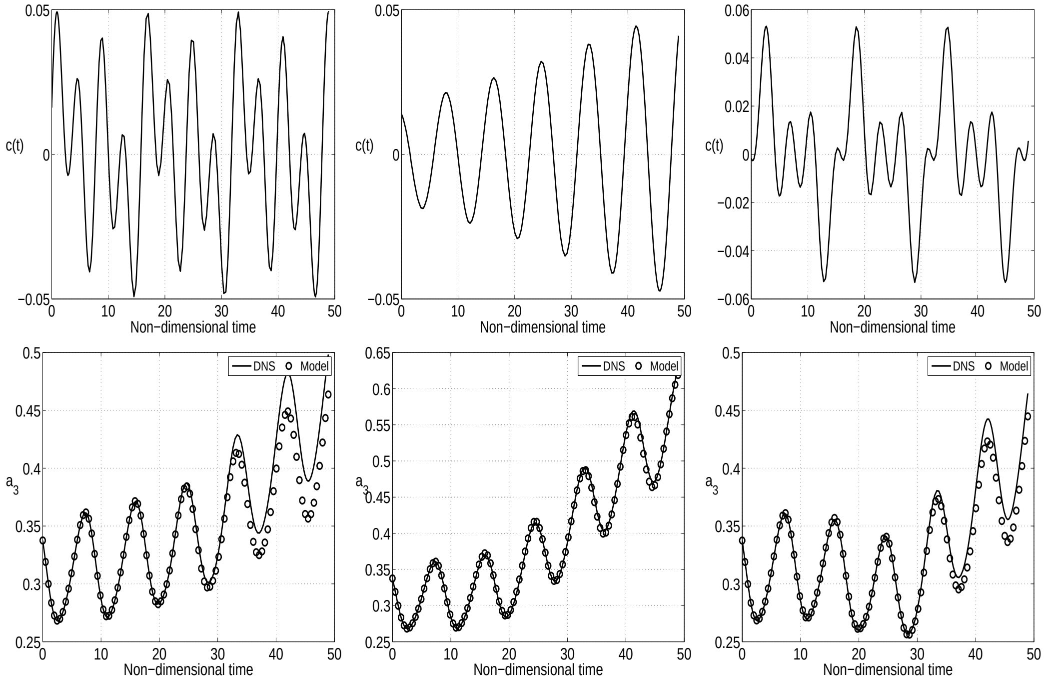

Figure 5.6: Control laws and time coefficients used for testing the 3-control model - $Re = 60$

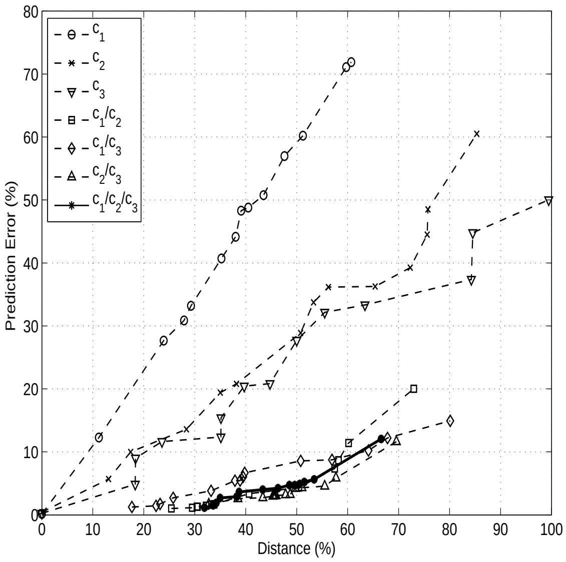

Figure 5.7: Prediction errors obtained using 1-control, 2-control and 3-control models at $Re = 60$

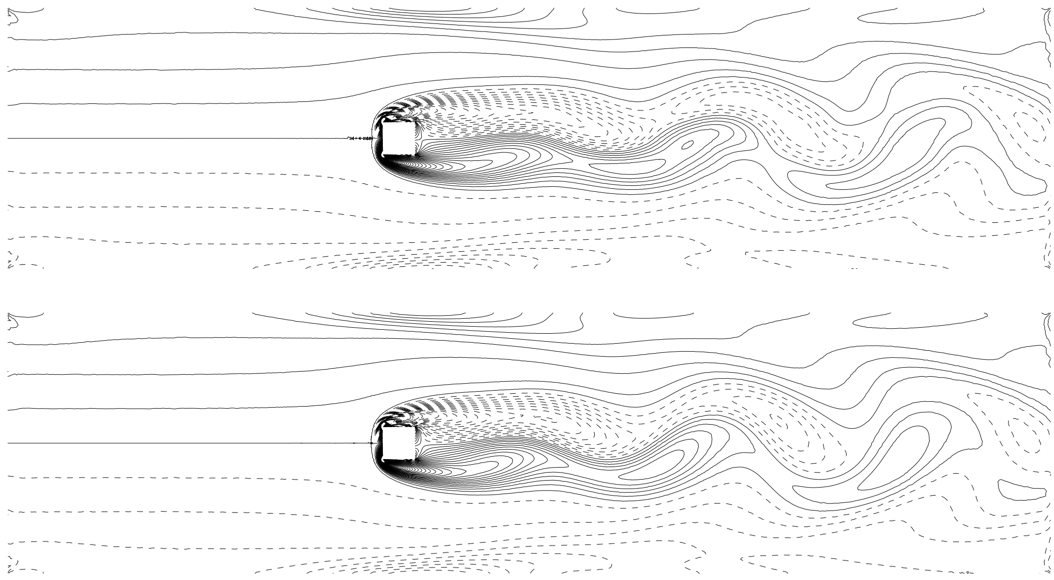

Figure 5.8: Model predicted vorticity field (top) and Navier-Stokes vorticity field at $t = T$. Positive (continuous lines) and negative (dashed lines) vorticity isolines

Results for $Re = 150$

For $Re = 150$ only feedback control laws are used both to build the models and to perform the tests. In figure 5.9 the three feedback control laws used to calibrate the model are shown. The laws are obtained with one sensor placed at $(x_s, y_s) = (0.7, 0.0)$ and by using gains $\mathsf{K} = 0.6$, $\mathsf{K} = 0.8$ and $\mathsf{K} = 1$. The figure also shows the third modal coefficients given by integrating the 3-control feedback model with each gain. Although the control laws induce different dynamics, the model is able to give an accurate prediction in all three cases. Six extra control laws were used for testing, each corresponding to a different choice of K. A few examples, with corresponding coefficients $\hat{a}_3(t)$ are plotted in figure 5.10. It appears that the dynamics are quite different when the distance, between the gain value and gains included in the model, is large. For example, when using a gain $\mathsf{K} = 0.1$ the average value of $\hat{a}_3(t)$ is low compared to that obtained with $\mathsf{K} = 1$. However, the 3-control model again gives an overall good prediction of the time dynamics. Figure 5.11 is built in the same way as figure 5.7. In particular the graph shows the disadvantage of using a 1-control model, with prediction errors of over 34% when the distance from the calibration dynamics increases over the 30%. As in the case $Re = 60$, the 2-control models give more accurate predictions than the 1-control models. The lowest errors are obtained with the 2-control model ($\mathsf{K} = 0.6, \mathsf{K} = 1$). This observation suggests that, in model construction, an optimized a priori choice of the sampling points could be useful to obtain a more robust model. We note that in this case it was the model built to fit the highest and lowest values of K that gave the best

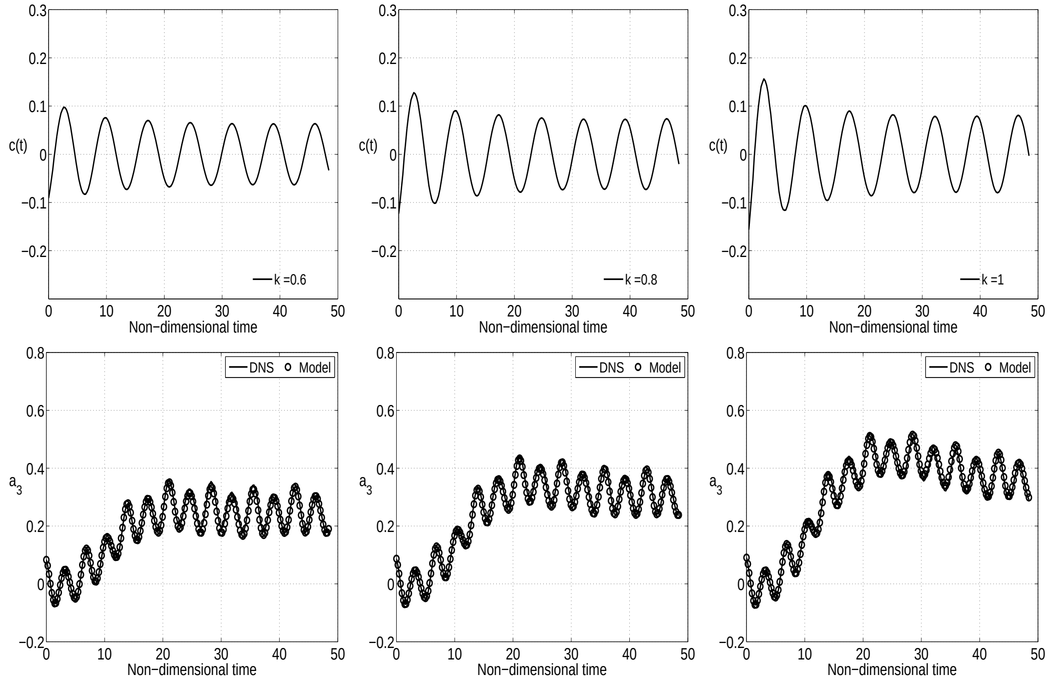

Figure 5.9: Control laws used to build the models (top); a_3 DNS (continuous line) vs prediction by 3-control model (symbols) - $Re = 150$

result, and that adding a third intermediate control to the model ($\mathsf{K} = 0.8$) did not bring any improvement: the 3-control model gives more or less the same results.
In figure 5.12 we plot isolines of the vorticity at time $t = T$ for the flow obtained using $\mathsf{K} = 0.1$ as feedback gain (the first one in figure 5.10). Time coefficients were obtained by integrating the 3-control model. The velocity field was then reconstructed using all the 60 coefficients and POD modes. The reconstructed vorticity is presented along with the vorticity obtained by running the Navier-Stokes equations with the test control law. The controls used to build the model were similar in the sense that they had a much stronger effect on the flow compared to the control obtained with $\mathsf{K} = 0.1$. We note that the model is able to accurately predict a flow snapshot and that the reconstructed flow is almost identical to that of the real flow.

Convergence of low-order models

In the above examples we considered the effect of calibration on model dynamics, and the errors in the resulting approximations. Here we investigate the convergence of the calibrated system coefficients as new datasets are added to the POD-database.
A convergence in modelling errors appears in figure 5.7 and figure 5.11. The 2-control models represent an improvement on the 1-control models. On the other hand the 3-control model has comparable performances with respect to the 2-control models. This

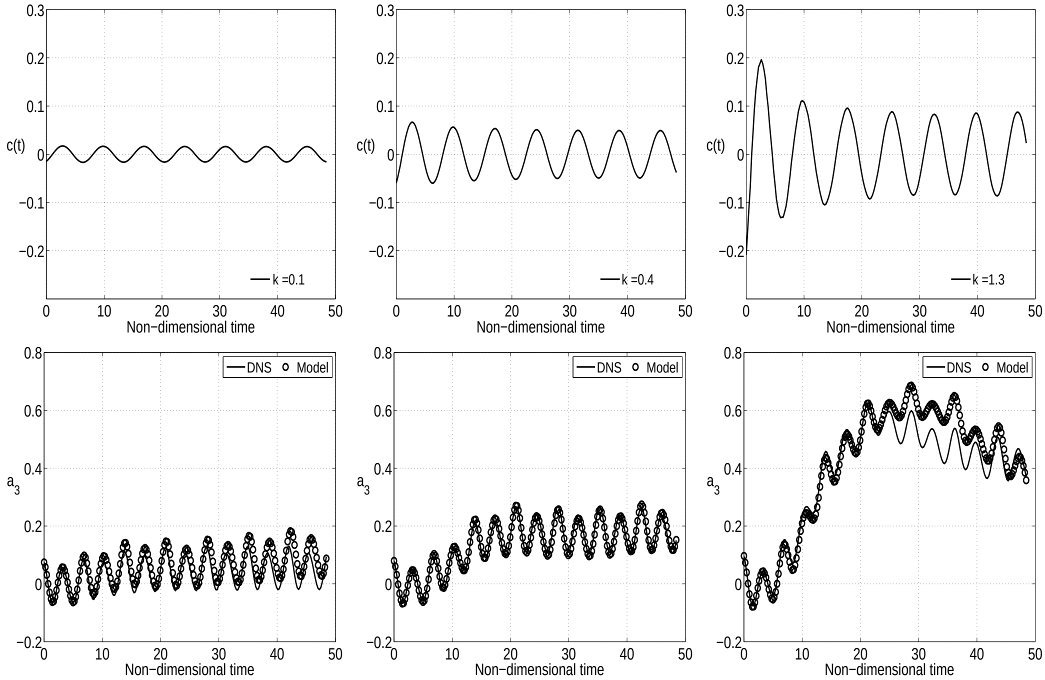

Figure 5.10: Control laws used to test the models (top); a_3 DNS (continuous line) vs prediction by 3-control model (symbols) - $Re = 150$

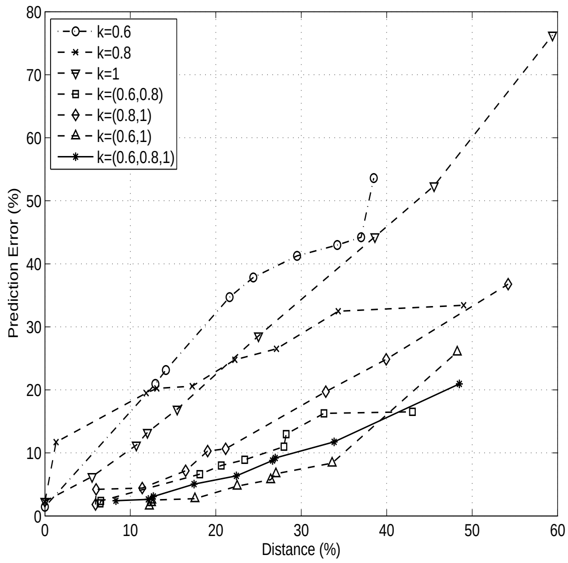

Figure 5.11: Prediction errors obtained using 1-control, 2-control and 3-control models at $Re = 150$

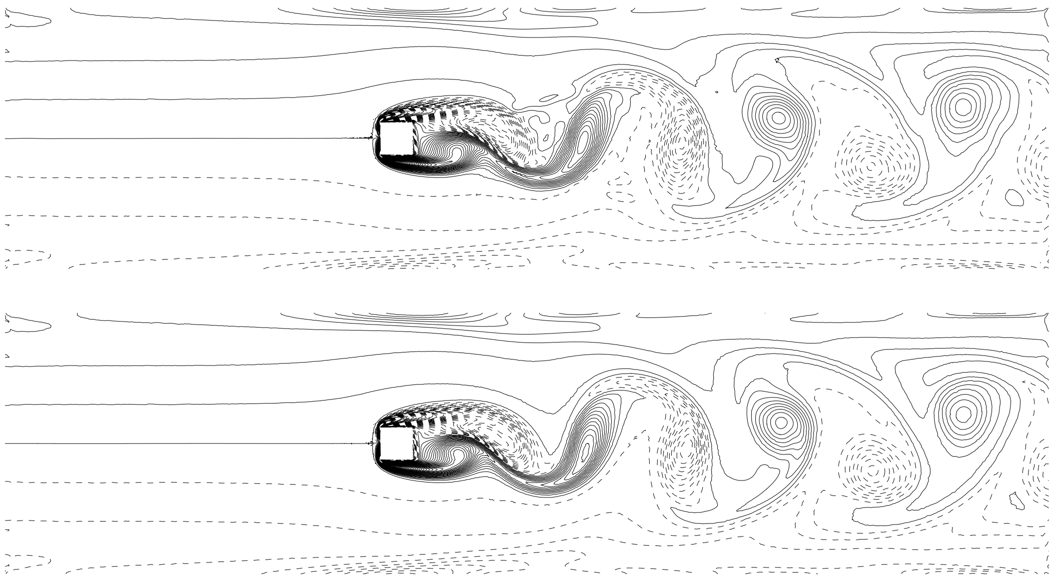

Figure 5.12: Model predicted vorticity field (top) and Navier-Stokes vorticity field at $t = T$ obtained with $\mathsf{K} = 0.1$. Positive (continuous lines) and negative (dashed lines) vorticity isolines - $Re = 150$

is true for both control strategies and Reynolds numbers.
If error reduction with the increase of information included in the problem can be expected, convergence of the system coefficients is not obvious, since each time the database increases, the calibration problem itself changes. In figure 5.13 we show some results in this direction.
We used the models obtained previously for $Re = 150$ and an extra model based on a 4-control dataset. The presence of coefficients E_r, F_r in the reduced-order model (5.3) are due to the control law being non-zero, so we show the convergence of their first ten components as the number of data sets increases.

For E_r convergence is clear, the 2-,3- and 4-control models lead to almost identical results. The same phenomena was observed for the other system coefficients, with the exception of the F_r for which the convergence rate is lower. This is related to the fact that the F_r are the coefficients of the term $c^2(t)$ in the reduced order model, and are therefore more sensitive to changes in the control law and to the effects of the calibration procedure. However, even for these coefficients, we note that their variation between the 2-, 3- and 4-control models is monotonically decreasing.

Final remarks

It is reasonable to ask how the above results would extend to other more complex flows such as three-dimensional wakes at high Reynolds numbers.

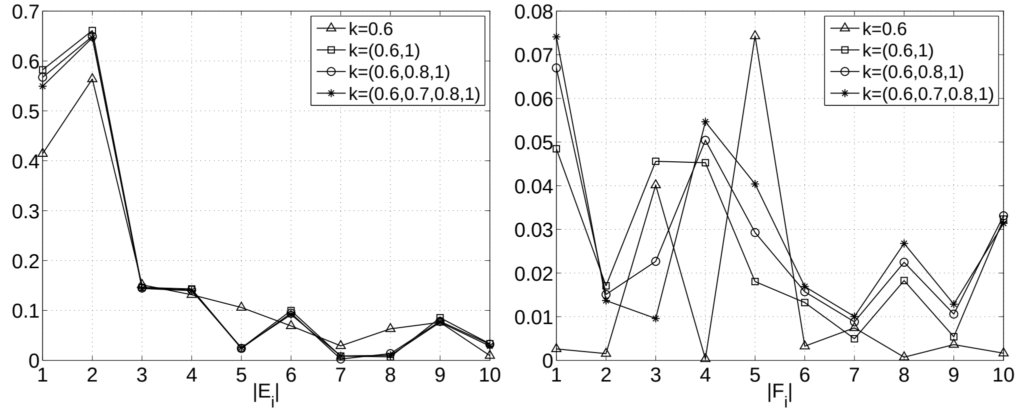

Figure 5.13: Values of system coefficients E_r and F_r for $r = 1 \cdots 10$ - $Re = 150$

We showed that at least two separate issues are involved in low-order modeling for control. One issue is the actual possibility of giving a low-dimensional representation of a flow: the task of modeling with a small number of degrees of freedom distributed systems relies on the ansatz that the dynamics is largely affected by the most energetic scales. Of course there exist flows where these conditions are marginally satisfied. When the flow is not characterized by large scale coherent structures as for high Reynolds number turbulence, then low-dimensional representation does not exist, as for example shown in (Telib *et al.*, 2004). However, it is well known that even at high Reynolds numbers the wake past bluff bodies is characterized by three-dimensional large-scale structures that can be described by a low-dimensional representation. Other flows have been shown to be amenable to a small dimensional representation when they develop large scale dynamical features such as for example shear flows (Wei & Rowley, 2006; Noack *et al.*, 2005) and cavity flows (Rowley & Williams, 2006).

Finally, the model must be robust to parameter variations, i.e., it should be predictive. For example, in the type of flow that we consider the solution can be strongly affected by the controls: the steady unstable solution of the Navier-Stokes equations corresponding to this configuration is significantly different from the mean flow. By calibrating the model over several control laws we take into account this variation. However we implicitly assume that in the neighborhood of the controls included in the database, the response of the system to the control is regular enough to attain local convergence of the parameters that we identify. Therefore highly irregular system responses are not likely to be captured by this method. Nevertheless, the present flow configuration is challenging. The actuators that we study in this chapter are difficult to be modeled as their effect is localized. In fact, low-order models of actuated flows found in the literature are very often relative to distributed volume forces which affect the flow on large scales (Tadmor *et al.*, 2004; Ahuja & Rowley, 2008).

5.4 Conclusions

The overall picture of controlled reduced-order modeling that results from the study of this chapter is the following. Given a control law, one can deduce a low-order model of the actuated flow by simply projecting the Navier-Stokes equations on POD modes. The coefficients of the quadratic model thus obtained are found by projection. However, a model constructed this way will show large time-integration errors even for the same control law used to generate the POD modes. Calibration can take care of that, in the sense that the model coefficients can be determined in order to match as closely as possible at least the solution from which the POD modes are obtained. This might lead to a numerically stable model. However, this model is generally not at all robust, in the sense that the predictions for a slightly different configuration from that it was generated from, fails. A symptom of such lack of robustness is observed in the ill-posedness of the inverse problem: the matrices to be inverted are almost singular.
In order to get around this deficiency, we regularize the solution by adding a constraint to the minimization method used to solve the inverse problem. We ask the coefficients of the polynomial expansion to be close enough to those obtained by projection. This method allows to synthesize models that adequately simulate the flow in a small vicinity of the control law used to generate the solution database. However, the actual real improvement in robustness is obtained by spanning the solution manifold, i.e., by including several control laws in the inverse problem definition. By doing this, the results presented show that the models are able to predict dynamical behaviors that are far, in terms of an energy norm, from the cases included in the database. A consequence of such an additional regularization is that the matrices involved in the inverse problem solution become well conditioned.

Another important aspect of the method proposed, is that its cost is that of a matrix inversion, and that it does not scale with the number or the size of data sets used to build the model. Therefore it seems reasonable to envisage an automatic strategy to enrich the model by spanning the control space. In this respect, the technique proposed in (Bui-Thanh *et al.*, 2008) to distribute in an optimal way the points where to test the control space, even if very demanding in terms of computational costs, can help to minimize the number of a priori simulations needed to build the model. For example, our results show that a model based on two controls might predict the effect of actuation laws not present in the data base, as precisely as a model based on three controls, if the two controls are appropriately placed. For this reason, in the next chapter we describe an alternative technique to perform an optimal placement of the sampling points in the data space with parameters variation.
In conclusion, the modeling we propose appears to be a viable approach to determine control strategies for those problems that, because of their computational size, cannot be treated in the framework of classical control theory. An application of this approach can be found in (Weller *et al.*, 2009) where a control optimization procedure is carried out for the same flow configuration considered in this chapter.

Chapter 6

A Residual based strategy to sample POD database

In the previous chapter we developed a technique to *calibrate* a low order model over several dynamics, with the aim to make it robust to parameters variations. The analysis of the results showed that an optimized choice of the sampling points on the space of the parameters could be useful. Indeed, we noticed that a model built by using two dynamics with two different control laws accurately reproduces dynamics that not belong the database as well as a 3-control model. Thus, the main drawback is that a **POD basis** built on a generic subspace is not optimal to represent a flow generated with different system parameters with respect to those used to build the basis. To get rid of this problem, different strategies can be employed. The first one is to update the POD basis during the optimization, for instance by using trust region method (TRPOD see Bergmann & Cordier (2008)). Another method is to build a robust POD basis that can be used all along the optimization process. This kind of POD basis can be generated using chirp excitation Bergmann *et al.* (2005) or using an appropriate sampling of the input parameter space.

In this spirit, this chapter is devoted to the identification of an efficient sampling of the input subspace. This method, coupled with the techniques described in the previous chapter, allows the construction of a robust model that can be used for control without updating (or with less updating possible) of the POD basis.

Normally, two classes of sampling methods are commonly used: the *one shot* method and the *iterative* one. In the *one shot* method the sampling is obtained by partitioning the range of variation of the input parameter space. The partition can be found using different strategies as, for instance, the uniform distribution, the orthogonal sampling, the Sobol algorithm etc... An alternative strategy to the classical partition strategies is the Centroidal Voronoi Tessellations (CVT, see Du *et al.* (1999); Burkardt *et al.* (2004, 2007)) which leads to an efficient partition. This kind of tessellations can be efficiently computed using the Lloyd algorithm Du *et al.* (2007). The main drawback of the *one shot* strategies is that the number of sampling points has to be chosen *a priori*. Moreover, a preliminary analysis of the density function used to compute the centroidal tessellation is necessary to determine the proper refinement when sampling the range of variation of the input parameter. The other class of methods consist to add sampling points in an iterative way. Thus, we can choose the degree of accuracy by fixing a stopping criterion. One efficient iterative method is based on Greedy sampling (see Bui-Thanh *et al.* (2008) and Grepl & Patera (2005)). In Greedy sampling, the new value of the input parameter to be sampled is chosen on the maximum of the density function, *i.e.* where the error or the residual given by the POD basis is larger. In this chapter we propose a new approach that couples Constrained CVT and Greedy methods.

In this chapter the two dimensional geometry is considered. Thus, with reference to figure 3.1, $L_z/L = 0.6$. The flow configuration and the flow behaviour are already analized in the previous chapters, for this reason we take no notice of it here. For simplicity we consider the Reynolds number as input parameter, but the whole procedure can be easily extended to the control parameters. Thus, the Reynolds number will be varied, while the other parameters will be the same. In particular the control actuation is not taken into account.

6.1 Reynolds dependent pressure extended reduced order model

6.1.1 Reynolds adaptive pressure extended reduced order model

In the previous chapters, as in many practical applications for incompressible flows, we computed the reduced order basis from the velocity fields.

Here, following the idea in Bergmann & Cordier (2008) the pressure term can be easily computed using $p = \widetilde{p}$ (see decomposition (6.1b)). An important key issue is that, knowing the pressure field, it is possible to evaluate the Navier-Stokes residuals that can be considered as an error estimator. This estimator can then be used to perform a robustness improvement procedure as described in section §6.2.2. Thus, we use a global basis for both the velocity and pressure fields (see Bergmann & Cordier (2008)). The exact flow fields $\boldsymbol{u}$ and p are then approximated by:

$$\widetilde{\boldsymbol{u}}(\boldsymbol{x},\, t) = \sum_{i=1}^{N_r} a_i(t)\boldsymbol{\phi}_i(\boldsymbol{x}) \tag{6.1a}$$

$$\widetilde{p}(\boldsymbol{x},\, t) = \sum_{i=1}^{N_r} a_i(t)\psi_i(\boldsymbol{x}). \tag{6.1b}$$

The velocity and the pressure basis functions, $\boldsymbol{\phi}_i$ and $\boldsymbol{\psi}_i$ respectively, are determined by a POD procedure carried out using global snapshots $\boldsymbol{U}(\boldsymbol{x},\, t) = (\boldsymbol{u}(\boldsymbol{x},\, t),\, p(\boldsymbol{x},\, t))^T$, with no subtraction of the average field. Then the basis functions $\boldsymbol{\phi}_i$ and $\boldsymbol{\psi}_i$ are defined as $\boldsymbol{\Phi}(\boldsymbol{x},\, t) = (\boldsymbol{\phi}(\boldsymbol{x},\, t),\, \psi(\boldsymbol{x},\, t))^T$, $\boldsymbol{\Phi}(\boldsymbol{x},\, t)$ being obtained by snapshot method.

The substitution of equations (6.1) in the Navier-Stokes momentum equations and a Galerkin projection lead to the new Reduced Order Model:

$$\sum_{j=1}^{N_r} L_{ij}\frac{\mathrm{d}a_j}{\mathrm{d}t} = \sum_{j=1}^{N_r} C_{ij}a_j + \sum_{j=1}^{N_r}\sum_{k=1}^{N_r} B_{ijk}a_ja_k, \tag{6.2}$$

with initial conditions

$$a_i(0) = (\boldsymbol{U}(\boldsymbol{x},\, 0),\, \boldsymbol{\Phi}_i(\boldsymbol{x}))_\Omega \quad i = 1, \cdots, N_r, \tag{6.3}$$

where the coefficientsL_{ij}, B_{ij} and C_{ijk} are given by:

$$L_{ij} = +\left(\boldsymbol{\phi}_i,\, \boldsymbol{\phi}_j\right)_\Omega, \tag{6.4a}$$

$$C_{ij} = -\left(\boldsymbol{\phi}_i,\, \frac{1}{Re}\Delta\boldsymbol{\phi}_j - \boldsymbol{\nabla}\psi_j\right)_\Omega, \tag{6.4b}$$

$$B_{ijk} = -\left(\boldsymbol{\phi}_i,\, \left(\boldsymbol{\phi}_j\cdot\boldsymbol{\nabla}\right)\boldsymbol{\phi}_k\right)_\Omega. \tag{6.4c}$$

Note that in a general way, we have $(\boldsymbol{\Phi}_i,\, \boldsymbol{\Phi}_j)_\Omega = \delta_{ij}$, but not $(\boldsymbol{\phi}_i,\, \boldsymbol{\phi}_j)_\Omega = \delta_{ij}$; thus, $L_{ij} \neq \delta_{ij}$. Any reference field is subtracted to the snapshots, then the constant terms A_i do not appear in the low order model. However, the first POD mode corresponds to the average field of the snapshots. In order to build a Reynolds adaptive Reduced Order Model we extract the viscous terms in the model from C_{ij}; this leads to the final model, which has the classical form with extra terms:

$$\sum_{j=1}^{N_r} L_{ij}\frac{\mathrm{d}a_j}{\mathrm{d}t} = \sum_{j=1}^{N_r} C_{ij}^{Re}a_j + \sum_{j=1}^{N_r} C_{ij}^{p}a_j + \sum_{j=1}^{N_r}\sum_{k=1}^{N_r} B_{ijk}a_ja_k, \tag{6.5}$$

where :

$$C_{ij}^{Re} = -\left(\boldsymbol{\phi}_i,\, \frac{1}{Re}\Delta\boldsymbol{\phi}_j\right)_\Omega, \tag{6.6a}$$

$$C_{ij}^{p} = +\left(\boldsymbol{\phi}_i,\, \boldsymbol{\nabla}\psi_j\right)_\Omega. \tag{6.6b}$$

Every dynamics associated with a Reynolds number belonging to a predefined interval can be approximated with more or less efficiency using model (6.5). For simplicity reasons, we considered only the Reynolds number as the system input parameter, but all the concepts introduced here for the Reynolds number can be easily extended to other system parameters, as for instance for high dimensional control space as in the previous chapter.

6.1.2 Calibration procedure

In order to build a robust order model we applied the *dynamics calibration* technique described in §2.1.2 and resumed in this section for a Reynolds dependent reduced order model. Setting:

$$\begin{aligned}\boldsymbol{X}_i^{\boldsymbol{G}} &= \Big[\{L_{ij}^{-1}\}_{j=1\cdots N_r}\cdot\{C_{ij}^{Re}\}_{j=1\cdots N_r},\ \{L_{ij}^{-1}\}_{j=1\cdots N_r}\cdot\{C_{ij}^{p}\}_{j=1\cdots N_r},\\ &\quad \{L_{ij}^{-1}\}_{j=1\cdots N_r}\cdot\{B_{ijk}\}_{j,k=1\cdots N_r}\Big]^T\end{aligned}$$

and

$$\boldsymbol{f}(\boldsymbol{a}(t),Re) = \left[\{a_j(t)\}_{j=1\cdots N_r},\ \{a_j(t)a_k(t)\}_{j,k=1\cdots N_r},\ \frac{1}{Re}\right]$$

the equation in (6.5) can be written in the compact form:

$$\dot{a}_i(t) = \boldsymbol{f}(\boldsymbol{a}(t),Re)\cdot\boldsymbol{X}_i^{\boldsymbol{G}}$$

We consider a data base that includes a simulation obtained with Reynolds number $Re = \hat{Re}$ to calculate the POD basis.The partial *dynamics calibration* procedure writes

$$\min_{\boldsymbol{X}_1^{\boldsymbol{C}}}\sum_{i=1}^{N_r}\int_0^T\left(\dot{\hat{a}}_i(t)-\boldsymbol{f}_1(t)\cdot\boldsymbol{X}_{i,1}^{\boldsymbol{C}}-\boldsymbol{f}_2(t)\cdot\boldsymbol{X}_{i,2}^{\boldsymbol{G}}\right)^2 dt+\alpha\sum_{i=1}^{N_r}\|\boldsymbol{X}_{i,1}^{\boldsymbol{C}}-\boldsymbol{X}_{i,1}^{\boldsymbol{G}}\|^2 \qquad (6.7)$$

where

$$\begin{aligned}\boldsymbol{X}_{i,1}^{\boldsymbol{C}} &= \left[C_i^{C\,Re}\right]\\ \boldsymbol{X}_{i,1}^{\boldsymbol{G}} &= \left[C_i^{C\,Re}\right]\\ \boldsymbol{X}_{i,2}^{\boldsymbol{G}} &= \left[C_i^{Gp},\ \{B_{ki}^{G}\}_{i=1\cdots N_r}\right]^t\end{aligned}$$

and

$$\begin{aligned}\boldsymbol{f}^1(t) &= \left[\tfrac{1}{\hat{Re}}\{a_k(t)\}_{k=1\cdots N_r}\right]\\ \boldsymbol{f}^2(t) &= \left[\{a_k(t)\}_{k=1\cdots N_r},\ \{a_k(t)a_s(t)\}_{k,s=1\cdots N_r}\right]\end{aligned}$$

and

$$\hat{a}_i(t) = \langle\boldsymbol{u}(\cdot,t),\boldsymbol{\Phi}_i\rangle$$

and where α is the Tikhonov regularization parameter and it is chosen by the L-shaped curve method described in §5.2. In this calibration procedure only the terms of C_{ij}^{Re} are calibrated. This is due to the assumption that the errors in the Galerkin model are due mainly to the fact that it neglects the small scales and therefore a large part of the viscous effects. C_{ij}^{Re} indeed results from the projection of the viscous term of the Navier-Stokes equations.

The multiple calibration can be performed on the POD basis calculated over N dynamics obtained with different Reynolds numbers $Re_1,\ldots,Re_N$. The new stable model is then calculated to fit the dynamics at various Reynolds numbers. Thus, the system (6.7) to solve becomes:

$$\min_{\boldsymbol{X}_1^{\boldsymbol{C}}} \sum_{i=1}^{N_r} \sum_{\ell=1}^{N} \int_0^T \left(\dot{\hat{a}}_i^\ell(t) - \boldsymbol{f}_1^\ell(t) \cdot \boldsymbol{X}_{i,1}^{\boldsymbol{C}} - \boldsymbol{f}_2^\ell(t) \cdot \boldsymbol{X}_{i,2}^{\boldsymbol{G}} \right)^2 dt + \alpha \sum_{i=1}^{N_r} \| \boldsymbol{X}_{i,1}^{\boldsymbol{C}} - \boldsymbol{X}_{i,1}^{\boldsymbol{G}} \|^2 \quad (6.8)$$

where

$$\hat{a}_i^\ell(t) \quad = \quad \langle \boldsymbol{u}^\ell(\cdot, t), \boldsymbol{\Phi}_i \rangle$$

with $\boldsymbol{u}^\ell(\cdot, t)$ the snapshots at the instant t calculated with $Re = Re_\ell$.

6.2 Improvement of the model robustness

The aim of this section is to improve, by adding snapshots to the starting database in an optimal manner, the representation capabilities of a POD basis of a given flow when the Reynolds number (input parameter of the system) varies in a given range, so as to provide a single reduced order model that is efficient and robust for the considered range. As already stated, all the concepts introduced in this study can be easily extended to other system parameters, as, for instance, to a set (even large) of control parameters.

The Reynolds number space (here, only a discrete interval) under consideration is denoted $\mathcal{I} = [Re_L, Re_R]$, where we chose $Re_R = 180$ and $Re_L = 40$ or $Re_L = 70$, depending on the considered case. Reynolds numbers $Re_L = 70$ and $Re_R = 180$ correspond to the lower and higher bound for the 2D periodic regime for the considered flow (see §3) around the confined square cylinder. The case with $Re_L = 40$ is considered to investigate if the reduced order model is robust enough to predict a (Hopf) bifurcation of the system (that occurs at $Re_c \approx 60$ in this case). Numerically, $\mathcal{I}$ is discretized with $\Delta Re = 5$, and it is denoted as $\mathcal{I}_h$.

In order to improve the POD basis, we want to enrich the database in an *one-shot* way by adding some sets of snapshots at different Reynolds numbers $Re_i^{new} \in \mathcal{I}$. Let $U^{[Re_1,\ldots,Re_N]}$ be the database composed by N sets of snapshots taken independently at $Re_1, \ldots, Re_N$, where N is a free parameter depending on the desired accuracy of the POD basis. The projection of the global numerical solution of the Navier-Stokes equations $\boldsymbol{U}(\boldsymbol{x}, t)$ onto the N_r retained POD modes is:

$$\widehat{\boldsymbol{U}}^{[N_r]}(\boldsymbol{x}, t) = \sum_{n=1}^{N_r} \hat{a}_n(t) \boldsymbol{\Phi}_n(\boldsymbol{x}) \quad (6.9)$$

In the following, we will always use $N_r = 31$. The number of basis functions is arbitrarily chosen quite large because it will be kept all along this study, even when they are

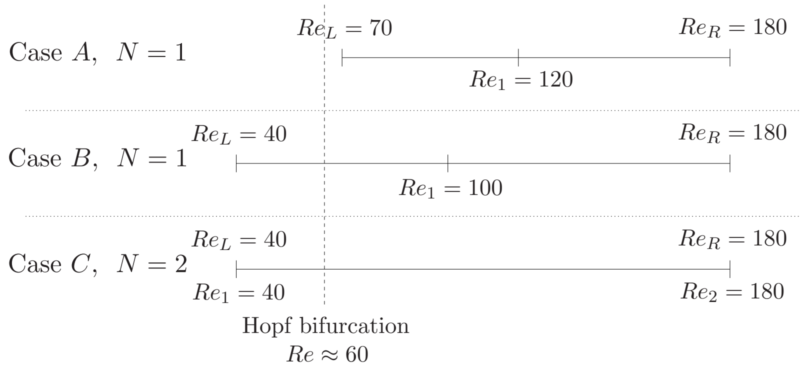

Figure 6.1: Sketch of the three test cases for sampling.

computed using a database collected using $N > 1$ different Reynolds numbers Re_i. Since we will always use $N_r = 31$ we simply note that

$$\widetilde{\boldsymbol{U}}(\boldsymbol{x}, t) \equiv \widehat{\boldsymbol{U}}^{[N_r]}(\boldsymbol{x}, t) = \sum_{n=1}^{N_r} a_n(t)\boldsymbol{\Phi}_n(\boldsymbol{x}). \tag{6.10}$$

Let us recall that the temporal coefficients $a_n(t)$ can be evaluated in two ways:

– by projecting the numerical solution of the Navier-Stokes equations onto the POD modes:
$$\hat{a}_n(t) = \int_\Omega \boldsymbol{U}(\boldsymbol{x}, t)\boldsymbol{\Phi}_n(\boldsymbol{x})\mathrm{d}\boldsymbol{x}, \tag{6.11}$$

– by integration of the reduced order model.

In what follows we denoted $\widetilde{\boldsymbol{U}}_{DNS}$ and $\widetilde{\boldsymbol{U}}_{ROM}$ the fields computed by projection and by using the coefficients given by the model prediction respectively. Without loss of generality, $\widetilde{\boldsymbol{U}}$ can be either $\widetilde{\boldsymbol{U}}_{DNS}$ or $\widetilde{\boldsymbol{U}}_{ROM}$

In order to test our criterion to improve the POD basis, described in section §6.2.3, we will consider three initial bases:

– case A, corresponds to an initial database $U^{[Re_1]}$ composed by N_t snapshots collected at $Re_1 = 120$ with $Re_L = 70$ and $Re_R = 180$;

– case B, corresponds to an initial database $U^{[Re_1]}$ composed by N_t snapshots collected at $Re_1 = 100$ with $Re_L = 40$ and $Re_R = 180$;

– case C, corresponds to an initial database $U^{[Re_1;Re_2]}$ composed by N_t snapshots collected at $Re_1 = 40$ plus N_t snapshots collected at $Re_2 = 180$ with $Re_L = 40$ and $Re_R = 180$;

The three cases are summarized in Fig. 6.1. In this study we will always arbitrarily consider $N_t = 200$.

6.2.1 Effect of the Reynolds number variations onto the projection error

In the following, the reconstruction capabilities of a given POD basis is estimated when the Reynolds number varies in the interval $\mathcal{I} = [Re_L, Re_R]$. A natural way to achieve this is to compare, at each $Re \in \mathcal{I}_h$, the numerical solution $\boldsymbol{U}(\boldsymbol{x}, t)$ of the Navier-Stokes equations to the POD reconstruction $\widetilde{\boldsymbol{U}}(\boldsymbol{x}, t)$ computed using a POD basis that corresponds to a given database $U^{[Re_1,\dots,Re_N]}$. The numerical solution of the Navier-Stokes equations can be formally written as:

$$\boldsymbol{U}(\boldsymbol{x}, t) = \widetilde{\boldsymbol{U}}(\boldsymbol{x}, t) + \boldsymbol{U}'(\boldsymbol{x}, t), \tag{6.12}$$

where $\boldsymbol{U}'(\boldsymbol{x}, t)$ denotes the missing scales, *i.e.* the error made restricting the solution to the first N_r basis functions

$$\boldsymbol{U}'(\boldsymbol{x}, t) = \boldsymbol{U}(\boldsymbol{x}, t) - \widetilde{\boldsymbol{U}}(\boldsymbol{x}, t). \tag{6.13}$$

We defined the average of the L_2 norm over a temporal horizon T for missing scales (6.13) by :

$$\langle \boldsymbol{U}' \rangle_2 = \int_T \|\boldsymbol{U}'(\boldsymbol{x}, t)\|_2 \mathrm{d}t. \tag{6.14}$$

Since we have to compute the numerical solution $\boldsymbol{U}(\boldsymbol{x}, t)$ of the Navier-Stokes equation onto $\mathcal{I}_h$ to achieve such comparison, the POD output flow fields $\widetilde{\boldsymbol{U}}(\boldsymbol{x}, t)$ can easily be computed with the projected coefficients $a_n(t)$ evaluated from (6.11). This error indicates how the description capability of the POD basis changes due to variations of the Reynolds number (system parameter). In what follows, the temporal horizon T is taken to be equal to three vortex shedding periods and thus depends on Re. Figure 6.2 shows the evolution of the error $\langle \boldsymbol{U}' \rangle_2$ versus the Reynolds number for the three initial databases described above. For all cases, we can see that the error is very small at Re_i inside the POD database (of the order of 10^{-7}), and then it growths when the value of the Reynolds number moves away from Re_i. This highlights the fact, as already seen for control in previous chapter, that the POD basis computed from a database collected from a given dynamics is not able to give a good representation of flows which are characterized by different dynamics. We can see in figure 6.2 that model C seems to be more robust than models A and B. Indeed, the maximal error is smaller for model C. The reason is that the POD basis for case C is computed from 2 different dynamics and the other cases from only one, and then it is more robust, as explained in the previous chapter. The aim is then to determine a sampling of K new sets of snapshots $\{Re_i^{new}\}_{i=N+1}^{N+K} \in \mathcal{I}_h$, to compute the most robust POD basis.

6.2.2 A residuals based error estimator

Since the evaluation of the error $\boldsymbol{U}'(\boldsymbol{x}, t)$ involved the computation of the numerical solutions $\boldsymbol{U}(\boldsymbol{x}, t)$ of the Navier-Sokes equations for each $Re \in \mathcal{I}_h$, the evaluation of errors based criteria (6.14) is demanding from a computational viewpoint (Greedy algorithm

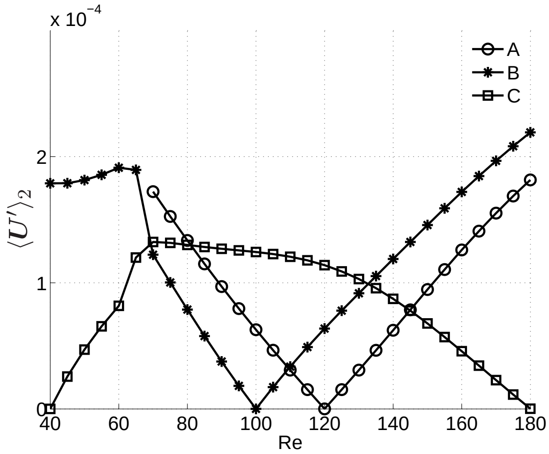

Figure 6.2: Evolution of the error $\langle \boldsymbol{U}' \rangle_2$ versus the Reynolds number.

in Bui-Thanh *et al.* (2008)). It is then interesting to find an accurate estimation of the error (6.14). To this purpose, we introduced the average of the L_2 norm, over the same temporal horizon T, of the residuals of the Navier-Stokes operator $\mathcal{R}$, evaluated using flow fields projected onto the POD basis $\widetilde{\boldsymbol{U}}(\boldsymbol{x}, t)$:

$$\langle \mathcal{R}(\widetilde{\boldsymbol{U}}) \rangle_2 = \int_T \| \mathcal{R}(\widetilde{\boldsymbol{U}}(\boldsymbol{x}, t)) \|_2 \mathrm{d}t. \tag{6.15}$$

A comparison between the (non-dimensional) error $\langle \boldsymbol{U}' \rangle_2$ and the (non-dimensional) residuals $\langle \mathcal{R}(\widetilde{\boldsymbol{U}}_{DNS}) \rangle_2$ over $\mathcal{I}_h$ is performed in figure 6.3. It is interesting to note that these two quantities show a similar behavior for all the considered test cases, especially after the Hopf bifurcation at $Re \approx 60$. Indeed, the ratio $\langle \mathcal{R}(\widetilde{\boldsymbol{U}}_{DNS}) \rangle_2 / \langle \boldsymbol{U}' \rangle_2$ is approximately a constant over $\mathcal{I}_h$ for all test cases. The residuals $\langle \mathcal{R}(\widetilde{\boldsymbol{U}}_{DNS}) \rangle_2$ is thus a good estimator of the error $\langle \boldsymbol{U}' \rangle_2$. However the use of the residual $\langle \mathcal{R}(\widetilde{\boldsymbol{U}}_{DNS}) \rangle_2$ is not practical since it requires the computation of the numerical Navier-Stokes solution $\boldsymbol{U}$. The idea is then to approximate the projection residuals $\mathcal{R}(\widetilde{\boldsymbol{U}}_{DNS})$ with the prediction ones $\mathcal{R}(\widetilde{\boldsymbol{U}}_{ROM})$.

A comparison between the projection and prediction residuals over $\mathcal{I}_h$ is performed in figure 6.4 for the cases A, B and C. We recall that the models are calibrated on the initial set of dynamics and are then integrated using each Reynolds number $Re \in \mathcal{I}_h$. Projection and prediction residuals show a close correlation for all the considered cases except for Reynolds number below the bifurcation. However, the predicted residuals are close to the error (compare figures 6.4 and 6.3). It is noticeable that the discontinuity in the residuals evolution marks the capability of the model to predict the exact position of the bifurcation at $Re \approx 60$ without any knowledge about the critical Reynolds number of the dynamical bifurcation.
Finally, the predicted residual $\langle \mathcal{R}(\widetilde{\boldsymbol{U}}_{ROM}) \rangle_2$ is a good estimator of the error $\langle \boldsymbol{U}' \rangle_2$ and can thus be used as a criterion to sample the input parameter space (here, $\mathcal{I}_h$).

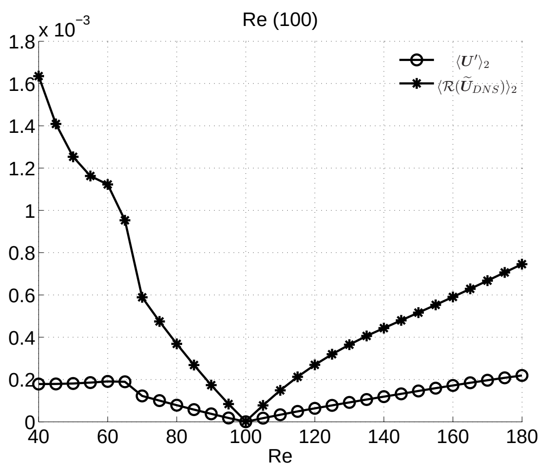

(a) Test case A.

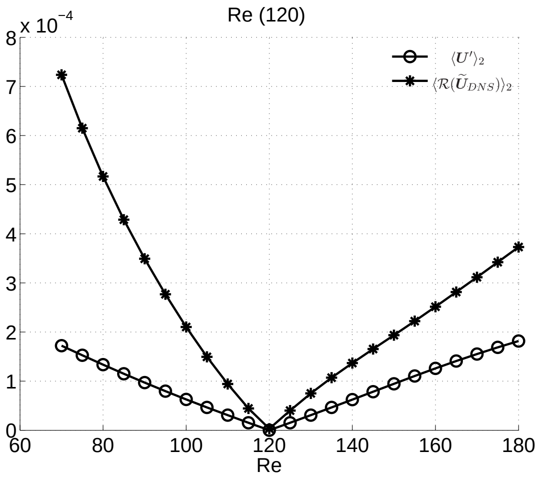

(b) Test case B.

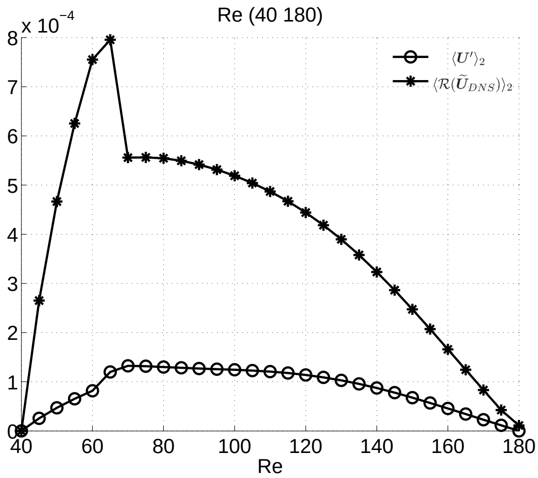

(c) Test case C.

Figure 6.3: Comparison between the mean projection error $\langle \boldsymbol{U}' \rangle_2$ and the mean residuals $\langle \mathcal{R}(\widetilde{\boldsymbol{U}}_{DNS}) \rangle_2$ for the three test cases under consideration.

6.2.3 A residual based sampling method

As described above, two classes of sampling methods are commonly used: the *one shot* and the *iterative* methods. In this study we propose an approach which couples the ideas of the two classes. In particular we will present a *one shot* method, a modified Centroidal Voronoi Tessellation, based on the Greedy ideas (Bui-Thanh *et al.* (2008)). The method proposed here is based on the residuals of the Navier-Stokes operator approximated by using the flow fields predicted by the POD reduced order model, wtih the same idea of Grepl & Patera (2005). This allows to reduce the computational costs with respect of using the reconstruction error $\boldsymbol{U}'$. We consider an initial database $U^{[Re_1,\ldots,Re_N]}$ composed

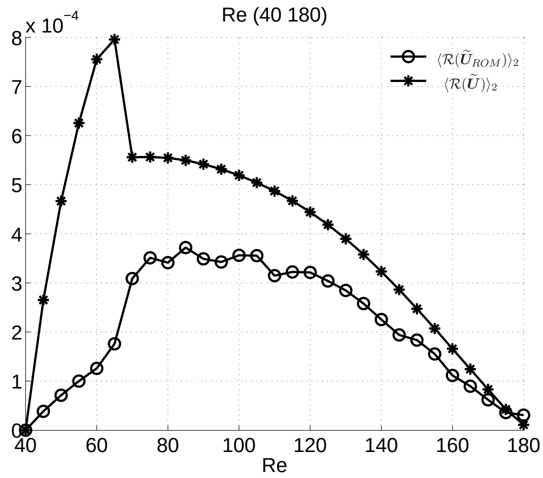

(a) Test case A.

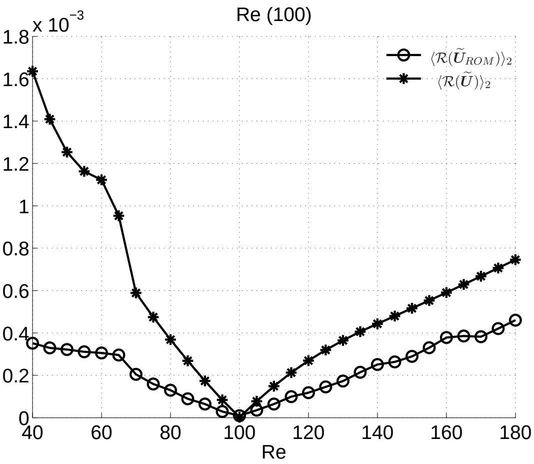

(b) Test case B.

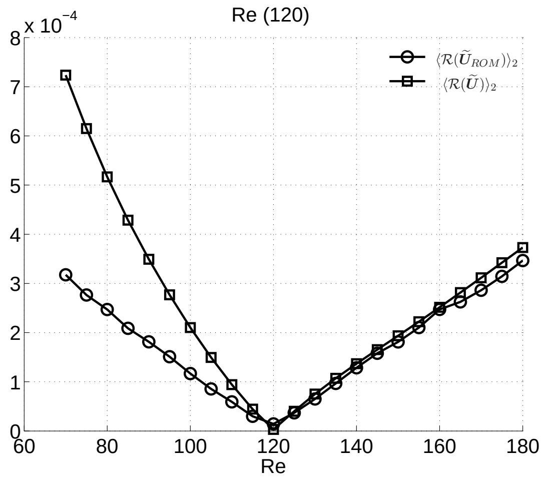

(c) Test case C.

Figure 6.4: Residuals obtained by a POD base built using Re = (40,180). Reynolds number considered between 40 and 180. Both the ROM predicted residuals (circle) and the DNS projection residuals (star) are shown

by $N \times N_t$ snapshots collected at $[Re_1, \dots, Re_N]$. By using this database the preliminary low order model is built. Since we want robust POD basis and model, we look for a sampling $\{Re_i\}_{i=1}^{M} \in \mathcal{I}_h^M$ such that the database $U^{[Re_1,\dots,Re_M]}$ produces models leading to reduction (or minimization in the optimal case) of the error evaluated over the whole subspace $\mathcal{I}_h$. M is the total number of final points, $M = K + N$, where N and K are the dimensions of the starting database and of the set of new Reynolds numbers respectively. The number of new sampling points to be added has to be fixed as a function of the desired robustness. However subsequent *one shot* sampling can be performed forming a sort of *iterative-one shot* method where the dimension of the new partial subspaces and the number of iterations have to be set. As already pointed out, the residuals of the Navier-Stokes equations $\mathcal{R}(\widetilde{\boldsymbol{U}}_{ROM})$ can be easily calculated by integration of the calibrated ROM (6.5) for all Reynolds numbers in the discretized space $Re \in \mathcal{I}_h$. Thus, the Navier-Stokes residuals predicted by the POD model can be used as density function in a Centroidal Voronoi Tessellation (CVT, see section §2.5) of the whole subspace $\mathcal{I}_h$.

Set the dimension of the final space equal to M, in order to choose an optimal placement of the new sampling points N, we propose a procedure based on a similar idea of the Constrained Centroidal Voronoi Tessellation (Du *et al.* (2003)), where a classical CVT is performed with the centers of mass of the regions constrained to belong to a surface. Here, we carry out a Centroidal Voronoi Tessellation where the new points are found as centroids of the Voronoi regions, while the starting set of Reynolds numbers are “frozen”. Thus, widely the older frozen points are not centroids of the resulting Voronoi regions. Therefore to compute the Frozen Centroidal Voronoi Tessellation (FCVT) a modified Lloyd’s algorithm can be used, where only the new points have to be centroids of their regions. The Lloyd’s algorithm described in §2.5 can be modified:

0. Begin with an initial set of M points. (the N first points frozen plus the new K points).
1. (At iteration i) consider the distribution of K points. (the N first points are frozen).
2. Construct a Voronoi tessellation associated with these points.
3. Determine the centers of mass of each Voronoi region.
4. Only the new K points are redefined to be the mass centroids while the old points are frozen.

Then repeat from one to four until the convergence. This algorithm is strongly dependent on the initial condition. This is clear in one dimensional tessellations. Indeed, for instance for our case, given a Reynolds number $Re_L < Re^* < Re_R$ as frozen point, each new Reynolds number resulting from the modified Lloyd’s algorithm cannot come out from the subspace ($[Re_L, Re^*)$ or $(Re^*, Re_R]$) where is placed as initial condition. In order to avoid this problem, we propose a degenerate method.

We perform a Frozen Centroidal Voronoi Tessellation procedure starting from a random subspace (or chosen with any sampling method) of new points ${Re_z^{new}}_{z=N+1}^{M_0} \in \mathcal{I}_{M_0-N}$, with $M_0 \gg K$. After the FCVT we exclude from the final configuration the new point $k > N$ with the smaller average density function over the k^{th} region. This is done following Greedy method in order to refine where the density function reaches higher values. The size of the space of the points is then $M_1 = M_0 - 1$. This is an iterative process, and while $M_i > M$ we recompute a new Degenerated FCVT and exclude a new point $k > N$. The final configuration $M_i = M$ is weakly dependent on the initial configuration for $M_0 \gg M$. The Degenerated FCVT is summed up below, where the goal is to find a K-dimensional sampling to add at the N-dimensional initial sampling.

0. Initial sampling with dimension $K_0 > K$. (the N first points are frozen).
1. At iteration i, start process with dimension $M_i = K_i + N$
   - Perform a Frozen Centroidal Voronoi Tessellation
   - if $M_i = M$ stop
   - if $M_i > M$ go to 2
2. Identify and exclude point $k > N$ of the element with minimum integral
   - $M_{i+1} = M_i - 1$. Increment $i = i + 1$, then go to 1

The sampling method presented above can be easily transposed for input parameter subspaces with dimension greater than one. The use of the residuals as error estimation leads to negligible computational costs, even for high dimensional input parameter spaces, as for instance active control space.

6.3 Results and discussion

The sampling technique described in the previous section was applied in order to improve the robustness of low order models for the three initial test cases described in section §6.2. The three models are calibrated over the dynamics of the databases as explained in section §6.1.2.

In order to increase the robustness we chose to add $K = 2$ new sampling points in Re. Starting with $K_0 = 6$ initial random Reynolds numbers, after four iterations the method gives the final sets of Reynolds numbers :

- Case A: $\overline{\mathcal{I}}_{N_f} = 100, 55, 160$
- Case B: $\overline{\mathcal{I}}_{N_f} = 120, 80, 165$
- Case C: $\overline{\mathcal{I}}_{N_f} = 40, 180, 90, 130$

For Constraint Uniform Sampling (CUS), approximated onto the discretized space $\mathcal{I}_h$, we have :

- Case A: $\overline{\mathcal{I}}_{CUS} = 100, 70, 140$
- Case B: $\overline{\mathcal{I}}_{CUS} = 120, 90, 150$
- Case C: $\overline{\mathcal{I}}_{CUS} = 40, 180, 85, 135$

The average error and the standard deviation evaluated over the whole subspace $\mathcal{I}$ are respectively defined by:

$$\mathrm{E} = \frac{1}{Re_R - Re_L} \int_{\mathcal{I}} \langle \boldsymbol{U}'(Re) \rangle_2 \, \mathrm{d}Re, \tag{6.16}$$

$$\mathrm{D} = \sqrt{\int_{\mathcal{I}} \left(\langle \boldsymbol{U}'(Re) \rangle_2 - E \right)^2 \, \mathrm{d}Re}. \tag{6.17}$$

While the error E measures the accuracy of the POD ROM, the standard deviation D measures its robustness.

Fig 6.6 shows the reconstruction error (6.14) obtained using the FCVT and the CUS strategies over the Reynolds number subspace $\mathcal{I}_h$ for the three test cases A, B and C. Both projection $\langle \boldsymbol{U}' \rangle_2$ prediction $\langle \boldsymbol{U}'_{ROM} \rangle_2$ errors are plotted. The POD ROM

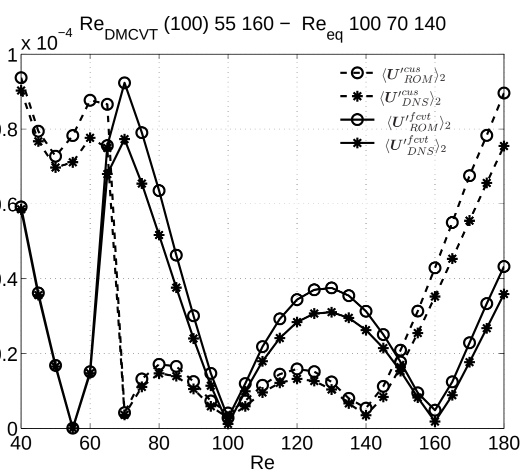

(a) Test case A.

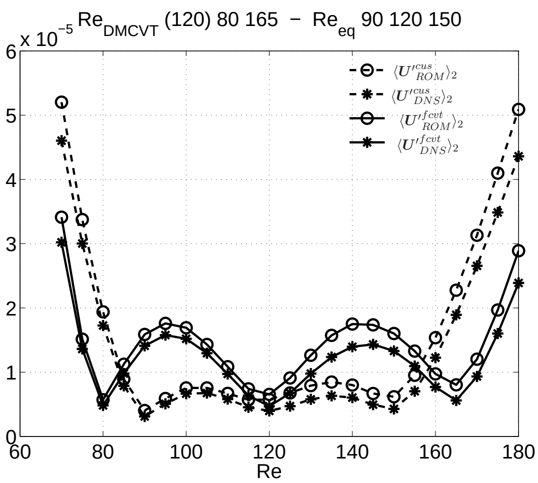

(b) Test case B.

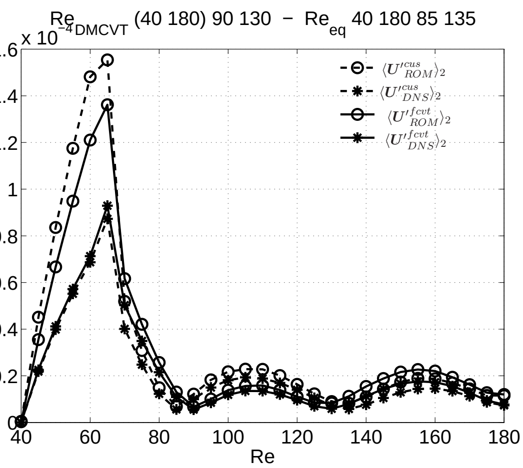

(c) Test case C.

Figure 6.5: Comparison of FCVT and CUS reconstruction error for test cases A, B and C. Both the ROM prediction reconstruction (circle) and the DNS projection (star) errors are shown.

prediction errors are close to the DNS projection ones. This proves the good behaviour of each calibrated reduced order model, showing that they are able to predict the system dynamics with a negligible error. The standard deviation has been evaluated for the POD models built using the sampling points found with both the Degenerated FCVT and the constraint uniform sampling CUS strategies.

	A		B		C	
	ΔE	ΔD	ΔE	ΔD	ΔE	ΔD
DNS Proj	16.150	47.711	11.120	123.373	-4.577	-7.991
ROM	12.850	41.470	10.854	125.741	9.150	19.804

Table 6.1: FCVT sampling efficiency ΔE and robustness ΔD.

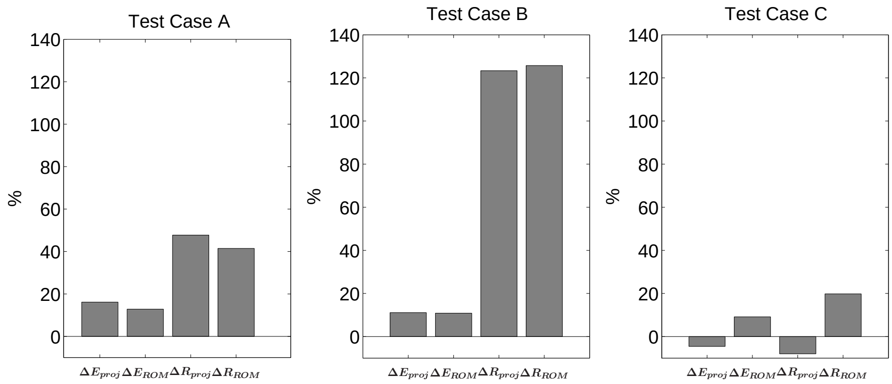

Figure 6.6: Histogram of difference between the reconstruction errors and standard deviations using CUS and FCVT sampling.

For a given quantity F we define the percentage of the relative difference by $\Delta F = 100(F_{CUS} - F_{FCVT})/F_{FCVT}$. The percentage of the relative difference errors and standard deviations are reported in table 6.1. Note that a positive difference suggests a smaller error or standard deviation for the Degenerated FCVT than for CUS. The average reconstruction errors given by ROM prediction are smaller when our sampling method is used. The reduced order model given by Degenerated FCVT are more robust in all the considered cases, even if in the third case the average error obtained by projection for the constraint uniform sampling is smaller. Indeed, for all the considered cases the average standard deviation is smaller when Degenerated FCVT is used.

As noted above, in the third case the error of reconstruction computed by the POD dynamical model obtained by Degenerated FCVT is smaller than the one computed by the CUS. Finally the ROM gives a good behaviour in terms of reconstruction error also in the case C, starting from constrained points placed on the boundaries of the parameter space, and in presence of a bifurcation.

Fig. 6.7 shows a comparison between projection and prediction residuals after FCVT sampling for all the considered test cases. The models are accurate in terms of residu-

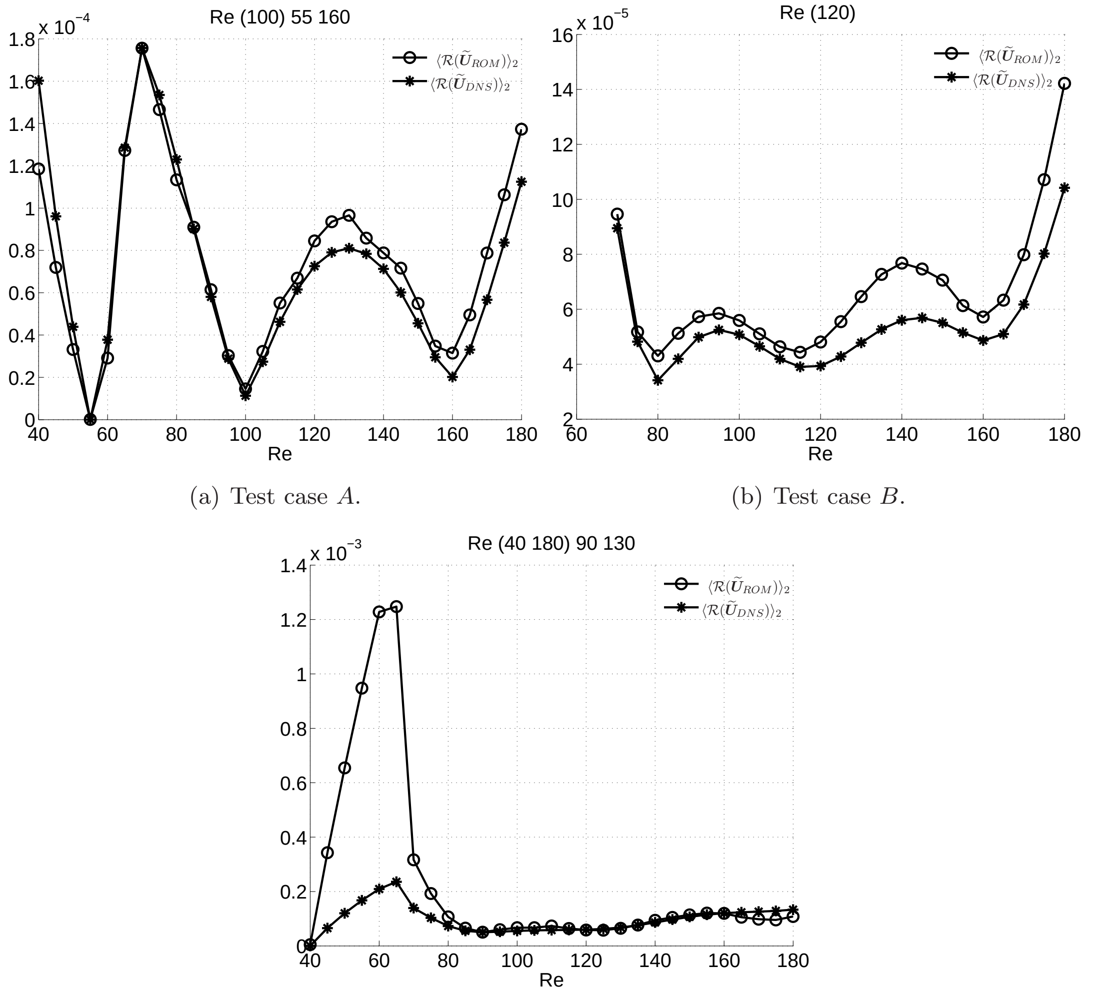

(a) Test case A.

(b) Test case B.

(c) Test case C.

Figure 6.7: Comparison between projection and prediction residuals after FCVT sampling.

als, in agreement with the assumption that the residuals can be used as error estimator. Again, in the case C, an error is visible. Indeed, the maximum on the predicted residuals reached across the bifurcation is larger than the maximum residual obtained by projection; this is due to the fact that the dynamics before $Re_c \approx 60$ are essentially steady solutions. For that, a small perturbation on the steady predicted coefficients given by the low order model is sufficient to give a larger error on the residual estimation.

Finally, for all the considered cases, which cover an adequate variety of possible situations, the low order models obtained by the proposed sampling method are robust and accurate in terms of reconstruction error as well as in terms of residuals estimation. Thus, in a sampling procedure, one can use the Degenerated FCVT to build robust parameter dependent reduced order model. This avoids huge computational costs by using residuals estimation of the calibrated ROM instead of the approximation error computed by projection. As explained above, this technique can be easily extended to high dimensional parameter space with negligible computational costs compared to those required by a procedure based on the reconstruction error evaluation.

6.4 Conclusions

In order to build a robust POD basis in this chapter we developed the degenerated Frozen Centroidal Voronoi Tessellation, a techniques aimed to an efficient sampling of the input parameter space. The sampling method is based on a Centroidal Voronoi Tessellation of the space, where the used density function is the residual of Navier-Stokes equations, calculated by using the prediction of a POD reduced order model. The use of such an error estimator, in the place of the approximation error as in the Greedy iterative method (Bui-Thanh *et al.*, 2008), produces negligible computational costs to perform the whole procedure. This approach is tested for a Reynolds number adaptive model, for a range of Reynolds number which covers the whole two-dimensional regime of the considered flow configuration. The resulting low order models, for all the considered cases, are accurate and robust to Reynolds variation if compared with those obtained by a classical Constraint Uniform Sampling of the input parameter space. The obtained models are robust both in terms of reconstruction error and in terms of residual approximation. Thus, the FCVT is an efficient method to include several solutions into the starting database. This result can be interpreted as the fact that the POD basis (and low order model) reaches the convergence (see section §5.3.2) with the least number of datasets when degenrated FCVT is used. The decribed techniques can be simply applied to other (even high dimensional) parameter spaces. For instance, this residual based sampling could be used in a control strategy, to compute an intial robust low order model, that, calibrated on the optimal dynamics, can be used in the optimisation without or with a few updating. The main computational cost being the evaluation of the Navier-Stokes residual, the technique can be applied easily also to complicated flow configurations. For high dimensional and large parameter space, the main drawback is to compute the model integration for huge number of inputs to build the density function. To avoid this, the residual density can be computed only in a limited number of points. Then the behaviour on the entire subspace can be recovered by an interpolation technique.

Chapter 7

Linearized low-order model of actuated transient flow

The aim of this chapter is to develop and test a linearized low order model of controlled transient flows. The capability of such a linearized low order model is assessed in a control optimisation. A linear model of the flow can be used when the target solution is a steady state. In this case the objective of the controller consists in stabilizing a steady state of the system. Thus, small oscillations of the system around this target state are well represented by a linear model. At the same time, designing the controller using a linear model involves standard techniques and is simpler than using a non-linear model. Moreover, it is also interesting to explore the capabilities of reduced order models in estimating unstable modes in the linear stability analysis of a flow since this aspect is typically very demanding in terms of computational costs. Indeed, this analysis requires codes simulating the linearized flow equations and, possibly, generating the matrix of the linearized system, which is not always possible when working with complex tools as those typically used in engineering applications. For this reason, the starting point of the present analysis is just the availability of a non-linear code for simulating the Navier-Stokes equations which cannot be linearized. The reduced order model of the linearized flow equations is built using only this tool.

On the other hand, the use of a non-linear reduced order model for flow control, although more expensive and complex, allows more general control strategies (*i.e.* minimization of general cost functions, different control targets etc...). In Weller *et al.* (2009) a control strategy based on a non-linear model is reported. In that reference it is also shown that the proposed strategy, when used for the particular objective of stabilizing a steady state for the system, has a clear behavior in terms of the spectrum of the linearized Navier-Stokes operator around the target flow. Thus, a linearized reduced order model is useful to investigate the effect of such a control strategy on the linear stability of the actual flow.

7.1 POD-based model of the linearized Navier-Stokes equations with feedback control

With reference to fig. 3.1 we consider the same two-dimensional geometry used in chapter 5. We take the same control device of chapter 5, *i.e.* two jets placed on the cylinder in opposite phase. We consider a feedback proportional control using some measurements of vertical velocity given by N_v sensors placed at $\boldsymbol{x}_j$ in the cylinder wake on the centre line. The control law with feedback gains K_j is :

$$c(t) = \sum_{j=1}^{N_v} \mathsf{K}_j v(\boldsymbol{x}_j, t) \tag{7.1}$$

The aim of a control optimisation is to find the set of feedback gains K_j that stabilizes the vortex shedding in the cylinder wake.

The POD-based linear model is built using the snapshots obtained by a **non-linear** simulation of the transient flow dynamics, performed with the non-linear Navier-Stokes code described in chapter 3. The simulation is started from the steady unstable solution. The starting flow field, which is also the target flow of the controller, is found using the same code, by imposing the velocity field to be symmetric with respect to the symmetry line $y = 0$ and advancing the simulation in time until a steady state is reached. Indeed, in this particular case, the unstable vortex shedding mode is antisymmetric with respect to $y = 0$, and the symmetry constraint is a physically-based trick to suppress the instability and, thus, to find the steady unstable solution. More general strategies, which can be straightforwardly applied to an evolutive non-linear code (without the need of deriving linearizations as needed for Newton-like methods) are described in Kervik *et al.* (2006) and Galletti *et al.* (2004).

N_t snapshots are obtained sampling a part of the transient dynamics, achieved by using a particular control law $c(t)$ and are used to build a POD model. To this purpose, every snapshot $\boldsymbol{u}(\boldsymbol{x}, t)$ is now decomposed as follows:

$$\boldsymbol{w}(\boldsymbol{x}, t) = \boldsymbol{u}(\boldsymbol{x}, t) - \boldsymbol{u_0}(\boldsymbol{x}) + c(t)\boldsymbol{u_c}(\boldsymbol{x}), \tag{7.2}$$

where $\boldsymbol{u_0}(\boldsymbol{x})$ is in this case the unstable steady state and $\boldsymbol{u_c}(\boldsymbol{x})$ is a flow field having a jet velocity equal to 1 on Γ_c and the velocity vanishing on all the other domain boundaries. This is obtained as in section §5.1.

Denoting $\{\boldsymbol{\phi}_n\}_{n=1\dots N_r}$ the N_r retained modes obtained by applying the POD to $(\boldsymbol{w}(\boldsymbol{x}, t_i))_{i=1\dots N_t}$, the low-dimensional solution is written :

$$\widetilde{\boldsymbol{u}}(\boldsymbol{x}, t) = \boldsymbol{u_0}(\boldsymbol{x}) + c(t)\boldsymbol{u_c}(\boldsymbol{x}) + \sum_{n=1}^{N_r} a_n(t)\boldsymbol{\phi}_n(\boldsymbol{x}) \tag{7.3}$$

The Galerkin projection of the Navier Stokes equations onto the POD modes yields to the low order model (5.3), already detailed in section §5.1.

The POD basis and the resulting model is built using the flow fields $\boldsymbol{w}(\boldsymbol{x},t)$, Eq. (7.2), collected using different control laws which derive from different sets of feedback gains. In accordance with the techniques developed in section §5.2, the POD model is then calibrated using a multiple *dynamics calibration* over all the simulations carried out to collect the snapshot database, and the conditioning of the calibration procedure is improved by Tikhonov regularization. A partial calibration is realized and all the terms of the projection matrices are calibrated, with the exception of the convective terms B_{krs}. Moreover, it is imposed that the steady unstable solution $\boldsymbol{u_0}$ is also a steady solution of the reduced order model and, consequently, the term A_r is forced to vanish.

When the feedback control is found using the velocity field approximated by the POD model, Eq. (7.1) becomes:

$$c(t) = \sum_{j=1}^{N_v} \mathsf{K}_j v(\boldsymbol{x}_j,t) = \sum_{j=1}^{N_v} \mathsf{K}_j \left(v_0(\boldsymbol{x}_j) + c(t) v_c(\boldsymbol{x}_j) + \sum_{r=1}^{N_r} a_r(t) \phi_v^r(\boldsymbol{x}_j) \right) \tag{7.4}$$

where $\phi_v^r(\boldsymbol{x}_j)$ are the values of the v-component of the POD modes at the sensors. Note that when steady unstable solution is used as target solution $\boldsymbol{u}_0$, because of the symmetry, $v_0(\boldsymbol{x}_j) = 0$. The control $c(t)$ can be found in explicit form from Eq. (7.4) by trivial manipulation. After algebraic manipulation, the low order model (5.3) in matricial form becomes :

$$\left\{ \begin{array}{rcl} \dot{\boldsymbol{a}}(t) & = & \left(\boldsymbol{I} - \boldsymbol{E}\boldsymbol{K}(\boldsymbol{I} - \boldsymbol{K} v_c(\boldsymbol{x}_v))^{-1} \boldsymbol{\phi}_v(\boldsymbol{x}_v)\right)^{-1} (\boldsymbol{A} + \boldsymbol{C}\boldsymbol{a}(t) + \boldsymbol{B}\boldsymbol{a}(t)\boldsymbol{a}(t) \\ & & + \left(\boldsymbol{K}(\boldsymbol{I} - \boldsymbol{K} v_c(\boldsymbol{x}_v))^{-1} \boldsymbol{\phi}_v(\boldsymbol{x}_v)\boldsymbol{a}(t)\right) \left(\boldsymbol{F}\left(\boldsymbol{K}(\boldsymbol{I} - \boldsymbol{K} v_c(\boldsymbol{x}_v))^{-1} \boldsymbol{\phi}_v(\boldsymbol{x}_v)\right)\boldsymbol{a}(t)\right. \\ & & \left. + \boldsymbol{G} + \boldsymbol{H}\boldsymbol{a}(t))\right) \\ \boldsymbol{a}(0) & = & \boldsymbol{a}^0 \end{array} \right. \tag{7.5}$$

where $\boldsymbol{x}_v$, the vector of the positions of the sensors, and $\boldsymbol{K}$, the set of feedback gains, are used as input parameters.

7.2 Linearized low-order feedback model

In order to perform a stability analysis of the target state $\boldsymbol{u}_0$ and to perform an optimisation of the feedback control gains, the POD model is linearized around the equilibrium state $\boldsymbol{a}^* = 0$, (which corresponds to the flow field $\boldsymbol{u}_0$):

$$\left\{ \begin{array}{rcl} \dot{\boldsymbol{a}}(t) & = & \boldsymbol{L}(\boldsymbol{K}, \boldsymbol{x}_v)\boldsymbol{a}(t) \\ \boldsymbol{a}(0) & = & \boldsymbol{a}^0 \end{array} \right. \tag{7.6}$$

where:

$$\boldsymbol{L}(\boldsymbol{K}, \boldsymbol{x}_v) = \left(\boldsymbol{I} - \boldsymbol{E}\boldsymbol{K}(\boldsymbol{I} - \boldsymbol{K} v_c(\boldsymbol{x}_v))^{-1} \boldsymbol{\phi}_v(\boldsymbol{x}_v)\right)^{-1}$$
$$\left(\boldsymbol{C}\boldsymbol{a}(t) + \left(\boldsymbol{K}(\boldsymbol{I} - \boldsymbol{K} v_c(\boldsymbol{x}_v))^{-1} \boldsymbol{\phi}_v(\boldsymbol{x}_v)\boldsymbol{a}(t)\right)\boldsymbol{G}\right)$$

Since the system matrix $\boldsymbol{L}$ of the linearized model depends explicitely on the feedback gains and on the position of the sensors, the model is predictive even when those parameters are changed with respect to the reference ones used for calibration. As already stated, the robustness of the model can be increased if, before linearization, a calibration procedure is used including several dynamics chosen by any sampling method.

The linearized equation (7.6) can be used to perform a classical linear analysis of the dynamical system. Given the position of the sensors and the set of feedback gains $\boldsymbol{K}$, the stable/unstable eigenvalues of the system $\boldsymbol{L}$ can be evaluated. For each eigenvalue, the associated eigenvector leads, by means of Eq. (7.3), to an estimation of the corresponding global mode of the linearized Navier-Stokes operator. A good accuracy on the estimation of the unstable modes of the full linearized Navier-Stokes problem allows to use the low order model in a transient control procedure, as described in the following. Note that the linearized reduced order model is obtained by using a simulation of a non-linear Navier-Stokes code. Moreover, the system matrix $\boldsymbol{L}$ depends non-linearly on the feedback gains $\boldsymbol{K}$ and on the position of the sensors $\boldsymbol{x}_v$.Thus, we propose here an iterative control procedure based on the minimisation of a functional cost, which is described in section §7.3.

As explained above, the accuracy of the linearized model is an important aspect, and this is investigated in the following. Note, that the non-linear low order model is able to reproduce the transient dynamics of actuated flows, as shown in (Galletti *et al.*, 2006) and in chapter 5. However, here we investigate the accuracy of the linearized low order model to identify the flow instability when the feedback control is active and varies. Then, as a first step, it is shown how to reconstruct a global mode associated to an eigenvector of the linearized POD system. The formal solution $\boldsymbol{a}(t)$ of the system (7.6) is:

$$\boldsymbol{a}(t) \quad = \quad \boldsymbol{R}e^{\boldsymbol{\Lambda}t}\boldsymbol{R}^{-1}\boldsymbol{a}^0 \tag{7.7}$$

where $\boldsymbol{\Lambda}$ is the diagonal matrix of the eigenvalues of $\boldsymbol{L}$, $\boldsymbol{R}$ is the matrix whose columns are the corresponding eigenvectors and $\boldsymbol{a}^0$ is the initial condition on $\boldsymbol{a}(t)$. When Eq. (7.7) is substituted in Eq. 7.2, the fluctuating part of the velocity field $\widetilde{\boldsymbol{u}}'(\boldsymbol{x},t) = \boldsymbol{u}(\boldsymbol{x},t) - \boldsymbol{u_0}(\boldsymbol{x})$ is obtained as follows:

$$\widetilde{\boldsymbol{u}}'(\boldsymbol{x},t) \quad = \quad \boldsymbol{Q}\boldsymbol{R}e^{\boldsymbol{\Lambda}t}\boldsymbol{R}^{-1}\boldsymbol{Q}^{-1}\widetilde{\boldsymbol{u}}'(\boldsymbol{x},0) \tag{7.8}$$

with $\boldsymbol{Q} = \left(\boldsymbol{K}(\boldsymbol{I} - \boldsymbol{K}v_c(\boldsymbol{x}_v))^{-1}\boldsymbol{\phi}_v(\boldsymbol{x}_v)\right)$ and $\widetilde{\boldsymbol{u}}'(\boldsymbol{x},0)$ the projection of the initial condition over the POD modes. Thus, assuming that the eigenvalues of the physical system are well approximated by the low order model, we can reconstruct the matrix containing physical eigenmodes :

$$\boldsymbol{P} \approx \widetilde{\boldsymbol{P}} \quad = \quad \boldsymbol{Q}\boldsymbol{R} \tag{7.9}$$

In particular we are interested in the estimation of the unstable modes, which correspond to eigenvalues with positive real part.

7.2.1 Results $Re = 85$

In order to assess the accuracy of the feedback linear model described above, we consider a Reynolds number $Re = 85$, at which the instability is fully developed after a slow transient. In Figure 7.1 time evolution of the lift coefficient calculated on the cylinder with no control actuation is plotted. We recall that the simulation is carried out by a non-linear Navier-Stokes code. Note the quick growth of the C_l after the slow transient regime. In the figure the portion of the transient used to build perform the POD model,

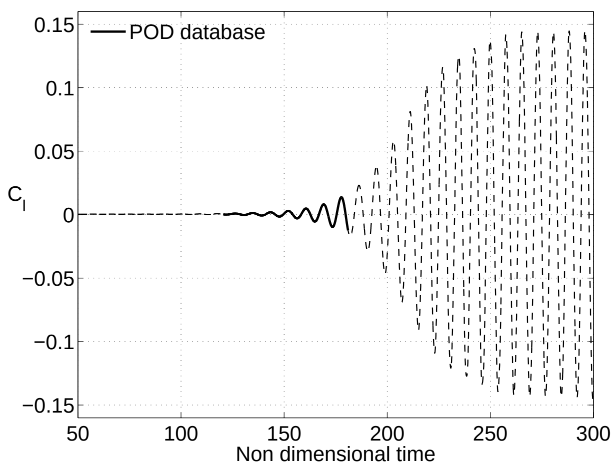

Figure 7.1: Lift coefficient C_l time evolution, with no control actuation at $Re = 85$.

which is sampled considering $N_t = 250$ snapshots, is plotted by a continuous line. This time interval is chosen starting when the lift coefficient reaches a value of $C_l \approx 0.001$ and including about six quasi-periodic flow oscillations. This choice is motivated by the need of capturing only the most energetic oscillations around the steady state while the system remains in a flow regime for which a linear approximation is still representative. We retain only $N_r = 6$ POD modes to build and calibrate the linearized low order model. This is motivated by the work documented in (Galletti *et al.*, 2006), where it is shown that a model similar to the one built here gives a good approximation of the unstable mode. Thus, the unstable mode estimated by the POD model can be analyzed to explore its observability and consequently to choose the position of the sensors for the feedback control. In particular we used only one sensor of vertical velocity, which is placed in $(x = 3.0, y = 0.0)$, in the area of the first local minimum (maximum in terms of module) of the v-component of the unstable mode. In figure 7.2 the v-component of the reconstructed mode is plotted; note that very close to the cylinder, before $x \approx 2.5$, the value of v is very small; thus, placing feedback sensors near the cylinder can be not an optimal choice to control the unstable mode. In order to test the capability of the feedback linear low order model to estimate the physical unstable mode in the presence of an actuation, we performed two numerical simulations of the actuated flow using two different proportional feedback gains for the sensor placed as described above,

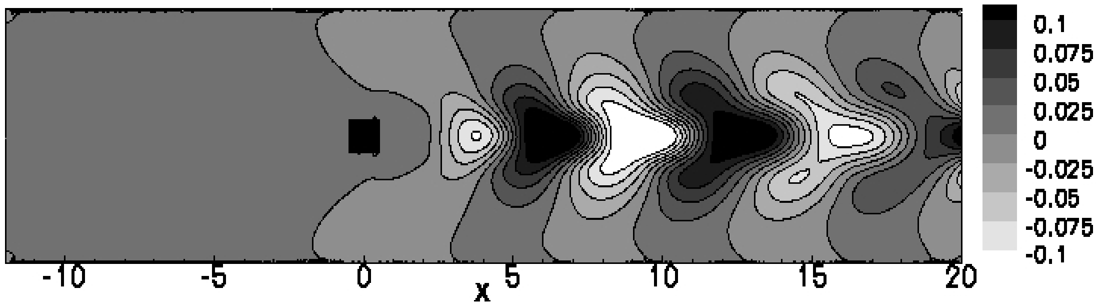

Figure 7.2: Reconstructed component v of the physical unstable mode. $Re = 85$

i.e. $k = 0.1$ and $k = 0.2$. In figure 7.3 the two lift coefficients obtained by the DNS

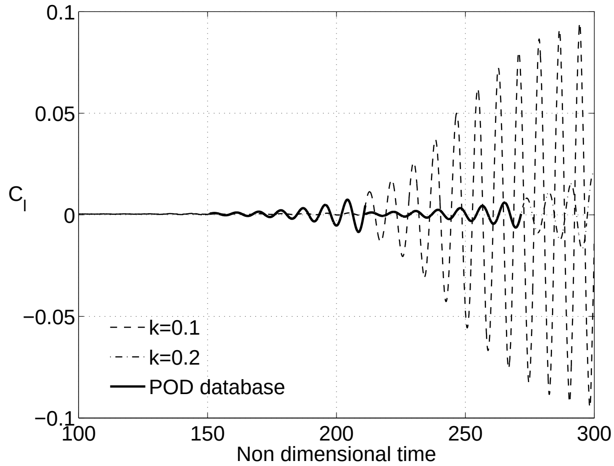

Figure 7.3: Lift coefficient C_l time evolution, with proportional gains $k = 0.1$ and $k = 0.2$ at $Re = 85$.

simulation are shown together with the two portions of the transient used to build the POD database (solid line). As in the previous case, the two time intervals include six flow oscillations starting from a value of $C_l \approx 0.001$, with $N_t = 250$ snapshots for each case. Note that the two initial gains are chosen in a random manner and the instability is not stabilized with those proportional parameters, even if the growth is retarded when $k = 0.2$ is used. Following the procedure explained in section §2.1.2, the low order model is calibrated over the two dynamics. Then the prediction of the eigenvalues and of the dynamics prediction and the estimation of the unstable modes are obtained using the feedback adaptive linearized model for $k = 0.1$ and $k = 0.2$. The linearized model is able to predict the part of transient dynamics used as database, as shown in figure 7.4, where the first two modal coefficients, obtained by integration of the feedback linear model with $k = 0.2$, are plotted together with the reference solutions. In figure 7.5 (half

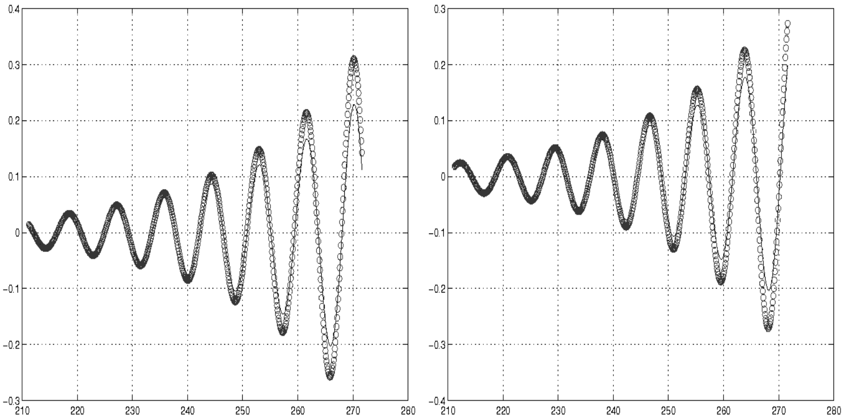

Figure 7.4: Projection of the DNS simulations onto POD modes (continuous line) vs. integration of the linear model (circles) for first (left) and second (right) mode. Feedback gain $k = 0.2$.

of) the spectrum of $\boldsymbol{L}(k)$, for $k = 0.1$ and $k = 0.2$, is sketched together the unstable mode estimated by a linearized analysis of the Navier-Stokes operator, denoted in the figure as DNS (we thank Simone Camarri (DIA, Università di Pisa) for providing the results obtained with a linearized Navier-Stokes code). As expected, only two unstable conjugate eigenvalues are predicted by the linear low order model. Note that, as the value of the feedback gain is increased, the unstable eigenvalues are displaced closer to the stable region of the complex plane. The estimation of the unstable eigenvalues given by reduced model is very accurate as well as the effect of the increase of the feedback gain on the instability. The percentage error on the estimation of the real and the imaginary part of the unstable eigenvalues are very low and respectively 7.62% and 0.26% when $k = 0.1$ is used and 0.11% and 0.12% for $k = 0.2$. Note that the predicted and physical unstable eigenvalues are overlapped when $k = 0.2$ is used. This shows the very good accuracy of the linearized low order model when used to simulate the linear unstable dynamics when the feedback control varies. Note that the estimation of the frequency of the instability (related to the imaginary part of the unstable eigenvalues) is almost perfect. This is due to the fact that the variation of the frequency is negligible between the two dynamics. Moreover the plot shows that the effect of the increase of the feedback gain is larger on the unstable eigenvalues than on all the other stable ones. Thus, in this configuration and for feedback gains around the values $k = 0.1$ and $k = 0.2$, the stable eigenvalues are not deplaced towards the unstable region by the control actuation. In figure 7.6 the velocity module of the reconstructed unstable mode for the case $k = 0.2$ and the one found by a linearized analysis of the Navier-Stokes operator are plotted. The prediction of the mode is very accurate in the whole domain; only a little difference can be noted at the outflow due to the influence of the imposed boundary conditions in the linear Navier-Stokes code. An analogous result is obtained in the case $k = 0.1$.

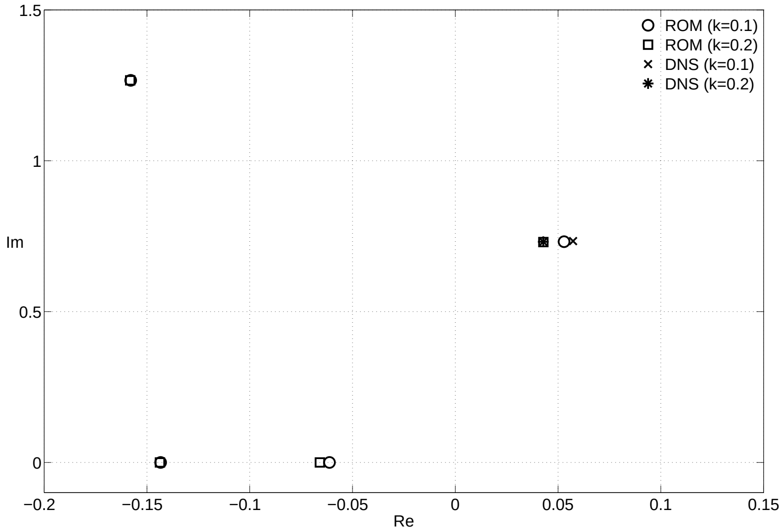

(a) Test case B.

Figure 7.5: Spectrum of the eigenvalues of the POD system matrix L vs. unstable physical eigenvalues (DNS).

7.3 Design of a control strategy based on the linear model

In this section we describe a control optimisation procedure based on the linear feedback low order model. In order to stabilize the steady state the unstable eigenvalues needs to be moved in the stable region of the complex plane. Classical tools for linear control are not used here; indeed, we have to take into account the robustness of the low order model. To this aim, while the position of the sensors are kept constant, a function of the gains $\boldsymbol{K}$ is proposed, such that its minimisation is equivalent to stabilize the system:

$$\mathcal{J}_7(\boldsymbol{K}) \quad = \quad \sum_{r=1}^{N_r} \tanh(Re(\lambda_r(\boldsymbol{K})) - \lambda^*_{Re}) + \alpha_K \sum_{j=1}^{N_v} \min_{l=1,\ldots,N_v}((\boldsymbol{K}_j - \boldsymbol{K}^0_l)^2) \tag{7.10}$$

where λ_r are all the N_r eigenvalues predicted by the linear feedback model as $\boldsymbol{K}$ varies, λ^*_{Re} is the stability margin required, $\boldsymbol{K}^{\mathbf{0}}$ is the set of gains used to build the model and the parameter α_K has to be chosen as a measure of the "trust region" of the low order model. In our application we use $\alpha = 0.1$. The function $\tanh(\cdot)$ is chosen to retain the position of the eigenvalues already stable with a margin larger than λ^*_{Re}, while the other eigenvalues are modified.

The minimisation, gives an optimal set of parameters $\boldsymbol{K}^*$ for the present model. This set of gains are tested in a non-linear Navier-Stokes simulation of the transient. If the target state is not stabilized a new reduced order model is built with a database obtained by adding a portion of the transient of the new dynamics to the old POD database. During the optimisation procedure a maximum number of dynamics in the POD database can be fixed *a priori*, then when the maximum number is reached, a

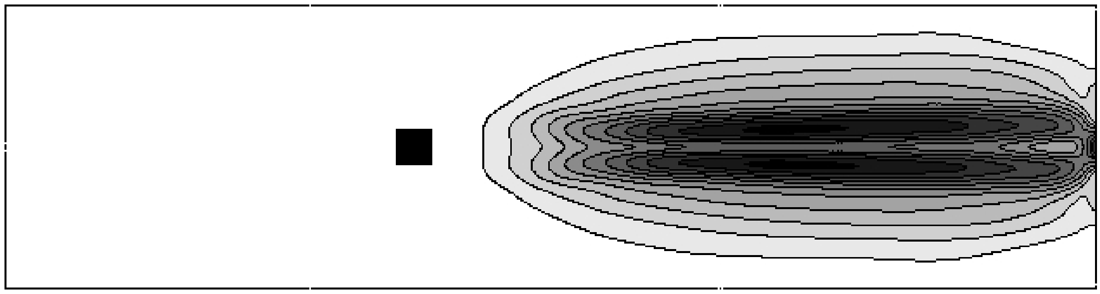

(a)

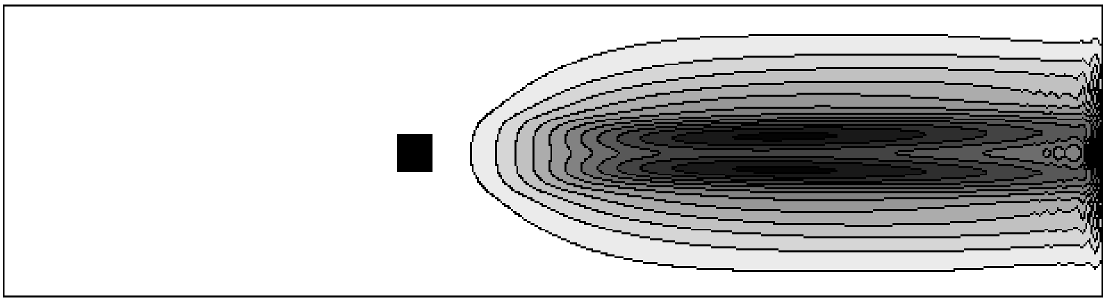

(b)

Figure 7.6: Isocontour of the velocity module of the predicted (a) and the physical (b) unstable eigenmode for the case $k = 0.2$. Plots obtained with the same scale level.

new set of snapshots substitutes the one with maximum distance $|\boldsymbol{K} - \boldsymbol{K}^*|$. Again, a minimisation of the functional (7.10) is carried out and a new set of parameters are obtained. The procedure is stopped when the steady state is stabilized.

7.3.1 Results $Re = 85$

In the test described here, the model built using the databases obtained with $k = 0.1$ and $k = 0.2$ is initially used for the optimization. The minimisation of (7.10) gives a new value of the feedback gain $k^* = 0.44$. A non-linear simulation of the Navier-Stokes equations starting from $\boldsymbol{u}^0$ is carried out, and the flow is completely stabilized, as shown in figure 7.7 and 7.8. In figure 7.7 the lift coefficients obtained with $k = 0.1$, $k = 0.2$ and k^* are plotted. The use of the optimised feedback gain leads to a steady state and vanishing lift coefficient. Thus, the flow is totally controlled as displayed in figure 7.8, where the vorticity field of the flow obtained with k^* at time $t = 480$ is shown.

Finally, the reduced order model obtained by a non-linear Navier-Stokes code and then linearized around a steady state, is able to represent, with limited computational costs, the unstable modes of the linearized Navier-Stokes operator, and a control optimisation based on such a linearized model gives a set of input parameters that stabilizes the actual flow. We recall that the whole procedure can be performed starting from the simulations of a generic non-linear code as those typically used in enginering applications.

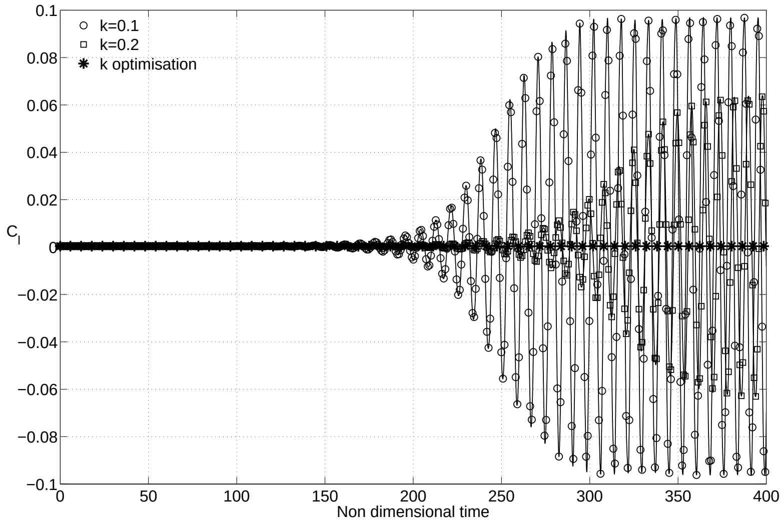

Figure 7.7: Lift coefficient obtained with $k = 0.1$, $k = 0.2$ and k^*. Sensor position (3.0,0.0) and $Re = 85$.

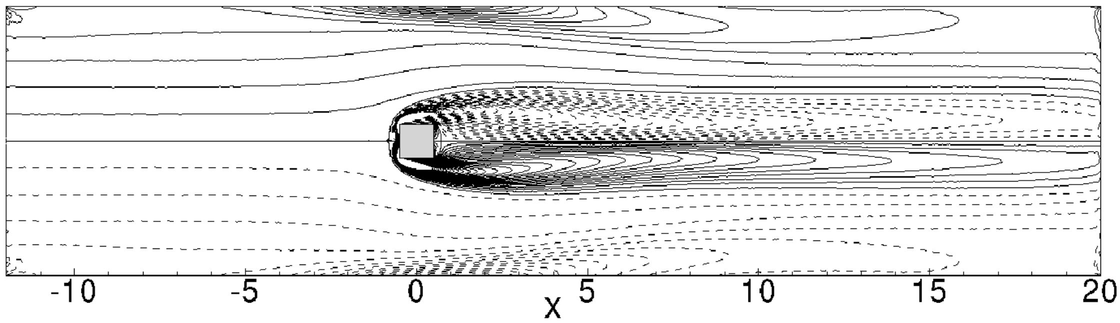

Figure 7.8: Vorticity snapshot of controlled flow with k^* at time $t = 480$.

The obtained results allow us to use the optimisation based on the linear feedback low order model in a control procedure for flow at higher Reynolds numbers and/or with a higher number of sensors.

In order to investigate the capability of such a method for a higher Reynolds number, in the next section we apply this approach to the flow at $Re = 150$.

7.3.2 Results $Re = 150$

In order to set the position of the sensor used in the feedback actuation, we perform a Navier-Stokes simulation of the uncontrolled flow transient starting from the steady unstable solution calculated with the same procedure described in section §7.1. A low order model is built, as for the case at $Re = 85$, by using a portion of this transient history. In particular we used an interval of about five vortex shedding cycles, starting from a value of $C_l \approx 0.01$. In figure 7.9 the transient of the C_l and the relative portion used to perform the POD for the uncontrolled case is shown together with a C_l time history which will analyze hereafter. We retain only $N_r = 15$ POD modes. This choice

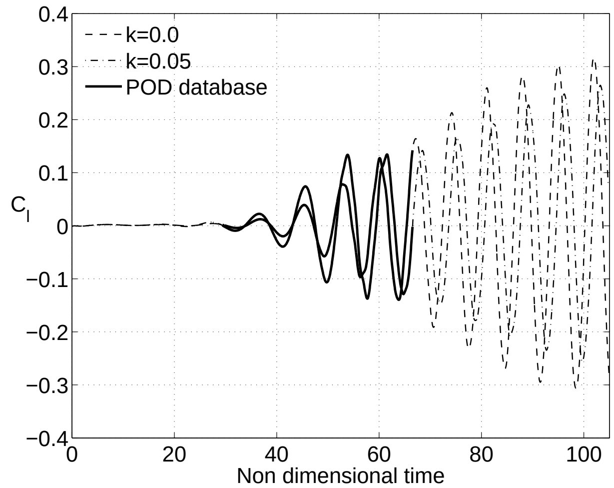

Figure 7.9: Lift coefficient C_l time evolution, with proportional gains $k = 0.0$ and $k = 0.05$ at $Re = 150$.

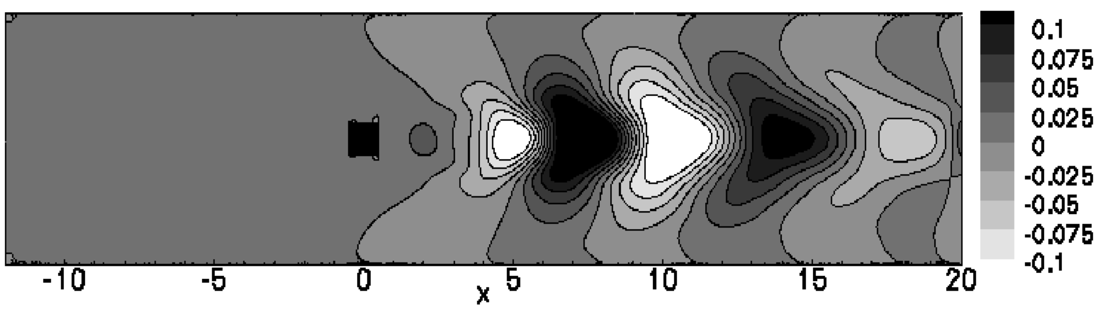

Figure 7.10: Reconstructed component v of the physical unstable mode for the uncontrolled flow. $Re = 150$

is motived by the fact that in this analysis we are interested especially in the accuracy of the primary instability estimation. The reconstructed physical unstable mode presents a first considerable maximum/minimum of the v-component at $(x, y) \approx (5.0, 0.0)$ (see figure 7.13). As for the case at $Re = 85$ we choose the position of this point to place the feedback sensor. We perform a controlled simulation to be used in the construction of the low order model for optimisation. We choose an initial value $k = 0.05$. The Navier-Stokes simulation gives an interesting result, in terms of stability. Indeed, the dynamics seems more unstable in the zone of linear growth, while the limit cycle reached has a smaller amplitude than the limit cycle of the uncontrolled case. This is displayed in figure 7.9, where the lift coefficient obtained with $k = 0.05$ is plotted together with the lift coefficient of the uncontrolled flow. The more rapid growth in the actuated case compared to the uncontrolled one is clearly visible, as well as the fact that the fully developed shedding is attenuated. Then, the POD basis and the calibrated low order model are built by using the two portions of the transient highlighted in figure 7.9. An optimisation step of the functional (7.10) is performed that gives an optimal gain with opposite sign $k^* = -0.015$. This result shows that the initial choice $k = 0.05$ was inappropriate. A non-linear simulation is performed with feedback gain k^* starting from the steady unstable solution. The evolution of the lift coefficient obtained is plotted in figure 7.11 together with the ones for $k = 0.0$ and $k = 0.05$. The plot presents again the same peculiar results described above. The instability in this case seems slightly more controlled in the first part of the transient (note that the resulting gain is weak), while, after about four shedding cycles, the shedding is intensified compared to the uncontrolled one. In figure 7.12 the evolution of the eigenvalue referred to the unstable mode is shown.

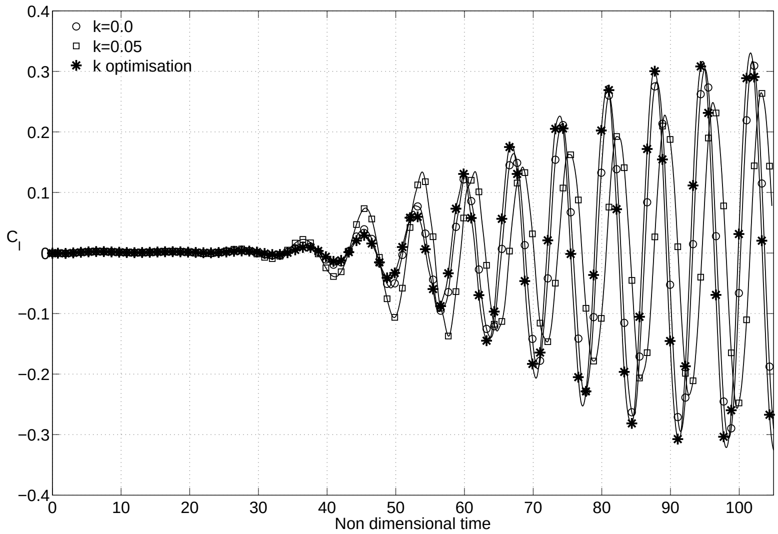

Figure 7.11: Lift coefficient obtained with $k = 0.0$, $k = 0.05$ and k^*. Sensor position (5.0,0.0) and $Re = 150$.

As expected the real part of the eigenvalue decreases when the optimized feedback gain is applied. Thus, the low order model identifies a weak stabilization of the instability, while the non-linear simulation, after a small time interval, shows that the flow is not stabilized and the shedding is amplified.

An interpretation of this phenomenon can be achieved considering the v-component of the unstable mode. Indeed, recall that the feedback sensor evaluates the v-component fo the flow velocity and, in order to observe the dynamics concerning the instability, it is placed in the first min/max of the v-component of the unstable mode. In figure 7.13

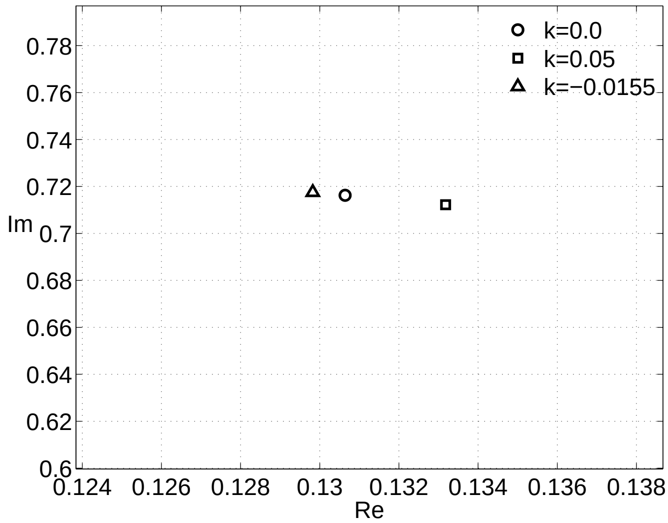

Figure 7.12: Spectrum of the eigenvalues of the POD system matrix L for feedback gains $k = 0.0$, $k = 0.05$ and k^*. $Re = 150$

the v-component of the actual unstable mode is plotted together with the reconstructed ones obtained by using two low order models. The first one is built on the transient given by using $(k = 0.0, k = 0.05)$, *i.e.* the initial low order model; thus, the predicted unstable mode does not belong to the simulations of the POD database. The second low order model is built on the dynamics simulated with $(k = 0.0, k = 0.05, k = k^*)$.

In the figure the good accuracy of both the reconstruction obtained by the model built on the three controls (bottom) and of the prediction of the initial model is clearly visible. Only a small error around the jet area is present together with a weak asimmetry due to the fact that a limited number of modes is retained and a small portion of transient is used to calculate the basis. The corresponding eigenvalue is estimated by the two models with a relative error of about 11%, but the relative error on the trend of the deplacement of the eigenvalue, when passing from $k = 0.0$ to $k = k^*$, is about 0.14%.

One interesting issue is that both low order models are able to reproduce the modification of the physical unstable mode. Indeed, the figure displays the translation of the unstable mode patterns towards the outflow. As a result of this translation, the position of the feedback sensor corresponds to a zone where the v-component of the unstable mode is almost null. This could be the reason of the apparent flow stabilization in the first instants of the transient followed by an amplified shedding instability. Indeed, in the first time portion the unstable mode is still unmodified and the feedback sensor is able to capture the instability; when the mode is more and more translated, the zone with v component equal to zero reaches the sensor and the instability grows.

This behaviour suggests, in agreement with similar results of Min & Choi (1999) for a circular cylinder, that a simple optimisation procedure with only one sensor is not possible for this Reynolds number (an analysis of the intensity of the modification of the

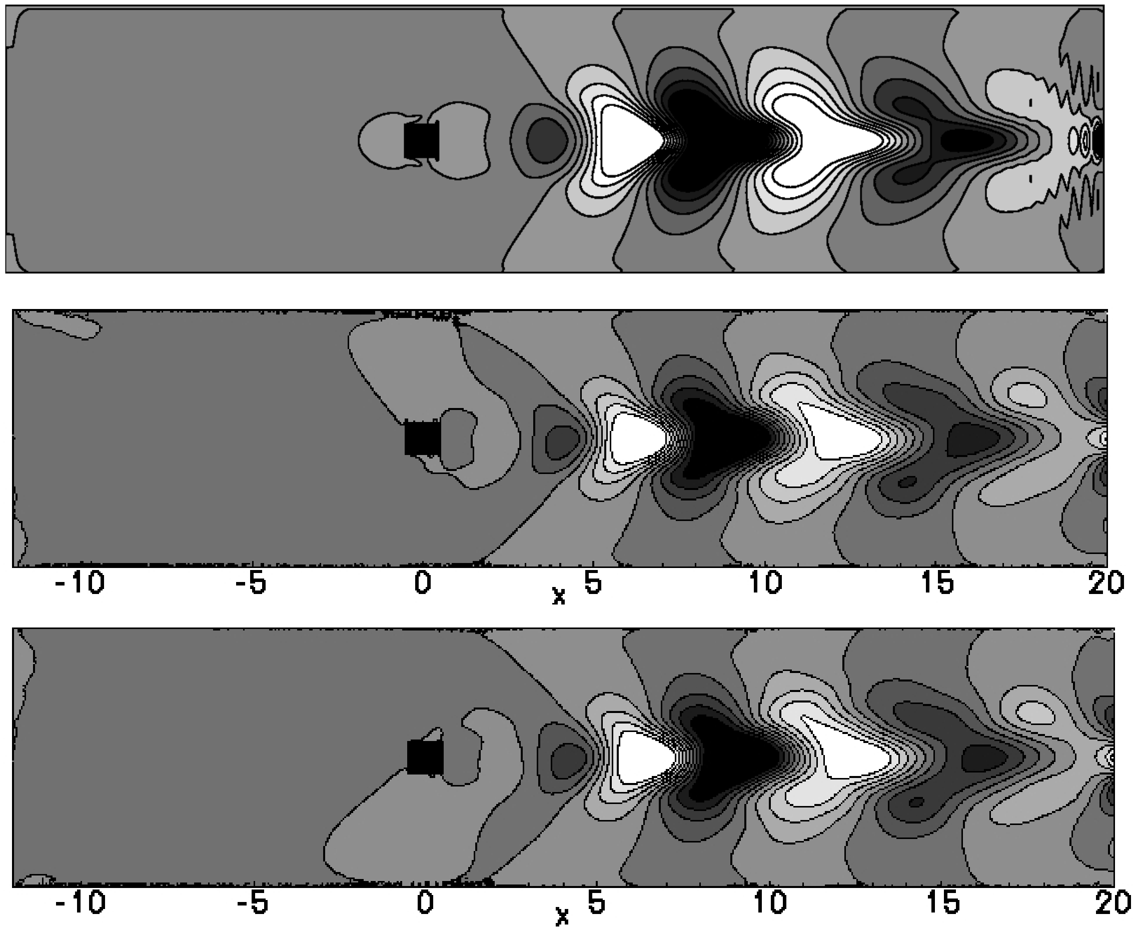

Figure 7.13: Reconstructed component v of the physical unstable mode with k^*. $Re = 150$. Physical mode (top) vs. Mode reconstructed by model built on $(k = 0.0, k = 0.05)$ (center) vs. Mode reconstructed by model built on $(k = 0.0, k = 0.05, k = k^*)$ (bottom). Plots obtained with the same scale level.

unstable mode when the Reynolds number varies could be of interest). Thus, several way to improve the control procedure exist. One way could be, during the optimisation procedure, to reconstruct the unstable mode at each optimisation step and, when the placed sensors are reached by the zero zone of the v-component, to add a sensor in the new modified max/min. This allows to follow the evolution of the unstable mode and to assure that its dynamics is well captured. Furthermore, one could optimize both on the feedback gain and on the sensor position, *i.e.* to find a an evolutive time dependent law $x_s(t)$ for the sensor position related to an evolutive feedback gain $K_s(t)$ that stabilizes the shedding.

7.4 Conclusions

The development of an accurate linearized low order model for transient flows with feedback actuation is performed. Such a reduced model is used in a linear stability analysis that can not be carried out with a non-linear Navier-Stokes code such as the one employed in this study. The low dimensional model, even by using a small number of modes, after calibration results robust to parameter variation, and provides an accurate prediction of the spectrum of the actual linear system as well as of the trend of the deplacement of the system eigenvalues when the feedback parameters vary. Moreover, the spatial reconstruction of the global unstable modes is accurate and the modification of the physical modes are well captured by the reduced model. This allows to use such an instrument during a non-linear optimisation in order to check on the effect of the actuation on the spectrum of the linearized Navier-Stokes system and to check on the spatial modification of the global unstable modes. Indeed, in Weller *et al.* (2009), is shown that other secondary modes can become unstable when a feedback control is actuated. In this way, even an optimisation on the sensors placement based on the analysis of the global modes can be performed.
On the other hand, such a linear model could be directly used in a control strategy of a fully developed flow. Indeed, as shown in Weller *et al.* (2009) a non linear optimisation, for Reynolds number $Re = 150$, is not able to completely stabilize the shedding wake; thus, by coupling a non linear modeling with a linearized reduced order model, a mixed optimisation procedure can be performed, by switching from a non-linear approximation to a linear one when approaching to the target solution.
The model is tested also in a simple feedback control optimisation for transient flows at $Re = 85$ and at $Re = 150$. The controlled steady solution is achieved at $Re = 85$ by using a sensor placed in a maximum/minimum of the reconstructed global unstable mode. On the contrary at $Re = 150$ a stabilization of the steady solution via feedback control by using only one sensor in the wake seems not possible, due to the spatial modification of the unstable mode during the control actuation.

Chapter 8

Experimental signal analysis by POD

Fluid dynamics signals are generally characterized by significant fluctuations that need to be investigated in order to portray their physical origins. A first attempt for the analysis of the signal fluctuations is a statistical characterization, which permits to detect the mean value of the signal and features of its time-variation as, e.g., its scattering through the standard deviation and/or the symmetry or not of the fluctuations around the mean amplitude through the skewness.

In several conditions, as for instance for wakes and jets, the flow fluctuations could be characterized by the presence of dominating spectral components, which can be detected through a conventional Fourier transform. However, this technique becomes highly inappropriate when a time-characterization of the amplitude and frequency of the spectral components is required or when a temporal analysis of the simultaneousness or alternateness of different spectral components must be performed.

When only one spectral component is present in a fluctuating signal, the time-variation of its amplitude and frequency can be analysed by using the classical Hilbert demodulation technique (Bendat & Piersol, 1986), providing that certain constraints on the modulation frequencies are satisfied. If multiple components are present, each component must be extracted from the source signal before applying the Hilbert demodulation, as proposed in Sreenivasan (1985), where a classical band-pass filtering is applied to extract each spectral component before applying the Hilbert demodulation.

Alternatively, the continuous complex wavelet transform may be directly applied to characterize the time-variation of a frequency range instantaneously contributing to the signal fluctuations. However, through the only application of the wavelet transform qualitative and statistical characteristics may be gained simultaneously for all the spectral components present in the considered frequency range and a component extraction may be performed by using, for instance, the so-called wavelet ridges, as reported in Carmona *et al.* (1998).

An interesting procedure for time-frequency analysis based on the wavelet and Hilbert transforms is proposed in Buresti *et al.* (2004). First, the main spectral components are detected qualitatively or statistically from the fluctuating energy map calculated through wavelet transform, then each component is extracted through a band-pass filter also based on wavelet transform, *i.e.* by neglecting the fluctuating energy outside of a chosen frequency range and applying the inverse wavelet transform. Once the time-history of a spectral component is evaluated the Hilbert demodulation may be applied. In that work the correlation of different spectral components is estimated through the definition of a cross-analytic signal also based on the Hilbert transform. A more sophisticated wavelet decomposition is proposed by Olhede & Walden (2004) that extract spectral components with ad-hoc filter banks, but with band-edge imperfections in correspondence of the boundary of contiguous frequency sub-bands for components spanning at least two sub-bands, and by almost losing the nonlinear characteristics of the signal. Summarizing, the wavelet based decomposition techniques are generally non adaptive because the filter bank must be selected properly for the considered signal, i.e. detect the main spectral frequencies and choose filter amplitudes *by-eye* or through a statistical control. Furthermore, the wavelet based techniques can detect only interwave modulations, i.e. nonlinearities over contiguous oscillations, and not intrawave modulations (see e.g. Kijewski-Correa & Kareem (2007)).

Doubtless the technique for spectral component detection and extraction from multi-component signals that has earned more interest in the last decade is the Empirical Mode Decomposition (EMD) proposed by Huang *et al.* (1998) (more than 1400 citations for this paper) and combined with the HT is the so-called Hilbert-Huang transform (HHT). EMD is a completely empirical technique with no theoretical foundations, producing an a posteriori basis completely data dependent. Here each spectral component is defined as an intrinsic mode function (IMF).

A shortcoming of the EMD is the so-called end effect, which is generally common to all time-frequency techniques. However, end effect can be alleviated through different methods as proposed in Wu & Qu (2008), Chiew *et al.* (2005) and Dätig & Schlurmann (2004) , or by extending the signal as carried out in Coughlin & Tung (2004) and Rilling *et al.* (2003).

Another source of error for the EMD is the algorithm used for the peak fitting in order to generate the upper and lower envelope. Usually a cubic spline is used but other algorithms can be used as the one presented in Xu *et al.* (2010), or the segment power function method proposed by Qin & Zhong (2006).

Beside the abovementioned shortcomings, an actual breakdown of the EMD for fluid dynamic signals is the so-called mode mixing. It consists in the presence of different spectral components with completely different frequencies into a single IMF. The origin of mode mixing seems to be the intermittency of the different spectral components. In fluid dynamics the signal decomposition aims to produce monocomponent signals for time-frequencies analysis of the flow features produced by different vorticity structures or turbulent scales. Therefore, if in a single IMF different spectral components are present the goal of the signal decomposition is not reached at all. However, mode mixing can be alleviated or eliminated through an intermittence test proposed by Huang *et al.* (1999) that enables to separate different scales, or through several masking signal-based techniques (see e.g. Deering & Kaiser (2005) and Senroy *et al.* (2007)), but this techniques are not adaptive and are efficient only for stationary signals.

Nevertheless, the primary limitation of the application of EMD for fluid dynamic signals is that it is basically a bank of dyadic filters, as proved by Flandrin *et al.* (2004) and Wu & Huang (2004), in fact Dätig & Schlurmann (2004) stated EMD's inability to separate spectral components that have frequency proportion near unity. A dyadic filter bank is a collection of band-pass filters that have an analogous shape but with neighboring filters covering half or double of the frequency range of any single filter in the bank. The frequency ranges of the filters can be overlapped. For example, a dyadic filter bank can cover frequency ranges as 50 to 120 Hz, 100 to 240 Hz, 200 to 480 Hz and so on. This feature is a real breakdown of EMD in time-frequency analysis of fluid dynamic signal and it is the main reason for which different techniques are still investigated.

In this chapter a POD based procedure for time-frequency analysis of one dimensional fluid dynamics signals is described. The source-signal is firstly manipulated in order to generate an ad-hoc data set composed by time-portions of the signal, each one composed by the same number of samples; this data set represents the *snapshots* for the POD procedure. The obtained POD modes with higher energy represent the time-histories of the most representative signal fluctuations, and their Fourier analysis could be used for a spectral characterization. However, the time-variation of each spectral component can be only performed by extracting them through a procedure based on the convolution of the source signal with the required POD modes. The main advantage of this technique is represented by the automatization in the detection and sorting by the mean fluctuating energy of the principal components present in a fluid dynamics signal. An iterative procedure can hence be implemented for extracting spectral components, starting from the most energetic one and then analysing the residual signal, *i.e.* the source-signal from which the extracted spectral component is subtracted. In this way the flow fluctuations can be considered adequately characterized when a sufficient fluctuating energy is extracted (e.g. a certain percentage of the total fluctuating energy) or when all the dominant spectral components are extracted. Finally, the time-characterization of each spectral component may be carried out through the Hilbert transform.

8.1 Application of POD for one-dimensional signals

In the context of experimental fluid dynamics POD is generally used for signal analysis of data acquired simultaneously from different points, like the ones obtained from different experimental measuring techniques like, e.g., Particle Image Velocimetry (see e.g. Weiland & Vlachos (2009)), pressure taps measurements (see e.g. Kitagawa *et al.* (2002)) or rakes of hot-wire anemometers (see e.g. Bakewell & Lumley (1967)). However, the aim of this study is to develop a technique based on POD for an automatic detection and extraction of principal components from one-dimensional fluid dynamics signals.

For our goals let us consider a generic one-dimensional zero-mean signal $u(t)$, which can represent a measurement performed in a fixed point of the flow field with a sampling frequency F_{samp} and a total number of samples equal to N_{samp}.

In order to perform POD, a certain number of observations of the analysed process are required (snapshots); to this end time-portions of the source-signal $u(t)$ are generated, all with the same number of samples N_{period}. The source-signal is divided into adjacent time-portions in order to generate the snapshots, whose total number, N_{snap}, depends on the total length of the source-signal, N_{samp}, and on the time-length of each snapshot, N_{period}. An adequately high number of snapshots, N_{snap}, is required to perform a satisfying POD, *i.e.* in order to separate the typical realizations of the main phenomena from other random processes. In case this condition is not adequately satisfied, a higher number of snapshots can be generated through non-adjacent time-portions of the signal, *i.e.* partially overlapped, although uniformly distributed along the time-length of the signal (the maximum number of snapshots that might be generated from a signal composed by N_{samp} samples is equal to $N_{samp} - N_{period} + 1$). This procedure is allowed because the statistics stationarity of the source signal $u(t)$ is generally satisfied, *i.e.* the statistical parameters of $u(t)$ do not change by increasing the total number of samples, N_{samp}, and thus the observations of the process are virtually increased in this way without changing its statistical and spectral features. Obviously with this technique the observations of the process are not totally statistically independent; however, this method results to be very useful to annihilate all random influences or disturbs present in a signal and better highlight all the typical realizations of the process. With reference to equation (2.3), in the case of discrete one-dimensional signals the space vector $\mathbf{x}$ becomes one-dimensional and represents the index of the samples of a certain snapshot ($x = 1, ..., N_{period}$), while the time t becomes the index of the snapshots ($t = 1, ..., N_{snap}$).

A crucial task of the procedure is represented by the choice of the time-length of each snapshot, *i.e.* the number of samples, N_{period}, composing each snapshot and that is strictly related to the frequency resolution of the analysis; in other words, if Δf is the frequency interval between two consecutive elements of the signal power spectrum, required to discern different spectral components, thus the required N_{period} will be equal to the ratio between the sampling frequency and the frequency resolution, $F_{samp}/\Delta f$. Therefore, the higher is the number of samples composing each snapshot, N_{period}, the better is the frequency resolution of the spectral analysis; however, in the following it will emphasized that with increasing frequency resolution the time-resolution of the POD tool of detecting spectral components with spotting amplitude is reduced. Moreover, it should be pointed out that the total number of samples of each snapshot, N_{period}, must be sufficiently high in order to characterize the lower frequencies of interest.

Let now consider the first computer-generated signal designed to assess the POD procedure for time-frequency analysis. The signal is composed by three different spectral components ($f_1 = 40$ Hz, $f_2 = 60$ Hz and $f_3 = 70$ Hz) and white noise with an energy equal to 23% of the total energy of the signal is also added:

$$y_1 = sin(2\pi f_1 t) + 2sin(2\pi f_2 t) + 4sin(2\pi f_3 t) + WN \tag{8.1}$$

The signal is sampled with a frequency of 1 kHz for 10500 total samples. A time-portion of the signal is reported in figure 8.1.

For this test-case 10^4 snapshots of the signal are generated, each comprising 501 samples, *i.e.* the used frequency resolution is about 2 Hz. Being the number of snapshots, N_{snap}, higher than the number of the samples of each snapshot, N_{period}, the POD is performed in the classical manner and not by using the snapshots method of Sirovich; thus, the POD modes are the vectors that maximize (2.1) and are in number equal to $N_{period} = 501$. In figure 8.2 the eigenvalues, which represent the fluctuating energy of the respective POD modes, are reported as percentage of the total energy of the signal.

The time-series of the first eight POD modes are reported in figure 8.3, while the respective power spectra are reported in figure 8.4. The most energetic POD modes are, as expected, POD modes 1 and 2, which are characterized by a dominant frequency at 70 Hz. The POD modes 3 and 4 are related to the component at a frequency $f_2 = 60$ Hz, while 5 and 6 to the component at $f_3 = 40$ Hz; as expected they are sorted by their energy. The remaining POD modes do not show any dominant spectral component and are due to white noise.

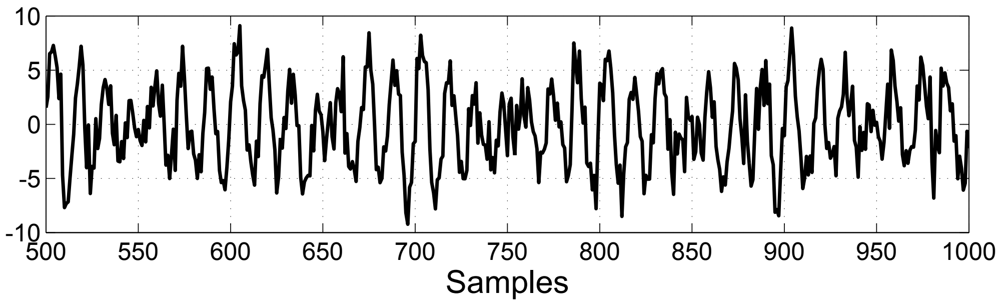

Figure 8.1: Time-portion of the computer-generated signal y_1.

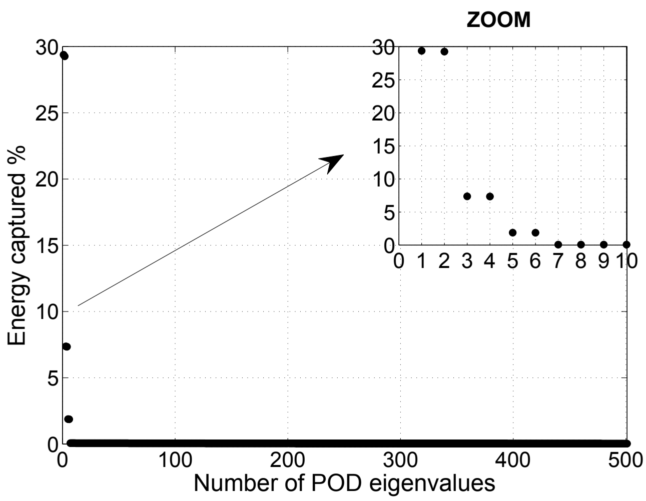

Figure 8.2: POD eigenvalues evaluated for the computer-generated signal y_1.

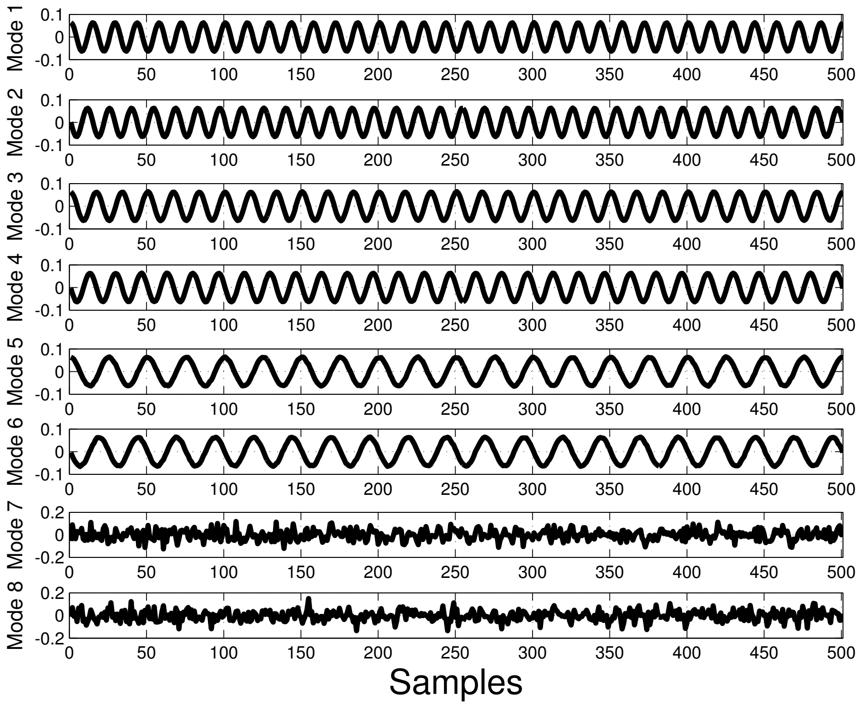

Figure 8.3: Time-series of the first eight POD modes evaluated for the signal y_1.

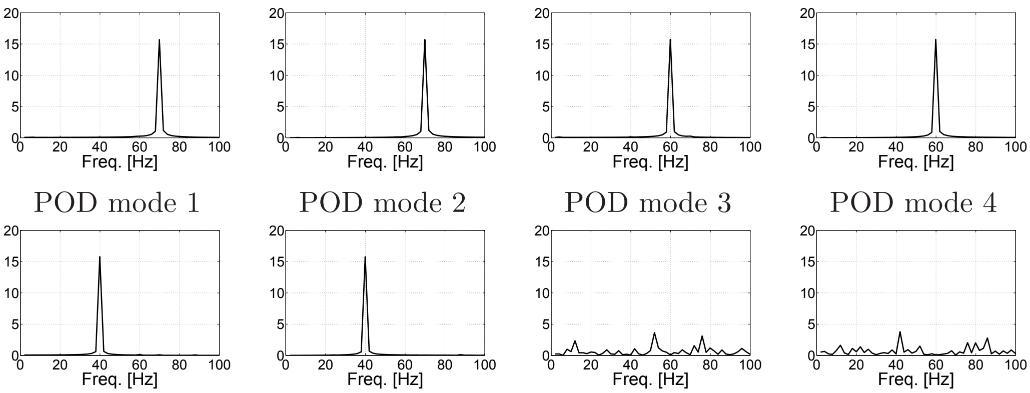

POD mode 1 POD mode 2 POD mode 3 POD mode 4

POD mode 5 POD mode 6 POD mode 7 POD mode 8

Figure 8.4: Fourier spectra of the first eight POD modes evaluated for the signal y_1.

From the power spectra of the POD modes the dominant frequencies of the signal are detected; however, their analysis along the time-length of the whole source-signal, $u(t)$, is not already performed. A first attempt might be carried out by dividing $u(t)$ into adjacent time-portions composed by N_{period} samples, and then projecting each time-portion onto the considered POD mode. However, when instantaneous amplitude of the component varies during the sampling period, a discontinuity can be evaluated at the junction between two consecutive time-portions, due to the average-effect performed through the scalar product on each time-portion (see figure 8.5 where discontinuities are highlighted by arrows).

Consequently, to avoid these non-physical features on the instantaneous amplitude of the principal components, an alternative procedure is developed. The technique for principal component extraction from a source-signal is based on the convolution of the latter with the considered POD mode. However, a generic POD mode is not a symmetric filter due to its initial phase, as can be appreciated from figure 8.3, and, thus, the convolution of the source signal with a function obtained from the convolution of a POD mode with its respective POD flip-mode is performed. This function, denoted as POD conv-mode, is characterized by the same power spectrum of the POD mode, and obviously of its POD flip-mode, but it is a symmetric filter and, thus, no phase-shift is produced through the convolution of the source-signal with the POD conv-mode. It must be pointed out that each POD conv-mode is composed by $2 \times N_{period} - 1$ samples, being obtained through the convolution of discrete functions consisting of N_{period} samples each.

An important step regarding principal component extraction through the convolution procedure consists in avoiding any amplification or damping. The basic idea of the filtering is that the convolution of a certain POD conv-mode with itself must produce the POD conv-mode without any amplification or damping. In order to reach this goal, the result of the convolution of the source-signal with the considered POD conv-mode must be multiplied by the factor K:

$$K = \frac{|conv - mode|}{|convolution(conv - mode, conv - mode)|} \tag{8.2}$$

where $| \bullet |$ represents the L_1-norm, *i.e.* the sum of absolute values of the elements, consistently to the precision adopted for the convolution algorithm.

As regarding the computer-generated signal y_1, the three different spectral components can now be extracted through the convolution of y_1 with the respective POD modes. The spectral component related to the frequency $f_1 = 70$ Hz can be evaluated through the POD mode 1 or 2; choosing the POD mode 1, its POD conv-mode is calcu-

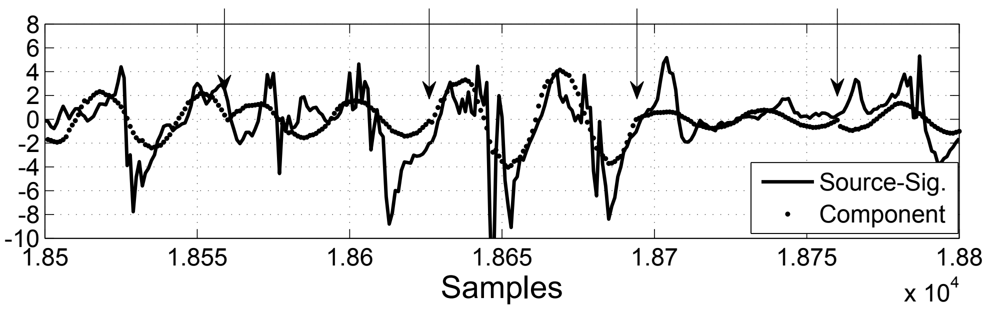

Figure 8.5: Evaluation of spectral components through projection of the source-signal on the considered POD mode (discontinuities highlighted through arrows).

lated as reported in figure 8.6a and its power spectrum is compared to the one of POD mode 1 in figure 8.6b.

The extracted spectral components are reported in figure 8.7 with their moduli obtained through Hilbert transform. Starting from the most energetic spectral component, *i.e.* the one related to $f_1 = 70$ Hz, its amplitude is equal to 4 (Eq. 8.1) and through the spectral component extraction its mean value is found to be 3.996 with a standard deviation of 0.087 (about 2% of the mean value), demonstrating that the spectral contribution of interest is completely captured by this spectral component. The instantaneous frequency of the spectral component is also evaluated through Hilbert transform and a mean value of 69.915 Hz and a standard deviation of 0.013 (about 0.02% of the mean value) are found.

Since the spectral component related to the POD mode 1 is extracted, a residual signal can be evaluated by subtracting the extracted spectral component to the source-signal y_1. Subsequently, the spectral component related to the POD mode 3 can be extracted, *i.e.* the one corresponding to $f_2 = 60$ Hz. The time-series of this spectral component is reported in figure 8.7b with its modulus evaluated through the Hilbert transform (mean value of 2 and standard deviation of 0.087). From the Hilbert transform of the extracted component a mean value of the instantaneous frequency equal to 59.961 Hz is found with a standard deviation equal to 0.025.

The last component related to the frequency $f_3 = 40$ Hz, is extracted by using the POD conv-mode 5. The extracted component is reported in in figure 8.7c (modulus with a mean value of 1.003 and standard deviation of 0.091). The mean instantaneous frequency evaluated through Hilbert transform is equal to 39.995 Hz with a standard deviation of 0.053.

Finally, by adding the three extracted spectral components together, it is seen in figure 8.7d that the reconstructed signal well reproduces the source-signal y_1, except for white noise that is removed.

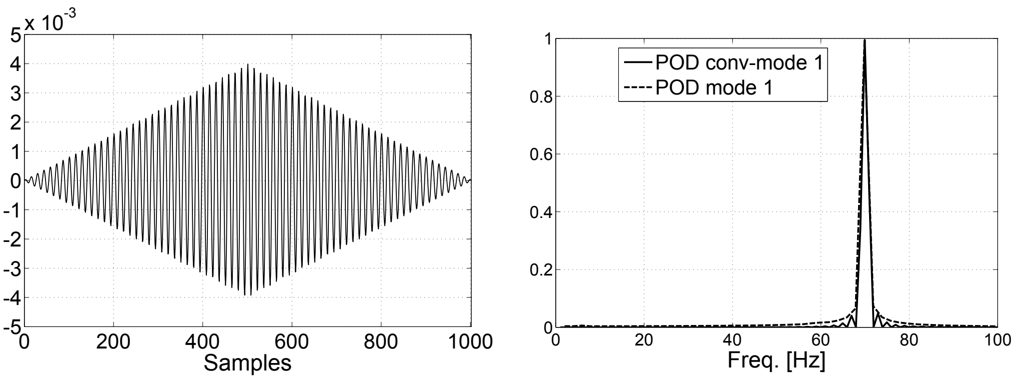

(a) (b)

Figure 8.6: POD mode 1 of the signal y_1: **a** time-series of the POD conv-mode 1; **b** power spectra of POD mode 1 and POD conv-mode 1.

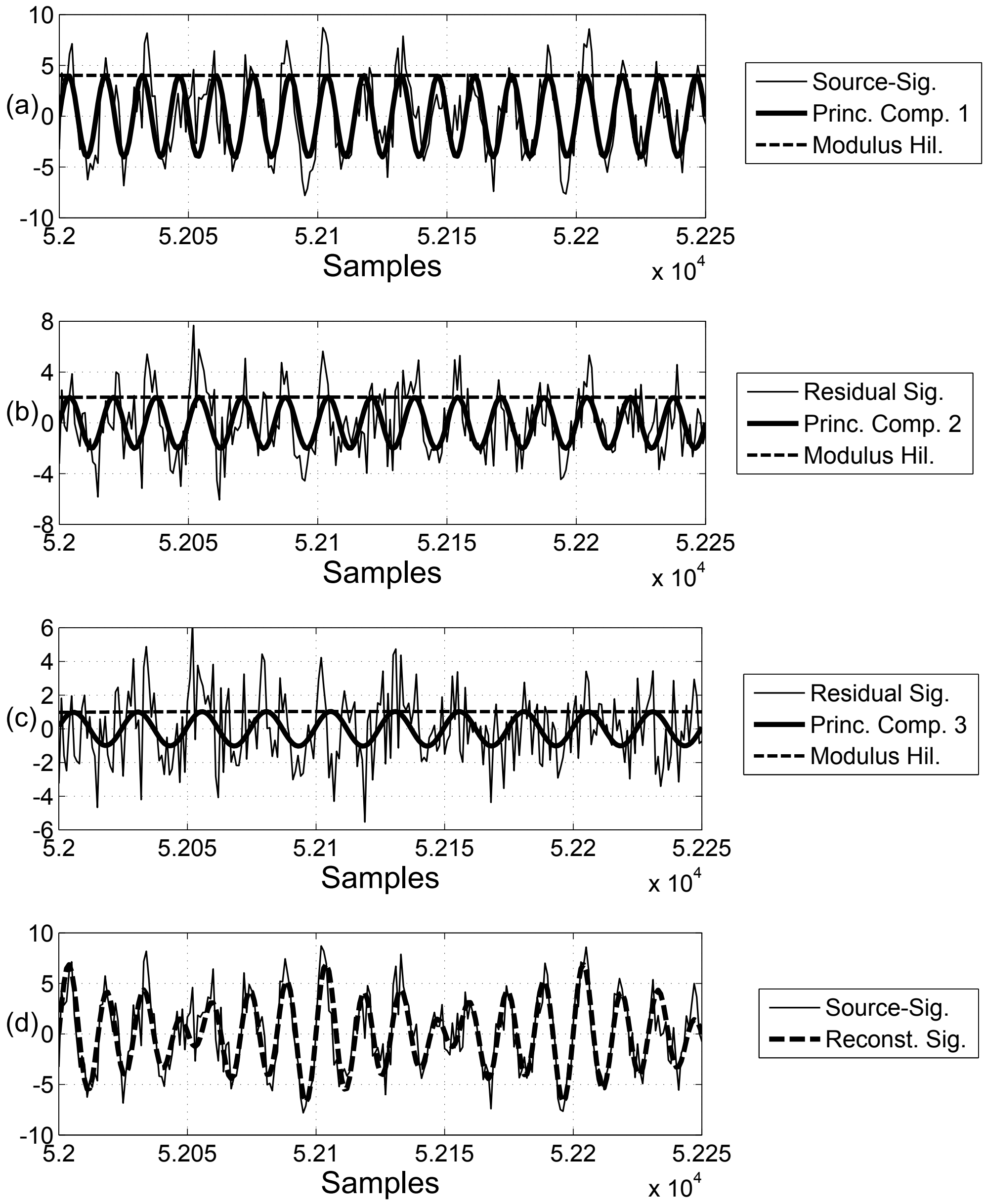

Figure 8.7: Spectral components extracted from the source-signal y_1: **a** spectral component related to $f_1 = 70$ Hz; **b** spectral component related to $f_2 = 60$ Hz; **c** spectral component related to $f_3 = 40$ Hz; **d** reconstructed signal.

The test case of the computer-generated signal y_1 well highlights the advantages of the POD procedure for time-frequency analysis of one-dimensional signals: the only parameter to chose is the frequency resolution of the spectral analysis, thus the number of samples for each snapshot, N_{period}. Conversely to other techniques, no frequency identifications of the main spectral components, preliminary spectral analysis or band-pass filtering are required (see e.g. Buresti *et al.* (2004) for details). Since the POD modes are calculated, in an automatic way the principal components can be extracted starting from the most energetic one, and the characterization of the signal can be considered adequately performed when a certain percentage of the fluctuating energy of the source-signal is extracted or when the dominant spectral contributions are captured.

Beside signals consisting of different spectral components, as simulated through the signal y_1, another case of interest for fluid dynamics is represented by a signal in which the main spectral component is modulated in amplitude with a certain frequency. This is the case of the computer-generated signal y_2; this signal is:

$$y_2 = [2 + sin(2\pi f_2 t)]sin(2\pi f_1 t) \tag{8.3}$$

where the main component at $f_1 = 50$ Hz has a mean amplitude equal to 2 and is modulated in amplitude with a frequency $f_2 = 20$ Hz. The signal is generated by using a sampling frequency $F_{samp} = 1$ kHz and it consists in 6000 snapshots composed by 1001 samples each one (*i.e.* the chosen frequency resolution is about 1 Hz). The power spectrum evaluated for the signal y_2 is reported in figure 8.8.

By performing POD of this signal, six POD modes with a significant energy are evaluated, as reported in figure 8.9 where the POD eigenvalues are plotted, and their respective power spectra are reported in figure 8.10. Six POD modes with a significant energy were expected being the power spectrum of y_2 characterized by the presence of three different spectral contributions.

The most energetic POD modes, *i.e.* POD modes 1 and 2, represent the main component at $f_1 = 50$ Hz, whereas the POD modes from 3 to 6 are composed by the two spectral contributions at frequencies $f_1 - f_2$ and $f_1 + f_2$, but not both exactly with the

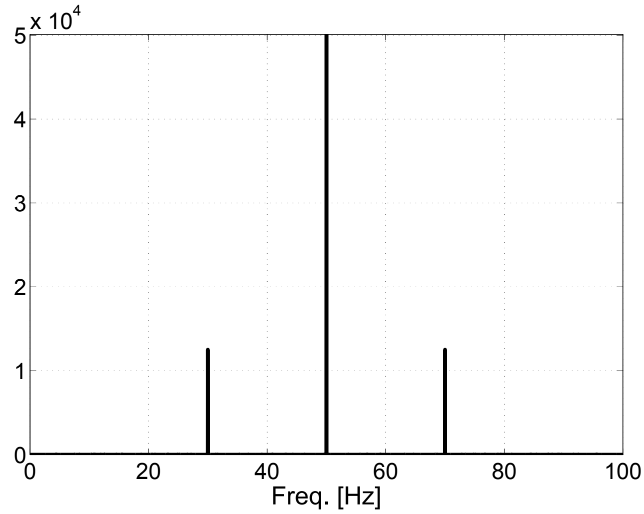

Figure 8.8: Power spectrum of the computer-generated signal y_2.

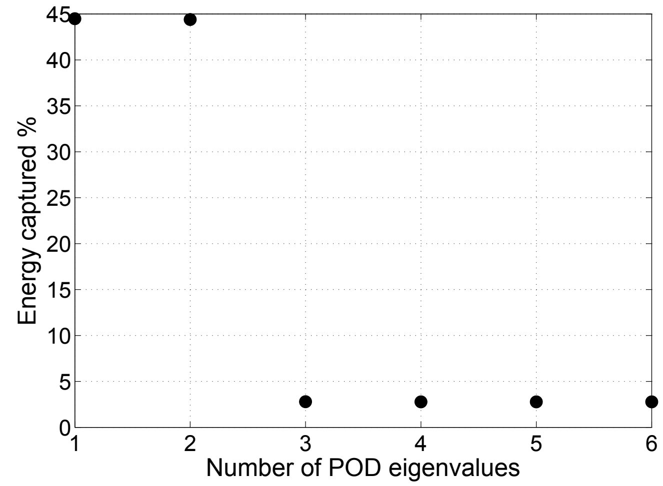

Figure 8.9: First six POD eigenvalues evaluated for the computer-generated signal y_2.

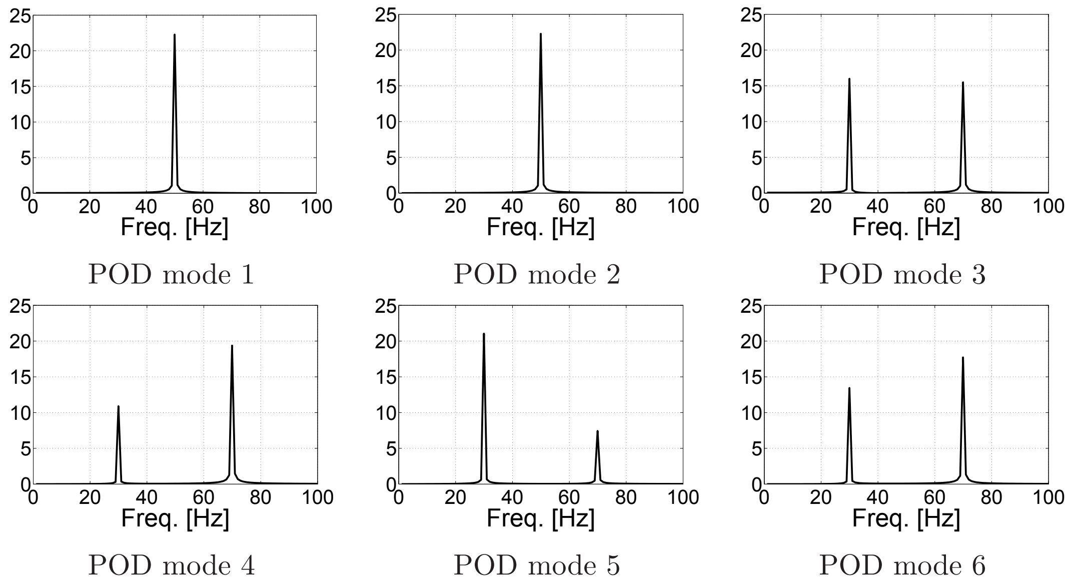

Figure 8.10: Fourier spectra of the first six POD modes evaluated for the signal y_2.

same energy. All these four POD modes are found with the same POD eigenvalues, *i.e.* they have the same significance regarding the energy of y_2, because they have the same origin, viz. the amplitude modulation. It should be noted that these two frequencies are always coupled and never found as separated spectral contributions, indicating the strict connection between them; this feature is difficult to highlight through other techniques for spectral analysis.

By extracting the principal component related to the POD mode 1, the main spectral contribution at $f_1 = 50$ Hz can be characterized. The accuracy on the reconstruction of the source-signal can be estimated through the calculation of the root mean square value of the difference between the reconstructed signal and y_2 as percentage of the root mean square value of the only y_2. By reconstructing the signal with only the component related to the POD mode 1 this parameter is equal to 33.6%, *i.e.* error is very significant because the amplitude modulation is completely missed. However, when the reconstructed signal is obtained as sum of the components related to the POD modes 1 and 3, this parameter is drastically reduced to 4.54% because with the only POD mode 3 the amplitude modulation at $f_2 = 20$ Hz is already well reproduced, as shown in figure 8.11. With the POD modes 1, 3 and 4 the parameter is slightly reduced to 4.37%; is 4.3% with the POD modes 1, 3, 4 and 5; finally, with POD modes 1, 3, 4, 5 and 6 is 4.27%.

The procedure for component extraction can be used easily for spectral components with time-varying amplitude. For instance if a signal comprising a spectral component with a frequency of 50 Hz and an amplitude that linearly increases with time is considered, the POD of this signal detects a POD mode characterized by a frequency of 50 Hz and a constant amplitude. When the respective component extraction is performed, the actual instantaneous amplitude of the spectral component can be evaluated as shown in figure 8.12.

However, when the component is not-continuously varying in time, as e.g. in the case of a spotting contributions, a certain time-delay in the modulus of the extracted spectral component is observed, as reported in figure 8.13. This delay is strictly dependent on the used frequency resolution, Δf, and, thus, on the number of samples of each snapshot N_{period}. This delay is due to the convolution operation that involves a time-period equal to $2 \times N_{period}$. Consequently this delay is reduced with reducing the frequency resolution and, thus, the number of samples of each snapshot, N_{period}. This feature does not depend on any other parameters like frequency or amplitude of the spectral contribution, or like the sampling frequency.

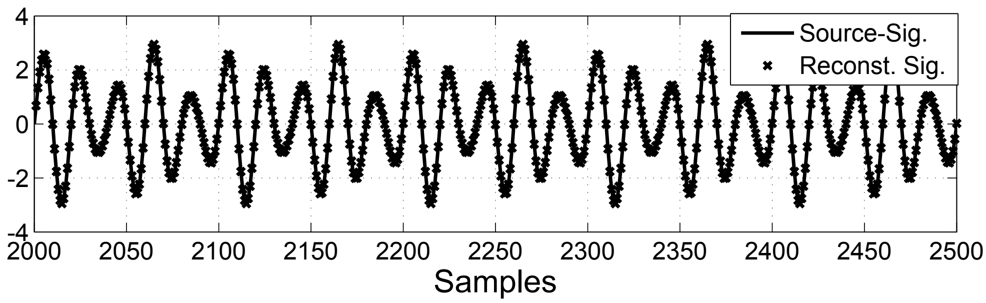

Figure 8.11: Comparison of the reconstructed signal through POD modes 1 and 3 with the source-signal y_2.

8.2 Application of POD for experimental fluid dynamics signals

The procedure based on POD for principal component detection and extraction from one-dimensional signals is now applied to hot-wire anemometer signals acquired in proximity of the wake generated from a triangular prism with finite height.

An experimental investigation on the near-wake flow field generated from a prism with equilateral triangular cross-section, aspect ratio $h/w = 3$, where h is the height and w the base edge of the model, and orientated with its apex edge against the incoming wind was presented in Buresti & Iungo (2009). A sketch of experimental setup is reported in figure 8.14, where the used frame of reference is also reported. The tests were carried out at a Reynolds number, based on w, of 1.5×10^5.

For this configuration flow fluctuations at three prevailing frequencies were singled out, with different relative intensities depending on the wake regions. In particular, the frequency connected with alternate vortex shedding from the vertical edges of the prism was found to dominate in the regions just outside the lateral boundary of the wake at a Strouhal number of about $\mathrm{St} = fw/U_\infty \approx 0.16$, where U_∞ is the freestream velocity. On the other hand, a lower frequency, at $\mathrm{St} \cong 0.05$, was found to prevail in the velocity fluctuations on the whole upper wake. Simultaneous measurements carried out over the wake of the prisms at symmetrical locations with respect to the symmetry plane showed that these fluctuations correspond to a vertical, in-phase, oscillation of two counter-rotating axial vortices detaching from the front edges of the free-end. This finding was confirmed by the results of a LES simulation of the same flow configuration, described in Camarri & Giannetti (2007), which also highlighted the complex topology of the upper near-wake produced by the vorticity sheets shed from all the edges of the prism. In Buresti & Iungo (2009) wake velocity fluctuations were also observed at an intermediate frequency $\mathrm{St} \cong 0.09$, and were found to prevail in the symmetry plane. By using the evidence provided by the abovementioned LES simulation, by flow visualizations and by pressure measurements over the prism surface, it was suggested that they may be

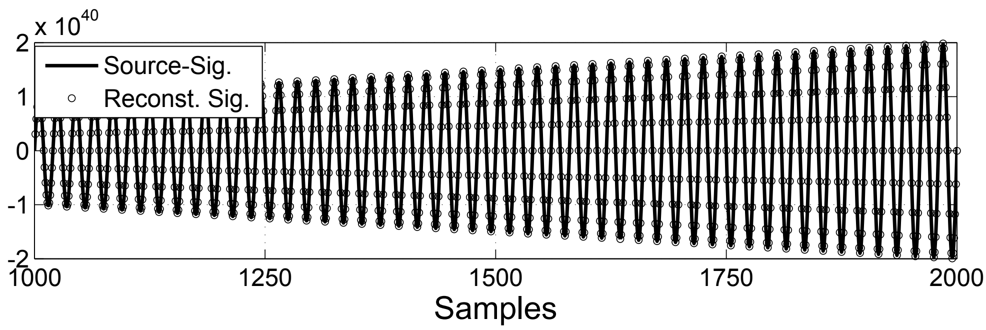

Figure 8.12: Comparison of the reconstructed signal with source-signal with linearly varying amplitude.

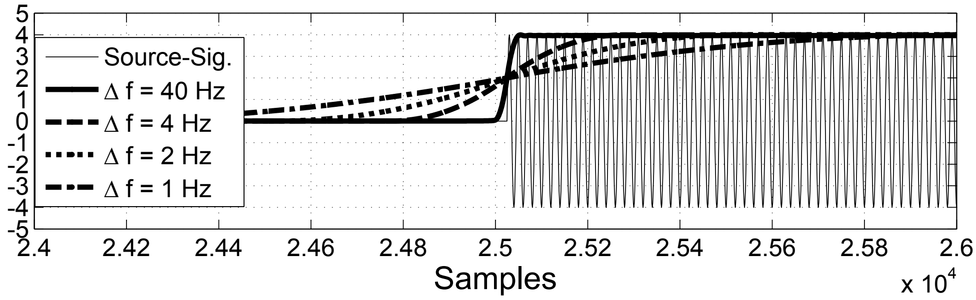

Figure 8.13: Extraction of a spotting spectral component with different spectral resolution, Δ f.

caused by a flag-like oscillation of the sheet of transversal vorticity shed from the rear edge of the body free-end, and approximately lying along the downstream boundary of the recirculation region in the central part of the near wake.

Let consider a velocity signal characterized by the presence of a single main spectral component, for instance the one connected to alternate vortex shedding at St ≈ 0.16. This is the case of the signal acquired aside the wake in correspondence of the point $x/w = 4$, $y/w = 1.5$, $z/h = 0.3$. The power spectrum of this signal is reported in figure 8.15. The velocity signals are acquired with a sampling frequency of 2 kHz and they consist of 2^{16} samples.

For this signal the POD is performed by generating snapshots composed by 1001 samples, indeed by considering a frequency resolution of about 2 Hz. From a preliminary analysis, a number of 4000 snapshots can be considered sufficiently high in order to separate the main spectral components from other random effects. The POD eigenvalues that represent the energy associated to the respective POD modes are reported

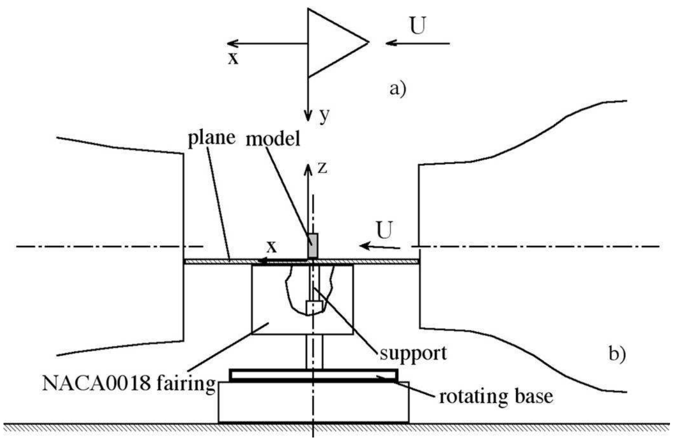

Figure 8.14: Sketch of the experimental setup: **a** model orientation; **b** test layout.

in figure 8.16.

For the sake of brevity, instead of showing the power spectra of the evaluated POD modes, the ones related to the extracted spectral components are directly illustrated. In figure 8.17a the power spectrum of the spectral component connected to the POD mode 1 shows that it corresponds to a narrow-band contribution with a mean Strouhal number of 0.162 (evaluated through the application of the Hilbert transform to the extracted spectral component), in good agreement with the findings of Buresti & Iungo (2009), where an analogous result was found by using the procedure based on wavelet and Hilbert transforms proposed by Buresti *et al.* (2004). In that work this result was gained by applying the wavelet transform to the signal, and through a careful analysis of the wavelet energy map a band-pass filter was applied after a preliminary sensitivity evaluation of the central frequency and amplitude of the filter. Subsequently, by applying the inverse wavelet transform to the selected spectral range, the spectral component of interest is obtained. With the POD procedure no preliminary spectral analysis is required and, through an easy eigenvalue problem and a convolution, the spectral component of interest is directly obtained. Beside the reduction of the required computational cost, the POD procedure is suitable for a complete automated implementation of a procedure for principal component detection and extraction since no action of the users are needed, except for choosing as input parameter the frequency resolution required for the spectral analysis.

Since the main spectral component is extracted, the remaining components can be evaluated from the residual signals calculated by subtracting from the source-signal the extracted component related to the POD mode 1. If the POD mode 3 is considered, as example, (even POD modes are not considered because represent the same spectral component of their respective odd POD modes) the spectral component whose power

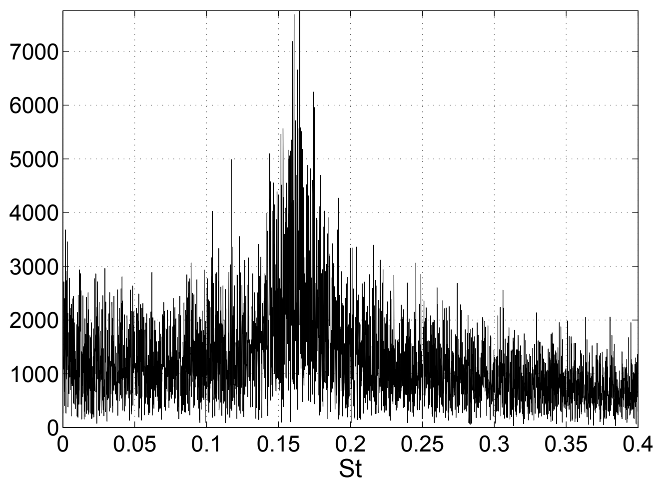

Figure 8.15: Power spectrum of the hot-wire anemometer signal acquired at $x/w = 4$, $y/w = 1.5$, $z/h = 0.3$.

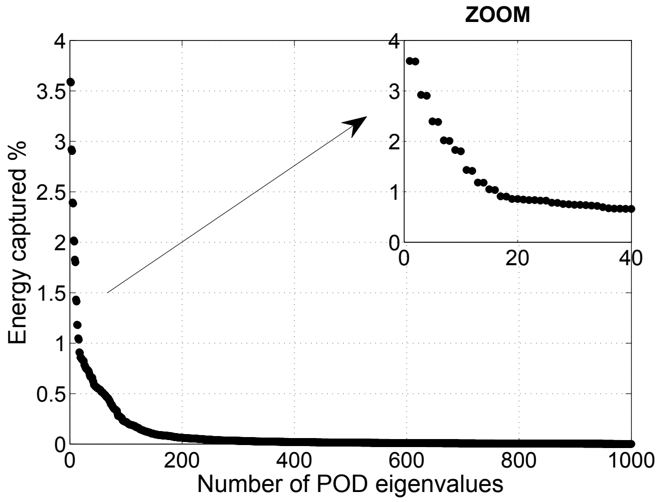

Figure 8.16: POD eigenvalues evaluated for the hot-wire anemometer signal acquired at $x/w = 4$, $y/w = 1.5$, $z/h = 0.3$.

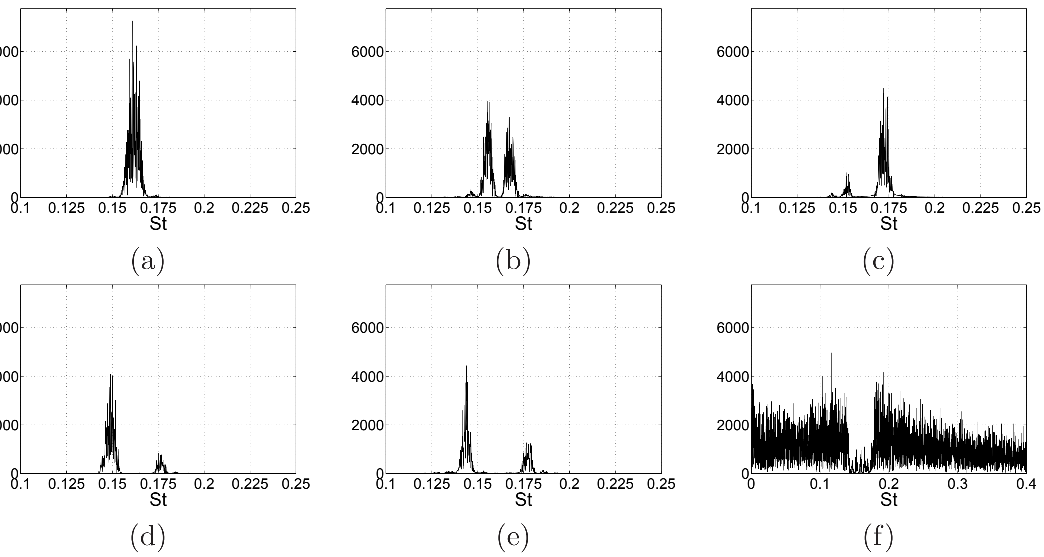

Figure 8.17: Power spectra of the components extracted from the hot-wire anemometer signal acquired at $x/w = 4$, $y/w = 1.5$, $z/h = 0.3$: **a** component related to the POD mode 1; **b** component related to the POD mode 3; **c** component related to the POD mode 5; **d** component related to the POD mode 7; **e** component related to the POD mode 9; **f** residual signal.

spectrum is reported in figure 8.17b can be obtained. It corresponds to a modulation with a frequency of about St ≈ 0.006. If this spectral component is added to the one corresponding to the POD mode 1, further characteristics of the process, viz. the alter-

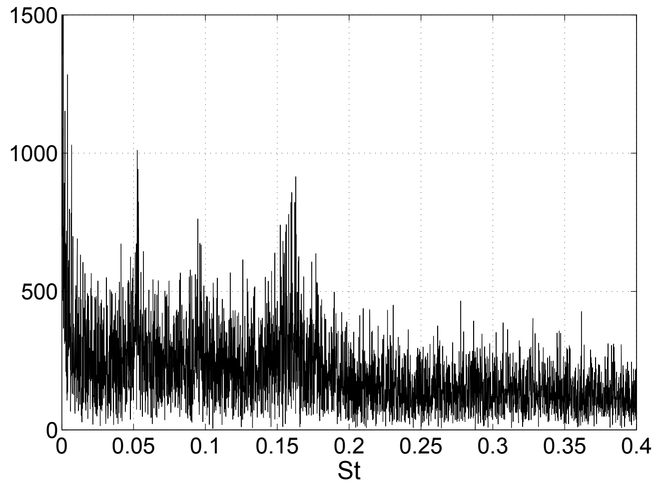

Figure 8.18: Power spectrum of the hot-wire anemometer signal acquired at $x/w = 4$, $y/w = 1$, $z/h = 0.9$.

nate vortex shedding, can be evaluated. Analogously, other components characterized by a decreasing energy, thus significance, can be evaluated like the ones reported in Figs. 8.17c, d and e. Finally, the power spectrum of the residual signal obtained after extracting the components related to the POD modes 1, 3, 5, 7 and 9, is reported in figure 8.17f; if compared to the one of the source-signal in figure 8.15 this demonstrates that the core of the fluctuating energy of the signal is extracted through these POD modes.

The time-frequency analysis of the hot-wire anemometer signal acquired at $x/w = 4$, $y/w = 1$ and $z/h = 0.9$ is also performed. The power spectrum of this signal, reported in figure 8.18, show that no evident dominant spectral components are present in the flow fluctuations of the considered signal.

The POD procedure is applied to the signal obtained through a high-pass filtering with a cut-off frequency St $= 0.03$ in order to remove the typical flow fluctuations present in the wind tunnel freestream. This time-frequency analysis is carried out by using a number of samples for each snapshot equal to 1001, *i.e.* a frequency resolution of about 2 Hz is used, and a total number of snapshots equal to 8000. The obtained first 100 POD eigenvalues are reported in figure 8.19.

Starting with the extraction of the spectral component related to the most energetic POD mode, viz. POD mode 1, it is seen from its power spectrum, reported in figure 8.20a, that represents a narrow-band spectral component with a mean Strouhal number of 0.053. As suggested in Buresti & Iungo (2009), this spectral component is connected to the dynamics of a couple of axial vortices detaching over the model free-end and, indeed, being this velocity signal acquired at a relative high position, this phenomenon results to be the most energetic one.

Moving to the extraction of the spectral component connected to the POD mode 3,

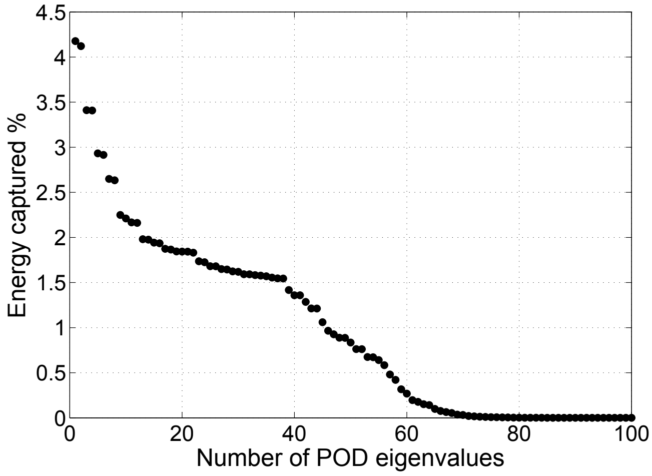

Figure 8.19: First 100 POD eigenvalues evaluated for the hot-wire anemometer signal acquired at $x/w = 4$, $y/w = 1$, $z/h = 0.9$.

the corresponding power spectrum (figure 8.20b) shows that this component is clearly due to the alternate vortex shedding being characterized by a mean Strouhal number of 0.161. The following analyzed POD mode, POD mode 5, represents a further contribution to the spectral component due to alternate vortex shedding and, thus, it will be considered just for obtaining further information regarding this phenomenon.

Interestingly, the spectral component related to the POD mode 7 is characterized by a mean Strouhal number of 0.096, indicating that it is connected to the oscillations of the shear layer bounding the recirculation area located just behind the model.

The analysis of the present signal well highlights the optimality of the POD procedure, that is it allows to detect easily the main phenomena that generate the flow fluctuations present in the signals. Subsequently, the obtained spectral components can be characterized statistically and in frequency by using, for instance, the Hilbert transform. Finally, in figure 8.21 a reconstructed signal obtained by adding the three spectral components connected to the POD modes 1, 3 and 7 is compared to the source-signal showing that a simplified signal can now be investigated in order to gain information on the originating phenomena.

8.3 Conclusions

A procedure based on Proper Orthogonal Decomposition (POD) for detection and extraction of principal components present in one-dimensional fluid dynamics signals has been presented. Time-series representing the source-signal is divided into different time-portions (snapshots) uniformly distributed along the signal time-length and composed by the same number of samples. POD is then applied to these snapshots.

The extraction of the principal component corresponding to a certain POD mode is

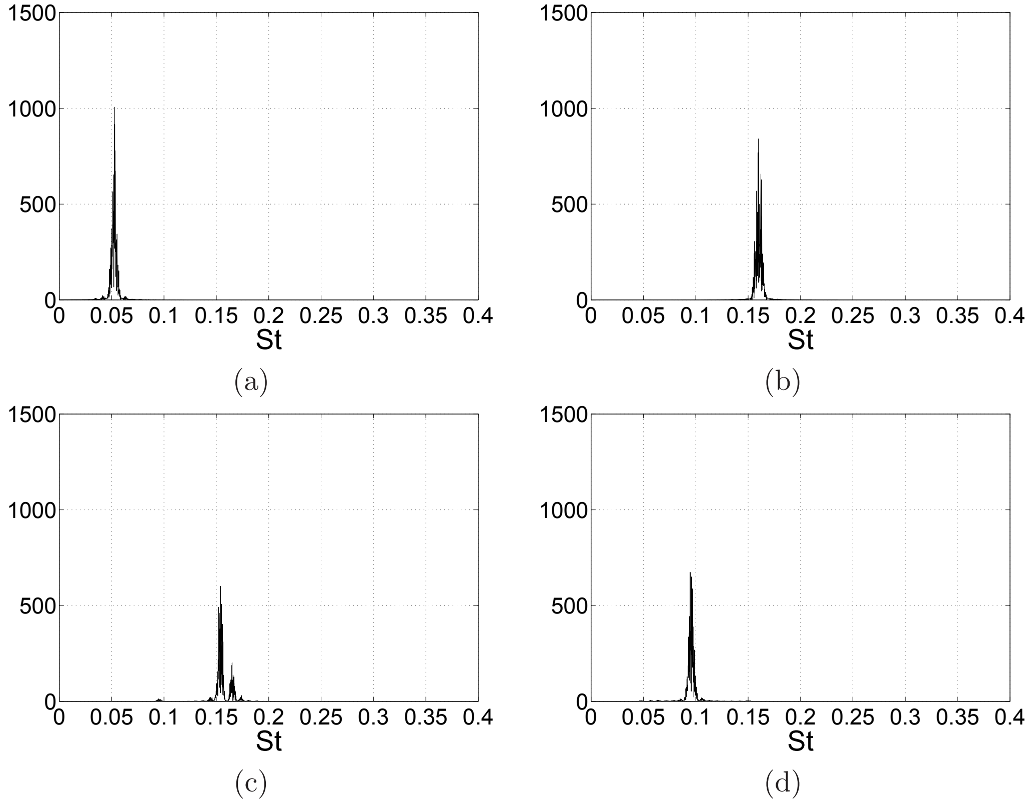

Figure 8.20: Power spectra of the components extracted from the hot-wire anemometer signal acquired at $x/w = 4$, $y/w = 1$, $z/h = 0.9$: **a** component related to the POD mode 1; **b** component related to the POD mode 3; **c** component related to the POD mode 5; **d** component related to the POD mode 7.

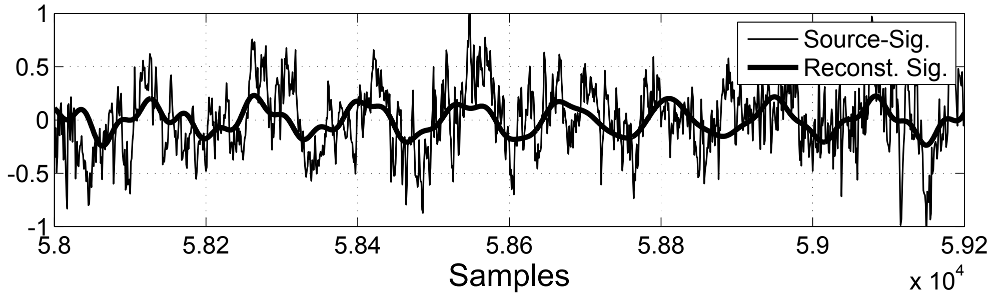

Figure 8.21: Reconstruction of the signal acquired at $x/w = 4$, $y/w = 1$, $z/h = 0.9$ by only using the POD modes 1, 3 and 7.

performed trough the convolution of the source-signal with the considered POD mode, suitably manipulated. The characterization of the extracted spectral component might be then performed by using the Hilbert transform in order to evaluate the instantaneous amplitude and frequency of the evaluated spectral component.

The procedure based on POD for principal component detection and extraction has been first assessed for computer-generated signals, like signals composed by different spectral components, with amplitude modulation, with time-varying amplitude and spotting amplitude. Subsequently, the procedure has been applied for hot-wire anemometer signals acquired in proximity of the wake generated from a triangular prism with finite height and placed with a vertical edge against the incoming flow. Flow fluctuations due to the dynamics of different vorticity structures can be easily characterized through the analysis of the most energetic POD modes.

One of the main advantages of this technique for time-frequency analysis of one-dimensional signals is that no detection of the dominant spectral components and no setting of the parameters necessary for the component filtering are required. Thus, a preliminary spectral analysis of the source signal is not needed. In the POD procedure the only input is the required frequency resolution needed to discern the different spectral components. The POD produces the most typical realizations of the process sorted by their significance. All these features allow to implement a procedure completely automated for principal component detection and extraction, and the fluctuations of a signal can be considered adequately characterized when a certain fluctuating energy is extracted or when the main spectral components are captured.

Conclusions

In this work we developed and analyzed the capability of some tools and methodologies for circumventing problematics present in the control of a flow over bluff bodies. All the tools developed are applied to the same test configuration, a flow past a confined square cylinder, but they can easily be extended to more complicated configurations.
In a closed-loop control strategy, two main issues are involved: the present state estimation of the flow and the optimization of the control parameters. The tools proposed in this work are based on low order modeling of the flow through Proper Orthogonal Decomposition. The dynamical reduced order models are obtained by projection of the Navier-Stokes equations onto the low dimensional subspace spanned by the empirical POD functions derived from a database of given solutions. The POD model reduction is widely used in fluid dynamics and for flow control. The main drawback of such low order modeling is that the resulted models are not robust to parameter variations and the POD basis is not optimal for representing flows that do not belong to the database.

Different parameter variations can be considered: *i.e.* time advancement outside the POD database for non-periodic flows, Reynolds numbers evolution, control input variation for actuated flows.

The development of an accurate and stable low order model is carried out through a *calibration* technique. The model is fitted to reproduce the reference solutions by minimizing the norm of its residual. The computational cost necessary for calibrating the reduced order model is negligible, consisting in solving low-dimensional regularized linear systems.

The construction of such an accurate model allowed us to devise a non-linear observer. The aim is to recover the entire flow fields starting from a limited number of measurements. Thus, the non-linear observer consists in coupling a dynamical reduced model with the information given by the measurements. This method provides a good estimation of the actual state of the flow. The reduced Poisson model is used within the non-linear observer in order to give an estimation of quantities of engineering interest such as the lift and drag coefficients.

Applications are carried out with several sensor configurations and at different Reynolds numbers: at $Re = 150$ where the flow is completely two-dimensional and for a three-dimensional flow at $Re = 300$ where complicated patterns are present. Even for the complicated three-dimensional flow the reconstruction of the velocity fields is sufficiently accurate. The major limitation is given by the ability of the POD basis to represent complicated flow fields that lie outside the database. A POD pressure model based on the projection of the Poisson equations for incompressible flows is also developed. The proposed method outperforms the existing linear techniques and seems viable for real-time control application. Indeed, the non-linear observer can be used for instance to reconstruct the state of a flow starting from some realistic measurements used in real feedback configurations, such as pressure sensors placed on the surface of the body.

Then, the study of a procedure, based on heterogeneous calibration, aimed at building a low order model which is robust to parameter variation is carried out. The aim was to devise an adaptive model useful for control purposes. Indeed, for a non-linear observer for control or for a control optimization via reduced order modeling, the employed model has to be accurate and especially robust to control input variation. The dependence on the control is integrated in the low order model for a precomputed control law as well as for a feedback control strategy. The controlled model is built and then *calibrated* by using an extended POD basis that includes several dynamics obtained with different control parameters. In this way, the low order model is improved in stability and accuracy on all the dynamics that belong to the database, due to the multiple calibration, and at the same time in robustness to the parameter variation, due to the fact that the POD basis is enriched by several dynamics. The technique is applied to two-dimensional flows at $Re = 60$ and $Re = 150$ and, for the considered cases, the presented results show that the models are able to predict dynamical behaviors that are far, in terms of an energy norm, from the cases included in the database. Moreover, the results show that by passing from a model built with one dynamic to a model built simply on two dynamics the behavior is considerably improved.
However, the results suggest that an optimal sampling of the parameter subspace would certainly be useful. Indeed, there can be cases where a model obtained with a smaller number of parameters is more robust than a model obtained with a higher number.

For this reason we studied a method to sample, in an optimal manner, the subspace of the parameters. In this way, given the desired dimension of the database, an efficient choice of the input parameters used to build a POD model is possible. Thus, we developed a "one-shot" method (called Frozen Centroidal Voronoi Tessellation) that consists in sampling the points corresponding to the centroids of a Voronoi tessellation, where the density function is the Navier-Stokes residual predicted by an initial low order model. We showed that the residual of the Navier-Stokes equations is a good estimator of the approximation error, this enables us to use it as a density function in the FCVT. Therefore, the sampling points are concentrated where the residual is highest, *i.e.* where the error of the low order model is large. The method is based on the Greedy idea, where new sampling points are iteratively placed in the maximum of the approximation error of the POD basis. The main drawback is that the computational costs of the Greedy method are huge, due to the fact that to compute the approximation error numerical simulations are needed. Conversely, by using the residual predicted by the low order model, the computational costs are negligible. Indeed, the main computation is simply the integration of the model with variations of the input parameters. The technique is applied for a Reynolds adaptive model, but it can be simply extended to the other

kind of adaptive models. In particular the optimal sampling can be applied to high dimensional spaces of control parameters.
In order to compute the Navier-Stokes residual the POD basis is derived by using the global snapshots, formed by velocity and pressure. However, if the low order model is achieved only for the velocity, through a reduced Poisson model the pressure field can be evaluated as well as the Navier-Stokes residual.
We tested the technique in a range of Reynolds numbers between $Re = 40$ and $Re = 180$, where the flow is completely two-dimensional. The obtained results showed that the FCVT provides an optimal sampling of the subspace and the low order model is robust over all the considered range.
Thus, a control optimization procedure, as in Weller *et al.* (2009), could be performed starting from a robust model built by sampling the parameter subspace with the FCVT method and without updating (or updating only a few times) the POD basis during the optimization.

However, a non-linear optimization procedure, as shown in Weller *et al.* (2009) can present a drawback. Indeed, for high Reynolds numbers, during the optimization of control parameters, other modes in addition to the modes associated to the primary instability can become unstable. For this, finally, we developed a linearized low order model of controlled transient flows. The model is used to perform a linear stability analysis of transient flows obtained by a non-linear simulation. The accurate results show that the technique can be useful to check the effect of a control actuation on the actual spectrum of the dynamical system when a linearization of the original system is inaccessible. The low order model is able to represent both the spectrum of the actual linearized system and the physical global modes associated to the shedding instability. Thus, through the linearized low order model, it is possible to observe the effect of the control actuation on the spatial structures of the global modes, *i.e.* how the global modes are modified by the control input.

Finally, for future perspectives, the developed techniques can be used in control applications. Indeed, the non-linear observer can be integrated in real-time applications together with the use of a robust low order model. In this way, the accuracy of the state observation can be guaranteed even for large parameter variations.
Furthermore, a low order model robust to parameter variation, built by using the developed techniques, can be used both in a complete control optimization and in real-time control applications, for instance by performing short control optimizations when the observations record an evolution of the state of the flow.

Conclusions

Dans ce travail nous avons élaboré et analysé la capacité de certains outils pour éviter les problématiques présentes dans le contrôle d'un écoulement autour de corps épais. Tous les outils développés sont appliqués à la même configuration test, à savoir un écoulement confiné autour d'un cylindre carré. Ces outils peuvent cependant facilement être étendus à des configurations plus complexes.
Dans une stratégie de contrôle en boucle fermée, deux questions principales sont posées : l'estimation de l'état réel de l'écoulement et l'optimisation des paramètres de contrôle. Les outils proposés dans ce mémoire sont basés sur la modélisation réduite de l'écoulement à travers la Décomposition Orthogonal aux valeurs propres (POD). Les modèles dynamiques réduits sont obtenus par projection des équations de Navier-Stokes sur le sous-espace de dimension réduite généré par les fonctions empiriques POD calculées à partir d'une base de données de solutions precalculées. La réduction de modèle POD est largement utilisé en méchanique des fluides et en le contrôle d'écoulement. Le principal inconvénient de la modélisation d'ordre réduit est que les modèles obtenus ne sont pas robustes aux variations des paramètres d'entrée du système et la base POD n'est pas optimale pour représenter les écoulements qui ne font pas partie de la base de données.

Différentes variations de paramètres peuvent être envisagées : *i.e.* l'avancement du temps en dehors de la base de données POD pour des écoulements non périodiques, l'évolution du nombre de Reynolds, la variation des param de contrôle pour écoulements actionnés.

Le développement d'un modèle réduit précis et stable est effectué par une technique de *calibration*. Le modèle est ajusté sur les solutions de référence en minimisant la norme de son résidu. Le coût de calcul nécessaire pour calibrer le modèle d'ordre réduit est négligeable, puisqu'il consiste uniquement en la résolution de systèmes linéaires régularisés de petites dimensions.

La construction d'un tel modèle precis a nous permis de créer un observateur non linéaire. L'objectif est de reconstruire le champ entier de l'écoulement à partir d'un nombre limité de mesures. Ainsi, l'observateur non linéaire consiste à coupler un modèle dynamique réduit avec les informations données par les mesures. Cette méthode fournit une bonne estimation de l'état réel de l'écoulement. Les applications sont réalisées avec plusieurs configurations des capteurs et à différents nombres de Reynolds : à $Re = 150$ (écoulement est à deux dimensions) et à $Re = 300$ (écoulement à trois dimensions). Même pour l'écoulement à trois dimensions qui est relativement complexe, la reconstruction des champs de vitesse est précise. La principale limitation est donnée par la capacité de la base POD à représenter les champs d'écoulement placés en dehors de la base de données. Un modèle POD pour la pression basé sur la projection des équations de Poisson pour des écoulements incompressibles est également développé. Le modèle réduit de Poisson est utilisé avec l'observateur non linéaire afin de donner une estimation de quantités d'intérêt industriel, comme le coefficient de portance et de traînée. La méthode proposée surpasse les techniques linéaires existantes et semble viable pour applications de contrôle en temps réel. En effet, l'observateur non linéaire peut être utilisé par exemple pour reconstruire l'état d'un écoulement à partir de quelques mesures réalistes utilisés dans des applications de feedback réelles, comme des capteurs de pression placés sur la surface du corps.

Ensuite, l'étude d'une procédure visant à construire un modèle d'ordre réduit, qui est robuste à la variation des paramètres, est effectuée. L'objectif était de développer un modèle adaptif utile pour applications de contrôle. En effet, pour un observateur non linéaire pour le contrôle ou pour une optimisation du contrôle par modélisation d'ordre réduit, le modèle utilisé doit être précis et particulièrement robuste à les variations des paramètres de contrôle. La dépendance de l'actuation est intégrée dans le modèle d'ordre réduit pour une loi de contrôle précalculée ainsi que pour une stratégie de contrôle en rétroaction. Le modèle avec le contrôle est construit et *calibré* en utilisant un base POD élargie qui inclut plusieurs dynamiques obtenus avec différents paramètres de contrôle. De cette façon, le modèle réduit est amélioré en stabilité et précision sur toute les dynamiques qui appartiennent à la base de données, due à la calibration multiple, et en même temps en robustesse à la variation des paramètres, en raison du fait que la base POD est enrichie par plusieurs dynamiques. La technique est appliquée à des écoulements à deux dimensions à $Re = 60$ et $Re = 150$ et, pour les cas considérés, les résultats présentés montrent que les modèles sont capables de prédire les comportements dynamiques qui sont loin, en termes de norme d'énergie, des cas inclus dans la base de données. En outre, les résultats indiquent que, en passant d'un modèle construit avec une dynamique à un modèle construit sur deux dynamiques, le comportement dynamique est considérablement amélioré.
Toutefois, les résultats suggèrent que l'échantillonnage optimal du sous-espace des paramètres est nécessaire. En effet, ils peuvent exister des cas où un modèle obtenu avec un petit nombre de paramètres est plus robuste qu'un modèle obtenu avec un nombre plus élevé.

Pour cette raison, nous avons étudié une méthode d'échantillonnage optimale du sous-espace des paramètres. De cette façon, compte tenu de la dimension désirée de la base, un choix efficace des paramètres à utiliser peut être effectué pour construire un modèle POD. Ainsi, nous avons développé une méthode "one-shot" (appelée Frozen Centroidal Voronoi tessellation) qui consiste dans l'échantillonnage des points correspondant aux centres de masse d'un pavage de Voronoi, où la fonction de densité est le résidu de l'opérateur de Navier-Stokes évalué avec la solution calculée à partir du modèle réduit initial. Nous avons montré que le résidu des équations de Navier-Stokes est un bon estimateur de l'erreur d'approximation, ce qui nous permet de l'utiliser comme une fonction densité dans la FCVT. Par conséquent, les points d'échantillonnage se con-

centrent là où le résidu est le plus élevé, *i.e.* où l'erreur du modèle d'ordre réduit est grande. La méthode est basée sur l'idée de la méthode Greedy, où de nouveaux points d'échantillonnage sont itérativement placé au maximum de l'erreur d'approximation de la base POD. Le principal inconvénient est que les coûts de calcul de la méthode Greedy sont importants, en raison du fait que pour calculer l'erreur d'approximation des simulations numériques sont nécessaires. Inversement, en utilisant les résidus prédits par le modèle d'ordre réduit les coûts de calcul sont négligeables. En effet, le calcul principal est simplement l'intégration du modèle réduit avec des variations des paramètres d'entrée. La technique est appliquée à un modèle adaptatif à la variation du nombre de Reynolds, mais peut être simplement étendue à autres types de modèles adaptatifs. En particulier, l'échantillonnage optimal peut être appliqué à des espaces de haute dimension (paramètres de contrôle).
Afin de calculer le residu des équations de Navier-Stokes, la base POD est obtenu en utilisant les champs complets, formés par la vitesse et la pression. Toutefois, si le modèle réduit est obtenu à partir seulement de la vitesse, grâce à un modèle réduit de Poisson, le champ de pression peut être évalué et donc le residu des équations de Navier-Stokes. Nous avons testé la technique dans une gamme de nombres de Reynolds entre $Re = 40$ et $Re = 180$, où l'écoulement est à deux dimensions. Les résultats obtenus ont montré que la FCVT fournit un échantillonnage optimal du sous-espace et le modèle réduit est robuste sur tout l'interval consideré.
Ainsi, une procédure d'optimisation du contrôle, comme dans Weller *et al.* (2009), pourrait être effectuée à partir d'un modèle robuste construit par échantillonnage du sous-espace des paramètres avec la méthode FCVT et sans que la base POD soit mise à jour (ou mise à jour un nombre limité de fois) pendant l'optimisation.

Toutefois, une procédure d'optimisation non-linéaire, comme decrite dans Weller *et al.* (2009) peut présenter un inconvénient. En effet, pour des nombres de Reynolds élevés, pendant l'optimisation des paramètres de contrôle, des autres modes que ceux-associés à l'instabilité primaire peuvent devenir instables. Pour cette raison, nous avons finalement développé un modèle réduit linéarisé du transitoire d'écoulements contrôlés. Le modèle est utilisé pour effectuer une analyse linéaire de stabilité des écoulements transitoires obtenus par simulation d'un code non-linéaire. Les résultats sont précis et montrent que la technique peut être utile pour vérifier l'effet d'une action de contrôle sur le spectre du système dynamique réel, quand une linéarisation du système original n'est pas disponible. Le modèle réduit est capable de représenter en même temps le spectre du système réel linéarisé et les modes globaux physiques associées à l'instabilité du sillage. Ainsi, avec le modèle linéarisé d'ordre réduit il est possible d'observer l'effet du contrôle sur les structures spatiales des modes globaux, *i.e.* comment les modes globaux sont modifiés par l'action du contrôle.

Enfin, les techniques développées pourraient être utilisées dans des applications de contrôle. En effet, l'observateur non linéaire peut être intégré dans des applications en temps réel ainsi que un modèle d'ordre réduit robuste. De cette manière, la précision de

l'observation de l'état peut être garantie même pour des variations des paramètres.
En outre, un modèle réduit robuste aux variations des paramètres construit en utilisant les techniques developpées, peut être utilisé et dans une optimisation complête de contrôle et dans des applications de contrôle en temps réel, par exemple en effectuant petits optimisations de contrôle lorsque les observations enregistrent une évolution de l'état de l'écoulement.

List of publications

International Journals

LOMBARDI E., BERGMANN M., CAMARRI S., IOLLO A. Low-order models: optimal sampling and linearized control strategies. *Notes on Numerical Fluid Mechanics and Multidisciplinary Design (NNFM)*, To appear.

WELLER J., LOMBARDI E., BERGMANN M., IOLLO A.(2009) Numerical methods for low-order modeling of fluid flows based on POD. *International Journal for Numerical Methods in Fluids*, In Press.

WELLER J., LOMBARDI E., IOLLO A.(2008) Robust model identification of actuated vortex wakes. *Physica D: Nonlinear Phenomena*, **238**, p. 416-427.

M. BUFFONI, S. CAMARRI, A. IOLLO, E. LOMBARDI, M.V. SALVETTI. (2008) A non-linear observer for unsteady three-dimensional flows. *Journal of Computational Physics*, **227**,p. 2626-2643.

Research Reports

LOMBARDI E., BERGMANN M., CAMARRI S., IOLLO A.(2009) Low-order models : optimal sampling and linearized control strategies. INRIA Research Report **RR-7092**.
`http://hal.inria.fr/inria-00430410`

WELLER J., LOMBARDI E., BERGMANN M., IOLLO A.(2009) Numerical methods for low-order modeling of fluid flows based on POD. INRIA Research Report **RR-6758**.
`http://hal.inria.fr/inria-00345184`

WELLER J., LOMBARDI E., IOLLO A.(2008) Robust model identification of actuated vortex wakes. INRIA Research Report **RR-6559**.
`http://hal.inria.fr/inria-00288089`

BUFFONI M., CAMARRI S., IOLLO A., LOMBARDI E., SALVETTI M.V. (2007) A non-linear observer for unsteady three-dimensional flows. INRIA Research Report **RR-6117**.
`https://hal.inria.fr/inria-00129332`

http://arxiv.org/pdf/math.OC/0702169

Conferences and Workshops

BERGMANN M., LOMBARDI E., IOLLO A. (2009) Amélioration de la robustesse des bases POD. *19h Congrès FranÃ§ais de Mécanique* Marseille, France. August $24-28$.WELLER J., LOMBARDI E., IOLLO A. (2008) Robust reduced order model of a wake controlled by synthetic jets. *7th ERCOFTAC SIG33 Workshop - Open issues in transition and flow control* Santa Margherita Ligure, Italy. October $16-18$.

LOMBARDI E., GABBANI M., BUFFONI M., SALVETTI M.V. AND IOLLO A. (2008) On the capabilities of POD based estimation techniques. *7th EUROMECH Fluid Mechanics Conference* Manchester, England. September $14-18$.

WELLER J., LOMBARDI E., IOLLO A. (2008) Modèle reduit pour un écoulement contrôllé par jets synthétiques. *Congrés national d'analyse numérique (CANUM)* Saint Jean de Monts, Vendée, France. May $26-30$.

LOMBARDI E., BUFFONI M., WELLER J.,IOLLO A. (2008) A POD based non-linear observer for unsteady flows *Industrial application of low order models based on POD* Bordeaux, France. March - April $31-2$.

WELLER J., LOMBARDI E., IOLLO A. (2008) An accurate reduced order model for unsteady flows controlled by synthetic jets. *Industrial application of low order models based on POD* Bordeaux, France. March - April $31-2$.

BERGMANN M., BUFFONI M., IOLLO A., LOMBARDI E., WELLER J. (2007) Simulation, estimation et contrôle par modèles reduits. *Journée sur l'estimation et le contrôle des écoulements aerodynamiques (ECEA)* Toulouse, France. November 09.

LOMBARDI E., BUFFONI M., IOLLO A. (2007) Un observateur non lineaire pour des écoulements instationnaires. *Congrès national de mathémathiques appliquées et industrielles - SMAI* Praz sur Arly, France. June $04-08$.

BUFFONI M., CAMARRI S., IOLLO A., LOMBARDI E., SALVETTI M.V. (2006) Modelling and identification of an unsteady 3D flow by an accurate reduced order model. *European Drag Reduction and Flow Control Meeting* Ischia, Italy. April $10-13$.

Bibliography

Abarbanel, H. D. I., Brown, R., Sidorowich, J. J. & Tsimring, L. S. 1993 The analysis of observed chaotic data in physical systems. *Rev. Mod. Phys.* **65** (4), 1331–1392.

Adrian, R. J. 1977 On the role of conditional averages in turbulent theory. In *Turbulence in Liquids: Proceedings of the 4th Biennial Symposium on Turbulence in Liquids* (ed. G. Patteson & J. Zakin), pp. 322–332. Princeton: Science Press.

Adrian, R. J. 1979 Conditional eddies in isotropic turbulence. *Physics of Fluids* **22**, 2065–2070.

Afanasiev, K. & Hinze, M. 2001 Adaptive control of a wake flow using proper orthogonal decomposition. In *Shape Optimization and Optimal Design*, *Lecture Notes in Pure and Applied Mathematics*, vol. 216, pp. 317–332. Marcel Dekker.

Ahuja, S. & Rowley, C. W. 2008 Low-dimensional models for feedback stabilization of unstable steady states. In *Proceedings of the 46th AIAA Aerospace Sciences Meeting and Exhibit*. AIAA Paper 2008-553.

Akcelik, V., Bielak, J., Biros, G., Epanomeritakis, I., Fernandez, A., Ghattas, O., Kim, E. J., Lopez, J., O'Hallaron, D., Tu, T. & Urbanic, J. 2003 High resolution forward and inverse earthquake modeling on terascale computers. In *SC '03: Proceedings of the 2003 ACM/IEEE conference on Supercomputing*, p. 52. Washington, DC, USA: IEEE Computer Society.

Antoulas, A. C., Sorensen, D. C. & Gugercin, S. 2001 A survey of model reduction methods for large-scale systems. *Contemp. Math.* **280**, 193–213.

Aubry, N., Holmes, P., Lumley, J. L. & Stone, E. 1988 The dynamics of coherent structures in the wall region of a turbulent boundary layer. *Journal of Fluid Mechanics* **192**, 115–173.

Bakewell, H. P. & Lumley, J. L. 1967 Viscous sublayer and adjacent wall region in turbulent pipe flow. *Phys. Fluids* **10**, 1880–1889.

Bendat, J. S. & Piersol, A. G. 1986 *Random data: analysis and measurement procedures*, 2nd edn. New York: Wiley.

BERGMANN, M. 2004 Optimisation aérodynamique par réduction de modèle POD et contrôle optimal. Application au sillage laminaire d'un cylindre circulaire. In *PhD Thesis*. Institut national polytechnique de Lorraine.

BERGMANN, M. & CORDIER, L. 2008 Optimal control of the cylinder wake in the laminar regime by trust-region methods and POD reduced-order models. *J. Comput. Phys.* **227** (16), 7813–7840.

BERGMANN, M., CORDIER, L. & J.-P.BRANCHER 2005 Optimal rotary control of the cylinder wake using proper orthogonal decomposition reduced-order model. *Physics of Fluids* **17**, 097101.

BEWLEY, T. R., MOIN, P. & TEMAM, R. 2001 Dns-based predictive control of turbulence: an optimal benchmark for feedback algorithms. *Journal of Fluid Mechanics* **447** (-1), 179–225.

BONNET, J., COLE, D., DELVILLE, J., GLAUSER, M. & UKEILEY, L. 1994 Stochastic estimation and Proper Orthogonal Decomposition: complementary techniques for identifying structures. *Experiments in fluids* **17**, 307–314.

BRETETON, G. 1992 Stochastic estimation as a statistical tool for approximating turbulent conditional averages. *Physics of Fluids (A)* **4**, 2046–2054.

BREUER, M., BERNSDORF, J., ZEISER, T. & DURST, F. 2000 Accurate computations of the laminar flow past a square cylinder based on two different methods: lattice-Boltzmann and finite-volume. *International Journal Heat and Fluid Flow* **21**, 186–196.

BUFFONI, M., CAMARRI, S., IOLLO, A. & SALVETTI, M. 2006 Low-dimensional modelling of a confined three-dimensional wake flow. *Journal of Fluid Mechanics* **569**, 141–150.

BUI-THANH, T., WILLCOX, K. & GHATTAS, O. 2008 Model reduction for large-scale systems with high-dimensional parametric input space. *SIAM Journal on Scientific Computing* **30(6)**, 3270–3288.

BURESTI, G. & IUNGO, G. V. 2009 Experimental investigation on the connection between flow fluctuations and vorticity dynamics in the near wake of a triangular prism placed vertivally on a plane. *J. Wind Eng. Ind. Aerodyn.* Doi:10.1016/j.jweia.2009.10.004.

BURESTI, G., LOMBARDI, G. & BELLAZZINI, J. 2004 On the analysis of fluctuating velocity signals through methods based on the wavelet and Hilbert transforms. *Chaos, Solitons and Fractals* **20**, 149–158.

BURKARDT, J., GUNZBURGER, M. D. & LEE, H.-C. 2004 Centroidal Voronoi Tessellation-Based Reduced-Order Modeling of Complex Systems. *Tech. Rep.*. Florida State University.

Burkardt, J., Gunzburger, M. D. & Lee, H.-C. 2007 Centroidal Voronoi Tessellation-Based Reduced-Order Modeling of Complex Systems. *SIAM J. Sci Comp* **28** (2), 459–484.

Camarri, S. & Giannetti, F. 2007 On the inversion of the Kármán street in the wake of a confined square cylinder. *J. Fluid Mech.* **574**, 169–178.

Camarri, S., Salvetti, M. V., Koobus, B. & Dervieux, A. 2004 A low-diffusion MUSCL scheme for LES on unstructured grids. *Comp. Fluids* **33**, 1101–1129.

Canuto, C., Hussaini, M. Y., Quarteroni, A. & Zang, T. A. 1988 *Spectral Methods in Fluid Dynamics*. Berlin: Springer-Verlag.

Cao, Y., Zhu, J., Navon, I. & Luo, Z. 2007 A reduced order approach to four-dimensional variational data assimilation using proper orthogonal decomposition .

Carmona, R., Hwang, W.-L. & Torresani, B. 1998 *Practical time-frequency analysis*. San Diego, CA: Academic Press.

Chiew, F. H. S., Peel, M. C., Amirthanathan, G. E. & Pegram, G. G. S. 2005 Identification of oscillations in historical global streamflow data using empirical mode decomposition. *Seventh IAHS Scient. Assembly* pp. 53–62.

Choi, H., Jeon, W.-P. & Kim, J. 2008 Control of flow over a bluff body. *Annual Review of Fluid Mechanics* **40**, 113–139.

Cohen, K., Siegel, S. & McLaughlin, T. 2006 A heuristic approach to effective sensor placement for modeling of a cylinder wake. *Comp. Fluids* **35**, 103–120.

Cohen, K., Siegel, S., Wetlesen, D., Cameron, J. & Sick, A. 2004 Effective sensor placements for the estimation of proper orthogonal decomposition mode coefficients in von Kármán vortex street. *Journal of Vibration Control* **10**, 1857–1880.

Cordier, L. & Bergmann, M. 2002 Proper Orthogonal Decomposition: an overview. In *Lecture series 2002-04 on post-processing of experimental and numerical data*. Von Kármán Institute for Fluid Dynamics.

Coughlin, K. T. & Tung, K. K. 2004 11-year solar cycle in the stratosphere extracted by the empirical mode decomposition method. *Advances in Space Research* **34**, 323–329.

Couplet, M., Basdevant, C. & Sagaut, P. 2005 Calibrated reduced-order POD-Galerkin system for fluid flow modelling. *J. Comput. Phys.* **207** (1), 192–220.

Daescu, D. & Navon, I. 2008 A dual-weighted approach to order reduction in 4dvar data assimilation. *Mon. Wea. Rev.* **136**.

Dätig, M. & Schlurmann, T. 2004 Performance and limitations of Hilbert-Huang transformation (HHT) with an application to irregular water waves. *Ocean Eng.* **31** (15), 1783–1834.

Davis, R. W., Moore, E. F. & P.Purtell, L. 1984 A numerical-experimental study of confined flow around rectangular cylinders. *Physics of Fluids* **27** (1), 46–59.

Deering, R. & Kaiser, J. F. 2005 The use of a masking signal to improve empirical mode decomposition. In *ICASSP IEEE*, *485-488*, vol. 4.

Du, Q., emelianenko, M. & Ju, L. 2007 Convergence of the lloyd algorithm for computing centroidal Voronoi tessellations. *SIAM journal on numerical analysis* **44** (1), 102–119.

Du, Q., Faber, V. & Gunzburger, M. D. 1999 Centroidal Voronoi tessellations: Applications and algorithms. *SIAM Review* **41** (4), 637–676.

Du, Q., Gunzburger, M. D. & Ju, L. 2003 Constrained centroidal Voronoi tessellations for surfaces. *SIAM Journal on Scientific Computing* **24** (5), 1488–1506.

Everson, R. & Sirovich, L. 1995 Karhunen-Loeve procedure for gappy data. *J. Opt. Soc. Am. A* **12**, 1657–1664.

Ewing, D. & Citriniti, J. 1999 Examination of a LSE/POD complementary technique using single and multi-time information in the axisymmetric shear layer. In *Proceedings of the IUTAM Symposium on simulation and identification of organized structures in flows* (ed. Sorensen, Hopfinger & Aubry), *Fluid Mechanics and Its Applications*, vol. 52, pp. 375–384. Springer.

Falb, P. L. 1970 Review: [untitled]. *SIAM Review* **12** (2), 308–309.

Flandrin, P., Rilling, G. & Gonçalvès, P. 2004 Empirical mode decomposition as a filter-bank. *IEEE Signal Process. Lett.* **11**, 112–114.

Galletti, B., Bottaro, A., Bruneau, C. & Iollo, A. 2006 Accurate model reduction of transient and forced flows. *Europ. J. Mech. / B Fluids* **26**, 354–366.

Galletti, B., Bruneau, C. H., Zannetti, L. & Iollo, A. 2004 Low-order modelling of laminar flow regimes past a confined square cylinder. *J.Fluid Mech.* **503**, 161–170.

Gillies, E. A. 1998 Low-dimensional control of the circular cylinder wake. *J. Fluid Mech.* **371**, 157–178.

Golub, G. & Van Loan, C. 1990 Matrix computations. Baltimora: The Johns Hopkins University Press.

Gordeyev, S. 2000 POD, LSE and Wavelet decomposition: Literature review. *University of Notre Dame* .

Graham, W. R., Peraire, J. & Tang, K. Y. 1998 Optimal control of vortex shedding using low-order models. part i. *Int. J. Num. Meth. Eng.* **44**, 945–972.

Grepl, M. A., Maday, Y., Nguyen, N. C. & Patera, A. T. 2005 Efficient reduced-basis treatment of nonaffine and nonlinear partial differential equations. *ESAIM-Mathematical Modelling and Numerical Analysis* **41(3)**, 157–181.

Grepl, M. A. & Patera, A. T. 2005 A posteriori error bounds for reduced-basis approximations of parametrized parabolic partial differential equations. *ESAIM-Mathematical Modelling and Numerical Analysis* **39 (1)**, 157–181.

Guillard, H. & Viozat, C. 1999 On the behaviour of upwind schemes in the low Mach number limit. *Computers and Fluids* **28**, 63–86.

Gunzburger, M. 1997a Introduction into mathematical aspects of flow control and optimization. In *In Lecture series 1997-05 on inverse design and optimization methods*. Von Kármán Institute for Fluid Dynamics.

Gunzburger, M. 2003 Perspectives in flow control and optimization. In *SIAM: New York*.

Hansen, P. 1997 *Rank-Deficient and Discrete Ill-Posed Problems: Numerical Aspects of Linear Inversion*. Philadelphia, PA, USA: SIAM.

Hinze, M. & Volkwein, S. 2005 Proper orthogonal decomposition surrogate models for nonlinear dynamical systems: Error estimates and suboptimal control. *Dimension Reduction of Large-Scale Systems* pp. 261–306.

Hoepffner, J., Chevalier, M., Bewley, T. & Henningson, D. 2005 State estimation in wall-bounded flow systems. Part 1. Perturbed laminar flows. *J.Fluid Mech.* **534**, 263–294.

Huang, N. E., Shen, Z. & Long, S. R. 1999 A new view of nonlinear water waves: the Hilbert spectrum. *Annual Review of Fluid Mech.* **31**, 417–457.

Huang, N. E., Shen, Z., Long, S. R., Wu, M. C., Shih, H. H., Zheng, Q., Yen, N., Tung, C. C. & Liu, H. H. 1998 The empirical mode decomposition and the Hilbert spectrum for nonlinear and non-stationary time series analysis. *Proc. of the Royal society of London Series A- Math. Phys. Eng sciences* **454** (1971), 903–995.

Iollo, A., Dervieux, A., Désiéri, J. A. & Lanteri, S. 2000 Two stable POD-based approximations to the Navier-Stokes equations. *Comput. Visual. Sci.* **3**, 61–66.

Ito, K. & Ravindran, S. S. 1998 A reduced-order method for simulation and control of fluid flows. *Journal of Computational Physics* **143(2)**, 403–425.

Joliffe, I. 1986 Principal component analysis. Springer-Verlag.

KALB, V. L. & DEANE, A. E. 2007 An intrinsic stabilization scheme for proper orthogonal decomposition based low-dimensional models. *Phys. Fluids* **19**, 054106.

KARHUNEN, K. 1946 Zur spektral theorie stochasticher prozesse. In *Ann. Acad. Sci. Fennicae*, *Ser. A1*, vol. 34.

KERVIK, E. A., BRANDT, L., HENNINGSON, D. S., HOEPFFNER, J., MARXEN, O. & SCHLATTER, P. 2006 Steady solutions of the navier-stokes equations by selective frequency damping. *Physics of Fluids* **18** (6), 068102.

KIJEWSKI-CORREA, T. & KAREEM, A. 2007 Nonlinear signal analysis: time-frequency perspectives. *J. of Eng. Mechanics-ASCE* **133** (2), 238–245.

KITAGAWA, T., FUJINO, Y., KIMURA, K. & MIZUNO, Y. 2002 Wind pressures measurement on end-cell-induced vibration of a cantilevered circular cylinder. *J. Wind Eng. Ind. Aerodyn.* **90**, 395–405.

LE DIMET, F. & TALAGRAND, O. 1986 Variational algorithms for analysis and assimilation of meteorological observations: theoretical aspects. *Tellus Series A* **38**, 97–+.

VAN LEER, B. 1977 Towards the ultimate conservative scheme. iv: A new approach to numerical convection. *J. Comput. Physics* **23**, 276–299.

LI, F. & AUBRY, N. 2003 Feedback control of a flow past a cylinder via transverse motion. *Phys. Fluids* **15**, 2163–76.

LOÈVE, M. 1955 Probability theory. Van Nostrand.

LUMLEY, J. L. 1967 The structure of inhomogeneous turbulent flows. In *Atmospheric Turbulence and Radio Wave Propagation,* edited by A. M. Yaglom and V. L. Tatarski, Nauka, Moscow pp. 166–178.

LUO, S., CHEW, Y. & NG, Y. 2003 Characteristics of square cylinder wake transition flows. *Physics of Fluids* **15** (9), 2549–2559.

MA, X. & KARNIADAKIS, G. E. 2002 A low-dimensional model for simulating three-dimensional cylinder flow. *J. Fluid Mech.* **458**, 181–190.

MARTIN, R. & GUILLARD, H. 1996 A second order defect correction scheme for unsteady problems. *Computers and Fluids* **25** (1), 9–27.

MIN, C. & CHOI, H. 1999 Suboptimal feedback control of vortex shedding at low Reynolds numbers. *Journal of Fluid mechanics* **401**, 123–156.

MOORE, B. C. 1981 Principal component analysis in linear systems: Controllability, observability, and model reduction. *IEEE Trans. Automat. Contr* **26 (1)**.

NAGUIB, A. M., WARK, C. E. & JUCKENHÖFEL, O. 2001 Stochastic estimation and flow sources associated with surface pressure events in a turbulent boundary layer. *Phys. Fluids* **13**, 2611–2626.

Noack, B., Afanasiev, K., Morzynski, M., Tadmor, G. & Thiele, F. 2003 A hierarchy of low-dimensional models for the transient and post-transient cylinder wake. *Comp. Meth. Appl. Mech. Eng.* **497**, 335 – 363.

Noack, B., Papas, P. & Monkewitz, P. 2005 The need for a pressure-term representation in empirical galerkin models of incompressible shear flows. *J. Fluid Mech.* **523**, 339–365.

Okajima, A. 1982 Strouhal numbers of rectangular cylinders. *J. Fluid Mech. Digital Archive* **123**, 379 – 398.

Olhede, S. & Walden, A. T. 2004 The Hilbert spectrum via wavelet projections. In *Proc. Roy. Soc. London A*, , vol. 460, pp. 955–975.

Park, Seon K., X. L., ed. 2009 *Data assimilation for Numerical Weather Prediction : a review*, , vol. XVIII. 475 p. 326 illus., Hardcover.

Protas, B. 2004 Linear feedback stabilization of laminar vortex shedding based on a point vortex model. *Physics of Fluids* **16** (12), 4473–4488.

Qin, S. R. & Zhong, Y. M. 2006 A new envelope algorithm of Hilbert-Huang transform. *Mech. Syst. Sign. Proc.* **20**, 1941–1952.

Ravindran, S. 2007 Optimal boundary feedback flow stabilization by model reduction. *Comp. Meth. Appl. Mech. Eng.* **196**, 2555–2569.

Ravindran, S. S. 2006 Reduced-order controllers for control of flow past an airfoil. *International Journal for Numerical Methods in Fluids* **50**, 531–554.

Rempfer, D. 2000 On low-dimensional Galerkin models for fluid flow. *Theor. Comput. Fluid Dyn.* **14**, 75–88.

Rempfer, D. & Fasel, H. 1994 Evolution of three-dimensional coherent structures in a flat-plate boundary layer. *J. Fluid Mech.* **260**, 351–375.

Rilling, G., Flandrin, P. & Gonçalvès, P. 2003 On empirical mode decomposition and its algorithms. *IEEE-EURASIP Workshop on Nonlinar Sign. Image Proc.* **NSIP-03**, 1–5.

Robert, C., Durbiano, S., Blayo, E., Verron, J., Blum, J. & Dimet, F.-X. L. 2005 A reduced order strategy for 4d-var data assimilation. *J. Mar. Syst.* **57**.

Robert, C., E. B. & Verron, J. 2006 Reduced-order 4d-var: A preconditioner for the incremental 4d-var data assimilation method **33**, L18609:1–4.

Robichaux, J., Balachandar, S. & Vanka, S. P. 1999 Three-dimensional Floquet instability of the wake of square cylinder. *Physics of Fluids* **11** (3), 560–578.

Roe, P. 1981 Approximate riemann solvers, parameters vectors, and difference schemes. *J. Comput. Physics* **43**, 357–372.

Rowley, C. & Williams, D. R. 2006 Dynamics and control of high reynolds number flow over open cavities. *Annual Review of Fluid Mechanics* **38**, 251–276.

Rowley, C. W. 2005 Model reduction for fluids using balanced proper orthogonal decomposition. *International Journal of Bifurcation and Chaos* **15(3)**, 997–1013.

Saha, A. K., Biswas, G. & Muralidhar, K. 2003 Three-dimensional study of flow past a square cylinder at low Reynolds number. *International Journal of Heat and Fluid Flow* **24**, 54–66.

Schmit, R. & Glauser, M. N. 2005 Use of low-dimensional methods for wake flowfield estimation from dynamic strain. *AIAA Journal* **43** (5), 1133–1136.

Senroy, N., Suryanarayanan, S. & Ribeiro, P. F. 2007 An improved Hilbert-Huang method for analysis of time-varying waveforms in power quality. *IEEE Trans. on Power Systems* **22** (4), 1843–1850.

Sirovich, L. 1987 Turbulence and the dynamics of coherent structures. Parts I,II and III. *Quarterly of Applied Mathematics* **XLV**, 561–590.

Sohankar, A., Norberg, C. & Davidson, L. 1999 Simulation of three-dimensional flow around a square cylinder at moderate Reynolds numbers. *Physics of Fluids* **11(2)**, 288–306.

Spazzini, P., Iuso, G., Onorato, M. & Zurlo, N. 1999 Design, test and validation of a probe for time-resolved measurement of skin friction. *Measurement Science and Technology* **10** (7), 631–639.

Sreenivasan, K. R. 1985 On the finite-scale intermittency of turbulence. *J. Fluid Mech.* **151**, 81–103.

Tadmor, G., Noack, B., Morzyński, M. & Siegel, S. 2004 Low-dimensional models for feedback flow control. Part II: Controller design and dynamic estimation. In *2nd AIAA Flow Control Conference*, pp. 1–12. Portland, Oregon, U.S.A., June 28 – July 1, 2004, aIAA Paper 2004-2409 (invited contribution).

Telib, H., Manhart, M. & Iollo, A. 2004 Analysis and low-order modeling of the inhomogeneous transitional flow inside a T-mixer. *Phisics of Fluids* **8**, 2717–2731.

Tinney, C., Coiffet, F., Delville, J., Hall, A., Jordan, P. & Glauser, M. 2006 On spectral linear stochastic estimation. *Experiments in Fluids* **45** (5), 763–775.

Venturi, D. & Karniadakis, G. 2004 Gappy data and reconstruction procedures for flow past a cylinder. *J. Fluid Mech.* **519**, 315–336.

WEI, M. & ROWLEY, C. 2006 Low-dimensional models of a temporally evolving free shear layer. *AIAA Paper 2006-3228, 36th AIAA Fluid Dynamics Conference and Exhibit* .

WEILAND, C. & VLACHOS, P. P. 2009 A mechanism for mitigation of blade-vortex interaction using leading edge blowing flow control. *Experiments in Fluids* **47** (3), 411–426.

WELLER, J. 2009 Réduction de modèles par identification de systèmes et application au contrôle du sillage d'un cylindre. In *PhD Thesis*. IMB, Bordeaux.

WELLER, J., CAMARRI, S. & IOLLO, A. 2009 Feedback flow control design by low-order modeling for laminar wake stabilization. *Journal of Fluid Mechanics* **634**, 405–418, to appear.

WILLCOX, K. 2000 Reduced-order aerodynamic models for aeroelastic control of turbomachines. In *PhD Thesis*. Massachusetts Institute of Technology.

WILLCOX, K. 2006 Unsteady flow sensing and estimation via the gappy proper orthogonal decomposition. *Comp. Fluids* **35**, 208–226.

WU, F. & QU, L. 2008 An improved method for restraining the end effect in empirical mode decomposition and its applications to the fault diagnosis of large rotating machinery. *J. of Sound and Vibration* **314**, 586–602.

WU, Z. & HUANG, N. E. 2004 A study of the characteristics of whire noise using the empirical mode decomposition method. *Proc. Roy. Soc. London A* **460**, 1597–1611.

XU, Z., HUANG, B. & LI, K. 2010 An alternative envelope approach for empirical mode decomposition. *Digital Signal Processing* **20**, 77–84.